Colección de Estudios de Física 89

X-ray magnetic circular dichroism using x-ray phase retarders in the hard x-ray region: Exploring the magnetism of the conduction band and of non-magnetic atoms

Roberto Boada Romero

X-ray magnetic circular dichroism using x-ray phase retarders in the hard x-ray region: Exploring the magnetism of the conduction band and of non-magnetic atoms

Colección de Estudios de Física
Vol. 89

Esta colección recoge las tesis presentadas en el Departamento de Física de la Materia Condensada de la Universidad de Zaragoza desde su constitución en 1987.

Colección de Estudios de Física Vol. 89

X-ray magnetic circular dichroism using x-ray phase retarders in the hard x-ray region: Exploring the magnetism of the conduction band and of non-magnetic atoms

Roberto Boada Romero

Prensas Universitarias de Zaragoza

BOADA ROMERO, Roberto

X-ray magnetic circular dichroism using x-ray phase retarders in the hard x-ray region : exploring the magnetism of the conduction band and of non-magnetic atoms / Roberto Boada Romero. — Zaragoza : Prensas Universitarias de Zaragoza, 2011

XIII, 169 p. ; 24 cm. — (Colección de Estudios de Física ; 89)

Bibliografía: p. 161-169. — ISBN 978-84-15274-01-8

Magnetismo–Tesis doctorales

537.6(043.2)

1.ª edición, 2011

Prensas Universitarias de Zaragoza. Edificio de Ciencias Geológicas, c/ Pedro Cerbuna, 12, 50009 Zaragoza, España. Tel.: 976 761 330. Fax: 976 761 063
puz@unizar.es http://puz.unizar.es

Impreso en España
Imprime: Servicio de Publicaciones. Universidad de Zaragoza
D.L.: Z- 1011/2011

Va por ustedes...

La inspiración existe, pero tiene que encontrarnos trabajando.

Inspiration exists, but it has to find us working.

Picasso (1881 - 1973)

Contents

Preface

Since the advent of the first dedicated synchrotron radiation sources, many efforts have been done for developing new X-ray based techniques for material science research. In particular, the use of X-rays to address the magnetic properties of the matter has focused a great deal of attention. X-ray Magnetic Circular Dichroism (XMCD) features prominently among the experimental techniques recently appearing. XMCD combines element and shell specificity, inherent to a core-level spectroscopy, with the possibility of obtaining a quantitative determination of spin and orbital magnetic moments by applying magneto–optical sum rules.

These capabilities are commonly exploited to study the magnetic behavior of localized states carrying a magnetic moment, i.e., the f-states of Lanthanides and Actinides ($M_{4,5}$-edges), and the d-states of transition metals ($L_{2,3}$-edges). However, the application of XMCD to study the magnetism of delocalized states is quite scarce. The main reason for such shortage resides in the difficulty of extracting direct quantitative magnetic information when XMCD probes these delocalized states.

This limitation affects the magnetic characterization of the $4p$ states (K-edge) of the $3d$ transition metals (T) and the $5d$ states ($L_{2,3}$-edges) of the rare-earths (R). However, the exact knowledge of their magnetic behavior renders fundamental in several cases, as in the R–T intermetallics, because the conduction band states mediate the R($4f$)-T($3d$) exchange interaction and, thus, they tune the magnetic properties of these materials.

A previous XMCD work performed on R-T systems provided a new insight into the interpretation of the T K-edge and R $L_{2,3}$-edges XMCD spectra in such a class of materials [1]. This work demonstrated that the XMCD spectra at the T K- and R $L_{2,3}$-edges are a simultaneous fingerprint of the magnetism of both Fe and rare-earth sublattices even when only an atomic element is tuned.

In this Thesis we aim to extend the current application of the XMCD technique to the study of delocalized states. Our objectives are twofold. On the

one hand, we have investigated the possibility of extracting quantitative magnetic information from the analysis of the rare-earth $L_{2,3}$- and transition metal K-edges XMCD in R-T intermetallics, especially regarding the R($5d$)–T($3d$) hybridization. This study is of special relevance for the understanding of unexpected magnetic effects that have been observed to emerge at the nanoscale in compounds which are *non-magnetic*[1] in their bulk state. In addition, this work reports the first XMCD measurements performed on the BM25–A SpLine beamline at the ESRF. To this end we have designed, built-up and operated an experimental setup for measuring XMCD on a standard X-ray Absorption Spectroscopy (XAS) beamline.

Overview:

Chapter 1 is devoted to the basic theoretical background related to both the magnetism of R-T intermetallic materials and the X-ray spectroscopy techniques employed in this work: XAS and XMCD.

In **Chapter 2** we present a description of the experimental techniques implicated in the development of this Thesis. Some of these techniques, such as X-ray diffraction (XRD) and magnetization measurements are of standard use in the study of intermetallic compounds, so that only a brief review will be given. A more detailed description is deserved to both X-ray Absorption Spectroscopy (XAS) and X-ray Magnetic Circular Dichroism (XMCD) techniques as they are less commonly used and constitute the main body of the experimental work done in this Thesis. On the other hand, the structural and magnetic characterization of the synthesized samples are presented in **Chapter 3**.

In **Chapter 4** we show a systematic XMCD investigation in selected R-T intermetallic systems with different magnetically active atoms (RT_2 and R_6Fe_{23} with T = Fe, Co). This detailed study has allowed us to develop a disentanglement procedure in order to unravel the dichroic $XMCD_R$ and $XMCD_T$ contributions of the total XMCD spectra recorded at the T K- and at the R $L_{2,3}$-edges. In particular, we have demonstrated the additivity of these contributions in the XMCD spectra involving the conduction band states. The acquired knowledge has been finally applied to study the magnetic compensation phenomena on $R_{1-x}R'_xFe_2$ compounds from a microscopic point of view.

In **Chapter 5** we present a XMCD study of the magnetic polarization of *non-magnetic* atoms in the presence of competing magnetic sublattices, rare-earth and Fe. We have performed this study in a tailored series of compounds, $R_{1-x}R'_x(Fe_{1-y}Al_y)_2$ and $R(Fe_{0.9}M_{0.1})_2$ (M = Ga, Ge), in which the polarization of the *non-magnetic* atoms is modified by varying the rare-earth and Fe

[1] Atoms which do not possess a localized magnetic moment.

content in a controlled way.

In **Chapter 6** we present a systematic study of the Element Specific Magnetic Hysteresis measurements performed by using XMCD (ESMH) on R-T intermetallic systems at Fe K-, R L_2- and Fe L_3-edges. We discuss about the capability of the ESMH technique to unravel the magnetism of the probed atom.

Finally, in **Chapter 7** we report on the implementation of an X-ray phase retarder to perform XMCD measurements in the BM25-A SpLine beamline of the ESRF.

Chapter 1

Basic theoretical concepts

1.1 Magnetic interactions in R-T intermetallic compounds.

Intermetallic compounds based on rare-earth (R) and transition metal (T) elements have attracted considerable attention during the last decades, owing to their industrial interest as permanent magnets. The combination of these elements in a single compound may lead to materials exhibiting high magnetic ordering temperature (associated to the presence of Fe), large magnetization and large magnetocrystalline anisotropy (owing to the R) [2, 3].

In R-T intermetallic compounds the spins of the magnetic atoms (coming from T($3d$) and R($4f$) unpaired electrons) interact via an exchange interaction which is supposed to be of the Heisenberg type:

$$\mathcal{H} = -\sum_{i,j} J_{ij} S_i . S_j \tag{1.1}$$

where S_i and S_j are the spin corresponding to the i and j sites. J_{ij} is the exchange parameter of the exchange interaction between these two spins, and gives information about the type (ferro or antiferromagnetic) and magnitude of the interaction.

Since three different kinds of spin pairs can be distinguished in the R-T compounds, the exchange interactions are usually classified as: T-T, R-T and R-R. These interactions depend on the specific atoms involved, since their electronic configurations are very different:

$$\text{Transition metal} = \text{T} :: [Ar]3d^n4s^2$$
$$\text{Rare-earth} = \text{R} :: [Xe]4f^n5d^16s^2$$

In general, in compounds where the transition metal carries a well established moment (Fe *vs.* Co), the T-T interaction dominates. Regarding those interactions involving the rare-earth (R-T and R-R), the R-T one is the most important because is the responsible of the coupling between the two magnetic sublattices. In the following we provide a brief outline of the nature of these magnetic interactions.

R-R interaction

The rare-earth magnetic moment arises from unpaired electrons in the well-localized $4f$ shell. Since these electrons lie deep inside the atom, the spin-orbit coupling is much larger than the crystal electric field (CEF) interaction. Consequently, the total angular momentum is a good quantum number and they can be dealt as localized magnetic moments. The magnetism of these electrons can be regarded as basically the same as in the free atom. Moreover, owing to the spatial extent of the $4f$ wave function, being rather small compared to interatomic distances, there is no overlap between $4f$ wave functions and, consequently, the R-R interaction propagates in an **indirect** way. Thus, it is assumed that the R-R interaction is mediated by the polarization of the conduction electrons, leading to a long-range spin interaction. Usually, this interaction is supposed to be a long-range oscillatory RKKY (Ruderman, Kittel, Kasuya, Yoshida) type, which is mediated by the s electrons of the rare-earth [4].

Because of the highly localized character of the $4f$ magnetic moments, the R-R interaction is about one order of magnitude weaker than the T-T and R-T ones. For this reason the R-R interaction is usually neglected in the study of R-T systems.

T-T interaction

The magnetic moment of a T atom originates from unpaired spins in the $3d$ shell. The $3d$ electrons are the outer electrons of the atom and their interaction with the neighboring charges is very large. The crystal electric field is therefore much stronger than the spin-orbit coupling, the orbital moment L is quenched (partly or completely) and J is not longer a good quantum number. More important, the $3d$ wave functions have a large spatial extent and, thus, a strong overlap with those of neighboring atoms. Owing to this overlap, the $3d$ electrons are not longer localized and no longer accommodated into atomic energy levels. These energy levels have broadened into energy bands

whose width depends on the interatomic separation. As a consequence, the $3d$ electrons do not have a well defined quantum number S and their magnetic behavior is best described by an **itinerant band-type model** [5]. However, the width of the $3d$ band is small and this implies that the $3d$ electrons are still rather localized at the $3d$ atoms [2]. This justifies the use of local moments in molecular field approximations for describing the magnetic coupling between $3d$ moments (T-T interaction) [6].

The interaction between the $3d$ electrons is the strongest exchange interaction in the R-T compounds.

R-T interaction

The R-T exchange interaction is larger than the R-R exchange and smaller, although of the same order of magnitude, than the T-T one. Experimental data indicate that for all the R-T intermetallics without exception, the coupling between the rare-earth and the transition metal moments is always antiferromagnetic for heavy rare-earths (R with more than half-filled $4f$ shell, $J = L + S$), and ferromagnetic for compounds with light R element (with a less than half-filled $4f$ shell, $J = L - S$) [2, 3].

In contrast to the R-R and T-T interactions, the R-T interaction is not well described by any theoretical model in the sense that no theoretical formalism can quantitatively account for this interaction. The main reason is the difficulty into treating the interaction between the highly localized R($4f$) and the itinerant-like T($3d$) magnetic moments on an equal footing. Based on the universal coupling scheme experimentally observed, *Campbell* proposed a phenomenological description for the R-T coupling in which the $5d$ spins of the rare-earth play a critical role [7]. Due to the localized character of R($4f$) moments, the R-T exchange is thought to be an indirect interaction involving an intra-atomic exchange between the R($4f$) and R($5d$) electrons, and an inter-atomic interaction between the spin polarized R($5d$) and the T($3d$) electrons [2]. According to Campbell's model, the R($4f$) spins are coupled parallel to the R($5d$) spins, while the coupling between the rare-earth and the transition metal spins is always antiparallel. If, in addition, we take into account the $L-S$ coupling of the R($4f$) electrons and the quenching of the orbital moment of T($3d$) electrons, this coupling scheme leads to the experimentally observed magnetic couplings, as illustrated in Fig. 1.1. Later, *Yamada et al.* and *Brooks et al.* proposed a simple approach, taking into account the hybridization between R($5d$) and Fe($3d$) bands, to account for this universal coupling picture. [8–14]

As a matter of fact, estimates of the R-T interaction are commonly derived from the experimental data by using a **mean-field two-sublattice model**. Within this framework the system can be divided into two magnetic sublat-

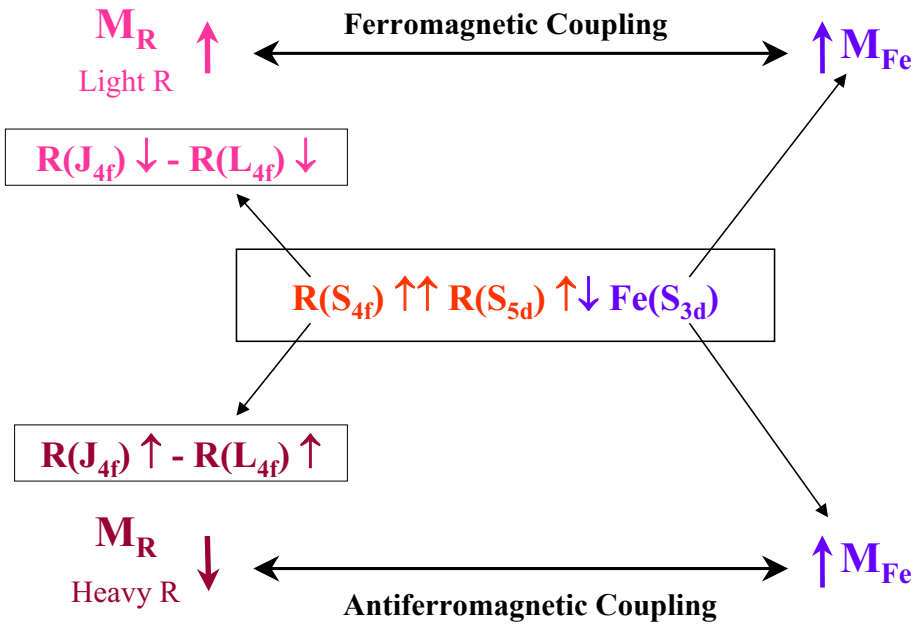

Figure 1.1: Schematic layout of the arrangement of the couplings that take place between the different magnetic moments in the R-T intermetallic compounds. See details in the text.

tices: R and T. Then, the magnetic behavior of the system can be described by the three types of interactions previously described: i) the R-R interaction between the magnetic moments within the R sublattice, ii) the T-T interaction between the magnetic moments of the T sublattice, and iii) the R-T intersublattice interaction. This model does not describe the nature of the interactions themselves, but it was developed to provide a simple way to quantitatively deal with them. Therefore, the interactions are described via the mean fields experienced by the rare-earth, H_R, and transition-metal, H_T, atoms:

$$H_R = H_0 + n_{RR}M_R + n_{RT}M_T$$

$$H_T = H_0 + n_{RT}M_R + n_{TT}M_T, \tag{1.2}$$

where H_0 is the external applied magnetic field, M_R and M_T represent the magnetization of the R and T sublattices, respectively, and n_{AB} are the macroscopic molecular field coefficients. These coefficients n_{AB} are related to

the J_{AB} ones[1] through:

$$n_{RR} = 2Z_{RR}J_{RR}(g_J - 1)^2/g_J^2\mu_B^2 N_R, \quad n_{TT} = Z_{TT}J_{TT}/2\mu_B^2 N_T,$$
$$n_{RT} = Z_{RT}J_{RT}(g_J - 1)/g_J\mu_B^2 N_T, \quad n_{TR} = Z_{TR}J_{TR}(g_J - 1)/g_J\mu_B^2 N_R \quad (1.3)$$

where Z_{RR} and Z_{RT} are respectively the number of the R and T nearest neighbors of a R atom, while and Z_{TR} and Z_{TT} those of the R and T nearest neighbors of a T atom. N_R (N_T) are the number of R (T) atoms per formula unit (f.u.), and g_J is the Landé factor. J_{ij} parameters are more appropriate to compare the intensity of the interactions. However, very often J_{ij} cannot be directly determined from experimental data, whereas this is possible for n_{ij}.

It can be shown that the previous approach leads to the following expression [15]:

$$T_C = \frac{1}{2}\left(T_T + T_R + \sqrt{(T_T - T_R)^2 + 4T_{RT}^2}\right) \quad (1.4)$$

where

$$T_T = n_{TT}C_T, \qquad T_R = n_{RR}C_R, \qquad T_{RT} = n_{RT}\sqrt{C_R C_T},$$
$$C_R = N_R g_J^2 J(J+1)\mu_B^2/3k_B \qquad and \qquad C_T = N_T g_T^2 S(S+1)\mu_B^2/3k_B$$

Once the Curie temperatures have been experimentally determined, the values of n_{TT}, n_{RT} and n_{TR} are obtained from these expressions. For a given R-Fe series, n_{TT} is calculated from the value of T_T, which is usually identified with the Curie temperature of the isostructural compound in which no magnetic rare-earth is present, i.e., R = Y or Lu. Conversely, n_{RR} can be determined from T_R, whose value is chosen as corresponding to the T_C of the isostructural compound in which T is non-magnetic, i.e., T = Ni. However, it is customary to neglect T_R in Eq. (1.4), since it is one order of magnitude smaller than T_T and T_{RT}. This latter simplification allows us to obtain the values of n_{RT} from Eq. (1.4) for all the compounds through a given R-T series:

$$n_{RT} = \frac{\sqrt{T_C(T_C - T_T)}}{\sqrt{C_R C_T}} \quad (1.5)$$

The value of n_{RT} is found to decrease as the atomic number of the rare-earth increases (from Pr to Tm). Additionally, in the case of light R, n_{RT} is

[1] J_{AB} are the coefficients of the exchange interaction between spins. Notice that in Eq. (1.1) the i and j subscripts are related to the i and j sites respectively. Within a mean-field model, however, A and B subscripts are related to the type of atom, R or T, ignoring the exact position in the lattice and distances between atoms.

about twice larger than for heavy R. According to *Belorizky et al.* [16], this reduction of n_{RT} is related to the decrease of the R($4f$)-R($5d$) interaction as the atomic number of R increases. In turn, this decrease is associated with the spatial reduction of the R($4f$) shell, which is about 10 times larger than the spatial reduction of the R($5d$) shell.

1.2 X-ray Absorption Spectroscopy (XAS)

XAS: basic principles

X-ray absorption spectroscopy is based on the interaction between electromagnetic radiation and matter. Photons passing through matter interact by means of three different processes: scattering, photoelectric absorption and pair production. In the energy region of our interest (up to $\sim$ 100 keV) photoabsorption is the dominating process.

The physical process of X-ray absorption is the excitation of electrons from deep core atomic levels by the absorption of an X-ray as is schematized in Fig. 1.2.

Initial core state	Final state	Edge
1s	*np*	**K**
2s	*np*	**L_1**
2p	*nd*	**$L_{2,3}$**
3d	*nf*	**$M_{4,5}$**

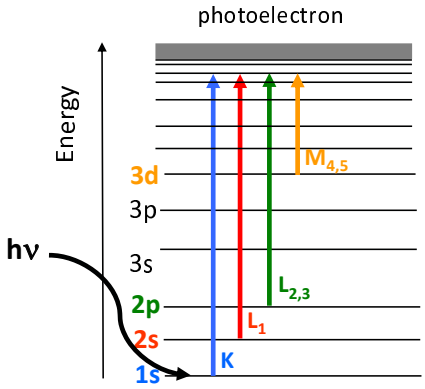

Figure 1.2: Scheme of the absorption process of an X-ray photon by a core electron. Each characteristic transition is determined by the initial and final states of the excited electron and the absorption edge is labeled by a letter and subindex to denote the initial subshell of the core electron.

According to Fermi's Golden Rule the transition probability per unit of time from a core to a final state can be written as:

$$W = \frac{2\pi}{\hbar} | < f|H_{int}|i > |^2 \rho_f(\hbar\omega - E_c), \tag{1.6}$$

where $| < f|H_{int}|i > |$ is the matrix element of the electromagnetic field operator, H_{int}, between the initial core-electron state $|i>$ and the final valence state $|f>$, $\rho_f(E)$ is the density of empty states at the energy E above the Fermi level, and E_c is the core-electron binding energy. The evaluation of this transition probability requires several approximations concerning both the description of the initial and final states and the interaction operator.

In relation to the description of initial and final states, the simplest approach to account for the X-ray absorption process employs the single-electron model as a starting point. In this picture, all the electrons of the system remain passive during the absorption process excepting the photo-excited core electron, which is promoted to the unoccupied states of the system. This picture allows an easy description of both the core initial states and the final states (bands, continuum states), as only the excited electron is taken into account.

Regarding the interaction operator, it is customary to make the electric dipolar approximation,[2]

$$| < i|H_{int}|f > | \propto | < i|\varepsilon \cdot \mathbf{r}|f > | \tag{1.7}$$

where ε is the polarization vector.

Since the electric dipole operator, $\varepsilon \cdot \mathbf{r}$, is odd and acts only on the radial part of the electronic wave-function (the X-ray photon carries angular momentum 1 and no spin), transitions are only possible between states which have opposite parity and which differ in angular momentum by one. These are the so-called **electric dipole selection rules**:

$$\Delta l \; = \; \pm 1 \qquad and \qquad \Delta s \; = \; 0 \tag{1.8}$$

It is important to highlight that the use of X-rays to excite the electrons along with the the dipole selection rules offers unique capabilities in comparison with typical laser light (∼1–4 eV):

- X-rays are energetic enough to excite electrons from core shells. As the inner-shell absorption occurs at energies that are characteristic of a given element, this method is **element-selective**.

[2]This approximation is correct if the wavelength is larger than the atomic size. If $\lambda \approx 1$ Å, this approximation becomes invalid, except for r << 1 Å, which is generally the case for core electrons. In the soft X-ray range ($\lambda \geq 5$ Å) all the electrons can be treated in this approximation. In the hard X-ray range ($0.5 \leq \lambda \leq 5$ Å), this approximation remains only valid if we consider interactions with very localized core electrons.

- By tuning the X-ray energy, and due to the dipole selection rules, it is possible to select the symmetry of the final states (p-, d-, f-like states). In the frame of the single electron approximation, and considering dipolar transitions only, the selection rules dictate that, for instance, an excited $1s$ core electron can only be sent to an empty level with p symmetry, while if a $2p$ electron is excited both s- and d-states are probed.[3] Hence, XAS spectra yields **shell selective** information.

XAS spectrum: structural and electronic information

As a result of this interaction between electromagnetic radiation and matter, an incident beam passing through any sort of material will be attenuated. The expression relating the intensity of the incident beam, I_0, and the intensity of the beam after crossing a sample of thickness x, I, is the so-called Beer-Lambert-Bouguer law [18]:

$$I = I_0 e^{-\mu x} \tag{1.9}$$

where μ is the absorption coefficient, which depends on the specific atom in a particular compound. μ smoothly varies with the photon energy except at some specific energies, called absorption edges, where an abrupt increase occur. These jumps correspond to the photon having enough energy to excite an electron from a core state. This is exemplified in Fig. 1.3, where an absorption spectrum is schematically illustrated. In this example two different absorption edges are observed in a sample containing Ho and Lu: at ∼9.244 keV electrons are excited from the $2p_{3/2}$ level of Lu (L_3-edge) whereas at higher energies, ∼9.394 keV, electrons from the $2s$ level of Ho (L_1-edge) are excited.

Depending on the energy of the incoming photons, the X-ray absorption spectrum is usually divided into three regions: the edge, the XANES (X-ray Absorption Near Edge Structure) region, which extends to 30–100 eV beyond the edge, and the EXAFS (Extended X-ray Absorption Fine Structure) region, which extends from 30–100 eV to 600–1000 eV beyond the edge.

The physical origin of the absorption features in the edge region depends on the material, i.e., Rydberg states in free atoms, bound valence states or bound multiple scattering resonances in molecules, unoccupied local electronic states in metals and insulators, etc [19]. Thus, analysis of these edge features in the spectrum of a particular sample can provide information about vacant orbitals, electronic configuration and/or the site symmetry of the absorbing atom.

[3] In the case of the $L_{2,3}$-edges of the lanthanides, the transition to the d final states is favored by a factor of ∼100 when compared to that to the s final states [17].

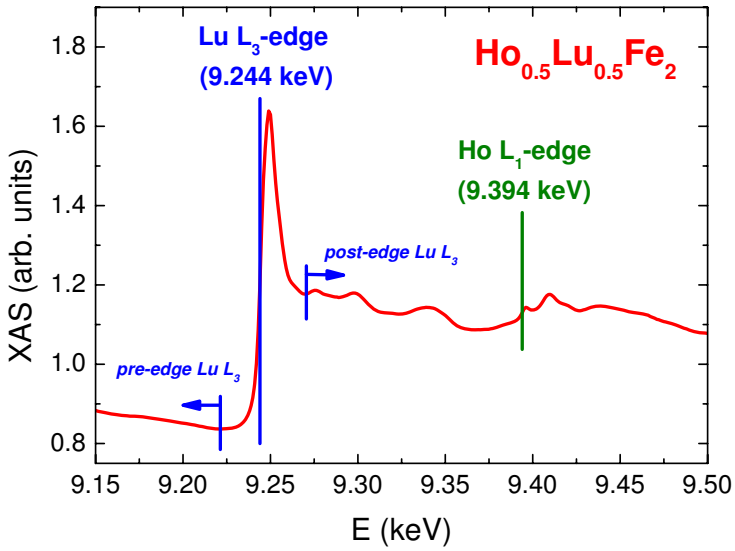

Figure 1.3: XAS spectrum measured at the Lu L_3- and Ho L_1-edges in a sample of $Ho_{0.5}Lu_{0.5}Fe_2$.

For more energetic X-rays, the absorption will vary monotonically in the case of isolated atoms, i.e., gaseous state. However, in condensed matter the absorption coefficient presents oscillations superimposed to the edge step that gradually damp as the X-ray energy increases. These oscillations are caused by the interference of the outgoing and backscattered photoelectron waves, and characterize both the XANES and EXAFS regions of the absorption spectra.

The physical processes giving the XANES and EXAFS structures in the X-ray absorption spectra can be understood as follows: when an X-ray photon of enough energy is absorbed by an atom, a core photoelectron is ejected from the central atom. The kinetic energy of the photoelectron is the difference between the photon's energy and the core binding energy. The outgoing photoelectron can be described by a spherical wave, whose wavelength decreases when the photon energy increases. The outgoing photoelectron is scattered by the neighboring atoms, and the backscattered photoelectron returns to the absorbing (central) atom (see Fig. 1.4). Since the absorption coefficient depends on the dipole matrix element between the initial core state and the photoelectron's final state, which in turn is a superposition of the outgoing and backscattered spherical waves, the phase relationship between outgoing and backscattered waves depends on the photoelectron wavelength and the interatomic distance R_0. The variation of this phase relationship as a function of photon energy influences the final state amplitude at the core site, giving rise to an interference phenomenon which modulates the absorption coefficient [19, 20].

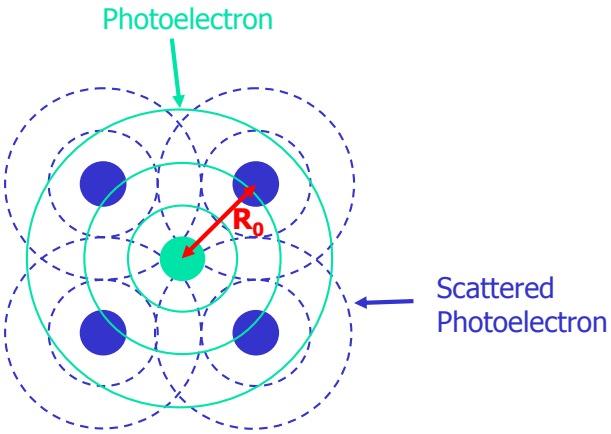

Figure 1.4: Schematic view of the interference of the outgoing photoelectron wave with the scattered wave by the neighboring atoms which surround the excited one.

In the EXAFS region the wave function is mainly backscattered by one of the neighboring atoms in a single-scattering process. This provides information about local structure only in terms of the atomic radial distribution function around the central atom (distances). On the contrary, in the XANES region the excited photoelectron is backscattered by several neighboring atoms due to its low kinetic energy, giving rise to multiple-scattering processes (see Fig. 1.5). It is because of this multiple scattering that XANES contains stereochemical information about the coordination geometry of the absorbing atom (number of neighbors and type, interatomic distances and bond angles) [19, 20].

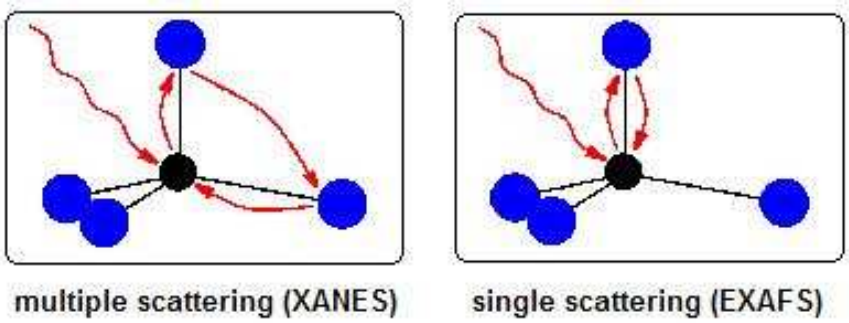

Figure 1.5: Schematic view of photoelectron scattering processes in the multiple scattering regime (XANES region) and in the single-scattering regime (EXAFS).

1.3 X-ray Magnetic Circular Dichroism (XMCD)

XMCD is defined as the difference of the X-ray absorption coefficient $\mu_c = (\mu^- - \mu^+)$ for antiparallel, μ^-, and parallel, μ^+, orientation of the incident photon helicity and the magnetization of the sample.[4] To measure XMCD one basically needs to record XAS spectra under two particular conditions: i) the incident light is circularly polarized and ii) the sample under study has a net magnetization. Therefore, XMCD exhibits the same element and shell selectivity properties as the standard XAS.

In addition, when XAS is performed with polarized X-rays, some extra selection rules have to be taken into account, thus extending the range of information available from this technique. Right circularly polarized light (RCP)[5] carries helicity, i.e., angular momentum along the direction of propagation, +1 (-1 for LCP). Therefore, within the electric dipolar approximation, $| < i|\mathrm{H}_{int}|f > | \propto | < i|\varepsilon \cdot \mathbf{r}|f > |$, and taking into account the conservation of angular momentum,[6] absorption of RCP light gives rise to transitions with $\Delta \mathrm{m}_j = +1$ ($\Delta \mathrm{m}_j$= -1 for LCP). That is, the **dipole selection rules for RCP (LCP) light** are:

$$\Delta j = 0, \pm 1 \quad \Delta l = \pm 1 \quad \Delta s = 0 \quad and \quad \Delta m_j = +1 \quad (\Delta m_j = -1)$$

The additional $\Delta \mathrm{m}_j = \pm 1$ is the origin of XMCD. Due to this extra selection rule XMCD reflects the difference in the density of empty states with different spin moment, thus providing **magnetic information** of the material under study.

One can qualitatively understand the basic principles of XMCD in terms of the **two-step approach** formulated by G. Schütz and coworkers [21, 22]. According to this model, in a first step partially spin-polarized core electrons are excited from an unpolarized initial core state [23] by a circularly-polarized photon. Due to the conservation of angular momentum in the absorption process, the angular momentum of the photon is entirely transferred to the photoelectron. As there is no explicit spin dependence, electronic spins remain

[4] Some authors define XMCD as the difference for antiparallel and parallel orientation of the incident photon helicity and the direction of the majority spins. This definition needs the knowledge of the relationship between $\vec{M}$ and $\vec{S}$ of the selected shell of the selected atom, which is not evident in some cases.

[5] In this Thesis we will use the following **sign convention** for handedness of circularly polarized light: *right* corresponds to positive helicity of photons, + $\hbar$, whereas *left* corresponds to negative helicity, -$\hbar$. This is the convention typically used in high energy physics. In the optics community, it is customary to use the opposite definition.

[6] We are considering that the quantization axis is parallel to the photon propagation direction.

unaltered unless they are coupled to the orbital momenta by a strong spin-orbit interaction. Thus, in the absence of a connection between the spin and orbital part of the electron angular momentum, both LCP and RCP light will excite 50% electrons with spin-up and 50% with spin down. However, when spin-orbit is present, the angular moment of the photon can be partially transferred to the spin through the spin-orbit coupling. The photoelectrons are therefore ejected with a net spin polarization[7] (i.e., there is an imbalance between spin-up and spin-down excited electrons). In the second step the spin-polarized photoelectrons will probe, according to the Pauli exclusion principle, the spin polarization of the final empty states. Consequently, the XMCD spectrum reflects the difference in the density of empty states with different spin moment. The magnetic properties of the sample are probed in the second step because the spin-split valence shell acts as a detector for the spin of the excited photoelectron.

The transition probability is proportional to both the electron polarization, P_e, also called Fano parameter[8] [23], and the spin-density differences $\Delta\rho = \rho\uparrow$ - $\rho\downarrow$, $\rho\uparrow$ and $\rho\downarrow$ being the majority- and minority-like final state densities, in the form:

$$\frac{\mu^-(E) - \mu^+(E)}{\mu^-(E) + \mu^+(E)} = P_e \frac{\Delta\rho}{\rho} \tag{1.10}$$

In order to understand more clearly this picture, we present below the application of this model to the particular case of the $L_{2,3}$-edges XMCD spectra ($2p \rightarrow 3d$ transitions) of a $3d$ transition metal.

In the first step the core electrons are excited by a circularly-polarized photon from the initial states $2p_{3/2}$ (L_3-edge) and $2p_{1/2}$ (L_2-edge) that can be characterized by the quantum numbers j and m_j with $j = l + s$ and $j = l - s$, respectively. For the final $3d$ states we shall assume a Stoner model: there is no spin-orbit splitting and the exchange interaction splits the band into spin-up and spin-down components. Therefore we will have five degenerate spin-up states with density of states, DOS, $\rho\uparrow$ and five degenerate spin-down states with DOS $\rho\downarrow$.

[7] If the photoelectron originates from a spin-orbit split level, e.g. the $p_{3/2}$ level (L_3-edge), its angular momentum can be transferred in part to the spin through the spin-orbit coupling. Right-circularly-polarized photons transfer to the electron a momentum opposite to that from left-circularly-polarized photons; hence, photoelectrons with opposite spins are created in the two cases. Since the $p_{3/2}$ (L_3) and $p_{1/2}$ (L_2) levels have opposite spin-orbit coupling (l + s and l - s, respectively) the spin polarization will be opposite at the two edges.

[8] The Fano parameter can be calculated under certain assumptions: P_e = 0.01 at K- and L_1-edges; P_e = -0.5 at L_2; P_e = 0.25 at L_3-edge. For further details see Ref. [23].

For evaluation of the matrix elements it is useful to express the dipole operator in terms of spherical harmonics:

$$\varepsilon \cdot \mathbf{r} = \sqrt{\frac{4\pi}{3}} Y_1^1 \cdot r \qquad \text{for RCP light} \tag{1.11}$$

$$\varepsilon \cdot \mathbf{r} = \sqrt{\frac{4\pi}{3}} Y_1^{-1} \cdot r \quad \text{for LCP light} \tag{1.12}$$

Since the dipole operator does not act on the spin-state, the matrix elements can be written with regard to a $|l, m_l, s, m_s\rangle$ basis (the product of spherical harmonics and a spin dependent function). According to the dipole selection rules the transitions occur from $2p$ states $|l, m_l\rangle$ into the $3d$ states with $|l+1, m_l \pm 1\rangle$ and the possible matrix elements are obtained from:

$$\sqrt{\frac{4\pi}{3}} \langle l+1, m_l \pm 1 | Y_1^{\pm 1} | l, m_l \rangle \mathcal{R} = -\sqrt{\frac{(l \pm m_l + 2)(l \pm m_l + 1)}{2(21+3)(2l+1)}} \mathcal{R} \tag{1.13}$$

where the radial part is given by:

$$\mathcal{R} = \langle n', l+1 | r | n, l \rangle \tag{1.14}$$

and can be assumed constant for the considered transitions.

The angular part of the matrix elements

$$I_{jm}^{\pm} = \left| \sqrt{\frac{4\pi}{3}} \langle j', m \pm 1 | Y_1^{\pm 1} | j, m \rangle \right|^2 \tag{1.15}$$

is listed in Table 1.1 for the $|jm_j\rangle$ sublevels with respect to the the spin and circular polarization of the X-rays. It shows that at the L_3-edge right circularly polarized light favors excitation of spin-up electrons, while the situation is the opposite at the L_2-edge.

In the second step, according to the Pauli exclusion principle and the different DOS for spin-up, $\rho\uparrow$, and spin-down, $\rho\downarrow$, (in a material with net magnetization) we obtain a different transition probability, i.e., a different absorption for left and right circularly polarized light, as shown in Table 1.2.

It is easy to see from this picture both, why the absorption is different for left and right circularly polarized light and why the XMCD is related to the magnetism of the band we are probing.

In the explanation given above we have used a band (Stoner) model to describe the final $3d$ states. Alternatively, one can consider an atomic picture

j, m_j	m_l, m_s	I^+	I^-
$\frac{3}{2}$, + $\frac{3}{2}$	$\vert+1\uparrow\rangle$	$(\frac{2}{5})\uparrow$	$(\frac{1}{15})\uparrow$
$\frac{3}{2}$, + $\frac{1}{2}$	$\sqrt{\frac{1}{3}}\vert+1\downarrow\rangle + \sqrt{\frac{2}{3}}\vert0\uparrow\rangle$	$(\frac{2}{15})\downarrow + (\frac{2}{15})\uparrow$	$(\frac{1}{45})\downarrow + (\frac{2}{15})\uparrow$
$\frac{3}{2}$, - $\frac{1}{2}$	$\sqrt{\frac{2}{3}}\vert0\downarrow\rangle + \sqrt{\frac{1}{3}}\vert-1\uparrow\rangle$	$(\frac{2}{15})\downarrow + (\frac{1}{45})\uparrow$	$(\frac{2}{15})\downarrow + (\frac{2}{15})\uparrow$
$\frac{3}{2}$, - $\frac{3}{2}$	$\vert-1\downarrow\rangle$	$(\frac{1}{15})\downarrow$	$(\frac{2}{5})\downarrow$
$\frac{1}{2}$, + $\frac{1}{2}$	$\sqrt{\frac{2}{3}}\vert+1\downarrow\rangle$ - $\sqrt{\frac{1}{3}}\vert0\uparrow\rangle$	$(\frac{4}{15})\downarrow + (\frac{1}{15})\uparrow$	$(\frac{2}{45})\downarrow + (\frac{1}{15})\uparrow$
$\frac{1}{2}$, - $\frac{1}{2}$	$\sqrt{\frac{1}{3}}\vert0\downarrow\rangle$ - $\sqrt{\frac{1}{3}}\vert-1\uparrow\rangle$	$(\frac{1}{15})\downarrow + (\frac{2}{45})\uparrow$	$(\frac{1}{15})\downarrow + (\frac{4}{15})\uparrow$

Table 1.1: The angular part of the matrix elements for excitations from $2p$ core levels $|jm_j\rangle$ decomposed into $|l=1, m_l, s=1/2, m_s\rangle$ and catalogued with respect to spin and circular polarization of light.

	I^+	I^-	ΔI ($\propto$ XMCD)
L_2	$\frac{1}{3}\ \rho\downarrow + \frac{1}{9}\ \rho\uparrow$	$\frac{1}{9}\ \rho\downarrow + \frac{1}{3}\ \rho\uparrow$	$\frac{2}{9}(\rho\downarrow$ - $\rho\uparrow)$
L_3	$\frac{1}{3}\ \rho\downarrow + \frac{5}{9}\ \rho\uparrow$	$\frac{5}{9}\ \rho\downarrow + \frac{1}{3}\ \rho\uparrow$	$\frac{2}{9}$(- $\rho\downarrow + \rho\uparrow$)

Table 1.2: The X-ray absorption for RCP (LCP) light involves preferentially spin up (spin down) electron on the $2p_{3/2}$ core level (L_3-edge). The opposite situation is observed for the $2p_{1/2}$ core level (L_2-edge).

with spin-orbit splitting in both initial and final states. In this case, dichroic intensity can be obtained following the procedure described above if the degeneracy of final states is assumed lifted and the different m_j final states have different occupation [24].

The one-electron picture can be also used to explain the XMCD signal at the K-edge of the transition metals. In these cases, however, due to the spherical symmetry of the initial state (no spin-orbit coupling in the initial state), a small spin-orbit coupling in the final p states is needed to account for spin-dependent X-ray absorption [23]. In addition, the XMCD signal at the K-edge of the $3d$ transition metal elements is much weaker than at the $L_{2,3}$-edges since we are not probing the $3d$ band, responsible for magnetism in $3d$ metals, but the extended $4p$ band. The XMCD effect at the K-edge of $3d$ transition metals is only 10^{-3} of the absorption jump, whereas at the $L_{2,3}$-edges is of the same order of the absorption jump.

Chapter 2

Experimental techniques and procedures

In this Chapter we present a description of the experimental techniques used in this Thesis. Some of them, such as X-ray diffraction (XRD) or magnetization measurements are of standard use in the study of intermetallic compounds. They are well known and only a brief review will be given. On the other hand, a more detailed description of the X-ray absorption spectroscopy (XAS) and X-ray magnetic circular dichroism (XMCD) techniques will be given since they are less commonly used.

The synthesis of the samples and their subsequent characterization by using conventional laboratory techniques were performed at the Instituto de Ciencia de Materiales de Aragón (ICMA). Synchrotron radiation based experiments have been performed at the branch A of the BM25–SpLine beamline of the European Synchrotron Radiation Facility (ESRF) located in Grenoble (France) and at the BL39XU and BL25SU beamlines of the SPring-8 facility located in Sayo-cho (Japan). At the end of this Chapter it will be shown the experimental XMCD setup used at the different beamlines.[1]

2.1 Synthesis and characterization of the samples

We have synthesized several series of Laves phase compounds in the form $R_{1-x}R'_x(Fe_{1-y}M_y)_2$, where R is a magnetic rare-earth (Gd, Ho, Er), R' is a non-magnetic rare-earth (Lu, Y) and M is a non-magnetic element (Al, Ga, Ge). A list of the samples is given in Table 2.1.

[1] Details about the experimental XAS station at BM25-A–SpLine will be given in Chapter 7.

series	rare-earth	concentration
$R_{1-x}Y_xFe_2$	Ho	x = 0, 0.25, 0.50, 0.80, 1
	Er	x = 0, 0.25, 0.5, 0.85, 1
$Ho_{1-x}Lu_xFe_2$		x = 0, 0.25, 0.50, 0.75, 1
$Ho_{0.5}Lu_{0.5}(Fe_{1-y}Al_y)_2$		y = 0, 0.25, 0.50, 0.75, 1
$R(Fe_{1-y}Ga_y)_2$	Ho, Gd, Y	y = 0, 0.10
$R(Fe_{1-y}Ge_y)_2$	Ho, Gd	y = 0, 0.10

Table 2.1: Series of synthesized compounds.

The samples were synthesized by melting the pure elements in a commercial arc furnace (MAM 1 from Edmund Bühler, left panel in Fig. 2.1). The starting elements were purchased from commercial companies (Alfa Aesar, Strem Chemicals and Goodfellow) in ingot form with the following nominal purity: rare-earths (99.9 % REO), Fe (99.98 %), Al and Ge (99.999 %), and Ga (99.9999 %).

It is worth to note that in order to have single-phase samples an excess of ∼1-3% wt. of some elements was necessary to compensate losses by evaporation. This is a consequence of the different vapor pressure of the constituent elements.

In order to ensure homogeneity the alloyed button should be re-melted several times. In our case, the Laves phase compounds blow up upon approaching the arc once the compound is synthesized. This is likely due to the cooling process producing many strains and cracks in the inner part of the sample. We have sort this inconvenience out by melting the pieces only twice for a longer time.

Some of the as-cast samples were thermally treated for about 3-7 days at a temperature of 800 - 1000 °C in a muffle furnace (Lenton AWF 12/13, right panel in the Fig. 2.1). The heating treatment is usually performed to ensure phase homogeneity and to improve the degree of crystallinity. For the annealing treatment the samples were wrapped in a piece of Ta foil and put into an Ar atmosphere sealed quartz tube. After the annealing, the samples were quenched by immersing the sealed tube in room temperature water. This procedure is necessary to avoid the appearance of secondary phases during a slow cooling process [25, 26]. XRD data have revealed that when the sample contains secondary phases (generally RFe_3) they vanish after the annealing procedure.

It should be noted that the synthesis of some of the studied compounds have been performed by other researchers before the beginning of this The-

Figure 2.1: Arc (left panel) and muffle (right panel) furnaces used for the synthesis and the subsequent annealing of the samples.

sis. RCo_2 and $R(Fe_{1-x}Al_x)_2$ series were synthesized and characterized by Dr. M. A. Laguna-Marco at the ICMA. Details about sample preparation, XRD analysis and magnetic characterization can be found in Ref. [1]. The arc-melting synthesis and XRD analysis of the R_6Fe_{23} compounds were carried out by Dr. A. S. Markosayan at the Laboratory of Problems of Magnetism at the Moscow State University. This work is not considered part of this Thesis; hence, no detailed further information will be given regarding synthesis, structural or magnetic properties unless it will be necessary to use these data as a reference value.

2.1.1 X-ray powder diffraction (XRD)

X-ray diffraction (XRD) patterns were recorded to determine the crystallographic structure and the degree of crystallinity of all the synthesized samples. Measurements have been performed on powdered samples at room temperature by using a Cu K_α radiation in Bragg-Brentano geometry (Rigaku RTO 500RC diffractometer at the EXAFS National Service of the University of Zaragoza). Sample powder was mixed with amorphous silica (Cab-O-sil ®) to avoid preferred orientation effects in the XRD pattern. Data have been collected between $2\theta = 15 - 80°$ with an step scan mode of $\Delta 2\theta = 0.03°$.

The diffraction patterns were Rietveld refined by using the FULLPROF code [27–29]. The theoretical concepts about the Rietveld method are described in the following part of this section.

Rietveld method.

The Rietveld method consists on a theoretical adjustment of the diffraction pattern by using a model including both structural and experimental factors [30]. The weighted sum of the squared difference between the observed and calculated intensity at the scattering angle $2\theta_i$ (y^i_{obs} and y^i_{calc} respectively) is minimized. If the set of model parameters is β=(β_1, β_2,... β_P), the Rietveld method tries to optimize the chi-square function:

$$\chi^2_P = \sum_i w_i \{y^i_{obs} - y^i_{calc}(\beta)\}^2 \tag{2.1}$$

where w_i is the inverse of the variance associated to the observation "i", $\sigma^2(y^i_{obs})$.

The calculated intensities, y^i_{calc}, are determined from the $|F_K|^2$ values calculated from the structural model by summing of the calculated contributions from neighboring Bragg reflections plus the background:

$$y^i_{calc} = s \sum_K L_K |F_K|^2 \phi(2\theta_i - 2\theta_K) P_K A + y^i_b \tag{2.2}$$

where:
s is the scale factor
K represents the Miller indices for a Bragg reflection
L_K contains the Lorentz polarization and multiplicity factors
ϕ is the reflection profile function
P_K is the preferred orientation factor
A is the transmission factor
y^i_b is the background intensity at $2\theta_i$

In order to judge the quality of the fit it is necessary to evaluate the Rietveld discrepancy values [31]. In our case we have considered the reflection-based R factor, R_{Bragg}, to evaluate the reliability of the refinement,

$$R_{Bragg} = \frac{\sum_i |y^i_{obs} - y^i_{calc}|}{\sum_i y^i_{obs}} \tag{2.3}$$

2.1.2 Magnetization measurements

We have determined the basic magnetic properties (magnetic order temperature, spontaneous magnetization and magnetization of saturation) of all the samples by measuring the dc magnetization *vs.* applied magnetic field and temperature, M(H) and M(T). This magnetic characterization was performed by using commercial superconducting quantum interference device (SQUID) magnetometers (Quantum Design MPMS-5S and MPMS-XL models) of ICMA located at the Instrumentation Service of the University of Zaragoza (see left panel of Fig. 2.2).

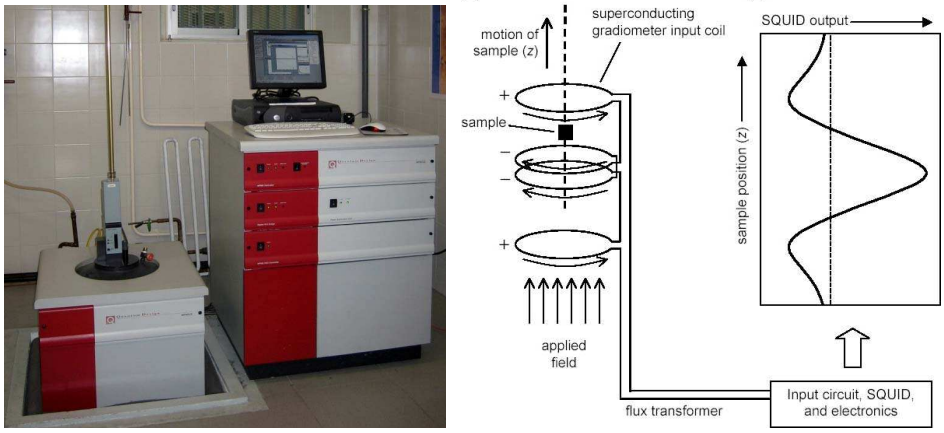

Figure 2.2: Left panel: SQUID magnetometer (MPMS-XL model). Right panel: schematic view of the sample movement inside the pick-up coils.

SQUID magnetometers are classified within the flux methods of measuring magnetization of a sample. The main components of a SQUID magnetometer are: superconducting magnet, superconducting pick-up coil which is coupled inductively to the sample and a SQUID sensor connected to the detection coil. Right panel of Fig. 2.2 illustrates schematically the measurement principle. The up and down movement of the sample yields a variation of the magnetic flux through the pick-up coil which leads to an alternating output voltage of the SQUID device. This signal is proportional to the magnetic moment of a sample which is magnetized by the magnetic field produced by a superconducting magnet. Further details about technical aspects of SQUID magnetometers and data acquisition system of the Magnetic Property Measurement System (MPMS) can be found elsewhere [32, 33].

For the measurements gelatin capsules (4 mm of diameter) were filled with powdered sample up to 3 mm height. The free space inside the capsule was

filled with cotton to avoid sample movement when the magnetic field, applied parallel to the longitudinal axis of the capsule, is varied.

2.2 XAS and XMCD spectroscopies

2.2.1 Synchrotron radiation facilities

The advent of intense, tuneable, polarized synchrotron radiation sources has stimulated world-wide interest in using X-rays to address electronic and magnetic aspects of condensed matter. Very schematically, synchrotron radiation is obtained as follows (see Fig. 2.3): electrons emitted from a thermionic electron gun are first bunched and accelerated in a linear accelerator (LINAC). Then, the bunches are injected into a circular accelerator (the booster synchrotron) where they are accelerated by electrical fields in radio frequency (rf) cavities. The bunches are accelerated up to reach an energy of the order of few GeV and afterwards injected into the storage ring, where they travel round the ring passing through different types of devices: bending magnets, wigglers and undulators, that we could denote in general as "magnets". The electron bunches are deflected by these "magnets" from their straight path by several degrees, which causes them to emit synchrotron radiation, which will be used in the beamlines to perform different kinds of experiments.

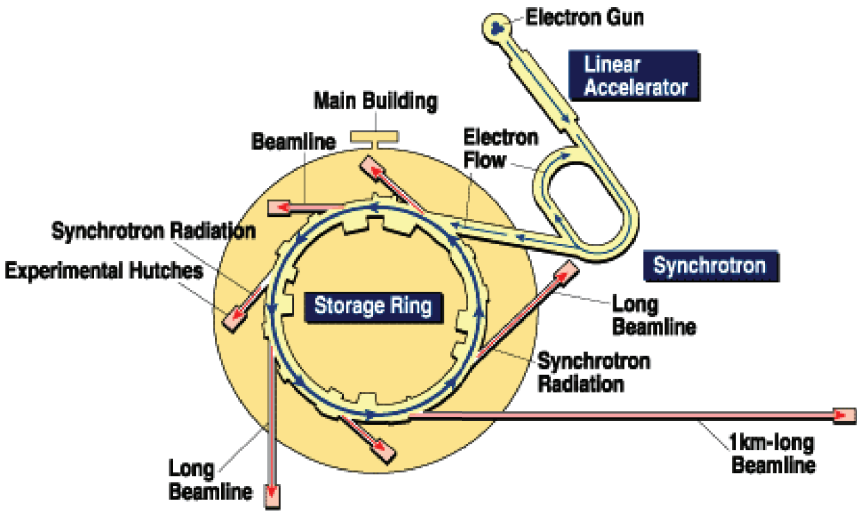

Figure 2.3: Schematic layout of a synchrotron facility: linac, booster synchrotron, storage ring and beamlines.

Synchrotron radiation [34] is superior to conventional radiation sources like X-ray tubes, with respect to several properties. Among them:

- **Its high intensity**. This is of tremendous importance for the experimentalist. To this respect it is important to note that XMCD is about 1000 times smaller than the XAS signal, so that a very intense source of radiation is necessary to get an acceptable signal to noise ratio.

- **It is a continuously tuneable radiation source**. The emitted radiation has a high intensity which is available over a broad region of the spectrum from the ultraviolet up to hard X-rays. A monochromatic source can be achieved with the aid of monochromators, which are adjusted to the required wavelength which can be varied throughout the course of the experiments as needed.

- **Synchrotron radiation is highly polarized**. In the orbital plane the electric field vector of the emitted radiation is in the direction of the instantaneous acceleration. Thus, radiation from bending magnets is linearly polarized in the plane of the orbit. Out of the orbit plane the polarization becomes elliptical and eventually circular, with opposite helicity above and below the plane. However, to get some circularly polarized intensity, the observer has to move out of the orbital plane at expenses of a weaker flux. This disadvantage can be overcome by using special insertion devices such as asymmetric wigglers or helical undulators, which provide high intensity circularly polarized radiation in the orbital plane. Alternatively, circular polarized light can be obtained by using phase retarders combined with extremely intense linearly polarized radiation. In the latter case, despite the flux loss at the phase retarder the intensity of the beam on the sample is still very high.

2.2.2 BL39XU beamline at SPring-8 facility

The XMCD measurements at the hard X-ray range have been performed at the BL39XU [35] beamline of the SPring-8 facility. BL39XU is an undulator beamline dedicated to research on magnetic materials by means of hard X-rays magnetic absorption/scattering. To control the X-ray polarization state the beamline is equipped with an X-ray polarization device and micro-focusing X-ray mirrors. One of the major applications of this beamline is X-ray magnetic circular dichroism (XMCD) spectroscopy. An schematic illustration of the XMCD set-up is displayed in Fig. 2.4.

The synchrotron radiation is produced by an in-vacuum undulator (SPring-8 standard type). It provides extremely high brilliance X-rays linearly polar-

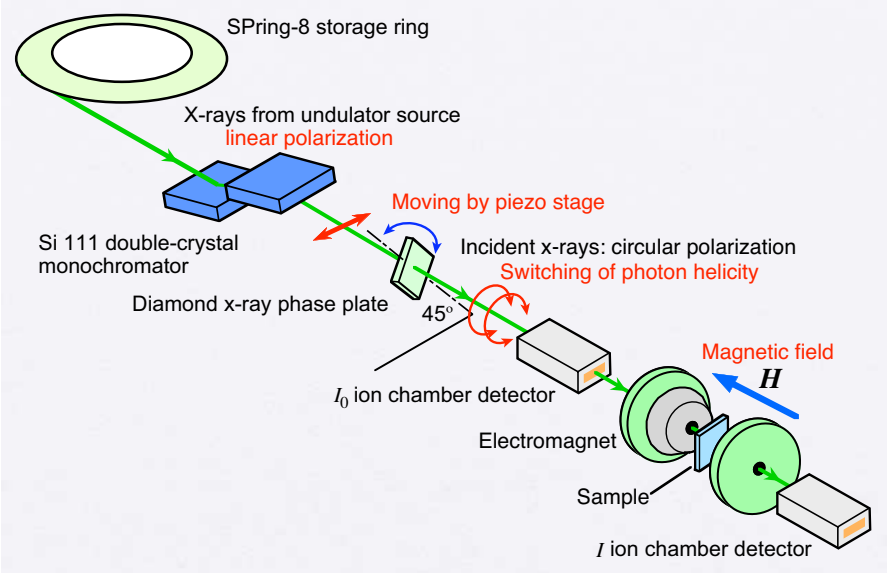

Figure 2.4: Schematic view of the XMCD set-up in BL39XU.

ized in the horizontal plane. The fundamental, third and fifth harmonics cover the photon energy range between 5 and 70 keV. BL39XU is also equipped with a rotated-inclined double-crystal monochromator (111-diamond). In order to maximize the incoming X-ray intensity and to obtain a smooth variation of I_0, synchronous tuning between the undulator gap and the angle of the monochromator is used [36].

Tunable right/left circular polarized X-rays are obtained by combining linear polarized radiation produced by the undulator and X-ray phase retarders (XPR) used as quarter wave phase plate [37]. The birefringence of perfect crystals close to the Bragg condition provokes a phase shift between both electric field components, π (in plane) and σ (out of plane) of the transmitted X-rays and, therefore, a change in the polarization state of the incoming linear polarized X-rays.[2]

In BL39XU there are available diamonds of various thicknesses to optimize both circular polarization rate and X-ray intensity after the XPR at the X-ray energy of interest. They are used either in the (220) Laue or (111) Bragg transmission geometry (see Table 2.2).

A Rh-Pt mirror is placed downstream the XPR to perform horizontal-focusing and also to reduce the higher harmonics content.

The experimental end-station is equipped with two ionization chambers to

[2] A detailed explanation about theoretical concepts of birefringence of perfect crystal and usage of XPR to obtain circular polarized X-rays is given in Chapter 7.

Thickness (mm)	Orientation	Geometry	Energy range (keV)	Transmittance (%)
0.34	(111)	111 Bragg	5 - 5.8	3 - 7
		220 Laue	5.8 - 7.5	7 - 41
0.45	(111)	220 Laue	6 - 9	5 - 53
0.73	(111)	220 Laue	8 - 12	22 - 65
2.7	(001)	220 Laue	11 - 16	13 - 47

Table 2.2: Diamond phase plates of different thickness which are available at BL39XU and respective X-ray energy range of use.

measure the intensity of the beam before and after the sample. In addition, there are two available sample environments: i) an 2 T-electromagnet (H = 0–20 kOe) with a 20–300 K closed-cycle helium refrigerator and ii) a 10 T split-type superconducting magnet (SCM) system for further high-field and low-temperature (see Fig.2.5). In the case of SCM the assembly of a Variable Temperature Insert (VTI) allows measurements between 2 and 288 K.[3] The SCM has X-ray transparent Be windows at both front and back (on the field axis) and on both right and left sides (perpendicular to the field). This design allows XMCD measurements in either transmission or fluorescence modes.

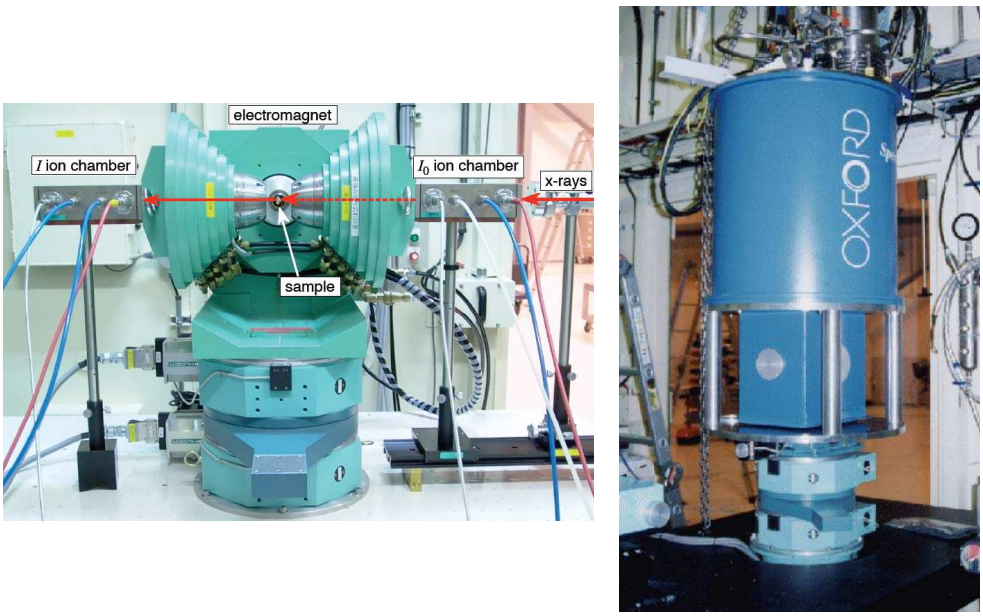

Figure 2.5: Electromagnet (left panel) and superconducting magnet (right panel) at BL39XU experimental hutch.

[3]Due to the thermal shield of the SCM the "room temperature" in the sample chamber is slightly lower than the ambient temperature at the experimental hutch (∼300 K).

2.2.3 BL25SU beamline at SPring-8 facility

Despite this Thesis is mainly devoted to the study of the capabilities of the XMCD technique by using hard X-rays, some measurements (presented in Chapter 6) have been performed in the soft X-ray region (Fe $L_{2,3}$-edges). These experiments were carried out at the BL25SU beamline of the SPring-8 facility [38]. For this reason we include here a brief description of the beamline and of the measurements method used.

The circularly polarized radiation is obtained at BL25SU along the same optical axis by twin helical undulators [39]. The helicity of the circularly polarized radiation can be periodically switched at 0.1, 1 or 10 Hz by using kicker magnets distributed around the two undulators. The beamline monochromator is a constant-deviation type with varied line-spacing plane gratings covering an energy region of 0.22–2 keV [38]. The resolving power of the monochromator is more than 10^4 in the whole energy region.

For the measurement, it was necessary to cut a rectangular rod of approximately $2\times2\times4$ mm^3 from the original alloy button. The rectangular rod was fixed at the sample holder with Torr Seal. Silver paste was put at the bottom part to improve the electric contact between the sample and the Cu-holder plate. The sample was mounted keeping the sample surface perpendicular to

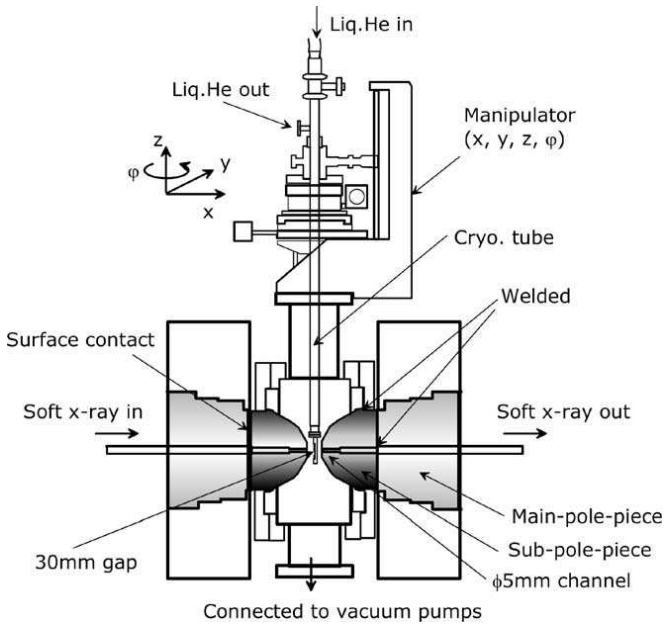

Figure 2.6: Schematic view of the UHV measurement chamber at BL25SU which is equipped with an electromagnet.

the applied magnetic field direction. The XMCD effect was recorded by the total electron yield method (TEY) applying a bias voltage of 18 V.[4] The photon helicity was switched at 1 Hz periodically. To avoid surface oxidation that could spoilt the measurement owing to the small probing depth in the TEY method, ∼20 Å, samples were broken *in-situ* inside the ultra high-vacuum (UHV) chamber, see Fig. 2.6, by using a small hammer-screw attached to Cu-holder plate as shown in the Fig. 2.7.

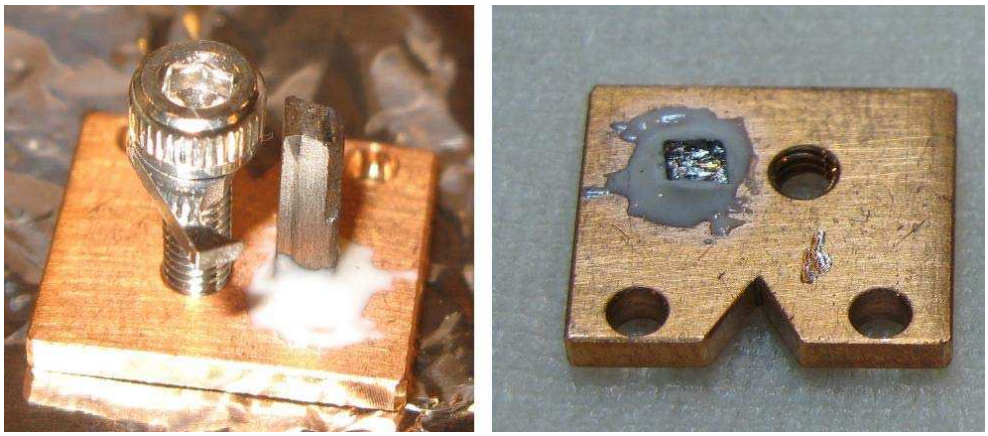

Figure 2.7: Sample holder used in the TEY measurements at BL25SU before (left panel) and after (right panel) the cleaving process.

2.2.4 XAS and XMCD: Experimental procedures

For the measurements,[5] homogeneous layers of powdered samples were made by spreading of fine powders of the material on an adhesive tape. Thickness and homogeneity of the samples are optimized to obtain the best signal-to-noise ratio, giving a total absorption edge jump ∼1.

All the spectra were recorded in the transmission geometry as displayed in Fig. 2.4. In the transmission mode, the intensity of the X-ray beam before and after the sample is directly measured by using ionization chambers; then,

[4]The absorbed X-ray intensity is not measured directly in TEY measurements, but rather the photoelectrons that are created by the absorbed X-rays. The created holes in the photoabsorption process are filled by Auger decay (dominant in the soft X-ray region). As they leave the sample, the primary Auger electrons create scattered secondary electrons which dominate the total electron yield (TEY) intensity. The TEY cascade involves several scattering events and originates from an average depth, the electron sampling depth L. Electrons created deeper in the sample lose too much energy to overcome the work function of the sample and therefore do not contribute to the TEY. The sampling depth L in TEY measurements is typically a few nanometers. [40]

[5]Excepting those in the soft X-ray region, as commented above.

the absorption coefficient is directly obtained by applying the Beer-Lambert-Bouguer law, Eq. (1.9).

As we have already explained, XMCD is the difference of the X-ray absorption coefficient for antiparallel, μ^-, and parallel, μ^+, orientation of the incident photon helicity and sample magnetization, $\mu_c = (\mu^- - \mu^+)$. Therefore, XMCD experiments can be performed in two equivalent ways: either by changing the helicity while keeping constant the applied magnetic field (*helicity reversal* method), or alternatively, by changing the direction of the magnetic field while the photon helicity remains invariable (*field reversal* method). In the field-reversal method the hysteresis effects might affect the XMCD signal and, moreover, sample vibration gives rise to noisy spectra. The helicity-reversal mode overcomes these limitations and is more advantageous than the conventional field-reversal mode [41].

Typically, the XMCD spectra are obtained following a "static procedure", i.e., after acquisition, normalization and substraction of μ^- and μ^+ spectra. However, at BL39XU the helicity-modulation (HM) technique [42] allows to record both XAS and XMCD signals simultaneously at each energy point. This technique gives rise to extremely high quality XMCD spectra recorded in an acquisition time shorter than the static method is used. A dichroic signal of the order of 10^{-4} of the absorption jump is obtained with a good signal-to-noise ratio for 10 s of integration time at each energy point. Helicity-modulation technique combines fast polarization switching by means of XPR oscillation and a phase-sensitive (lock-in) detection system.

Fig. 2.8 illustrates the set up and the basic principle of HM. The magnetic field remains fixed through the measurement. The XPR is mounted on a piezo-driven stage which oscillates at a reference frequency (40 Hz) around the Bragg angle θ_B with an amplitude $\Delta\theta$. As a result, the helicity of the incident X-ray beam alternates from right (RCP) to left circular polarization (LCP) and, consequently, the absorption coefficient also changes as a function of time with a 40 Hz frequency as illustrated in Fig. 2.8. The incident and transmitted beam intensities are measured with ionization chambers and converted into voltage signals, $V(I_0)$ and V(I), by current amplifiers. The logarithmic converter gives a voltage signal $V(\mu t)$ which corresponds to the absorption coefficient $\ln(I/I_0)$. The amplitude of the ac component is proportional to the XMCD signal and is obtained by using a dual lock-in amplifier to perform a phase-sensitive detection. On the other hand, the dc component corresponds to the average absorption coefficient and is measured with a digital voltmeter. Consequently, with this technique the XMCD values are directly recorded at each energy point, thus minimizing possible errors coming from data treatment of the μ^- and μ^+ spectra.

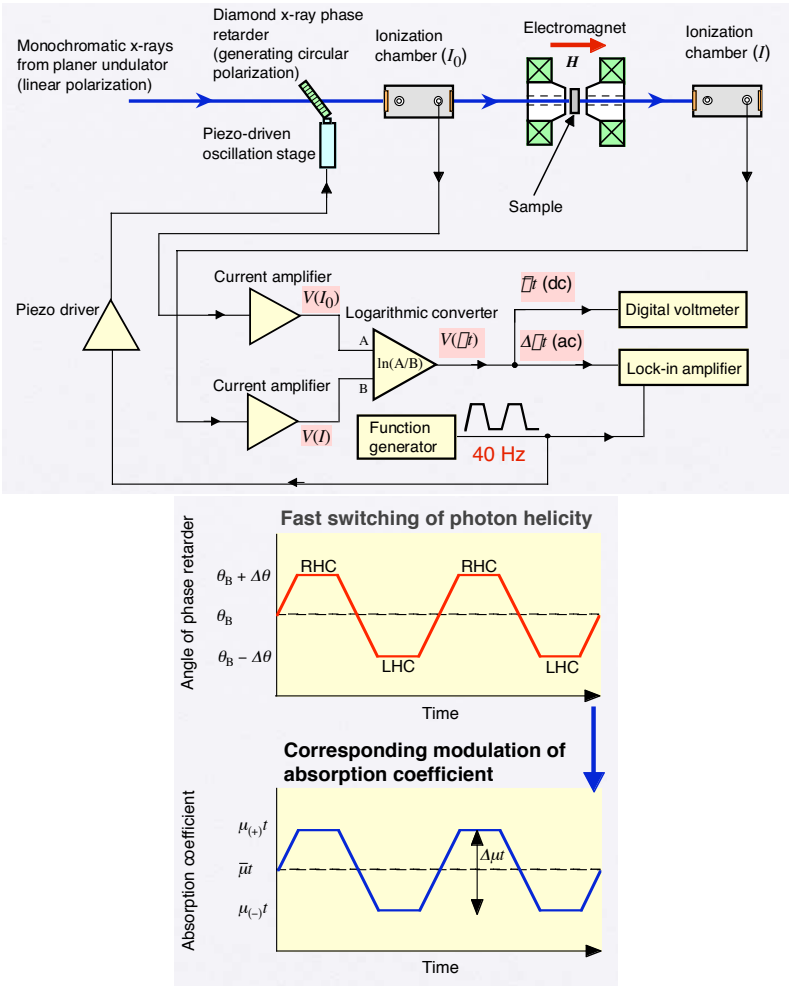

Figure 2.8: Upper panel: set-up of helicity modulation XMCD measurement. Lower panel: phase sensitive (lock-in) detection of the modulated XMCD signal (see text for details).

This XMCD recording procedure has been carried out for both directions of the applied magnetic field, XMCD(+ H) and XMCD(- H), which yields the same signal but with opposite sign. The final XMCD signal is then obtained as the average: $\frac{XMCD(+\ H)\ -\ XMCD(-\ H)}{2}$. This procedure allows to improve the statistics (reducing the noise) and remove any possible non-magnetic spurious contribution to the signal. Through this Thesis we refer to this spurious contribution as the "artifact". The artifact can be simply obtained by direct sum of the XMCD recorded for opposite magnetic fields: $\frac{XMCD(+\ H)\ +\ XMCD(-\ H)}{2}$, as exemplified in Fig. 2.9. In this case, the *artifact* shows a "step-like" shape.

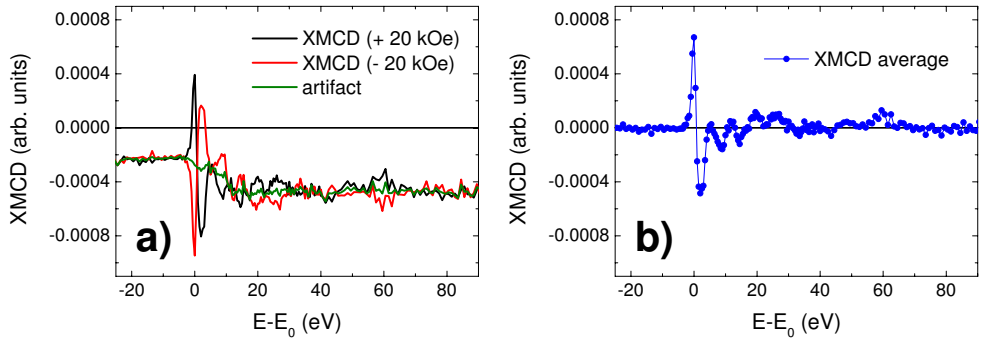

Figure 2.9: Panel (a): XMCD signal recorded at both directions of the applied magnetic field, XMCD(+ H) and XMCD(- H), and the corresponding "artifact" signal. Panel (b): final XMCD spectra obtained by averaging the dichroic spectra of both magnetic applied fields.

Analysis of experimental XAS and XMCD data.

Once the XAS spectra have been recorded, it is necessary to follow a simple normalization procedure prior to perform direct comparisons between spectra. The XAS spectrum is superimposed over a background due to all the possible absorptions corresponding to less energetic edges. This background is typically fitted to a Victoreen curve,

$$\mu_V = A - C/E^3 + D/E^2 \tag{2.4}$$

and subtracted from the raw spectra. Usually, for single edge studies involving a short energy range the use of a straight line is equivalent to use a Victoreen curve. In order to remove the sample thickness dependence from the XAS spectra we have normalize to the unity the absorption jump, i.e., the averaged value of the spectra at the high energy region ($>$ 100 eV above the absorption edge).

Usually, the origin of the energy scale, E_0, is chosen at the inflection point of the rising absorption edge, i.e., first derivative peak of the absorption spectrum. The spectra are referred to the $E\text{-}E_0$ energy scale in order to avoid spurious energy shifts due to an incorrect calibration of the monochromator or step losses of the motor.

The XMCD spectra are obtained as $\mu_c = (\mu^- - \mu^+)$. If the substraction is made after both XAS spectra (μ^- and μ^+) have been normalized, no extra normalization is required. By using the helicity modulation technique we obtain directly both XMCD signal (μ_c) and the unpolarized absorption spectra ($\frac{\mu^- + \mu^+}{2}$) at each energy point. In this case, the normalization of the XMCD

spectra is performed by dividing the raw spectra by the same absorption jump as used for the XAS normalization.[6]

2.2.5 Element Specific Magnetic Hysteresis measurements by using XMCD

The Element Specific Magnetic Hysteresis measurement by using XMCD (ESMH) consists of recording the dichroic signal for a fixed energy while the applied magnetic field is varied, similarly to the magnetization hysteresis measurements with conventional magnetometers.

ESMH at BL39XU

At BL39XU, ESMH measurements have been performed by using the helicity modulation technique. The experimental set-up was the same as for the XMCD measurements. The unique difference is that we have been performed a magnetic field scan instead of an energy scan.

Some authors assert that the optimal energy to measure ESMH is the one that maximize the asymmetry ratio $|\frac{\mu^- - \mu^+}{\mu^- + \mu^+}|$ [43]. Regardless the photon energy chosen, the functional form of the measured ESMH curves is always nearly identical as long as there is sufficient XMCD signal to measure with.

We have recorded ESMH cycles in Er_6Fe_{23} at the energy of each peak of the Fe K-edge XMCD spectra [see Fig. 2.10(a)]. The results are displayed in Fig. 2.10(b). We found that, with the same acquisition time, all the ESMH cycles show the same functional shape. Indeed, only the signal-to-noise ratio of ESMH curve is improved as the dichroic peak is more intense.

The acquisition system at BL39XU yields the values of both absorption and dichroic (ESMH) spectra at each magnetic field point along the scan. The simultaneous recording of the absorption value is useful because it allows us to check if there had been any problem through the measurement. For example, sample vibrations might vary the point at which the beam hits the sample and, consequently, the sample thickness probed. This effect can be critical with non-homogeneous samples.

As commented above, in order to eliminate any spurious non-magnetic contribution, the so-called *artifact*, from the XMCD spectra it is necessary to

[6] In the helicity modulation technique, the output of the lock-in amplifier is the root-mean-square (rms) of the detected ac signal, which is proportional to the absolute XMCD amplitude (peak-to-peak value), but includes a scale factor. This scale factor depends on the waveform of the reference signal used to modulate the oscillation of the XPR. In our case we have used a trapezoidal signal with 50% duty ratio, being necessary a scale factor equal to 2.53.

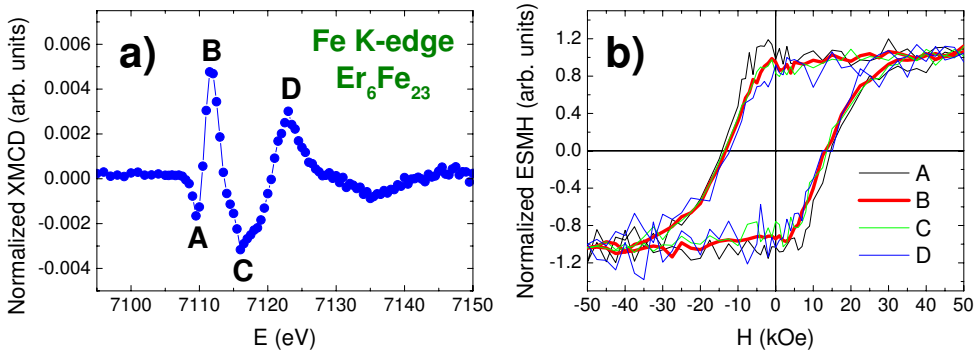

Figure 2.10: Fe K-edge XMCD spectra [panel (a)] and ESMH cycles [panel (b)] of Er_6Fe_{23} at T = 5 K. ESMH cycles have been scaled to the unity at the highest magnetic field for the sake of comparison.

measure the XMCD signal for both orientations of the applied magnetic field and subtract them: $\frac{XMCD(+H) - XMCD(-H)}{2}$. In a similar way, we can isolate the *artifact* as the addition of both dichroic signals: $\frac{XMCD(+H) + XMCD(-H)}{2}$. This is illustrated in Fig. 2.11(a) for the Fe K-edge XMCD measurements of the $Ho_{0.5}Lu_{0.5}Fe_2$ compound at T = 300 K and under a magnetic field of H = ±20 kOe. XMCD spectra recorded for opposite orientations of the magnetic field show the presence of a spurious contribution, i.e., the *artifact*. As shown in Fig. 2.11(c) the *artifact* is canceled by subtracting the XMCD spectra recorded for opposite orientation of the magnetic field.

As shown in Fig. 2.11(b), this spurious contribution provokes a vertical shift of the ESMH cycles, that could give rise to misinterpretations. This is of special significance in the case of exchange biased FM/AFM multilayer systems, because in these compounds there might be a real vertical displacement ascribed to pinned moments [44–46]. To compensate the vertical shift of the raw ESMH cycle it is necessary to subtract the value of the *artifact* curve at the energy point at which the ESMH has been recorded. That is, in the example shown in Fig. 2.11, the value of the *artifact* curve at the energy point *A* [panel (a)] is subtracted to the raw ESMH cycle [panel(b)] recorded at peak *A*, ESMH(*A*), of the XMCD spectrum. Fig. 2.11(d) shows the result after compensating the spurious vertical offset of the ESMH cycle.

Finally, to normalize the ESMH cycles it is necessary to perform the same procedure as for the XMCD spectra, i.e., to factorize the ESMH cycle by $1/J$, where J is the absorption jump obtained at the high energy region of the XAS spectrum.

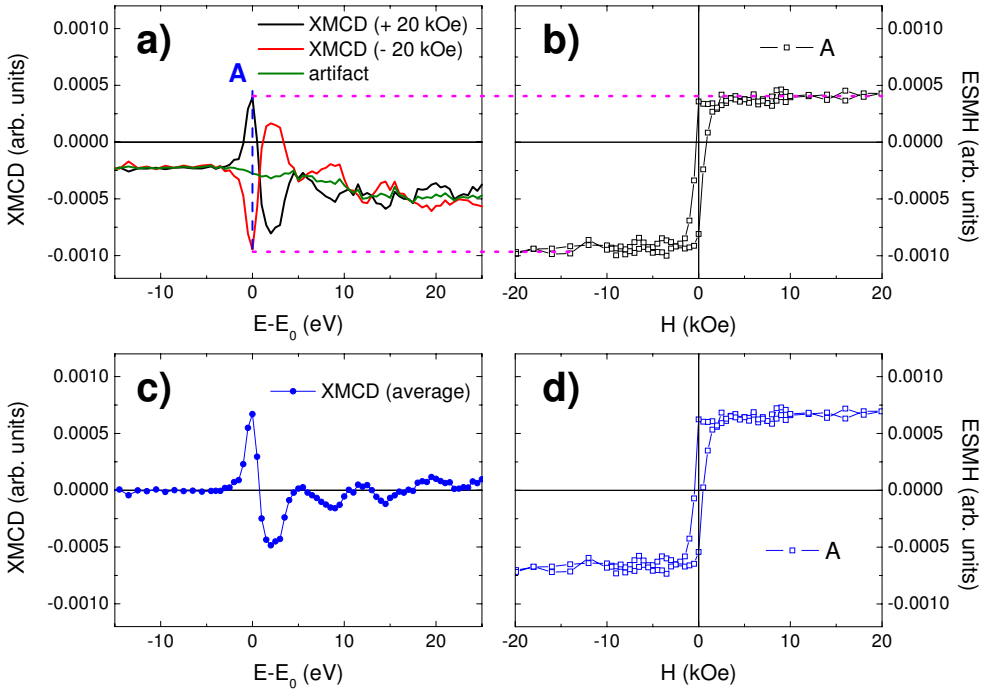

Figure 2.11: Procedure followed to eliminate spurious non-magnetic contributions in XMCD signals and similar procedure for the ESMH measurements. Exemplified with signals measured on $Ho_{0.5}Lu_{0.5}Fe_2$ compound at the Fe K-edge at T = 300 K. Doted lines between panels (a) and (b) serve as a guide for the eye to compare the amplitude of both XMCD spectra and ESMH curve (see text for details).

ESMH at BL25SU

We have also recorded the ESMH curves at the BL25SU beamline. The measurements were carried out in Total Electron Yield (TEY) mode, and the magnetic field was applied perpendicular to the in-vacuum broken surface of the rectangular rod (see Fig. 2.7). The experimental set-up used for ESMH measurements was the same as the one described above for XMCD measurements. The soft X-ray ESMH cycles have been normalized to the value of the dichroic signal at the energy point used to measure the cycle.

It should be noted that sometimes, artificial dips appear near zero field values of the ESMH [see Fig. 2.12(a)]. These dips are due to the variation of electron yield efficiency, which depends on the applied magnetic field [47]. They are provoked by the spirals traces of the electron trajectories under the presence of an applied magnetic field or the sample magnetization. The radii of the spirals depends on the applied magnetic field. Some electrons are carried back to the sample surface and, therefore, the TEY current is modified. This magnetic force effect is problematic, because the sample magnetization itself

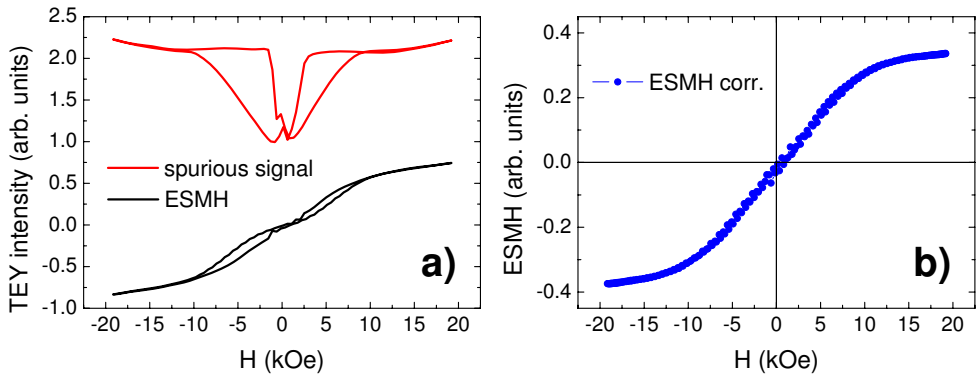

Figure 2.12: Panel (a): ESMH curve data recorded by using TEY detection method and spurious contribution. Panel (b): ESMH curve corrected after applying the procedure to eliminate spurious contributions (see text for details).

will influence the TEY signal.

The ESMH intensity is corrected by dividing by the averaged absorption intensities between the positive and negative helicity ($\frac{\mu^+ + \mu^-}{2}$) in order to compensate for the effect due to the influence of the external magnetic field to the sample current. Fig. 2.12(b) shows the ESMH cycle after correction which proves the success of this simple compensation analysis. For further details see for example Refs. [47, 48].

Chapter 3

Structural and magnetic characterization of the samples

We have studied three different series of R-T intermetallic compounds: $R_{1-x}R'_xFe_2$, $R_{1-x}R'_x(Fe_{1-y}Al_y)_2$ and $R(Fe_{1-y}M_y)_2$ (with R = Gd, Ho, Er; R' = Lu, Y; and M = Ga, Ge). The quality of the samples has been checked by different complementary techniques. These experiments help us to certify the crystallographic and magnetic properties of the newly synthesized alloys. In addition, a detailed magnetic characterization is necessary to get a correct interpretation of the dichroic signals.

3.1 Structural characterization

In this section we describe the crystallographic structure of the Laves phase compounds which have been synthesized in this Thesis.

Laves phases form the largest group of intermetallics, with more than 1400 representatives having the ideal composition AB_2. An intermetallic compound is classified as a Laves phase purely on the basis of the crystal structure geometry. The Laves phases crystallize in three structure types, which are named after the representatives cubic $MgCu_2$ (C15), hexagonal $MgZn_2$ (C14) and hexagonal $MgNi_2$ (C36).[1] In the first half of the last century it was shown by J.B. Friauf [49, 50], F. Laves [51, 52], G.E.R. Schulze [53], F.C. Frank and J.S. Kasper [54, 55] that the three Laves phase structures are closely related

[1] C14, C15 and C36 corresponds to the Strukturbericht designation of the Laves phases.

and they can be regarded as tetrahedrally close packed structures of A and B atoms.

We are dealing with Laves phases crystallizing in the C15 or C14 structure types. The crystalline cell of the C15 structure prototype, space group $Fd\bar{3}m$ (N. 227), is shown in left panel of Fig. 3.1. In this structure, the Mg and Cu atoms occupy the 8a and 16d crystallographic sites, respectively. The Mg atoms form a diamond lattice and the remaining space inside the cell is occupied by regular tetrahedra formed by Cu atoms. The crystalline cell of the C14 structure prototype, space group $P6_3/mmc$ (N. 194), is shown in right panel of Fig. 3.1. The Mg atoms occupy the 4f sites, while the Zn atoms occupy the 2a and 6h sites. Details about the crystallographic sites and their nearest-neighbors atoms in cubic C15 ($MgCu_2$) and hexagonal C14 ($MgZn_2$) prototype structures are given in Table 3.1.

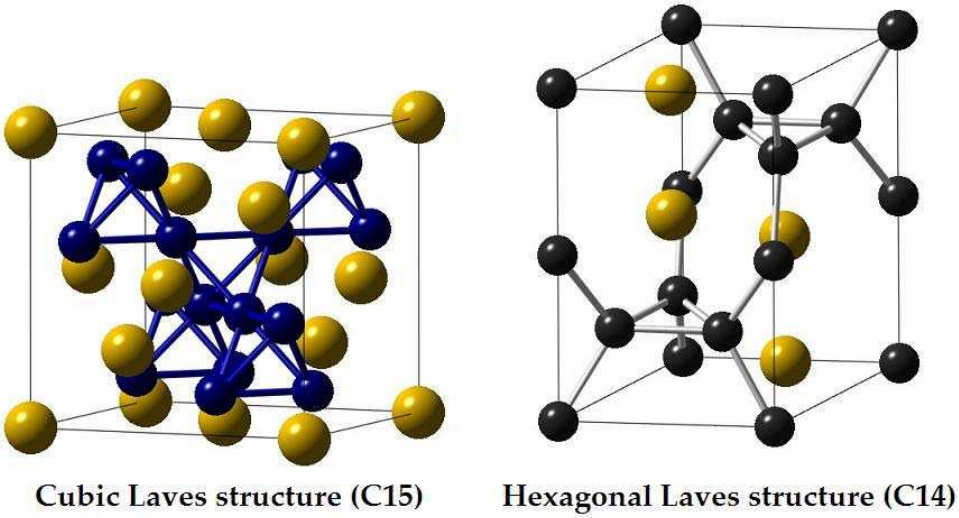

Figure 3.1: Crystal structure of the cubic (C15) and hexagonal (C14) Laves phases. Left panel: $MgCu_2$ prototype (Mg: yellow, Cu: blue). Right panel: $MgZn_2$ prototype (Mg: yellow, Zn: black).

C15	atom	Cu	Mg
atom	site	16d	8a
Cu	16d	6	6
Mg	8a	12	4

C14	atom	Zn1	Zn2	Mg
atom	site	2a	6h	4f
Zn1	2a	0	6	6
Zn2	6h	2	4	6
Mg	4f	3	9	4

Table 3.1: Crystallographic sites and the number of their neighbors atoms in cubic C15 ($MgCu_2$) and hexagonal C14 ($MgZn_2$) prototype structures.

As commented above, we have synthesized three series: $R_{1-x}R'_xFe_2$, $R_{1-x}R'_x(Fe_{1-y}Al_y)_2$ and $R(Fe_{1-y}M_y)_2$ (with R = Gd, Ho, Er; R' = Lu, Y; and M = Ga, Ge). The cubic C15 structure is preserved for all the concentrations through the $R_{1-x}R'_xFe_2$ series, whereas for the other two series the structure changes depending on the Fe concentration.

The $R_{1-x}R'_x(Fe_{1-y}Al_y)_2$ pseudobinary Laves phases present cubic C15 crystal structure in the concentration regions close to binary compounds, RFe_2 and RAl_2 (see Fig. 3.2). For an intermediate concentration range near equiatomic composition y ∼0.5 they crystallize in the hexagonal C14 structure.[2] In addition, C15 and C14 phases coexist for concentrations around y ∼0.3 and ∼0.7, although these coexistence regions depend on the constituent elements [57, 58].

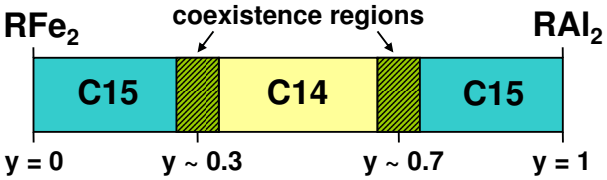

Figure 3.2: Phase diagram of the C15 and C14 Laves phases structure through the $R(Fe_{1-y}Al_y)_2$ series as a function of the Al content. The lined area correspond to the region where C15 and C14 phases coexist.

The C15 cubic structure of the RFe_2 parent compounds is not preserved through the $R(Fe_{1-y}M_y)_2$ (M = Ga, Ge) series due to the different crystal structure of the RM_2 end members. RGa_2 crystallizes in the AlB_2-type hexagonal structure (space group P6/mmm) [59], whereas the ideal composition RGe_2 is not realized in most cases [60, 61], and the Laves phase structure is only preserved for low concentrations of the non-magnetic M atoms (M = Ga, Ge) [62].

The diffraction patterns were Rietveld refined using the FULLPROF code. The diffraction pattern of $Ho_{0.5}Lu_{0.5}Fe_2$ (C15) and $Ho_{0.5}Lu_{0.5}(Fe_{0.5}Al_{0.5})_2$ (C14) are shown in Fig. 3.3 as an illustrative example.

Fig. 3.4 shows the evolution of the XRD patterns through the $Ho_{1-x}Lu_xFe_2$ and $Ho_{0.5}Lu_{0.5}(Fe_{1-y}Al_y)_2$ series. The profile does not change through the series with the exception of the $Ho_{0.5}Lu_{0.5}(Fe_{0.5}Al_{0.5})_2$, which possesses hexagonal C14 structure The patterns of the compounds with C15 structure are nearly identical and only a small shift upon dilution is found. This shift is due

[2]It is worth to note that in the particular case of $R_{1-x}R'_x(Fe_{0.5}Al_{0.5})_2$ the Fe and Al atoms are distributed on both the 2a and 6h sites without exhibiting any preferential occupancy [56].

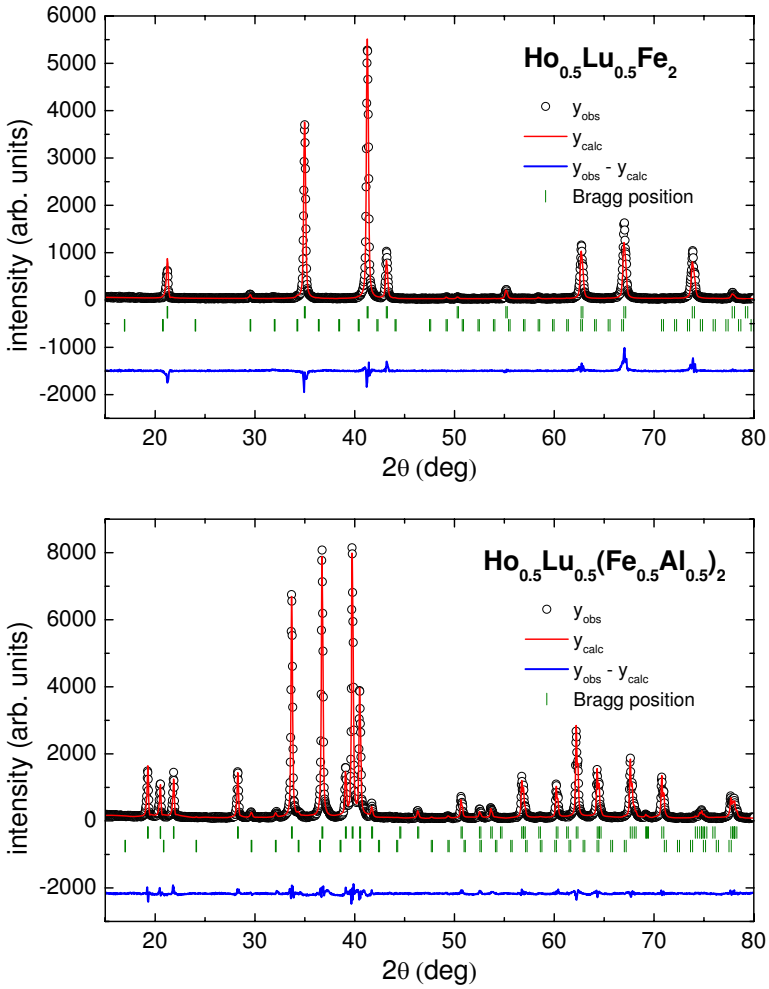

Figure 3.3: Rietveld refinement of $Ho_{0.5}Lu_{0.5}Fe_2$ (upper panel) and $Ho_{0.5}Lu_{0.5}(Fe_{0.5}Al_{0.5})_2$ (lower panel) as representative examples of the cubic C15 and hexagonal C14 structures.

to the modification of the crystal cell parameters: lattice expansion (contraction) occurs upon replacing Fe by Al (Ho by Lu) leading to a displacement of the peaks towards lower (higher) 2θ angle.

The structural information derived form the Rietveld refinement is summarized in Table 3.2: crystal structure, lattice parameters and the reliability Bragg factor associated to the main phase. Good crystallinity of the samples is indicated by the low Bragg factors obtained. The presence of secondary phases and their content (in %) have also been obtained from the Rietveld refinement. Typically, a small amount of R_2O_3 ($\lesssim 2\%$) has been found in our samples, as indicated in Table 3.2. In addition, secondary RFe_3 phases

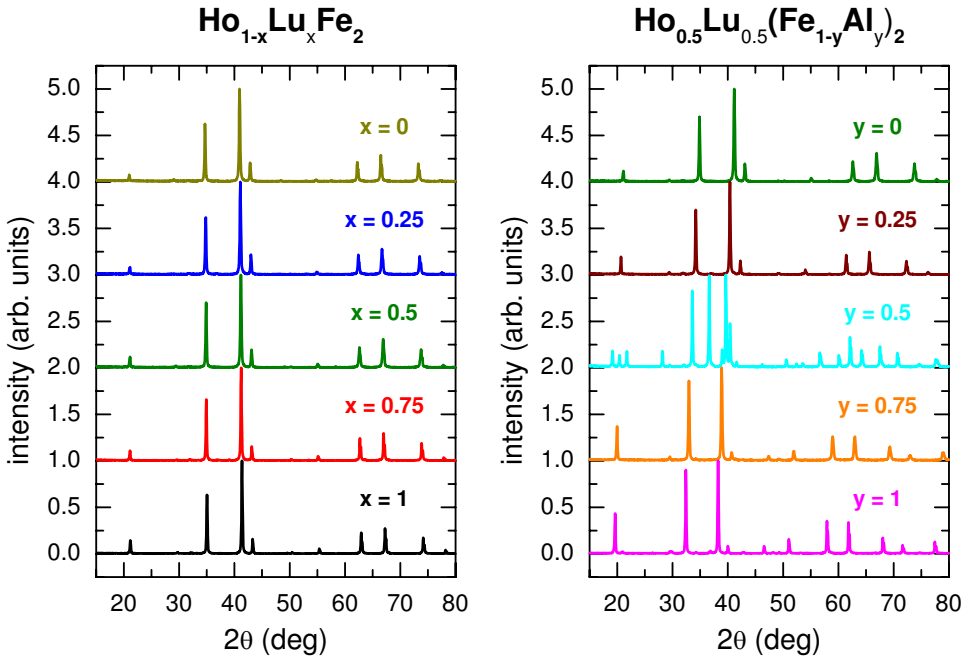

Figure 3.4: Evolution of the XRD diffraction patterns through the $Ho_{1-x}Lu_xFe_2$ (left panel) and $Ho_{0.5}Lu_{0.5}(Fe_{1-y}Al_y)_2$ (right panel) series.

have been occasionally found (less than 4%). The percentage of this phase is greater in the case of compounds containing Ga and Ge.[3]

The cell parameter, see Fig. 3.5, shows a linear variation with x and y through the $R_{1-x}R'_x(Fe_{1-y}Al_y)_2$ series. In $R_{1-x}Y_xFe_2$, the cell parameter increases linearly by increasing the Y content, whereas it diminishes in $R_{1-x}Lu_xFe_2$ upon increasing the Lu content [see Fig. 3.5(a)]. Moreover, there is a lattice expansion by increasing the Al content [see Fig. 3.5(b)]. The crystalline cell volume through the $Ho_{1-x}Lu_x(Fe_{1-y}Al_y)_2$ also varies linearly as shown in the inset of Fig. 3.5(b).[4]

[3]For example, the content of RFe_3 phase in $R(Fe_{0.9}Ge_{0.1})_2$ compounds is ∼50% and, strictly speaking, it is not correct to consider RFe_3 as a secondary phase. However, both RFe_2 ($Fd\bar{3}m$) and RFe_3 ($R\bar{3}m$) crystal structures are similar [63]: (1) the tetrahedral clustering of the Fe atoms as well as the stacking of these tetrahedral units in the two structures are closely related, and (2) the hexagonal arrangements of the R atoms in the two structures have a common stacking sequence; the only difference is that the hexagonal array of R atoms is double layered in RFe_2 and triple layered in RFe_3. These differences do not affect the purpose of the XMCD study that will be presented in Chapter 5.

[4]For sake of comparison it has been included the C15-equivalent volume of the C14 compound obtained by assuming the same number of formula units (f.u.) as in the C15 structure, i.e., $\frac{a^2 \times c \times \sin(120^\circ)}{2}$.

Sample	Structure	a(Å)	c(Å)	R_{Bragg}	Secondary Phases
YFe_2	C15	7.350	-	3.55	<2% R_2O_3
$HoFe_2$	C15	7.294	-	9.44	<2% R_2O_3
$ErFe_2$	C15	7.278	-	16.96	-
$LuFe_2$	C15	7.217	-	7.51	<2% R_2O_3
$HoAl_2$	C15	7.812	-	14.54	-
$Ho_{0.75}Y_{0.25}Fe_2$	C15	7.314	-	17.5	<3% RFe_3
$Ho_{0.5}Y_{0.5}Fe_2$	C15	7.325	-	7.15	<3% RFe_3
$Ho_{0.2}Y_{0.8}Fe_2$	C15	7.341	-	5.90	<2% RFe_3
$Er_{0.75}Y_{0.25}Fe_2$	C15	7.293	-	8.23	-
$Er_{0.5}Y_{0.5}Fe_2$	C15	7.312	-	7.04	<4% RFe_3
$Er_{0.15}Y_{0.85}Fe_2$	C15	7.341	-	4.79	-
$Ho_{0.75}Lu_{0.25}Fe_2$	C15	7.278	-	9.83	<1% RFe_3
$Ho_{0.5}Lu_{0.5}Fe_2$	C15	7.254	-	10.5	<1% R_2O_3
$Ho_{0.25}Lu_{0.75}Fe_2$	C15	7.241	-	9.78	-
$Ho_{0.5}Lu_{0.5}(Fe_{0.75}Al_{0.25})_2$	C15	7.372	-	7.83	<2% R_2O_3
$Ho_{0.5}Lu_{0.5}(Fe_{0.5}Al_{0.5})_2$	C14	5.320	8.658	1.04	<2% R_2O_3
$Ho_{0.5}Lu_{0.5}(Fe_{0.25}Al_{0.75})_2$	C15	7.657	-	10.1	<3% R_2O_3
$Ho_{0.5}Lu_{0.5}Al_2$	C15	7.773	-	10.5	<4% RAl_3 + <2% R_2O_3
$Ho(Fe_{0.9}Ga_{0.1})_2$	C15	7.335	-	7.95	∼10% RFe_3
$Gd(Fe_{0.9}Ga_{0.1})_2$	C15	7.429	-	10.8	<4% RFe_3
$Y(Fe_{0.9}Ga_{0.1})_2$	C15	7.395	-	2.28	<6% RFe_3
$Ho(Fe_{0.9}Ge_{0.1})_2$	C15	7.310	-	10.6	∼50% RFe_3
$Gd(Fe_{0.9}Ge_{0.1})_2$	C15	7.372	-	7.83	∼40% RFe_3

Table 3.2: Structural information derived from Rietveld refinement of XRD patterns: crystal structure, lattice parameter ($\pm$ 0.5 $\times$ 10^{-3}), reliability Bragg factor associated to the main phase and percentage of secondary phases (see text for details).

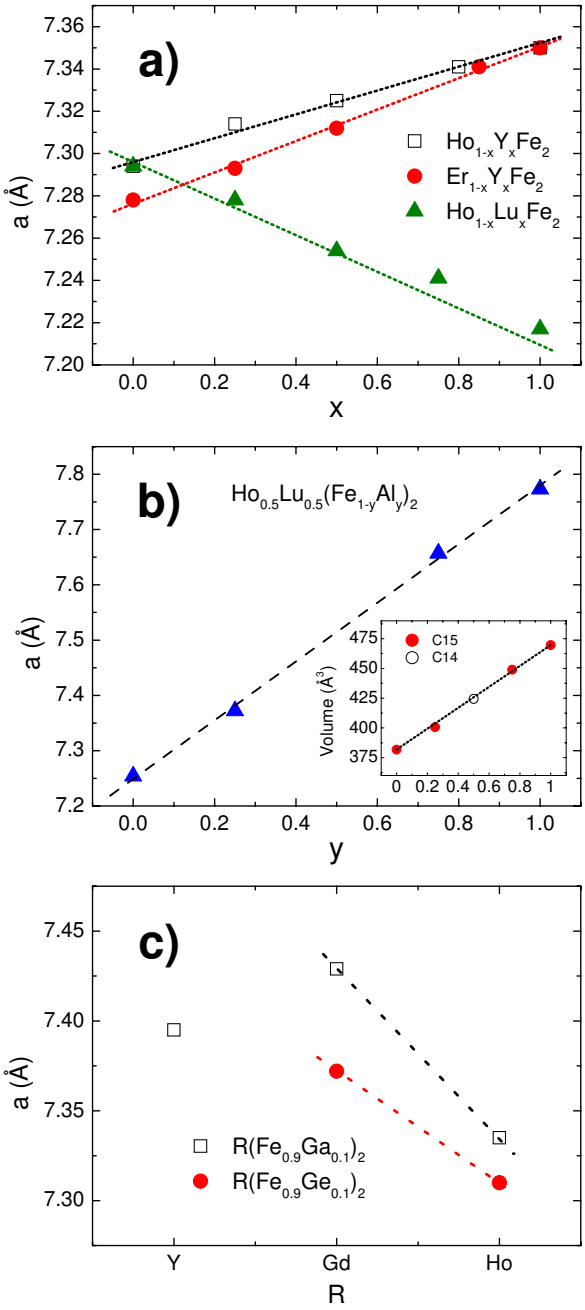

Figure 3.5: Dependence of the cell parameter a in the series synthesized: (a) $Ho_{1-x}Y_xFe_2$, $Er_{1-x}Y_xFe_2$ and $Ho_{1-x}Lu_xFe_2$, (b) $Ho_{0.5}Lu_{0.5}(Fe_{1-y}Al_y)_2$ and (c) $R(Fe_{0.9}Ga_{0.1})_2$ and $R(Fe_{0.9}Ge_{0.1})_2$. Inset in panel (b) shows the comparison of the cell volume in the $Ho_{0.5}Lu_{0.5}(Fe_{1-y}Al_y)_2$ series (see text for details).

3.2 Magnetic characterization

The main objective of this Thesis is the understanding of the XMCD spectra in R-T intermetallics. To this end it is necessary to get a proper magnetic characterization of the compounds under study at the same experimental conditions that will be fixed for the XMCD experiments. Most of these XMCD measurements have been performed at low temperature (T = 5 K) and high magnetic fields (H = 50 kOe). In addition, we have taken advantage in several cases of the peculiar temperature dependence of the magnetization, M(T). For these reasons we focus ourselves in the following to study the M(H) and M(T) behavior of the synthesized samples for this work.

3.2.1 $R_{1-x}R'_xFe_2$ series

Fig. 3.6 shows the magnetic field dependence of the magnetization recorded at T = 5 K for the $R_{1-x}R'_xFe_2$ series: a) $Ho_{1-x}Y_xFe_2$, b) $Er_{1-x}Y_xFe_2$ and c) $Ho_{1-x}Lu_xFe_2$.

In all cases, the magnetization is nearly saturated at H > 10 kOe. Hence, the saturation magnetization will be taken as the magnetization measured at T = 5 K and H = 50 kOe (see Table 3.3). As the content of the magnetic rare-earth is reduced, the magnetocrystalline anisotropy decreases and the M(H) curves saturate at lower magnetic fields. Moreover, in the $Er_{1-x}Y_xFe_2$ compounds a smooth increase of the initial magnetization is observed. Such a behavior has been related with the propagation of the domain walls. The domains walls are blocked for magnetic fields lower than the propagation field, H_p. In the case of $Er_{1-x}Y_xFe_2$ compounds, H_p ~3 kOe at T = 5 K and it decreases by increasing the temperature [64].

The magnetization measured at T = 5 K and H = 50 kOe can be accounted for by applying a two sublattice model. This model considers that the total magnetization of RFe_2, M_{Tot}, corresponds to the simple addition of the magnetization of both magnetic sublattices: $\overrightarrow{M}_{Tot} = \overrightarrow{M}_R + \overrightarrow{M}_{Fe}$. In the case of the diluted $R_{1-x}R'_xFe_2$ compounds in which R' is a non-magnetic rare-earth, the magnetization of the whole rare-earth sublattice can be written as: $\overrightarrow{M}_R + \overrightarrow{M}_{R'} \sim \overrightarrow{M}_R = (1 - x)\ \overrightarrow{\mu_R}$. Hence, by considering that $\overrightarrow{M}_R$ and $\overrightarrow{M}_{Fe}$ are collinear and antiferromagnetically coupled, the absolute value of the total magnetization can be expressed as:

$$M_{Tot} = |(1 - x)\mu_R - 2\ \mu_{Fe}| \tag{3.1}$$

The total magnetization of the system can be calculated by assuming that

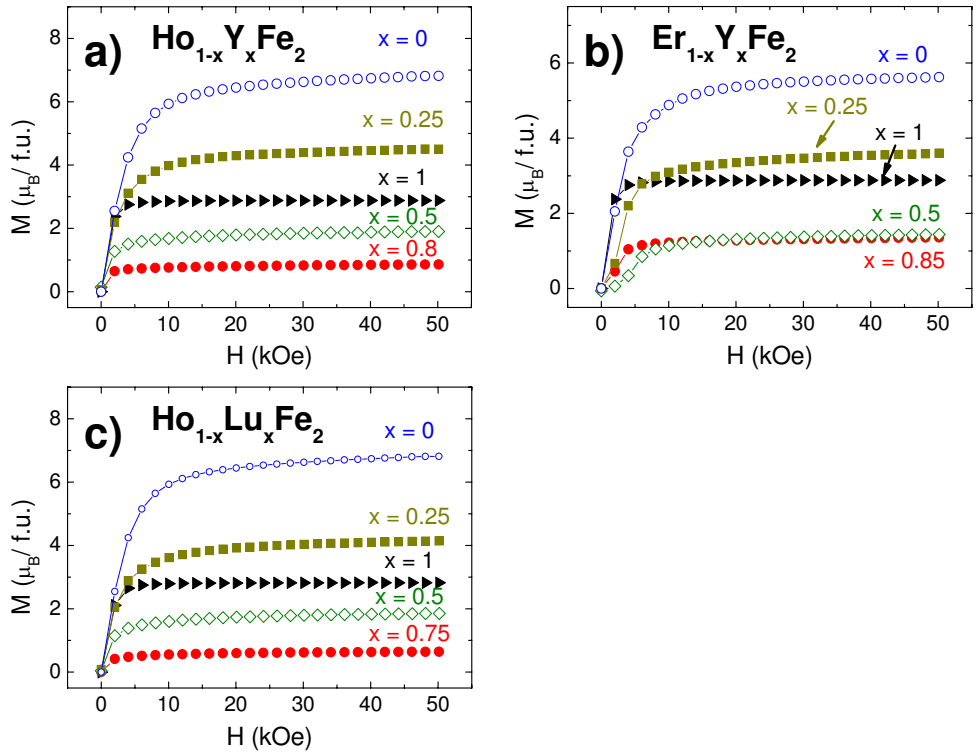

Figure 3.6: Isothermal magnetization curves measured at T = 5 K for: (a) $Ho_{1-x}Y_xFe_2$, (b) $Er_{1-x}Y_xFe_2$ and (c) $Ho_{1-x}Lu_xFe_2$ series.

both μ_{Fe} and μ_R remain constant through the $R_{1-x}R'_xFe_2$ series [65], and considering some approximations for the values of μ_{Fe} and μ_R. First, it is assumed that M_{Fe} corresponds to the magnetization of the RFe_2 compounds in which R is no magnetic, that is $\mu_{Fe} \approx 1.4\ \mu_B$. Then, two different approximations can be considered to derive μ_R: (a) μ_R is taken as its free ion value, independently on x ($\mu_{Ho} \sim 10\mu_B$ and $\mu_{Er} \sim 9\mu_B$) and, (b) μ_R is taken as the magnetization value of the RAl_2 compounds measured at the same experimental conditions ($\mu_{Ho} \sim 9.25\ \mu_B$ and $\mu_{Er} \sim 7.90\ \mu_B$).

Fig. 3.7 and Table 3.3 show the comparison of the magnetization measured at T = 5 K and H = 50 kOe with those obtained after applying the two sublattice model, Eq. (3.1). In both (a) and (b) cases there is a good agreement between the calculated and experimental values. Only slightly differences are found due to the lower magnetization value of the RAl_2 compounds respect to the μ_R free-ion ones. That is, the magnetization of the $R_{1-x}R'_xFe_2$ compounds is well described with a two sublattice model.

Additionally, it is worth to mention that the magnetization values at T = 5 K and H = 50 kOe do not exhibit a linear variation with x (see Fig. 3.7).

Sample	M ($\mu_B/f.u.$)		
	Experimental	Two sublattice model	
		case (a)	case(b)
$HoFe_2$	6.82	7.12	6.37
$Ho_{0.75}Y_{0.25}Fe_2$	4.50	4.62	4.06
$Ho_{0.5}Y_{0.5}Fe_2$	1.90	2.12	1.74
$Ho_{0.2}Y_{0.8}Fe_2$	0.86	0.88	1.03
YFe_2	2.88	2.88	2.88
$ErFe_2$	5.62	6.12	5.02
$Er_{0.75}Y_{0.25}Fe_2$	3.60	3.87	3.04
$Er_{0.5}Y_{0.5}Fe_2$	1.44	1.62	1.07
$Er_{0.15}Y_{0.85}Fe_2$	1.36	1.53	1.70
YFe_2	2.88	2.88	2.88
$HoFe_2$	6.82	7.18	6.43
$Ho_{0.75}Lu_{0.25}Fe_2$	4.14	4.68	4.12
$Ho_{0.5}Lu_{0.5}Fe_2$	1.86	2.18	1.80
$Ho_{0.25}Lu_{0.75}Fe_2$	0.65	0.32	0.50
$LuFe_2$	2.82	2.82	2.82
$HoAl_2$	9.25	–	–
$ErAl_2$	7.90	–	–

Table 3.3: Experimental magnetization values of $R_{1-x}R'_xFe_2$ and RAl_2 compounds recorded at T = 5 K and H = 50 kOe, and magnetization values obtained by applying a two sublattice model in the two considered (a) and (b) cases (see text for details). The estimated error of the magnetization values is ± 0.05 $\mu_B/f.u.$

There is a slope change which reveals the reversal of the dominant magnetic sublattice through the $R_{1-x}R'_xFe_2$ series. According to Eq. (3.1) there is a critical concentration of the non-magnetic rare-earth, x_c, for which the total magnetization of the system becomes zero. For concentrations below x_c the magnetization of the rare-earth sublattice predominates over the Fe one, while the contrary holds for $x > x_c$.

The critical concentration can be experimentally obtained as the minimum of the saturated magnetization *vs.* concentration curves [65, 66] by fitting the experimental M(H = 50 kOe) data at both sides of the extrapolated minimum, x ∼0.7 (see Fig. 3.8). The critical concentration values obtained, denoted as $x_c^{(1)}$, are reported in Table 3.4. The critical concentration can also be obtained by applying the two sublattice model, Eq. (3.1). At the critical concentration the magnetization is zero, and then: (1-x) $\mu_R = 2\ \mu_{Fe}$. Accordingly, the critical concentration is given by

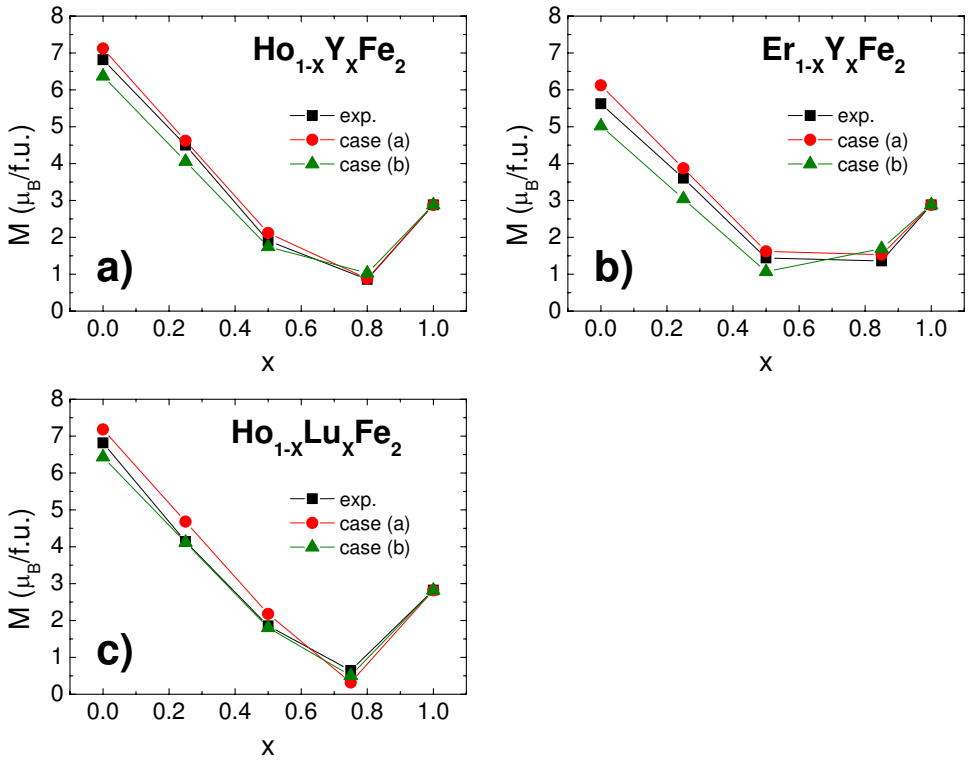

Figure 3.7: Comparison of the experimental magnetization recorded at T = 5 K and H = 50 kOe with the values obtained after applying the two sublattice model (see text for details).

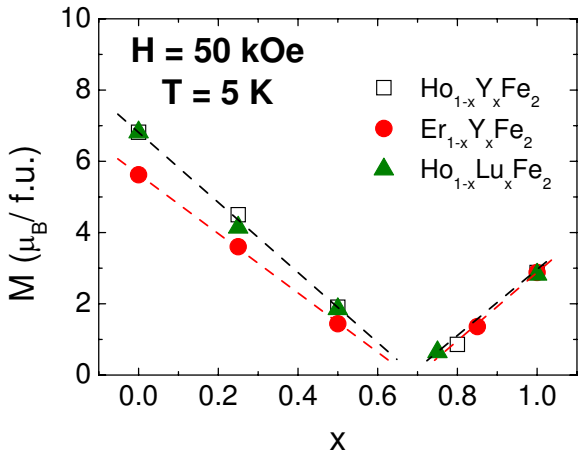

Figure 3.8: Magnetization values at T = 5 K and H = 50 kOe as a function of concentration (lines are guide for the eye).

$$x_c = 1 - 2\frac{\mu_{Fe}}{\mu_R} \tag{3.2}$$

An estimation of x_c can be obtained by considering that μ_R corresponds to the free-ion value and μ_{Fe} ∼1.4 μ_B. The calculated critical concentrations, denoted as $x_c^{(2)}$, are reported in Table 3.4. There is a good agreement between the values obtained by using both methods. Consequently, we can consider that x_c ∼0.7 for the three studied series.[5]

	$x_c^{(1)}$	$x_c^{(2)}$
$Ho_{1-x}Y_xFe_2$	0.7(1)	0.7(2)
$Ho_{1-x}Lu_xFe_2$	0.6(8)	0.7(2)
$Er_{1-x}Y_xFe_2$	0.7(0)	0.6(9)

Table 3.4: Calculated critical concentrations, x_c, for the $R_{1-x}R'_xFe_2$ series: (1) by linear fitting of the experimental data and, (2) by applying the two sublattice model (see text for details).

Regarding the M(T) behavior, Fig. 3.9 shows the zero field cooled (ZFC) magnetization curves recorded on $R_{1-x}R'_xFe_2$ compounds upon warming from 5 to 310 K and under a magnetic field of H = 1 kOe (left panels) and 50 kOe (right panels).

Broadly speaking, the ZFC M(T) curves exhibit similar temperature dependence at both magnetic fields, except the ZFC M(T) curves recorded at H = 1 kOe through $Er_{1-x}Y_xFe_2$ series. These curves exhibit an abrupt decrease of the magnetization at low temperature (T ∼ 30–40 K), which is absent when measuring at H = 50 kOe. We can ascribe this behavior to the blocking of the domain walls occurring when the applied magnetic field is lower than the propagation field. As commented above, in the case of $Er_{1-x}Y_xFe_2$ compounds the propagation field is ∼3 kOe at T = 5 K and it decreases by increasing the temperature [64].

At higher temperature, a magnetic compensation point is evidenced in the $Ho_{1-x}Lu_xFe_2$ and $Er_{1-x}Y_xFe_2$ compounds as a minimum at T = T_{Comp} (see Fig. 3.9). This is a consequence of the different temperature dependence of both R and Fe sublattice magnetization. Above T_{Comp} the Fe sublattice magnetization dominates the overall magnetization. Upon cooling, the rare-earth sublattice magnetization increases up to exceed the Fe one, becoming the dominant magnetic sublattice. Hence, when $x < x_c$ ($x_c \approx 0.7$ in all cases),

[5]The similarity of the x_c values for the Ho and Er series can be easily understood since μ_{Fe} remains constant through both series and, hence, x_c depends only on the rare-earth moment which yields a x_c^{Ho}/x_c^{Er} ratio of 0.9.

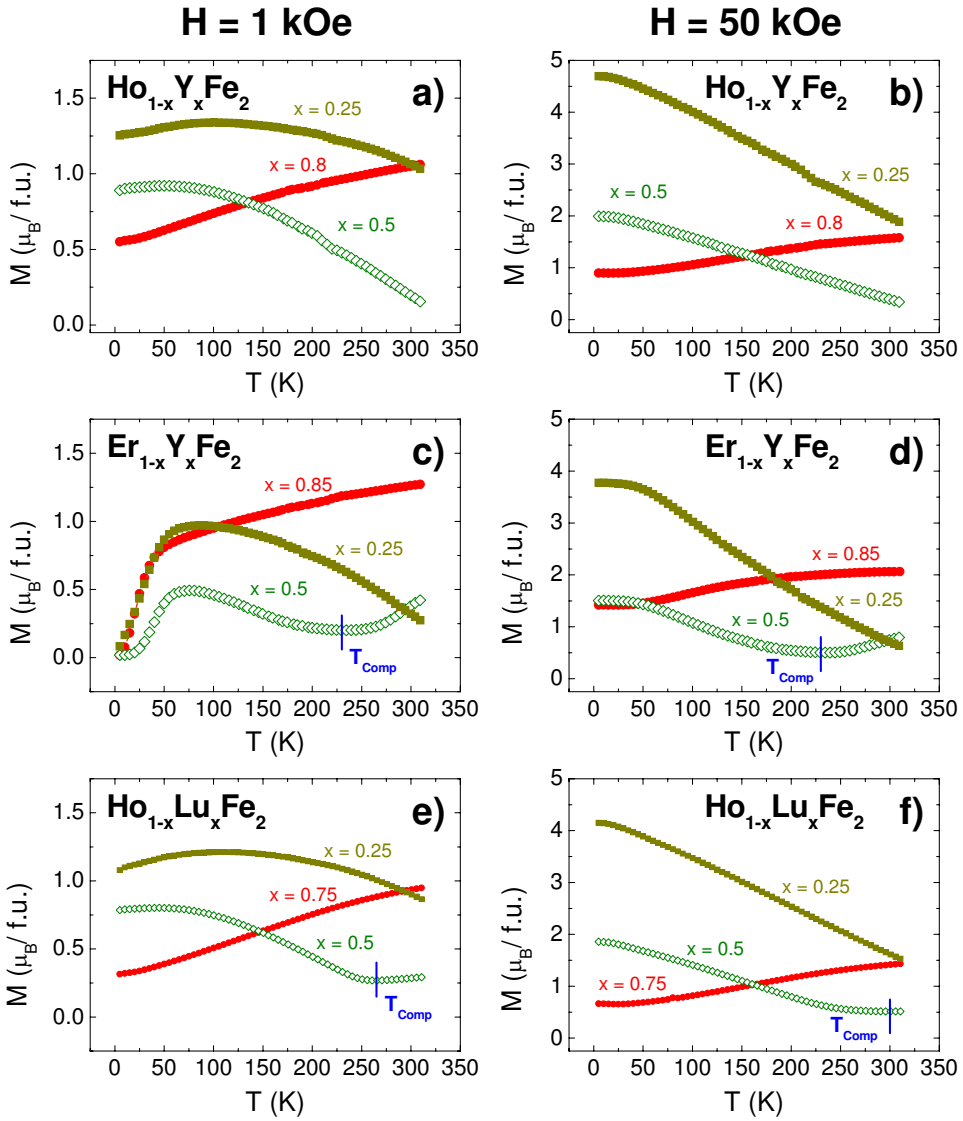

Figure 3.9: Magnetization of the $R_{1-x}R'_xFe_2$ systems as a function of the temperature at H = 1 kOe (left panel) and 50 kOe (right panel).

at $T > T_{Comp}$ the rare-earth sublattice dominates the overall magnetization, and M increases when the temperature is lowered. In contrast, M decreases when the temperature is lowered when the Fe sublattice is the dominant one ($x < x_c$ or $T > T_{Comp}$).

For ideal systems, a vanishing of the total magnetization is expected at $T = T_{Comp}$. However, the magnetization of the studied compounds is not exactly equal to zero at T_{Comp} (see Fig. 3.9). The presence of a non negligible magnetization at T_{Comp} has been ascribed to the presence of uncompensated

canting moments, to the microstructure of the samples or to the magnetic contribution of the conduction electron polarization [67–69]. Hence, in most cases, the occurrence of a magnetic compensation phenomenon is reflected as a minimum in the M(T) curve.

In order to investigate the magnetic field dependence of T_{Comp}, we have recorded the M(T) curves at different magnetic fields, as displayed in Fig. 3.10. Since the ZFC M(T) curves do not exhibit a sharp minimum, T_{Comp} has been determined as the zero crossing of the first derivative of magnetization curve. The T_{Comp} values obtained at different magnetic fields are displayed in Table 3.5. In $Er_{0.5}Y_{0.5}Fe_2$ the compensation temperature is the same for all the applied magnetic fields, T_{Comp} ~230 K, whereas in $Ho_{0.5}Lu_{0.5}Fe_2$ it slightly diminish from T_{Comp} ~300 K for H = 20 kOe to 265 K for H = 1 kOe.

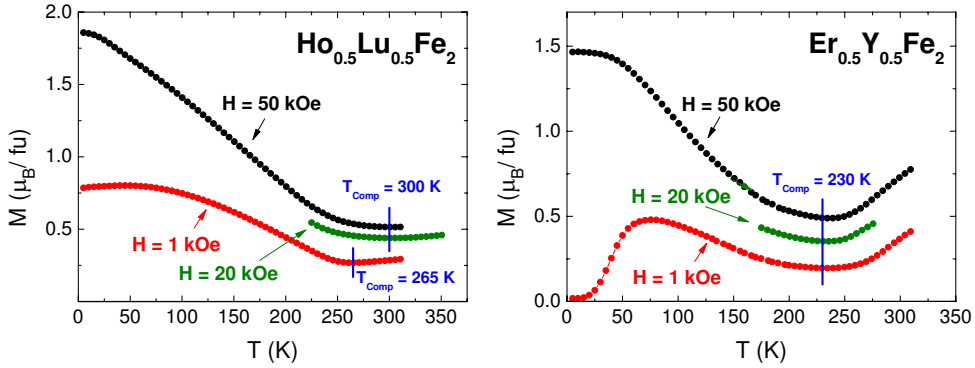

Figure 3.10: Temperature dependence of the zero-filed cooled (ZFC) magnetization for different magnetic fields (H = 1, 20, 50 kOe): $Ho_{0.5}Lu_{0.5}Fe_2$ (left panel) and $Er_{0.5}Y_{0.5}Fe_2$ (right panel).

	T_{Comp}	
	$Ho_{0.5}Lu_{0.5}Fe_2$	$Er_{0.5}Y_{0.5}Fe_2$
ZFC: H = 50 kOe	300 K	230 K
ZFC: H = 20 kOe	300 K	230 K
ZFC: H = 1 kOe	265 K	230 K

Table 3.5: Compensation temperature for $Ho_{0.5}Lu_{0.5}Fe_2$ and $Er_{0.5}Y_{0.5}Fe_2$ determined from the M(T) curves displayed in the Fig. 3.10.

3.2.2 $R_{1-x}R'_x(Fe_{1-y}Al_y)_2$ series

The M(H) curves recorded at T = 5 K on the $Ho_{0.5}Lu_{0.5}(Fe_{1-y}Al_y)_2$ compounds are displayed in Fig. 3.11. The saturation magnetization, see Table 3.6,

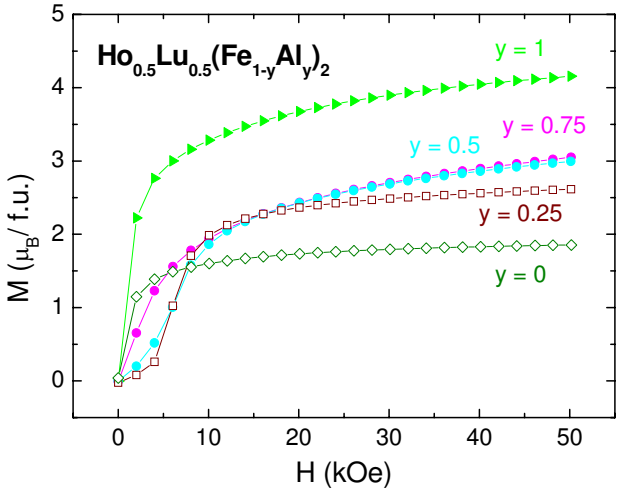

Figure 3.11: Isothermal magnetization curves through $Ho_{0.5}Lu_{0.5}(Fe_{1-y}Al_y)_2$ series recorded at T = 5 K.

Sample	M ($\mu_B/f.u.$)
$Ho_{0.5}Lu_{0.5}Fe_2$	1.86
$Ho_{0.5}Lu_{0.5}(Fe_{0.75}Al_{0.25})_2$	2.62
$Ho_{0.5}Lu_{0.5}(Fe_{0.5}Al_{0.5})_2$	2.99
$Ho_{0.5}Lu_{0.5}(Fe_{0.25}Al_{0.75})_2$	3.05
$Ho_{0.5}Lu_{0.5}Al_2$	4.16

Table 3.6: Magnetization values of $Ho_{0.5}Lu_{0.5}(Fe_{1-y}Al_y)_2$ compounds at T = 5 K and H = 50 kOe. The estimated error of the magnetization value is ± 0.05 $\mu_B/f.u.$.

increases when Fe is progressively diluted by Al due to the antiferromagnetic coupling. However, it does not follow a linear variation, as it would be expected from a simple dilution effect if both μ_{Fe} and μ_R will remain constant [65]. Moreover, all the compounds, except $Ho_{0.5}Lu_{0.5}Al_2$, present a significant high-field slope in the M(H) curves. The diluted compounds also display pronounced curvatures at low fields.

It is known from previous works that in compounds with non magnetic rare earth, $Y(Fe_{1-y}Al_y)_2$ and $Lu(Fe_{1-y}Al_y)_2$, the substitution of Fe by Al induces magnetic disorder in the Fe sublattice, the formation of magnetic clusters and spin glass like behavior [70, 71]. These compounds also show a rapid decrease of the Curie temperatures and magnetization towards nearly zero values for y > 0.20 [72–74]. Moreover, several neutron diffraction experiments performed on $R(Fe_{1-y}Al_y)_2$ compounds report a low ordered rare earth sublattice, in which the R magnetic moments are not fully collinear [73, 75, 76].

Similar magnetic behavior has also been observed for $R_{1-x}R'_xAl_2$ compounds, in which the partial quenching of M_R is explained in terms of random magnetic anisotropy and spin glass like behavior [77, 78]. In systems where an anisotropic R is placed into a randomized environment, crystal field effects on R dictate a partially randomized structure. Moreover, the combination of magnetic disorder and large anisotropy fields can combine to be responsible for very thin domain walls. These domain walls can be pinned by obstacles of atomic dimension, giving rise to the development of strong magnetic hardness [79].

All these results indicate that a complex scenario arises when both R and Fe sublattices are diluted by non-magnetic atoms. This interesting problem is, however, beyond the scope of this Thesis. The main objective of this Thesis is to provide a better understanding of the Fe K- and R $L_{2,3}$-edges XMCD signals. For this reason, we will mainly focus on the XMCD signals recorded at low temperature and under an applied field of H = 50 kOe. In this case, the magnetic state of the $Ho_{0.5}Lu_{0.5}(Fe_{1-y}Al_y)_2$ ($0 < y < 1$) compounds is expected to be close to the ideal situation with saturated M_{Fe} and M_R.

Fig. 3.12 shows the magnetization temperature dependence of the $Ho_{0.5}Lu_{0.5}(Fe_{1-y}Al_y)_2$ compounds. Both ZFC M(T) curves at H = 1 kOe and 50 kOe have been recorded upon warming. The substitution of Fe by Al causes a drastic reduction of the ordering temperature. This might be ascribed to a decrease of the Fe-Fe and Fe-R interactions as a consequence of the magnetic disorder provoked by the Fe-Al substitution.

The ZFC M(T) curves recorded at relatively low magnetic field, H = 1 kOe, show an abrupt decrease of the magnetization at low temperature (T $\sim$ 25–50 K) for the intermediate diluted compounds. A similar reduction of the magnetization has been observed in the $Lu(Fe_{1-y}Al_y)_2$ [71] and, also in the $Er_{1-x}Y_xFe_2$ compounds as shown in the previous subsection. In the former case, the decrease has been interpreted in terms of spin glass like behavior [71] and, in the latter case, it has been ascribed to the blocking of domain walls [64].[6] Probably, both phenomena influence the behavior of the $Ho_{0.5}Lu_{0.5}(Fe_{1-y}Al_y)_2$ magnetization, and further experiments are needed to get a deeper insight in the origin of such behavior.

[6] As we have discussed before, very thin domain walls are expected for this type of compounds, where magnetic disorder and large anisotropy fields coexist. This thin domain walls are easily blocked, especially at low T when the magnetic anisotropy increases [80]

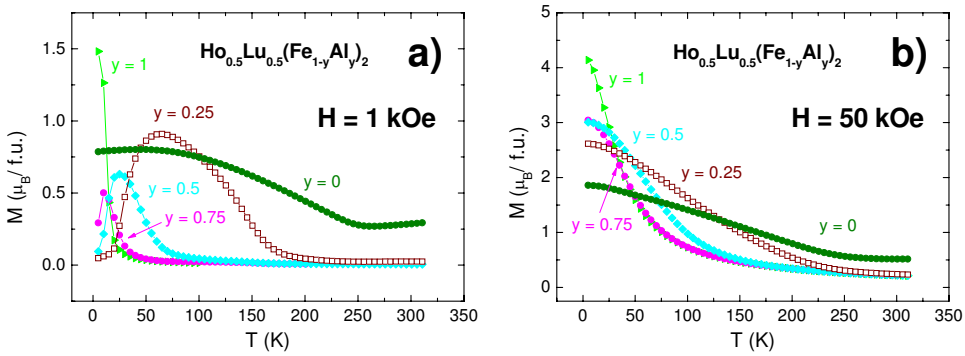

Figure 3.12: Magnetization of the $Ho_{0.5}Lu_{0.5}(Fe_{1-y}Al_y)_2$ series as a function of the temperature at H = 1 kOe [panel (a)] and 50 kOe [panel (b)].

3.2.3 $R(Fe_{0.9}M_{0.1})_2$ compounds

Fig. 3.13 shows the comparison of the M(H) curves for both RFe_2 and $R(Fe_{0.9}M_{0.1})_2$ recorded at T = 5 K. The values of magnetization at T = 5 K and H = 50 kOe are given in Table 3.7.

The replacement of 10% of Fe by Ga in YFe_2 provokes a decrease of ∼20% of the magnetization at H = 50 kOe. Hence, we can consider that, similarly to the case of Fe-Al substitution in $Y(Fe_{1-y}Al_y)_2$ [70], the replacement of Fe by Ga atoms introduce magnetic disorder in the lattice.

When R = Gd and Ho (heavy rare earths), an increase of the saturation

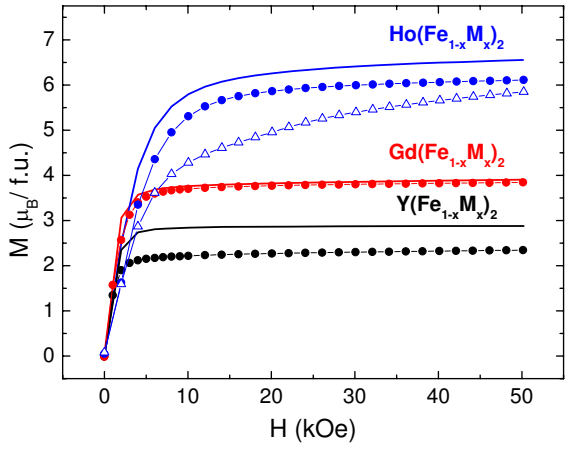

Figure 3.13: Isothermal magnetization curves measured at T = 5 K for $R(Fe_{0.9}M_{0.1})_2$ (•: Ga and △: Ge compounds). For sake of comparison it has been included the magnetization curves of RFe_2 parent compounds (solid line).

Sample	M ($\mu_B/f.u.$)
YFe_2	2.88
$Y(Fe_{0.9}Ga_{0.1})_2$	2.34
$GdFe_2$	3.91
$Gd(Fe_{0.9}Ga_{0.1})_2$	3.84
$HoFe_2$	6.82
$Ho(Fe_{0.9}Ga_{0.1})_2$	6.11
$Ho(Fe_{0.9}Ge_{0.1})_2$	5.85

Table 3.7: Magnetization values of RFe_2 and $R(Fe_{0.9}M_{0.1})_2$ compounds at T = 5 K and H = 50 kOe. The estimated error of the magnetization value is ± 0.05 $\mu_B/f.u.$.

magnetization is expected when Fe is progressively diluted by non magnetic M (Al, Ga or Ge). Such an increase is not experimentally observed, neither in $Gd(Fe_{1-y}M_y)_2$ nor $Ho(Fe_{1-y}M_y)_2$.

In $GdFe_2$ the substitution of 10% of Fe by Ga provokes a tiny reduction of the magnetization, $\lesssim 2$ %. This is in agreement with the results reported for the $Gd(Fe_{1-y}Al_y)_2$ series [81]. In this series, a tiny decrease of the magnetization is observed for compounds with Al concentration up to 0.15. By assuming that the Gd moment remains constant and close to its free ion value, this depletion can be ascribed to an increase of the Fe magnetic moment.

In $HoFe_2$, the magnetization is reduced by 10% and 15% upon substitution of 10% of Fe by Ga or Ge, respectively. These results do not agree with previous results reported on $R(Fe_{0.9}Ga_{0.1})_2$ and $R(Fe_{1-y}Al_y)_2$ with R a heavy magnetic rare-earth [62, 73, 81, 82]. The different behavior upon dilution found in $Ho(Fe_{0.9}Ga_{0.1})_2$ and $Ho(Fe_{0.9}Ge_{0.1})_2$ are probably due to the presence of RFe_3 secondary phase. The RFe_3 phase has a lower saturation magnetization [83], what can lead to the observed decrease of the magnetization.

Fig. 3.14 shows the ZFC M(T) curves for $R(Fe_{0.9}M_{0.1})_2$ compounds at H = 1 kOe and 50 kOe. For both measuring fields, similar temperature dependence is observed. For the Y and Gd based compounds the magnetization increases as the temperature is lowered. The same behavior is observed in the Ho compounds when they are measured at H = 50 kOe. However, the ZFC M(T) curves recorded at H = 1 kOe for the Ho based compounds, see Fig. 3.14(a), exhibit a strong decrease of the magnetization upon cooling. Similar behavior has been observed in $R(Fe_{1-y}Al_y)_2$ and $Ho_{0.5}Lu_{0.5}(Fe_{1-y}Al_y)_2$ compounds. As commented above, it can be related with the blocking of the domain walls and/or with a spin-glass like behavior.

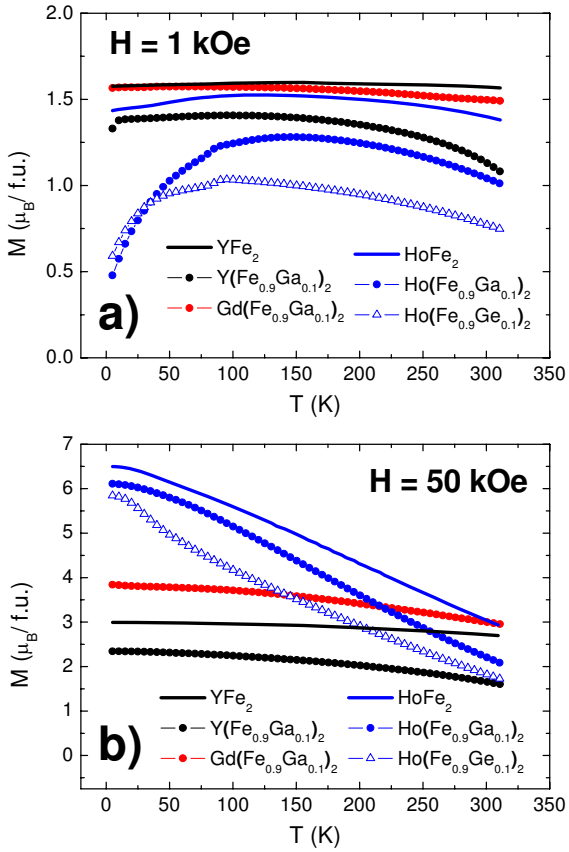

Figure 3.14: Magnetization of the $R(Fe_{0.9}M_{0.1})_2$ compounds as a function of the temperature at H = 1 kOe [panel (a)] and 50 kOe [panel (b)].

Chapter 4

XMCD in R-T intermetallic compounds with different magnetic atomic species: R($4f$) and T($3d$)

The disentanglement of the magnetic contributions coming from different atomic species within the same material has been a challenge for a long time. Most of the experimental techniques used to study the magnetic properties of a given material are sensitive to the total magnetization of the system. Consequently, they can not discern between the contributions of different magnetic species in the material.

Within this scenario X-ray Magnetic Circular Dichroism (XMCD) emerges as an outstanding tool to study magnetism by incorporating the element specificity of core level spectroscopies [84–86]. However, while the capabilities of XMCD have been exploited in the case of localized states carrying a magnetic moment, the same does not hold when the delocalized states are being probed. The soft X-ray atomic calculations reproduce quantitatively the XMCD signal in favorable cases (see for example Ref. [87] and references therein); however, the theoretical representation of the XMCD gets complicated in the hard X-ray domain [21, 88–92]. For this reason, most of these selective magnetometry experiments are limited to the soft X-ray energy. However, in this energy range the XAS techniques do not probe the whole sample volume. The surface sensitivity may affect the magnetic characterization of the samples. The higher penetration depth of the hard X-rays allows to avoid surface effects in order to guaranty that the XMCD becomes a real bulk probe.

However, as previously discussed, no simple interpretation of the XMCD spectra in the hard X-ray range is envisaged, due to the delocalized character of the final states in the photoabsorption process. This is the case, for example, of the K-edge of the $3d$ transition metals (T) and of the $L_{2,3}$-edges of the lanthanides (R), in which the $4p$ and $5d$ conduction states are respectively probed.

This limitation constitutes a serious concern to the nominal capabilities of the XMCD, as one of its most promising applications lies on the possibility of characterize magnetically those states, as T($4p$) or R($5d$), whose response to standard magnetic tools is hindered by that of the more localized T($3d$) and R($4f$) states. This drawback is of special significance in the case of R-T intermetallic compounds. The understanding of the magnetic properties of these systems is still incomplete due to the lack of a detailed magnetic characterization of the conduction band. In particular, of the rare-earth $5d$ states that mediate the R($4f$)-T($3d$) exchange interaction between the rare-earth and the transition metal ions. Consequently, it is necessary to provide a deeper insight into the exact nature of the XMCD spectra corresponding to the conduction band states of the R-T systems. In this respect, it should be noted that previous works have shown that when both atomic species, T and R, are present in the same material the interpretation of the XMCD spectra is further complicated by the occurrence of the so-called "crossed" contributions. That is, both T and R influence the XMCD spectra recorded at both the R L_2-edge [1, 91, 93–98] and the T K-edge [96, 98–104]. These findings mean that, despite the atomic selectivity inherent to the X-ray absorption, the transition metal also contributes to the R L-edges XMCD and, conversely, there is a non-negligible contribution of the lanthanide metal to the T K-edge XMCD.

Aimed to get a correct interpretation of the XMCD spectra at the R $L_{2,3}$- and T K-edges and thus fixing the limits of XMCD into the characterization of the conduction sates, we have performed a systematic XMCD study for different R-T intermetallics. To this end we have selected R-T compounds, as the RT_2 and R_6T_{23} series, whose magnetic properties have been previously well determined by using a plenty of experimental techniques, including macroscopic magnetic characterization tools, neutron diffraction and Mössbauer spectroscopy among others [83].

4.1 Disentanglement of the R and T contributions at the R L_2- and T K-edges XMCD spectra

As discussed above, when a delocalized final state is probed, the XMCD is a simultaneous fingerprint of both the rare-earth and the transition metal magnetism, even when only a single absorption edge of an atomic element is tuned. This does not mean that the atomic selectivity is lost. On the contrary, it provides the possibility of studying at the same time the magnetic behavior of different magnetic species. To verify this hypothesis we have performed a systematic XMCD study at the rare-earth L_2-edge and at the K-edge of the transition metal in selected RT_2 (T: Fe, Co and Al) and $R(Fe_{1-y}Al_y)_2$ compounds.

The rare-earth L_2-edge XMCD spectra of $ErAl_2$ and $HoAl_2$ recorded at T = 5 K and H = 50 kOe are shown in Fig. 4.1. In both cases, the spectral profile consists of a main negative peak A located at E-E_0 ∼1 eV, and a positive structure B at E-E_0 ∼7 eV. The intensity ratio of these main peaks is the same, I_A/I_B ∼ -3, in both Er and Ho L_2-XMCD spectra. Moreover, both absorption edges show a shoulder-like feature at the low energy side of the main negative peak. This feature is due to a quadrupolar ($2p \rightarrow 4f$) transition that accompanies the main dipolar ($2p \rightarrow 5d$) transitions at the L_2-edge [105, 106]. The commonly accepted description states that the shape and the amplitude of the dichroic signal are governed by the $4f$ magnetism through the intra-atomic R($4f$)-R($5d$) hybridization [89].

The simultaneous presence of both quadrupolar and dipolar transitions [105, 106], and the need of including the $4f$-$5d$ intra-atomic exchange interaction [107–110] points out the crucial role of the $4f$ electrons into determining the R L_2-edge XMCD even when the empty $5d$ band is probed [111].

Within this framework, the similar spectral shape observed for both $ErAl_2$ and $HoAl_2$ compounds is in agreement with the atomic-like picture used to account for the XMCD at the rare-earth $L_{2,3}$-edges (see Chapter 1). In the RT_2 series of compounds, the $4f$ magnetic moment is commonly assumed to be close to the free-ion values in all the studied compounds, in agreement with magnetization data [91]. Consequently, no significant variation of the intra-atomic R($4f$)-R($5d$) polarization effect is expected and the experimental behavior of the XMCD cannot be explained in terms of a different magnetism of the rare-earth through the series. However, as shown in Fig. 4.1(a)-(c), the Er L_2-edge XMCD spectra recorded through the $Er(Fe_{1-y}Al_y)_2$ series are quite different from that of $ErAl_2$. Similar modification is observed when Al is substituted by Co in both $ErAl_2$ and $HoAl_2$ compounds (see panels (d) and (e) of Fig. 4.1, respectively). When a magnetic (Co or Fe) $3d$ metal is placed in

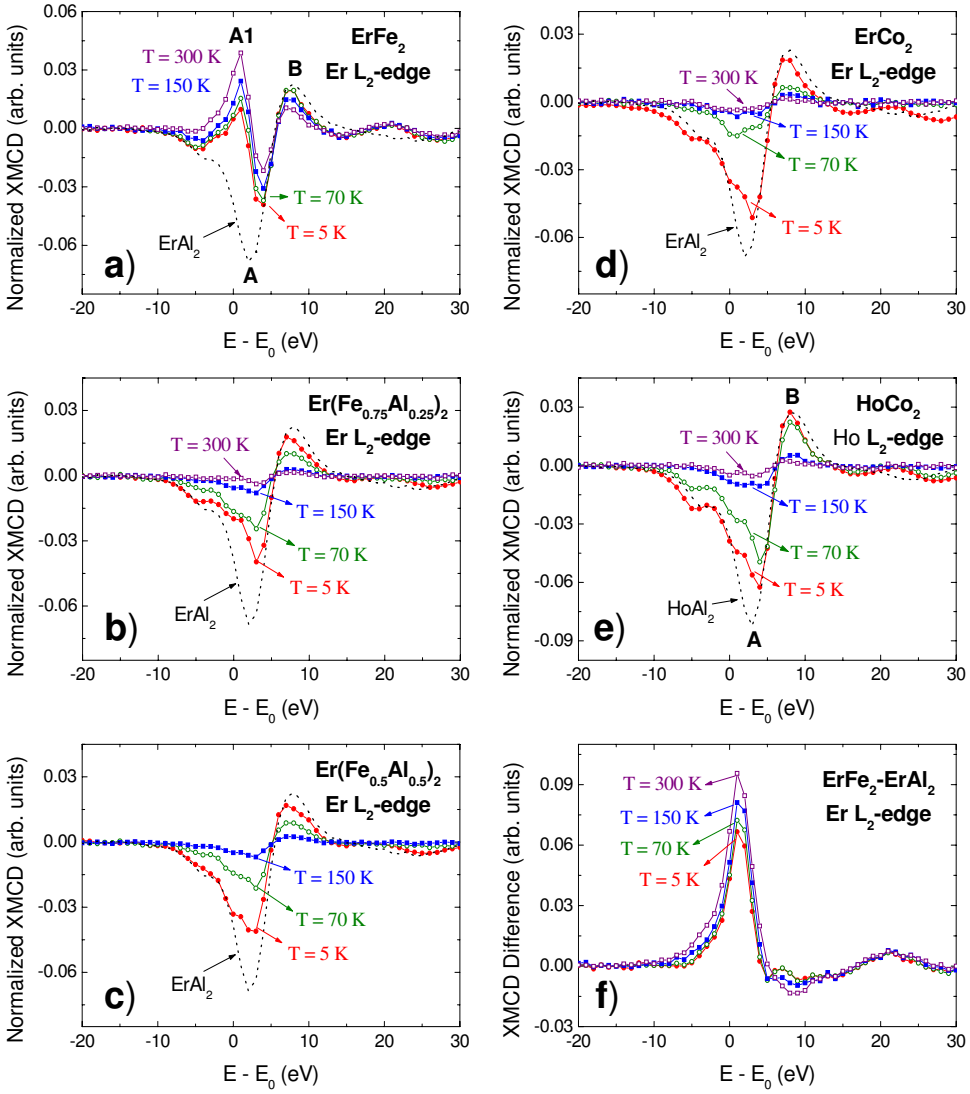

Figure 4.1: Normalized XMCD spectra recorded at H = 50 kOe at the Er L_2-edge in $ErFe_2$ (a), $Er(Fe_{0.75}Al_{0.25})_2$ (b), $Er(Fe_{0.5}Al_{0.5})_2$ (c) and $ErCo_2$ (d), together with those at the Ho L_2-edge XMCD from $HoCo_2$ (e): T = 5 K (red, •), 70 K (green, ○), 150 K (blue, ■) and 300 K (purple, □). The dotted line in each panel shows the spectrum from the RAl_2 compound (R = Er and Ho) measured at T = 5 K. In all the cases the applied magnetic field was 50 kOe. Panel (f) shows the extracted Er L_2-XMCD spectra from $ErFe_2$, obtained by subtracting that of $ErAl_2$.

the RAl_2 lattice both the shape and the amplitude of the peak A are modified. The amplitude of this peak is strongly reduced by a factor $\sim 40\%$ and $\sim 25\%$ for Fe and Co compounds, respectively. In addition, the spectral shape evolves from a single negative peak in RAl_2 to a more structured profile, showing two components, when the $3d$ metals are present. To this respect, the case of $ErFe_2$ is of special significance since a positive peak, $A1$, clearly emerges close to the threshold, E-$E_0 \simeq 0$.

Previous systematic studies suggested that this behavior is due to the magnetic contribution of the specific transition metal, even when the rare-earth is being probed by the X-rays [1, 91, 93, 94, 96]. Therefore, the XMCD spectra at the L_2-edge of the rare-earth in this class of R-T materials is a simultaneous fingerprint of the magnetism of both the rare-earth and the transition-metal. The question to answer now is wether this peculiarity can also provide quantitative information about the magnetic properties of both sublattices separately. To this end we have studied the dependence in temperature of the XMCD signals recorded at the R-L_2 absorption edge (see Fig. 4.1). The temperature behavior of $ErFe_2$ is a paradigmatic case. As noted above, a positive peak $A1$ emerges at the absorption edge and its intensity increases as the temperature does. This behavior is not envisaged at all as response of the rare-earth magnetization. Indeed, one expects that the amplitude of the XMCD signal decreases as temperature increases reflecting the reduction of the Er magnetic moment.

To account for such behavior we have considered that the R L_2-edge XMCD is not exclusively due to the rare-earth, but there is also a contribution coming from the neighboring magnetic transition-metal atoms. In this way, the XMCD signal might be decomposed as the addition of two contributions:

$$XMCD_{RT_2}(T) = XMCD_R(T) + XMCD_T(T) \tag{4.1}$$

one exclusively due to the rare-earth, $XMCD_R$, and the second due to the transition metal, $XMCD_T$.

Within the atomic picture commented above, the rare-earth contribution to the R L_2-edge XMCD spectra is mainly determined by the $4f$ magnetic moments. Because they are close to the free-ion values, it is assumed that $XMCD_R$ corresponds to the whole XMCD spectrum of the RAl_2 compound, as Al atoms do not carry magnetic moment. Under these assumptions it is possible to isolate the $XMCD_T$ contribution by subtracting from each recorded dichroic spectrum that of RAl_2 with the same R and at the same temperature:

$$XMCD_T = XMCD_{RT_2} - XMCD_{RAl_2} \tag{4.2}$$

It should be noted that this procedure also cancels any contribution stemming from the atomic-like quadrupolar transition to the R($4f$) states since these $4f$ states are not affected by the substitution at the T sites.

After applying this subtracting procedure to the $ErFe_2$ compound, see Fig. 4.1(f), we found a peak signal which can be identified as the $XMCD_{Fe}$ contribution. Similar results are found for all the compounds. The extracted $XMCD_T$ contribution shows an intense positive peak at the absorption edge. The profile is basically the same no matter the rare-earth nor the transition metal. Therefore, we can conclude that the transition metal contribution to the R L_2-edge XMCD spectrum is mainly limited to the absorption edge, i.e., to the energy region where the negative peak A appears. The higher energy region, where peak B appears, is significantly less affected; for example, in $ErFe_2$ at T = 5 K, the intensity of the subtracted signal at the peak B is one order of magnitude smaller than at peak A, and its becomes 20 times smaller at room temperature.

These results open the possibility of disentangling the temperature dependence of both contributions from a single XMCD spectra. According to our hypothesis, the intensity of peak B recorded as a function of the temperature should reflect the temperature dependence of the rare-earth sublattice magnetization, M_R(T). Moreover, the intensity of peak A should contain the dependence in temperature of the magnetization of both the rare-earth and transition metal sublattices. Then, we have derived M_R(T) from the intensity of peak B as:

$$M_R(T) = M_R(T = 5K) \times \frac{I_B(T)}{I_B(T = 5K)} \tag{4.3}$$

We have assumed free-ion values at low temperature and then M_R(T = 5 K) equals 9 μ_B and 10 μ_B for Er and Ho compounds, respectively. Next step into determining the temperature dependence of the transition metal magnetization, M_T(T), from the rare-earth L_2-edge XMCD spectrum is to determine the $XMCD_T$(T) term acting in Eq. (4.1). The substraction method described above can be applied by considering that the dependence in temperature of the rare-earth contribution, $XMCD_R$(T), is the same as for the RAl_2 compound. However, the magnetic ordering temperatures of both RT_2 ($T_C \sim 600$ K) and RAl_2 ($T_C \sim 13$ K) compounds significantly differ. Thus, it is not possible to simply identify $XMCD_R$(T) with $XMCD_{RAl_2}$(T). For this reason we have considered that $XMCD_R$(T) is given by the signal recorded at T = 5 K for the RAl_2 compound factorized by the reduction of the rare-earth magnetization:

$$XMCD_R(T) = f(T) \times XMCD_{RAl_2}(T = 5K) \tag{4.4}$$

where f(T) = M_R(T)/M_R(T=5K) has been derived from the temperature dependence of the intensity of peak B according to Eq. (4.3). Then, M_T(T) is obtained as:

$$M_T(T) = M_T(T = 5K) \times \frac{XMCD_T(T)}{XMCD_T(T = 5K)} \tag{4.5}$$

where the values at T = 5 K are determined from the macroscopic magnetization measured upon the same conditions, and by applying a two-sublattices model:

$$\vec{\mathbf{M}}_{Tot} = \vec{\mathbf{M}}_R + \vec{\mathbf{M}}_T \tag{4.6}$$

in which free-ion values (μ_R = gJ) are assumed for the rare-earth magnetic moments. In this way, the same absorption edge yields the temperature dependence of the magnetization of both sublattices, M_R(T) and M_T(T). The result of applying this procedure is reported in Fig. 4.2 and Table 4.1. The total magnetization built up (Fig. 4.3) from the values determined from the XMCD spectra (Fig. 4.2 and Table 4.1) shows a remarkable good agreement with the macroscopic magnetization measured in a commercial SQUID magnetometer at the same experimental conditions (temperature and applied magnetic field). It should be noted that this remarkable agreement is hold throughout both the ferrimagnetic (FM) and paramagnetic (PM) regimes. $ErFe_2$ shows FM ordering from 5 K to room temperature (T_C = 582 K) whereas the magnetic ordering temperature decreases as the Al content increases through the $R(Fe_{1-x}Al_x)_2$ series. In this way T_C is 140 K and 60 K for $Er(Fe_{0.75}Al_{0.25})_2$ and $Er(Fe_{0.5}Al_{0.5})_2$, respectively.

This method provides additional information such as the temperature dependence of both μ_R and μ_{Co} in the RCo_2 compounds, which is not affordable from macroscopic tools. In these systems the Co 3d-band states are near the critical conditions for the Co moment formation [112]. The R magnetic moment is essentially constant in the whole phase diagram while the Co magnetic moment is generally thought to be developed when the rare-earth sublattice undergoes the magnetic ordering transition. Then, the Co subsystem is magnetically ordered in zero external magnetic field ($\mu_{Co} \sim 1\ \mu_B$) due the effect of the molecular field, B_{eff}, created by the R moments acting on the Co sites.

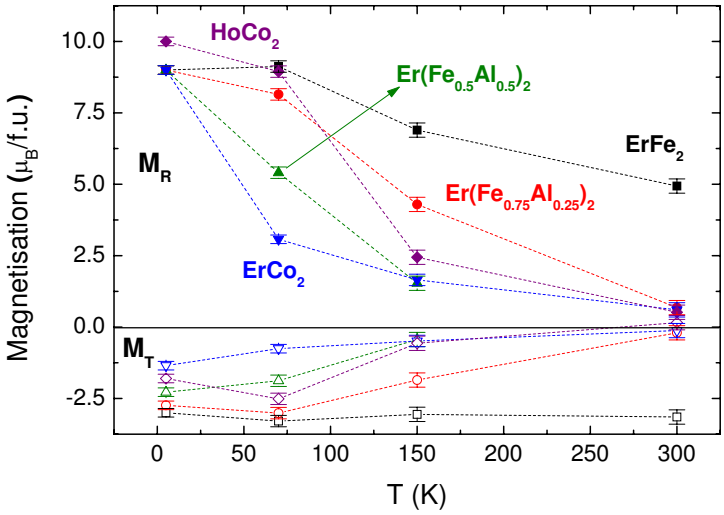

Figure 4.2: Temperature dependence of the magnetization of the rare-earth (solid symbols) and transition-metal (open symbols) sublattices, M_R and M_T, determined from the rare-earth L_2-edge XMCD spectra: $ErFe_2$ (black, $\square$), $Er(Fe_{0.75}Al_{0.25})_2$ (red, $\circ$), $Er(Fe_{0.5}Al_{0.5})_2$ (green, $\triangle$), $ErCo_2$ (blue, $\bigtriangledown$) and $HoCo_2$ (purple, $\diamond$). The dotted lines are a guide for the eye.

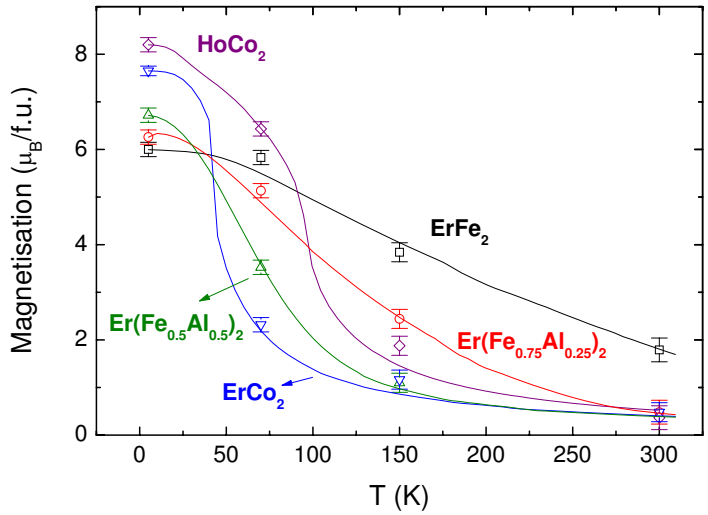

Figure 4.3: Comparison of the temperature dependence of the magnetization measured at H = 50 kOe by using a standard SQUID magnetometer (solid lines) and that derived from the rare-earth L_2-edge XMCD spectra (open symbols) in the case of: $ErFe_2$ (black, $\square$), $Er(Fe_{0.75}Al_{0.25})_2$ (red, $\circ$), $Er(Fe_{0.5}Al_{0.5})_2$ (green, $\triangle$), $ErCo_2$ (blue, $\bigtriangledown$) and $HoCo_2$ (purple, $\diamond$).

T(K)	M(μ_B/f.u.)	$ErFe_2$	$Er(Fe_{0.75}Al_{0.25})_2$	$Er(Fe_{0.5}Al_{0.5})_2$	$ErCo_2$	$HoCo_2$
5	M_R	9.00	9.00	9.00	9.00	10.00
	M_T	-3.00	-2.74	-2.28	-1.35	-1.80
	M_{Calc}	6.00	6.26	6.72	7.65	8.20
	M_{Exp}	6.00	6.26	6.72	7.65	8.20
70	M_R	9.12	8.15	5.41	3.07	8.94
	M_T	-3.29	-3.01	-1.88	-0.76	-2.51
	M_{Calc}	5.83	5.13	3.53	2.32	6.43
	M_{Exp}	5.50	4.88	3.56	2.18	6.45
150	M_R	6.90	4.30	1.53	1.65	2.44
	M_T	-3.06	-1.85	-0.44	-0.49	-0.57
	M_{Calc}	3.84	2.44	1.10	1.17	1.88
	M_{Exp}	4.03	2.46	0.97	0.86	1.47
300	M_R	4.94	0.68	–	0.60	0.52
	M_T	-3.15	-0.20	–	-0.12	-0.15
	M_{Calc}	1.79	0.48	–	0.48	0.37
	M_{Exp}	1.82	0.46	–	0.41	0.52

Table 4.1: Temperature dependence of the macroscopic magnetization in an applied field of H = 50 kOe, M_{Exp}, and that derived from the rare-earth L_2-edge XMCD spectra, M_{Calc}. The magnetization of the rare-earth, M_R, and the transition metal, M_T, sublattices have been derived respectively from the $XMCD_R$ and $XMCD_{Fe}$ contributions of the total R L_2-edge XMCD spectra.

However, a recent work calls for the existence of an intrinsic Co moment in the paramagnetic phase of $ErCo_2$ [113], that opens again the debate concerning the existence of an intrinsic Co magnetic moment in RCo_2 systems [112]. To date, no direct information regarding the behavior of both R and Co sublattices can be obtained separately at the same experimental conditions. Our method fills this lack of knowledge as the temperature dependence of the magnetization of both sublattices M_R(T) and M_T(T) can been determined from the same experimental spectrum. In the case of $ErCo_2$ (T_C = 32 K) and $HoCo_2$ (T_C = 78 K), as shown in Fig. 4.2, the magnetic ordering transition is visible in the disentangled M_R(T) and M_{Co}(T) curves of both $ErCo_2$ and $HoCo_2$ compounds. As shown in this Figure, the Co sublattice magnetization suddenly drops and near disappears above T_C, in agreement with the expected destabilization of the itinerant *d* subsystem as the molecular field created by the R moments becomes ineffective to induce the appearance of Co moment.

The results reported in Fig. 4.2 and Fig. 4.3 show the success into disentangling the magnetic contributions coming from different atomic species by using a single X-ray absorption edge. The addition of both individual sublattice magnetization values according to their antiferromagnetic coupling

reproduces fair well the temperature dependence of the macroscopic magnetization. As discussed above, the temperature dependence of the rare-earth magnetization has been derived from the modification of the intensity of the higher energy peak B ($\sim$7 eV above the edge). Trying to confirm the validity of our results, we have followed a different approach to determine $M_R(T)$. In this way, we have determined this dependence by using the XMCD spectra recorded at the K-edge of the transition metal as a function of the temperature. Systematic XMCD studies performed at the K-edge of the transition metal in both R-Fe [96, 99–102] and R-Co [98, 103, 104] intermetallic compounds have demonstrated that the dichroic signal measured at this absorption edge carries magnetic information not only of the T ions but also of the rare earth ions. The influence of the rare-earth is specially important in the case of the RFe_2 Laves phases compounds, in such a way that the amplitude of the rare-earth contribution hinders the signal coming from the transition metal [92]. This can be seen in Fig. 4.4 where the XMCD spectra recorded at the Fe and Co edges in the compounds under study [panels (a)-(e)] and in the case of YFe_2 and $Y(Co_{0.85}Al_{0.15})_2$ [panel (f)] are compared.

The Fe K-edge XMCD spectrum of YFe_2, see Fig. 4.4(f), closely resembles that of Fe metal [88]. It shows a narrow positive peak at the absorption threshold, and a wide negative dip, $\sim$12 eV, at higher energies. Despite the magnetic properties of the Fe sublattice in YFe_2, $ErFe_2$ and $HoFe_2$ compounds are thought to be similar, their Fe K-edge XMCD spectra present noticeable differences. As shown in Fig. 4.4, the Fe K-edge XMCD spectrum of $ErFe_2$ exhibits a narrow and intense peak close to the edge (peak A) but, in addition, a second peak of similar intensity, and broader, grows up at $\sim$15 eV above the edge (peak B). This peak was not present in the case of YFe_2 nor in Fe foil. Similar situation occurs when the Co K-edge is considered. The Co K-edge XMCD spectrum of $ErCo_2$, see Fig. 4.4(d), is similar to the Fe K-edge one of $ErFe_2$, presenting both A and B peaks. In contrast, the XMCD spectrum of $Y(Co_{0.85}Al_{0.15})_2$, see Fig. 4.4(f), similar to that of hcp cobalt, presents a single negative dip. These results indicate that the magnetism of the rare-earth not only influences, but dominates the spectral shape of the XMCD recorded at the transition metal K-edge. The same behavior is found for the whole set of compounds here studied. It is concluded from these results that the intensity of the main peaks (A and B) reflects the magnetization of the rare-earth sublattice. However, whereas both T and R contribute to the shape and intensity of peak A, only the latter is the main responsible for peak B. Consequently, the temperature dependence of its intensity would be a measurement of the temperature dependence of the rare-earth magnetization, $M_R(T)$.

We have derived $M_R(T)$ from the intensity of peak B, as indicated in

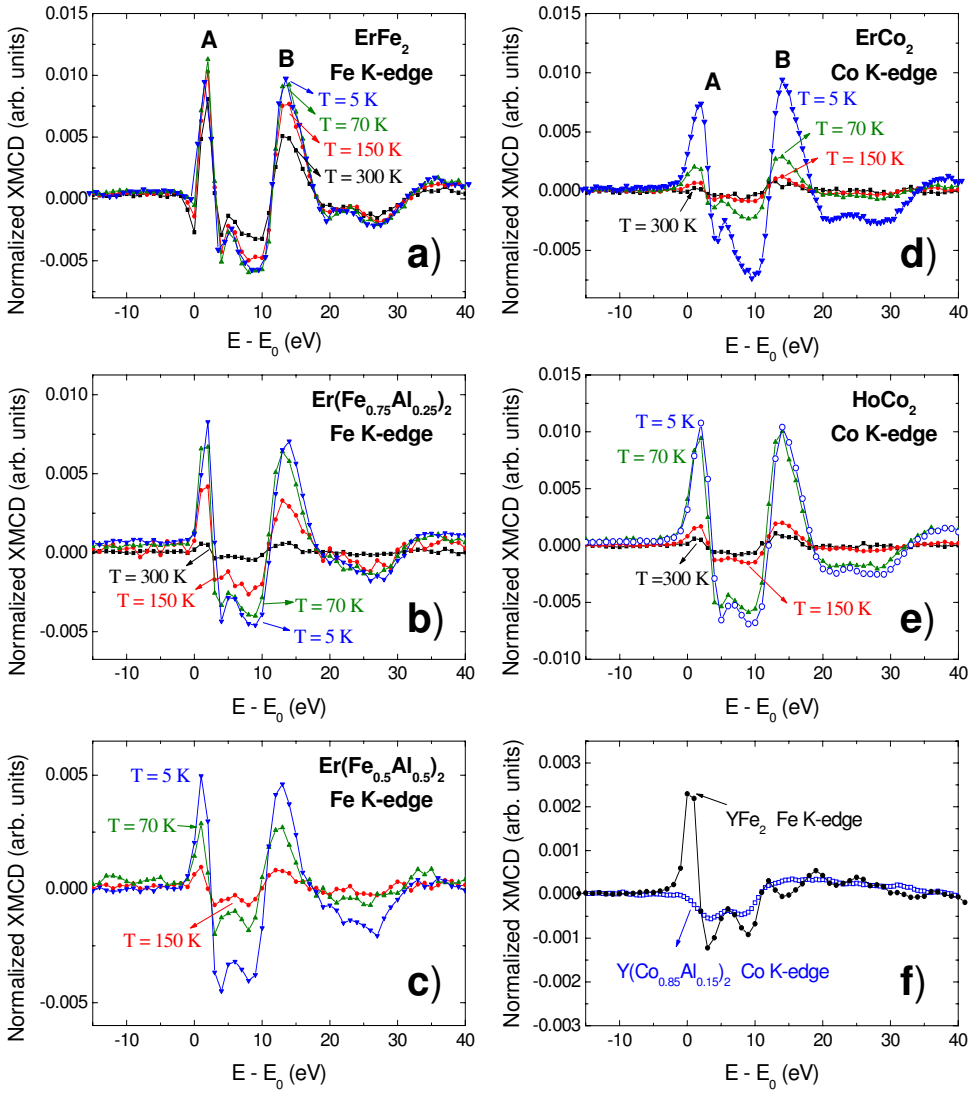

Figure 4.4: Temperature dependence of the normalized XMCD spectra recorded at H = 50 kOe at the Fe K-edge in the case of $ErFe_2$ (a), $Er(Fe_{0.75}Al_{0.25})_2$ (b) and $Er(Fe_{0.5}Al_{0.5})_2$ (c), and at the Co K-edge in $ErCo_2$ (d) and $HoCo_2$ (e): T = 5 K (blue, •), 70 K (green, ○), 150 K (red, ■) and 300 K (black, □). For the sake of completeness, the Fe and Co K-edge XMCD spectra recorded at the same applied field in YFe_2 and $Y(Co_{0.85}Al_{0.15})_2$, respectively, are shown in panel (f).

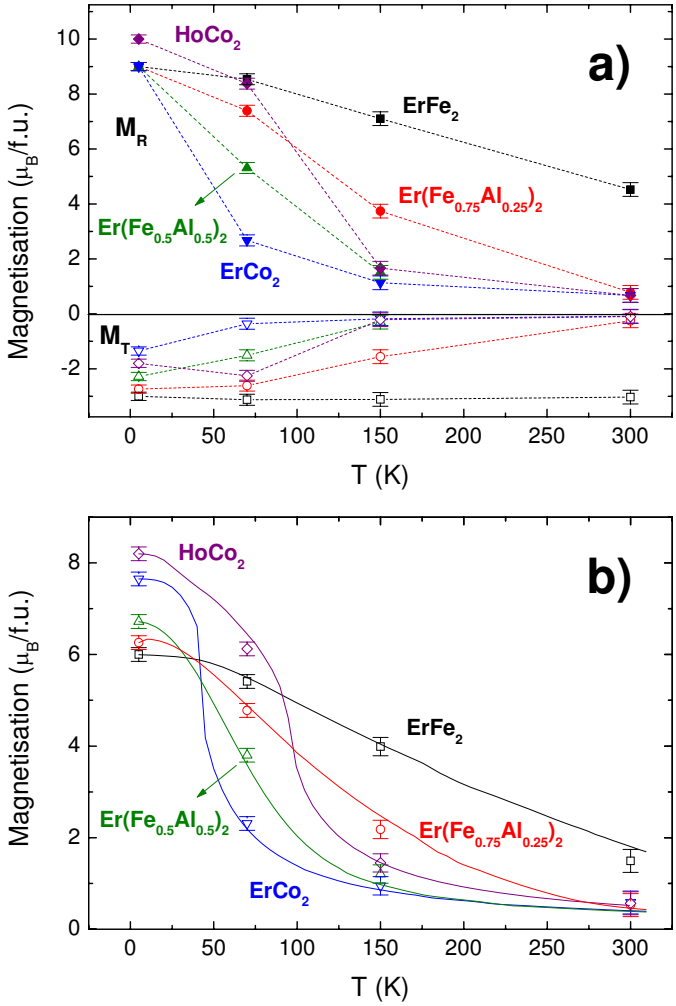

Figure 4.5: Panel (a): Temperature dependence of the magnetization of the rare-earth (solid symbols) and transition-metal (open symbols) sublattices, M_R and M_T, determined from XMCD spectra: $ErFe_2$ (black, $\square$), $Er(Fe_{0.75}Al_{0.25})_2$ (red, $\circ$), $Er(Fe_{0.5}Al_{0.5})_2$ (green, $\triangle$), $ErCo_2$ (blue, $\triangledown$) and $HoCo_2$ (purple, $\diamond$). The dotted lines are a guide for the eye. Panel (b): Comparison of the temperature dependence of the magnetization measured at 50 kOe by using a standard SQUID magnetometer (solid lines) and that derived by combining both the rare-earth L_2-edge and the transition-metal K-edge XMCD spectra (open symbols) in the case of: $ErFe_2$ (black, $\square$), $Er(Fe_{0.75}Al_{0.25})_2$ (red, $\circ$), $Er(Fe_{0.5}Al_{0.5})_2$ (green, $\triangle$), $ErCo_2$ (blue, $\triangledown$) and $HoCo_2$ (purple, $\diamond$).

T(K)	M(μ_B/f.u.)	$ErFe_2$	$Er(Fe_{0.75}Al_{0.25})_2$	$Er(Fe_{0.5}Al_{0.5})_2$	$ErCo_2$	$HoCo_2$
5	M_R	9.00	9.00	9.00	9.00	10.00
	M_T	-3.00	-2.74	-2.28	-1.35	-1.80
	M_{Calc}	6.00	6.26	6.72	7.65	8.20
	M_{Exp}	6.00	6.26	6.72	7.65	8.20
70	M_R	8.54	7.39	5.31	2.67	8.38
	M_T	-3.13	-2.61	-1.51	-0.36	-2.26
	M_{Calc}	5.41	4.78	3.80	2.31	6.12
	M_{Exp}	5.50	4.88	3.56	2.18	6.45
150	M_R	7.10	3.74	1.51	1.13	1.66
	M_T	-3.11	-1.56	-0.30	-0.18	-0.21
	M_{Calc}	3.99	2.18	1.21	0.95	1.45
	M_{Exp}	4.03	2.46	0.97	0.86	1.47
300	M_R	4.52	0.78	–	0.67	0.67
	M_T	-3.03	-0.25	–	-0.09	-0.10
	M_{Calc}	1.49	0.53	–	0.59	0.57
	M_{Exp}	1.82	0.46	–	0.41	0.52

Table 4.2: Temperature dependence of the magnetization in an applied field of 50 kOe, M_{Exp}, and that derived from the XMCD spectra, M_{Calc}. The magnetization of the rare-earth, M_R, and transition-metal, M_T, sublattices have been derived respectively from the K-edge and L_2-edge XMCD data.

Eq. (4.3), and by assuming also free-ion values at T = 5 K for the rare-earth magnetic moments. The M_R(T) dependence has been included as the factor *f(T)* in Eq. (4.4). Then, we have applied again the subtraction procedure to the L_2-edge by using this temperature dependence of the rare-earth contribution but now extracted from the transition metal K-edge XMCD. Finally, the temperature dependence of the transition metal magnetization has been obtained from the isolated $XMCD_T$(T), contribution according to Eqs. (4.3) and (4.5). The results of applying this procedure are shown in Fig. 4.5. The total magnetization obtained from the combination of both K-edge and L_2-edge XMCD spectra provides a good reproduction of the macroscopic magnetization data.

The agreement between the M_R(T) and M_T(T) values derived by using both L_2-edge (Table 4.1) and combined L_2 + K edges (Table 4.2) methods is better than 10% over the ferrimagnetic regime for all the studied compounds. Consequently, these results show the capability of this new approach to obtain the disentanglement of the magnetic contributions coming from different atomic species in R-T compounds by using XMCD measured at a single X-ray absorption edge.

4.2 Temperature dependence of the Ho and Fe magnetic sublattices from Ho $L_{2,3}$-edges XMCD spectra

We have shown in the previous section that the correct interpretation of the R L_2- and T K-edge XMCD signals opens the possibility of disentangling the magnetic contributions coming from different atomic species within the same material by using a single X-ray absorption edge. This study has been performed on RT_2 compounds in which the total magnetization of the system is dominated by the rare-earth. Now, the question posed is to verify whether the above results are common to all R-T intermetallic systems, independently of their stoichiometry and the dominant magnetic sublattice. To this end, we have analyze the temperature dependence of the XMCD signal recorded at the $L_{2,3}$-edges of Ho in Ho_6Fe_{23}. The suitability of this material to the present study resides in the fact that owing to the antiferromagnetic coupling of the Fe and Ho moments, and to the 6 : 23 stoichiometry, the overall magnetization of the system is determined either by the Fe sublattice or the Ho one depending on the temperature range studied.

The ferrimagnetic Ho_6Fe_{23} compound exhibits a magnetization compensation phenomenon stemmed from the different temperature dependence of both the iron, μ_{Fe}, and Ho, μ_{Ho}, magnetic moments. In a first approach, following a simple two sublattice model, the magnetization of the compound can be described as corresponding to the addition of the magnetization of each Fe and Ho magnetic sublattices. Fig. 4.6 shows the temperature dependence of the total magnetization of the Ho_6Fe_{23} compound measured at H = 4 kOe. The minimum of the total magnetization reflects the magnetic compensation of both sublattices, $T_{Comp} \sim 192$ K. Above T_{Comp} the Fe sublattice magnetization dominates the overall magnetization. Upon cooling, the rare-earth sublattice magnetization increases up to exceed the Fe one, becoming the dominant magnetic sublattice. The Ho magnetic moment can be extracted from the magnetization measurements by assuming that the temperature dependence of the Fe sublattice in Ho_6Fe_{23} corresponds to that of Y_6Fe_{23} [67]. In this way it has been determined that μ_{Ho} increases from 4.70 μ_B at room temperature to 9.26 μ_B at T = 5 K. While the relative modification of μ_{Ho} between ambient and low temperature is ∼97%, it is only ∼17% for μ_{Fe} (from 1.61 to 1.87 μ_B).

The XMCD spectra recorded at both Ho $L_{2,3}$-edges are reported in Fig. 4.7. A magnetic field of H = 6 kOe was applied at 45° away from the incident beam direction and the spectra were recorded at different fixed temperatures from room temperature down to T = 80 K. It should be noted that the XMCD

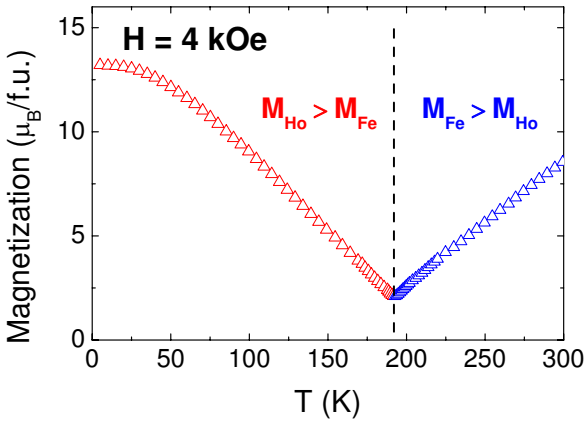

Figure 4.6: Temperature dependence of the macroscopic magnetization of Ho_6Fe_{23} compound measured at H = 4 kOe.

spectra show a sign reversal below the compensation temperature, reflecting the change of the magnetic sublattice governing the sign of the total magnetization above (Fe) and below (Ho) T_{Comp}. However, for the sake of clarity, all the spectra are displayed with the same sign as the low temperature ones, i.e., when Ho dominates the overall magnetization of the system.

In the case of the Ho L_3-edge, see Fig. 4.7(a), the XMCD spectra exhibit two main features of opposite sign located, respectively, at $\sim$ -5 eV (peak C) and $\sim$ 3 eV (peak D) above the edge. This spectral shape is not modified when the temperature varies and only the amplitude of the overall signal is concerned. In this way, the integration of Ho L_3-edge XMCD spectra yields a temperature dependence that fits well the variation of the Ho magnetic moment derived from magnetization data. This comparison is shown in Fig. 4.7(b), in which the variation of both XMCD integral and μ_{Ho} are plotted in relation to their room temperature values. The same criterion will be followed hereafter to evaluate the relative variation of the signals. By contrast to the Ho L_3-edge case, the spectral shape of the Ho L_2-edge XMCD is modified as a function of temperature as shown in Fig. 4.7(c). At room temperature, the main structures of the Ho L_2-edge XMCD spectrum are a positive peak $A1$ at $\sim$ 1 eV, a negative one A at $\sim$3 eV and a positive peak B at $\sim$8 eV. As temperature decreases, the amplitude of the peaks A and B increases as expected from the enhancement of the Ho magnetic moment. The intensity of peak $A1$ shows the contrary trend since this peak is progressively depleted upon cooling. As discussed in the previous section, this behavior stems from the influence of the Fe sublattice contribution to the Ho L_2-edge XMCD spectra. The integral of the total Ho L_2-edge XMCD signal shows a temperature dependence with a relative variation one order of magnitude greater than the

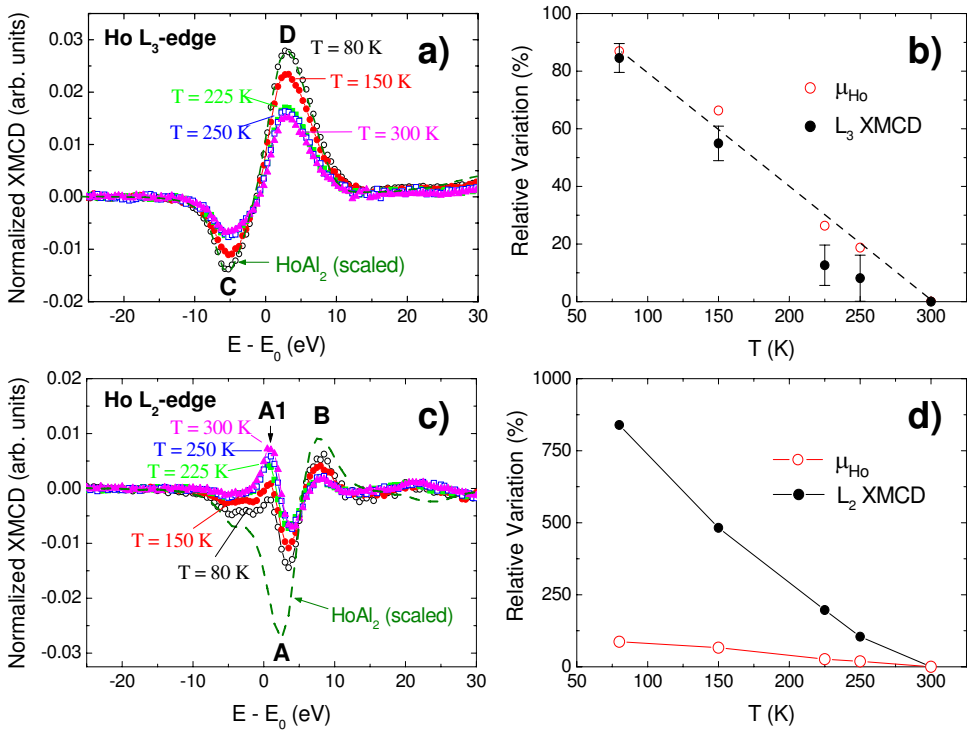

Figure 4.7: Panels (a) and (c): Temperature dependence of the XMCD spectra of Ho at the L_3- [panel (a)] and L_2-edge [panel (c)] in Ho_6Fe_{23}: T = 80 K (black, ○), T = 150 K (red, ●), T = 225 K (green, ■), T = 250 K (blue, □) and T = 300 K (purple, △). Panels (b) and (d): Comparison of the temperature dependence, relative to the room temperature values, of the Ho magnetic moment, derived from magnetization data (red, ○) and the integrated XMCD signals (black, ●) of the Ho L_2 [panel (b)] and L_3 [panel (d)] absorption edges. For sake of comparison the scaled XMCD spectra of $HoAl_2$ at both Ho $L_{2,3}$-edges (dark green, dash) is also shown (see text for details).

expected for μ_{Ho}. This effect is due to the Fe contribution that, in addition, is of the same order than the rare-earth one.

At this point, our main aim is to disentangle both Fe and Ho contributions from the Ho L_2-edge XMCD spectra as a function of temperature in order to determine both $\mu_{Fe}(T)$ and $\mu_{Ho}(T)$ from the same absorption spectra.

To this end we have considered the XMCD signals recorded at the Ho $L_{2,3}$-edges in $HoAl_2$ at T = 5 K and under the action of an applied magnetic field H = 50 kOe. Under these experimental conditions the Ho magnetic moment is close to its free-ion value. Consequently, one can assume that these signals would reflect, in a first approximation, the Ho contribution to the Ho_6Fe_{23} $L_{2,3}$-edges spectra in the absence of any Fe contribution. To verify this hypothesis, and to take into account that the Ho magnetic moment at

T = 80 K does not correspond to the free-ion value, we have scaled the Ho L_3-edge XMCD of $HoAl_2$ as to match that of Ho_6Fe_{23} at T = 80 K [see Fig. 4.7(a)]. The perfect match between both spectra after scaling confirms that the Ho $L_{2,3}$-edges XMCD of $HoAl_2$ reflect the Ho contribution of the Ho_6Fe_{23}. This scaling factor has been further applied to the Ho L_2-edge spectrum of $HoAl_2$ displayed in Fig. 4.7(c). By subtracting now the scaled $HoAl_2$ signal to the L_2-edge spectra of Ho_6Fe_{23}, the Ho contribution is canceled and the remaining signal would correspond to the Fe contribution.

The result of applying this procedure is shown in the panel (a) of Fig. 4.8. The difference signal is characterized by an intense positive peak at the edge whose intensity should be proportional to the Fe magnetization. Obviously, this procedure is only valid at T = 80 K. Indeed, despite the shape of the extracted signal does not vary with the temperature, the intensity of the extracted Fe contribution increases as temperature does, while μ_{Fe} is expected to decrease. The reason for this discrepancy is that as temperature increases, μ_{Ho} decreases faster than μ_{Fe}. Accordingly, the Ho contribution has to be subtracted from the Ho_6Fe_{23} by taking into account its temperature dependence. Then, we have assumed that the amplitude of the Ho L_3-edge XMCD signal is directly related to μ_{Ho} and, consequently, $\mu_{Ho}(T)$ is given by the temperature dependence of the XMCD amplitude at this absorption edge.

In this way, as in previous section, see Eq. (4.1), we have considered that the Ho L_2-edge XMCD signal can also be decomposed as the addition of two contributions, $XMCD_{Ho}$(T) and $XMCD_{Fe}$(T), where the Ho contribution is taken as:

$$XMCD_{Ho}(T) = f(T) \times XMCD_{HoAl2}(T = 80K) \tag{4.7}$$

and the proportionality factor in the present case is derived from the intensity ratio of the Ho L_3-edge XMCD spectra

$$f(T) = \frac{XMCD_{L_3}(T)}{XMCD_{L_3}(T = 80K)} \tag{4.8}$$

After applying this procedure, the intensity of the obtained signal, the Fe contribution, decreases as temperature increases as shown in Fig 4.8(b), in agreement to the expected variation of μ_{Fe}(T).

Final step in this research is to determine how reliable are the obtained μ_{Ho}(T) and μ_{Fe}(T) temperature dependence. At T = 80 K, the magnetic moments of Ho and Fe are, respectively, $\mu_{Ho} = 8.15\ \mu_B$ and $\mu_{Fe} = 1.77\ \mu_B$,

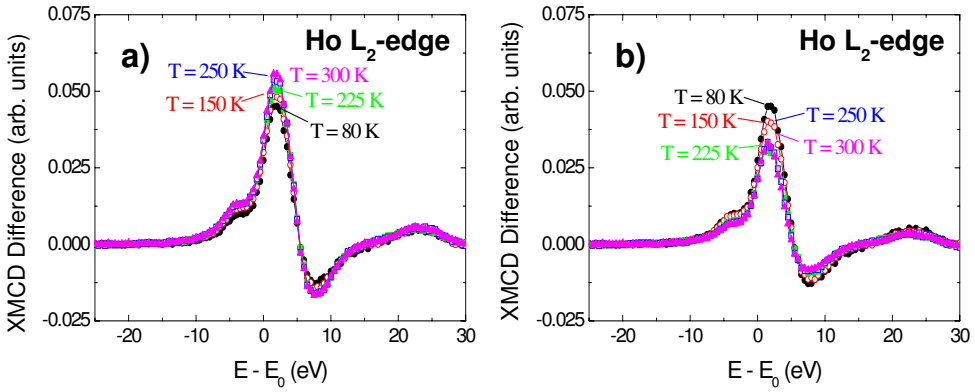

Figure 4.8: Panel (a): Comparison of the signal obtained after subtracting the scaled XMCD spectrum of $HoAl_2$ to the Ho L_2-XMCD Ho_6Fe_{23} XMCD signals: T = 80 K (black, •), T = 150 K (red, ○), T = 225 K (green, ■), T = 250 K (blue, □) and T = 300 K (purple, △). Panel (b): Same comparison as (a) after weighting the $HoAl_2$ signal with the temperature dependence observed at the Ho L_3-edge (see text for details).

as derived from magnetization data [96]. By considering these values and the temperature dependence of the Ho L_3-edge XMCD spectra we obtain the quantitative determination for μ_{Ho}(T):

$$\mu_{Ho}(T) = f(T) \times \mu_{Ho}(T = 80K). \tag{4.9}$$

On the other hand, it is assumed that the temperature dependence of μ_{Fe} is the same than that of the peak $A1$ of the Ho L_2-edge XMCD difference spectra, as displayed in Fig. 4.8(b):

$$\mu_{Fe}(T) = \frac{XMCD_{A1}(T)}{XMCD_{A1}(T = 80K)} \times \mu_{Fe}(T = 80K). \tag{4.10}$$

The results after applying Eqs. 4.9 and 4.10 are shown in panel (a) of Fig. 4.9. The Ho magnetic moment decreases faster than the Fe one as the temperature increases. Fig. 4.9(b) shows the comparison of the Ho_6Fe_{23} magnetization measured by conventional magnetometry methods and the one built from the μ_{Ho}(T) and μ_{Fe}(T) determined from the XMCD data. The good agreement between both magnetization values confirms the success into disentangling the magnetic contribution of both Fe and Ho sublattices by using only the Ho X-ray absorption $L_{2,3}$-edges.

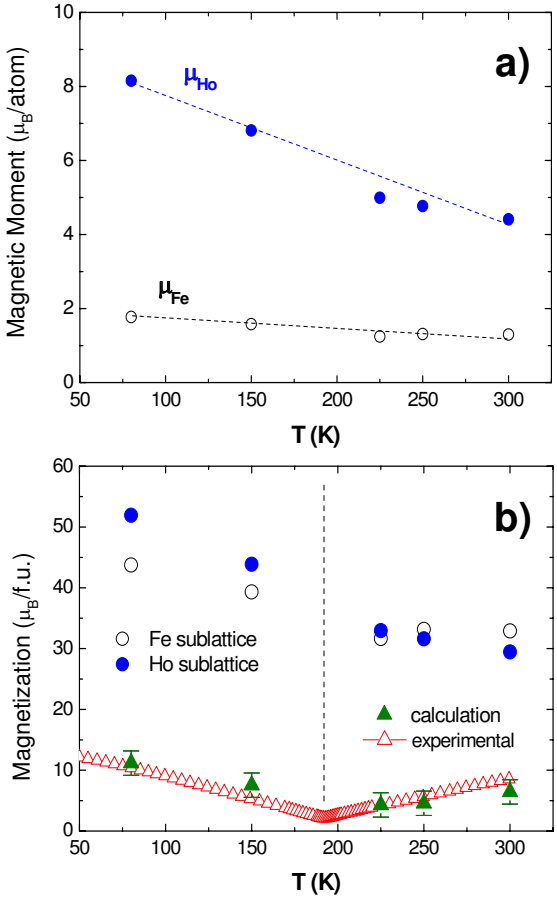

Figure 4.9: Panel (a): Comparison of the temperature dependence of the magnetic moment of Ho (blue, •) and Fe (black, ○) extracted, respectively, from the L_3 and L_2 XMCD spectra of Ho_6Fe_{23}. Panel (b): Comparison of the temperature dependence of magnetization of Ho_6Fe_{23} measured at SQUID (red, △) and obtained (green, ▲) by using the magnetization of the Ho and Fe sublattices derived from the Ho $L_{2,3}$-edges XMCD spectra.

4.3 Additivity of magnetic contributions to the XMCD spectrum

In the previous sections it has been shown that, in R-Fe intermetallic compounds, it is possible to explore the magnetic behavior of the different elements by using a single element absorption edge. This possibility stems from the contribution coming from the different magnetic species to the XMCD at the conduction band. In several cases, the rare-earth contribution dominates the K-edge XMCD of the transition metal [99–101]. This result has been interpreted in terms of the rare-earth determining not only the shape

of the XMCD spectra [92], but also the magnetism of the transition-metal $4p$ electrons [114]. Accordingly, the polarization of the transition-metal sp band, should not follow that of the $3d$ band, but it should be determined by the rare-earth magnetization [114].

So far, we have considered that both contributions at the conduction band behave in an additive way; however a direct experimental evidence is still missing. To this aim, we have performed the study of the XMCD recorded at the Fe K-edge through the $Ho_{1-x}Lu_xFe_2$ series. The dilution of the Ho sublattice is expected to reduce the Ho contribution to the Fe K-edge XMCD spectra and, consequently, this might allow us to unravel both contributions.

The Fe K-edge XMCD spectra recorded through the $Ho_{1-x}Lu_xFe_2$ series at T = 5 K and H = 50 kOe are shown in panel (a) of Fig. 4.10. The observed sign reversal between the XMCD signal of $Ho_{0.25}Lu_{0.75}Fe_2$ and of those compounds with higher Ho content reflects the change of the dominant magnetic sublattice. As it has been shown in the description of the magnetic properties of these $Ho_{1-x}Lu_xFe_2$ compounds, see Chapter 3, at low temperature the Ho sublattice dominates the total magnetization for concentrations less than the critical value, $x_c \sim 0.7$, whereas for higher concentrations the dominant sublattice is the Fe one.

When all the XMCD spectra are referred to the Fe sublattice magnetization direction, the overall shape of the XMCD signal of the Ho compounds is markedly different from that of $LuFe_2$ [see Fig. 4.10(b)]. The Fe K-edge XMCD spectrum of $LuFe_2$ is similar to that of Fe metal, showing a main narrow positive peak at the absorption threshold and a negative dip at higher energies. As Ho substitutes Lu in the $Ho_{1-x}Lu_xFe_2$ series, the Fe K-edge XMCD spectral shape is strongly modified, and new spectral features in the high energy region can be observed. The amplitude of the spectra enhances as the Ho content increases, with the exception of the first positive peak at the threshold, which shows the opposite trend. This behavior has been observed in other R-Fe intermetallic compounds and accounted for in terms of an additional contribution arising from the magnetic rare-earth sublattice [92, 99, 101]. The question posed now is to determine if both Fe and Ho magnetic sublattices contribute in an additive way to the XMCD [96, 101] or, on the contrary, the Ho $4f$ magnetic moments are which determine the magnetic properties of the Fe(sp)-band. In the former case there should be always a separable contribution from each magnetic element. By contrast, in the latter, the Fe($3d$) magnetic moments should not play any significant role in the magnetic polarization of the Fe(sp)-band and, consequently, in the Fe K-edge XMCD [114].

Starting from the additivity model, discussed in the precedent sections, the Fe K-edge XMCD spectrum of $HoFe_2$ is composed of an Fe component,

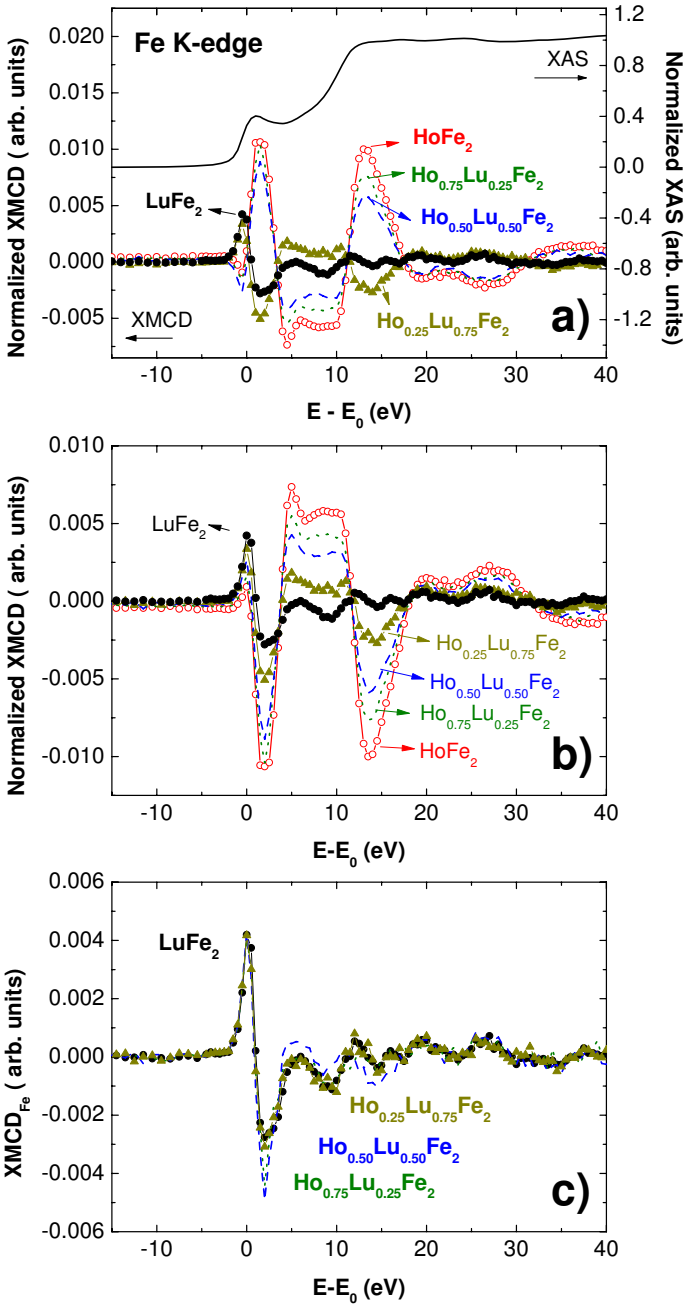

Figure 4.10: Panel (a): Normalized Fe K-edge XMCD spectra recorded at T = 5 K and H = 50 kOe through the $Ho_{1-x}Lu_xFe_2$ series. Panel (b): Same as a) but with the sign of the XMCD signals referred to the direction of the Fe sublattice magnetization. Panel (c): Comparison of the Fe K-edge XMCD of $LuFe_2$ with the $XMCD_{Fe}$ contribution (see text for details). In all the panels: x = 0 (red, ○), 0.25 (green, dots), 0.5 (blue, dash), 0.75 (dark yellow, △) and 1 (black, •).

$XMCD_{Fe}$ and a contribution coming from Ho, $XMCD_{Ho}$. According to magnetization measurements, the magnetic properties of the Fe sublattice remain nearly unvaried through the RFe_2 series [1, 115]. Then, we can assume that the contribution of the Fe sublattice to the Fe K-edge XMCD spectra is the same for both $LuFe_2$ and $HoFe_2$ compounds. Therefore, by subtracting both spectra the contribution of the Ho sublattice to the XMCD spectrum of $HoFe_2$ is obtained ($XMCD_{Ho}$ = $XMCD_{HoFe_2}$ - $XMCD_{LuFe_2}$). In a second step we consider that this $XMCD_{Ho}$ contribution has an atomic-like character, i.e., it reflects the polarization of the $5d$ states due to the localized $4f$ states of the rare-earth which stands from an intra-atomic interaction. At the present experimental conditions, T = 5 K and H = 50 kOe, it is expected that the Ho magnetic moment, μ_{4f}(Ho), does not vary through the $Ho_{1-x}Lu_xFe_2$ series. Hence, the Ho contribution to the total XMCD signal should be proportional to the extracted signal from $HoFe_2$ weighted by the Ho concentration, [(1-x) × $XMCD_{Ho}$]. By subtracting this scaled Ho contribution from the experimental XMCD spectra we obtain a residual signal that should correspond to $XMCD_{Fe}$. If our assumptions are valid, the obtained signal will show the same spectral shape and similar intensity as the experimental spectrum of $LuFe_2$, in which only the Fe dichroic contribution is present as there is no localized $4f$ moment. The comparison reported in the panel (c) of Fig. 4.10 evidences a perfect agreement between both the $XMCD_{Fe}$ contribution and the experimental $LuFe_2$ XMCD spectrum, giving validity to our hypothesis.

Next step is to verify if the successful application of the additivity model is limited to the present experimental conditions, T = 5 K and H = 50 kOe, in which all the magnetic moments are close to their saturation values, or

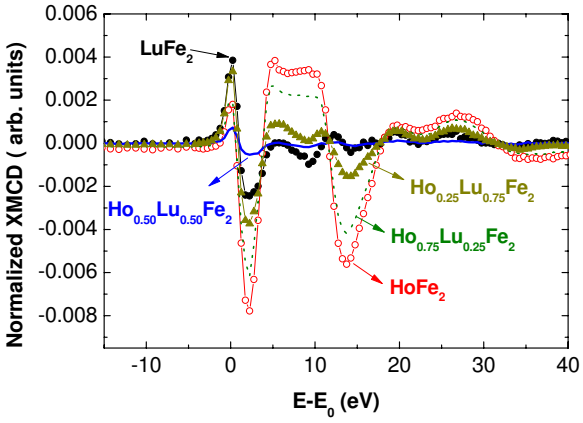

Figure 4.11: Normalized Fe K-edge XMCD spectra recorded at T = 300 K and H = 20 kOe through the $Ho_{1-x}Lu_xFe_2$ series: x = 0 (red, ○), 0.25 (green, dots), 0.5 (blue line), 0.75 (dark yellow, △) and 1 (black, ●).

if it can be extended through all the accessible range of temperature and applied magnetic field. Consequently, we have recorded the XMCD signals at T = 300 K under an applied magnetic field of H = 20 kOe. These experimental conditions coincide with the magnetic compensation point of the $Ho_{0.5}Lu_{0.5}Fe_2$ compound. The results of the XMCD measurements are shown in Fig. 4.11 (for the sake of simplicity, the spectra have been plotted referred to the direction of the Fe sublattice magnetization). This comparison shows that the shape of the Ho compounds XMCD signals, except x = 0.5, is almost the same as at low temperature, and only their amplitude has been modified due to the reduction of the R magnetic moment upon increasing the temperature.[1] This result gives further support to the atomic-like nature of the Ho contribution to the XMCD of Fe. In $Ho_{0.5}Lu_{0.5}Fe_2$ the compensation condition has been reached, T_{Comp} ∼300 K, and the Fe K-edge XMCD spectrum has lost all the hallmarks of this Ho contribution. Indeed, as shown in panel (a) of Fig. 4.12, the XMCD spectrum perfectly matches with that of $LuFe_2$, i.e., with the compound in which no $4f$ localized moments are present. The spectra of the $Ho_{0.5}Lu_{0.5}Fe_2$ compound have been scaled with the $LuFe_2$ one at the main peak of the XMCD signal (E-E_0 ∼ 0 eV). The scaling factor needed coincides with the ratio of the magnetization value of both $LuFe_2$ and $Ho_{0.5}Lu_{0.5}Fe_2$ at the same experimental conditions.

According to our hypothesis, this result might be addressed to the absence of a net Ho magnetization in the direction of the magnetic applied field at the compensation temperature. At temperatures relatively far from the compensation, the magnetic coupling between both sublattices is recovered. As shown in Fig. 4.13, the XMCD signal at the Fe K-edge at T = 5 K and 125 K shows the polarization of the Fe($4p$)-states due to the Ho atoms.

These results show that the rare-earth contribution to the K-edge XMCD of the transition-metal reflects the net magnetization of the rare-earth and can be considered of atomic-like nature, i.e., the rare-earth $5d$ states become spin-polarized by the intra-atomic interaction with the $4f$ localized moments and the spin-polarization of the $5d$ states is probed in the photoabsorption process due to the R-T hybridization. The fact that it arises from the localized $4f$ states explain why for a fixed rare-earth in a R-T series the shape of the observed contribution to the K-edge XMCD of the transition-metal is similar independently of the specific transition-metal [1, 92]. Moreover, even when in several cases the rare-earth contribution dominates the observed XMCD, this work proves that the Fe intra-atomic $3d$ polarization always influences the Fe(sp)-band.

[1] The relative amplitudes of the dichroic contributions have also been modified due to the different temperature dependence of both magnetic sublattices.

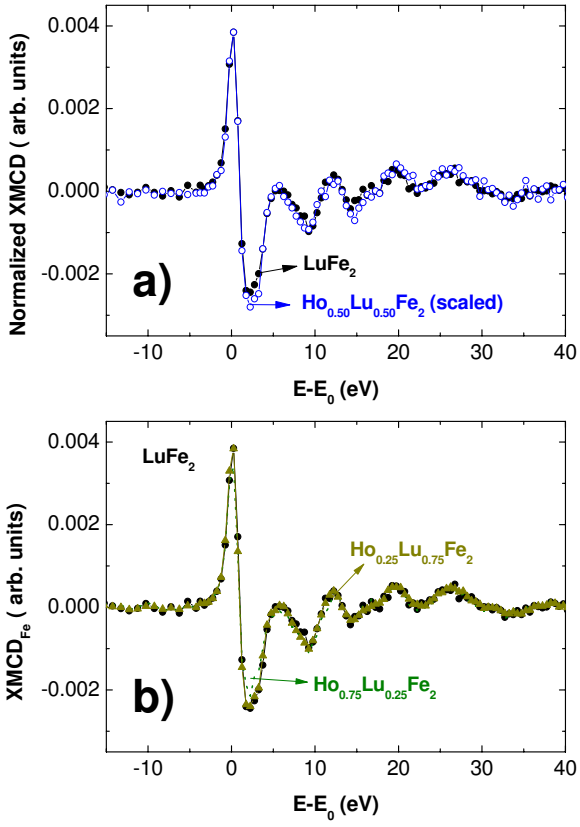

Figure 4.12: Panel (a): Detailed comparison of the XMCD signal recorded for $LuFe_2$ (black, •) and $Ho_{0.5}Lu_{0.5}Fe_2$ (blue, ○). Panel (b) Comparison of $LuFe_2$ XMCD (black, •) and the extracted $XMCD_{Fe}$ signals of x = 0.25 (green, dots) and 0.75 (dark yellow, △).

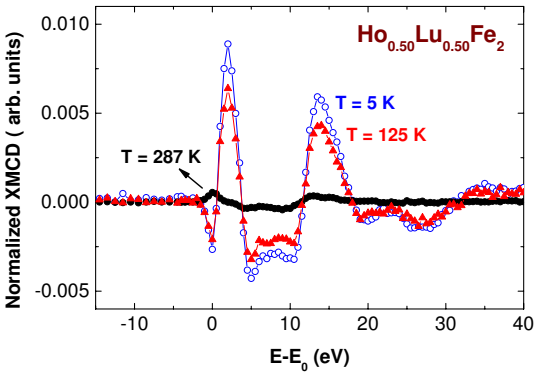

Figure 4.13: Comparison of the Fe K-edge XMCD spectra of $Ho_{0.5}Lu_{0.5}Fe_2$ recorded at H = 50 kOe and at different temperatures: T = 287 K (black, •), 125 K (red, ▲) and 5 K (blue, ○).

4.4 Study of the R-Fe interaction at the magnetic compensation point

As shown in Chapter 3, the magnetic compensation in R-Fe intermetallic compounds (R = heavy rare-earth) originates from the cancelation of the net magnetization, resulting from the antiparallel coupling of both R and Fe magnetic moments, and their different evolution with the temperature. Despite that this simple scheme accounts for the observed macroscopic properties [67, 68], little is known regarding the behavior of the individual magnetic sublattices and their coupling through the compensation point.

In previous sections we have shown that the combined study of the Fe K- and R L_2-edges XMCD spectra provides the disentanglement of the magnetic behavior of both magnetic sublattices at the microscopic level [116, 117]. In this section we will apply this disentangling procedure in order to obtain a new insight into the behavior of the individual magnetic moments as well as the spin polarization of the hybridized R($5d$) states through the magnetic compensation transition.

To this end we have performed a detailed study of the magnetic compensation phenomena from a microscopic point of view. We have carried out a systematic XMCD study of the magnetic compensation phenomena in two $R_{1-x}R'_xFe_2$ intermetallic compounds which exhibit a magnetic compensation point: $Ho_{0.5}Lu_{0.5}Fe_2$ and $Er_{0.5}Y_{0.5}Fe_2$.

4.4.1 Thermal evolution of the Fe K- and R L_2-edges XMCD signals through a magnetic compensation point

The temperature dependence of the magnetization of both $Er_{0.5}Y_{0.5}Fe_2$ and $Ho_{0.5}Lu_{0.5}Fe_2$ compounds under a magnetic field of H = 50 kOe is shown in Fig. 4.14. By contrast to the flat curve of YFe_2 and $LuFe_2$, the magnetization passes through a minimum at T_{Comp} = 230 and 300 K for the Er and Ho compounds, respectively. This temperature dependence reflects the existence of a magnetic compensation point at T_{Comp}; the Fe sublattice dominates the overall magnetization of the system at temperatures above T_{Comp} but, upon cooling, the magnetization of the rare-earth sublattice increases and surpass the Fe one below T_{Comp}.[2]

Fig. 4.15 shows the Fe K-edge XMCD signals recorded on each compound at temperatures below and above T_{Comp}. Both signals are similar and resemble

[2]It is worth to remember, see Chapter 3, that the compensation temperature for the studied compounds does not change for magnetic fields equal or higher than H = 20 kOe.

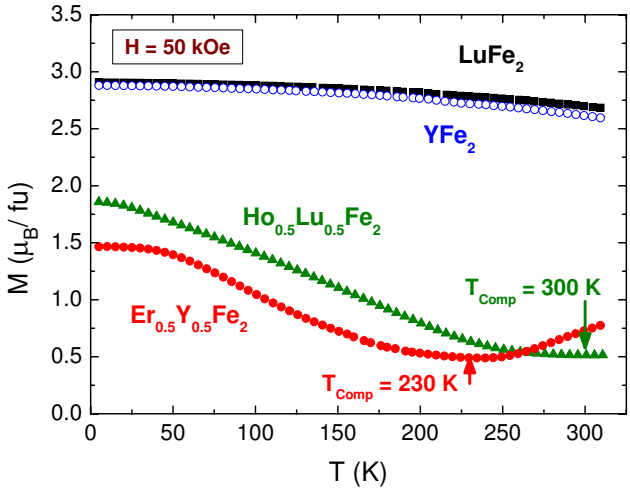

Figure 4.14: Temperature dependence of the zero-filed cooled (ZFC) magnetization of the $Er_{1-x}Y_xFe_2$ and $Ho_{1-x}Lu_xFe_2$ series measured under an applied magnetic field of H = 50 kOe.

the characteristic Fe K-edge XMCD of R-Fe intermetallics in which R is a magnetic rare-earth [99–101]. Since the Fe K-edge XMCD spectra reported in Fig. 4.15 are referred to the direction of the total magnetization of the system, the change of sign of the signal for temperatures above and below T_{Comp} directly reflects the change of the dominant magnetic sublattice.

The Fe K-edge XMCD spectrum of these compounds is originated from the addition of two contributions associated to both the Fe and rare-earth sublattices [92, 96, 118]. As it has been shown in precedent sections, this characteristic absorption profile is lost at the compensation point, and the XMCD spectra are similar to those of YFe_2 and $LuFe_2$ (compounds in which no $4f$ magnetic moments are present). In fact, the dichroic signals at T_{Comp} perfectly match to those of YFe_2 and $LuFe_2$ [see Fig. 4.15(c)]. This result can be interpreted by assuming that, at T_{Comp}, the rare-earth sublattice is fully magnetically disordered, whereas there is still some magnetic order in the Fe sublattice. Indeed, if the rare-earth sublattice was locally ordered the magnetic moments of the rare-earths would create a molecular field at the Fe sites and, consequently, the rare-earth contribution to the Fe K-edge XMCD should be present, contrary to the experimental results.

Aimed to go deeper into these results we have studied the behavior of the XMCD spectra recorded at the rare-earth L_2-edge through the compensation point. As shown in previous sections, the XMCD at the rare-earth L_2-edge is made by the addition of two components [91, 94], one due to the rare-earth

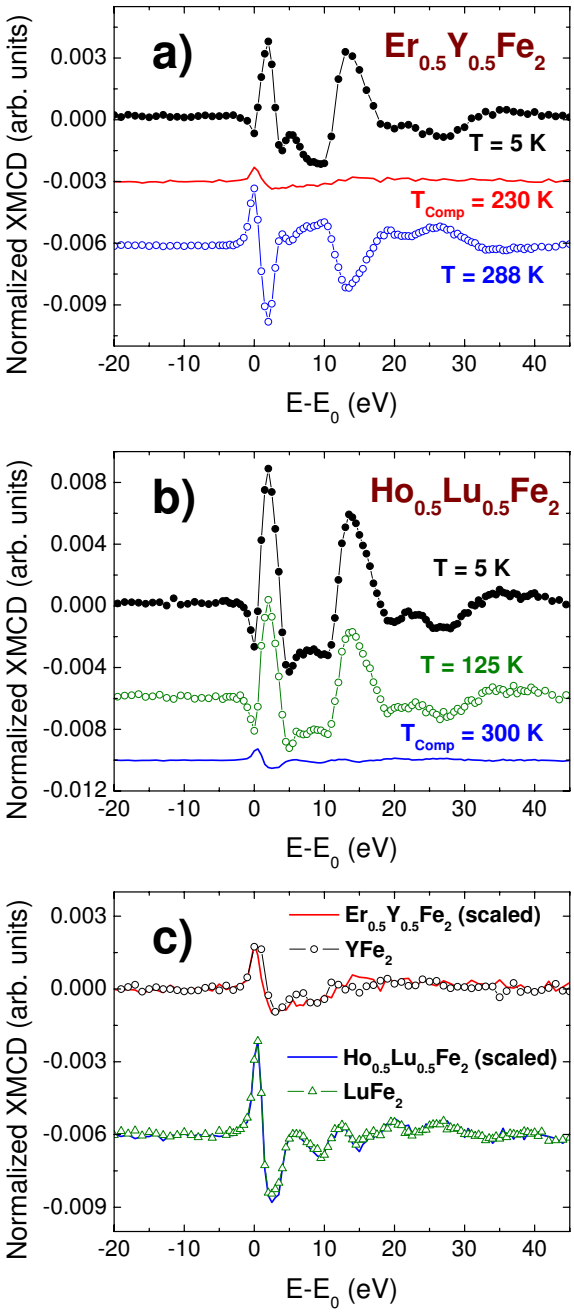

Figure 4.15: Temperature dependence of XMCD signal at the Fe K-edge for $Er_{0.5}Y_{0.5}Fe_2$ [panel (a)] and $Ho_{0.5}Lu_{0.5}Fe_2$ [panel (b)]. Panel (c): Detailed comparison of the XMCD signals at the compensation temperatures (from panels (a) and (b), and the dichroic signal at room temperature of YFe_2 and $LuFe_2$. For a better comparison, the signals at T_{Comp} have been scaled to the YFe_2 and $LuFe_2$ ones.

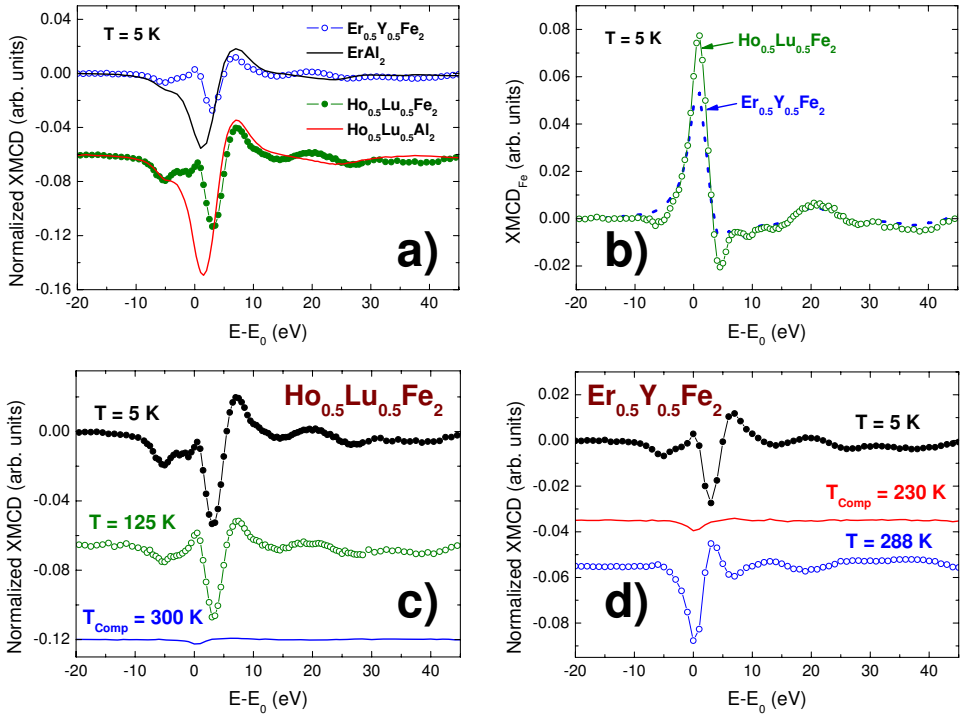

Figure 4.16: Panel (a): Normalized XMCD spectra recorded at T = 5 K at the Ho and Er L_2-edge for $Ho_{0.5}Lu_{0.5}Fe_2$ and $Er_{0.5}Y_{0.5}Fe_2$, respectively, and comparison with $Ho_{0.5}Lu_{0.5}Al_2$ and $ErAl_2$. Panel (b): extracted $XMCD_{Fe}$ component (see text for details). Panels (c) and (d): temperature dependence of the XMCD signal at the Ho and Er L_2-edge for $Ho_{0.5}Lu_{0.5}Fe_2$ and $Er_{0.5}Y_{0.5}Fe_2$, respectively.

sublattice, mainly reflecting the $4f$-$5d$ intra-atomic polarization, and a second one in which the magnetic state of Fe is reflected through the hybridization of the Fe($3d$,$4p$) and R($5d$) states [87, 97]. The Fe contribution yields a characteristic positive peak in the dichroic signal at the threshold energy, E_0. As shown in the comparison of the Er L_2-edge XMCD spectra of $Er_{0.5}Y_{0.5}Fe_2$ and $ErAl_2$, and that of the Ho L_2-edge XMCD of $Ho_{0.5}Lu_{0.5}Fe_2$ and $Ho_{0.5}Lu_{0.5}Al_2$ reported in Fig. 4.16(a), it is clear that this peak is not present in absence of Fe. Indeed, by subtracting the $Ho_{0.5}Lu_{0.5}Al_2$ and $ErAl_2$ XMCD spectra from the $Ho_{0.5}Lu_{0.5}Fe_2$ and $Er_{0.5}Y_{0.5}Fe_2$ ones, respectively, we find in both cases a similar difference signal that corresponds to the Fe contribution, $XMCD_{Fe}$ [see Fig. 4.16(b)]. The sign of this Fe contribution is opposite to that of the rare-earth itself, and its relative weight decreases as temperature diminishes because the Fe magnetization remains nearly constant while the rare-earth one significantly increases ($\sim$100 % [116]) as the temperature decreases from room temperature down to 5 K.

Panels (c) and (d) of Fig. 4.16 shows the Er and Ho L_2-edge XMCD spec-

tra of $Er_{0.5}Y_{0.5}Fe_2$ and $Ho_{0.5}Lu_{0.5}Fe_2$ respectively. At temperatures far from T_{Comp} the XMCD spectra of both compounds are as described above. The dichroic signal is composed by two components $XMCD_R$ and $XMCD_{Fe}$ and they evolve with the temperature as detailed in the first section of this Chapter. However, the XMCD signals exhibit a dramatic change at T_{Comp}. In both cases the XMCD spectra only show a negative peak at the absorption threshold, i.e., at the energy region in which the Fe sublattice contributes to the rare-earth L_2-edge. As shown in Fig. 4.17, this signal matches with the $XMCD_{Fe}$ extracted from the data at T = 5 K. This result indicates that, at T_{Comp}, only Fe is contributing to the XMCD recorded at the rare-earth L_2-edge. Additionally, its negative sign indicates that the Fe sublattice governs the direction of the total magnetization of the system.

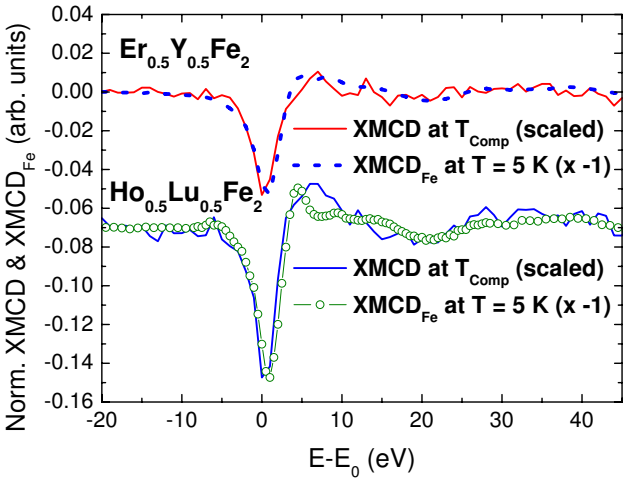

Figure 4.17: Detailed comparison of the XMCD signals of $Er_{0.5}Y_{0.5}Fe_2$ and $Ho_{0.5}Lu_{0.5}Fe_2$ at the compensation temperatures with the $XMCD_{Fe}$ ones extracted from data at T = 5 K. For a better comparison signals at the compensation temperature have been scaled and multiplied by -1.

A final confirmation is given by the comparison of the XMCD signal of $Ho_{0.5}Lu_{0.5}Fe_2$ at Ho L_2-edge at T_{Comp} with that of $LuFe_2$ at Lu L_2-edge at T = 5 K. In the latter case the polarization of the Lu $5d$ states is undoubtedly due to the action of the Fe magnetic moments. The excellent agreement between both signals, see Fig. 4.18, corroborates that at the compensation point the Ho $5d$ states are only polarized by the Fe sublattice. These results are in agreement with those obtained at the Fe K-edge XMCD study: at the compensation point the Fe sublattice is locally ordered and the Fe conduction states are polarized. As these states are hybridized with the $5d$ states of the rare-earth, there is also a polarization of the conduction states projected at the rare-earth sites due to the local order of the Fe sublattice.

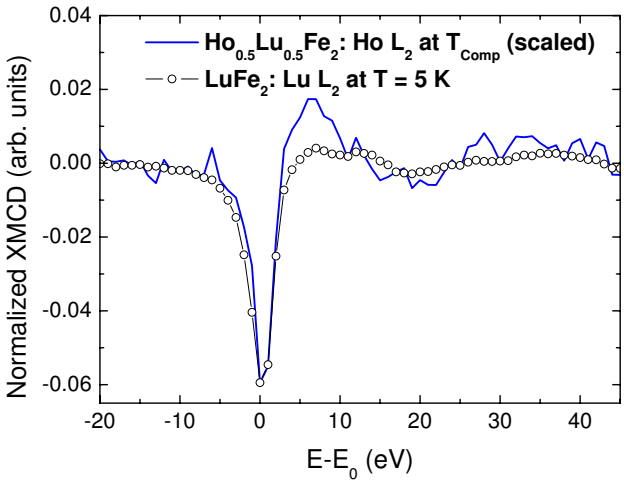

Figure 4.18: Comparison of the Ho L_2-edge XMCD in $Ho_{0.5}Lu_{0.5}Fe_2$ (T = T_{Comp}) and Lu L_2-edge XMCD in $LuFe_2$ (T = 5 K). For a better comparison the signal at the Ho L_2-edge has been scaled to the Lu L_2-edge one.

These results suggest that at the compensation point the R and the Fe magnetic sublattices behaves in a different way. The XMCD data demonstrate that the R sublattice is completely magnetically disordered, while some magnetic order is still present in the Fe sublattice. This different behavior might be ascribed to the hierarchy of the magnetic interactions in R-Fe intermetallics: Fe-Fe $\gg$ R-Fe $\gg$ R-R. At the compensation point both R and Fe sublattices would be magnetically disordered since there is no preferred magnetic direction. However, the local Fe-Fe exchange interaction is strong enough to maintain a certain local order among the Fe magnetic moments, while the R-Fe interaction is not strong enough and the R magnetic moments remain magnetically disordered.

4.4.2 Transient regimen: recovering the ferrimagnetic ordering

In order to verify the previous hypothesis, we have explored the transient regime between the anomalous magnetically disordered state at the compensation point and the ferrimagnetic state. To this end we have slightly decreased the temperature of the $Ho_{0.5}Lu_{0.5}Fe_2$ compound from T_{Comp} = 300 K down to T = 288 K. As shown in Fig. 4.19(a), new spectral features appear in the spectra recorded at T = 288 K. These peaks B, C and D are due to the Ho contribution to the Fe K-edge XMCD spectra. The intensity of these features is enhanced by increasing the magnetic field from H = 20 to 100 kOe, up to

resemble the XMCD signal recorded at low temperature.[3] Peaks B, C and D have the same sign in both cases, indicating that at T = 288 K, the Ho moments are orientated parallel to the magnetic field, becoming the dominant magnetic sublattice. On the other hand, the peak at the threshold (peak A), surprisingly, has the same sign in both the T = T_{Comp} and T = 288 K spectra. This peak should reverse its sign if both sublattices were antiferromagnetically coupled. Hence, this result suggests that the Fe magnetic moments remain parallel to the net magnetization of the system and the magnetic sublattices are still decoupled at T = 288 K. Similar results are found at the Ho L_2-edge XMCD. As shown in Fig. 4.19(b), the slightly reduction of the temperature changes the shape of the XMCD spectrum as to resemble the one measured at low temperature. However, the characteristic peak associated to Fe (A' peak in Fig. 4.19) is not positive, as occurring at temperatures far below T_{Comp}, but negative, indicating that both the Fe and Ho moments are parallel to the net magnetization of the system.

Another interesting result can be inferred from a closer inspection of the data displayed in Fig. 4.19(a). We have shown in previous sections that the tail of peak B overlaps with the peak A, giving rise to a depletion of the peak A due to their opposite sign. This is exemplified in Fig. 4.20(a), the peak A is notably less intense in $HoFe_2$ than in $LuFe_2$. Regarding the evolution with the magnetic field and temperature of peak A, we found that this peak is more intense at the compensation condition than at T = 288 K for all the magnetic fields. However, at T = 288 K the intensity of peak A should be enhanced by the growing of peak B with the magnetic field because both peaks have the same sign. Therefore, it would be expected a more intense peak A out of the compensation condition because of: i) we have shown that at T_{Comp} the system is more disordered than at any other temperature below T_C, and ii) we have demonstrated that there is a parallel alignment of both magnetic sublattices at T = 288 K. Both factors will contribute to an enhancement of the peak A at T = 288 K respect to its intensity at T_{Comp}. Therefore, in the case of $Ho_{0.5}Lu_{0.5}Fe_2$ compound at T = 288 K, we can consider that two different Fe contributions to the XMCD, parallel and antiparallel to the net magnetization of the system, are evidenced as the Ho sublattice become more ordered by increasing the magnetic field.

As detailed in previous sections, it is possible to recover the XMCD signal at T = 288 K by linear combination of both $XMCD_{Ho}$ and $XMCD_{Fe}$ components due to their additive character. Therefore, by fitting a linear combination of both contributions to the experimental XMCD spectra we should be able to demonstrate the presence of this antiparallel Fe contribution. To this end, we

[3] In the case of peak B this tendency is not so clear because the emerging peak overlaps with the negative dip of the Fe contribution close to the threshold.

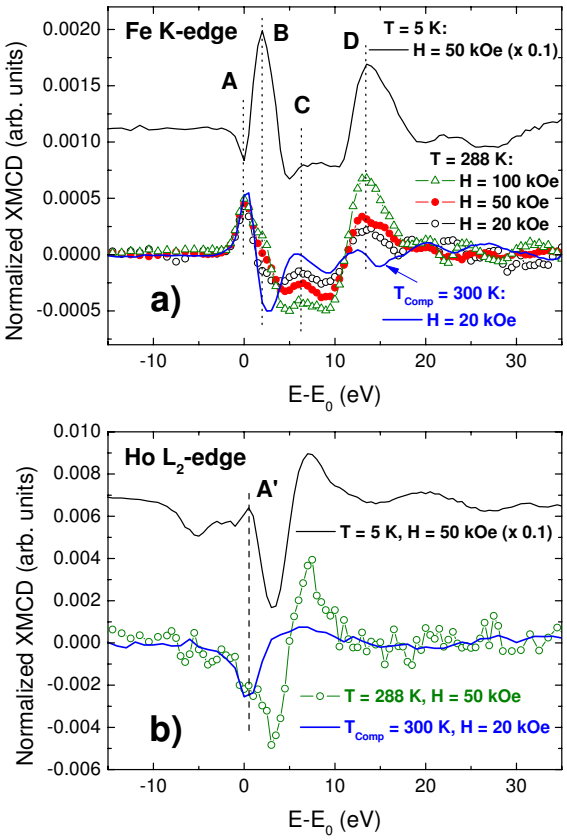

Figure 4.19: Evolution with the magnetic field of the XMCD signals recorded at the Fe K-edge [panel (a)] and Ho L_2-edge [panel (b)] in $Ho_{0.5}Lu_{0.5}Fe_2$ compound when the system is driven out the compensation condition by decreasing the temperature. The signals recorded at T = 5 K and H = 50 kOe are also included for the sake of clearness (see text for details).

have extracted the $XMCD_{Ho}$ contribution by subtracting the $LuFe_2$ XMCD spectrum to that of the $HoFe_2$ both recorded at T = 300 K and H = 20 kOe [see Fig. 4.20(a)]. Moreover, we have assumed that the $XMCD_{Fe}$ contribution at T = 288 K is approximately equal to the XMCD spectra of $Ho_{0.5}Lu_{0.5}Fe_2$ measured at T_{Comp} (T = 300 K). Then, we have recovered the XMCD signal at T = 288 K fitting a linear combination of $XMCD_{Fe}$ and $XMCD_{Ho}$ to the experimental data. Two different cases have been considered: a) Ho and Fe magnetic sublattices are parallel to the net magnetization, and b) there are two Fe contributions, parallel and antiparallel.

Fig. 4.20(b)-(d) shows for different magnetic fields the comparison of the experimental XMCD signal at T = 288 K with the composed signal obtained after performing the fitting procedure for both cases a) and b). We found that

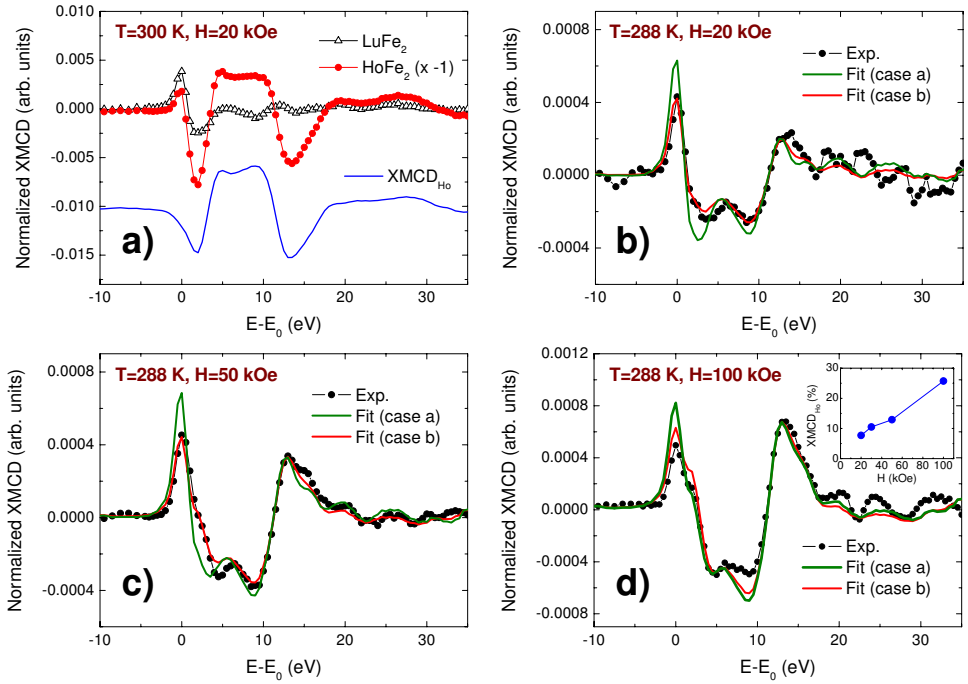

Figure 4.20: Panel (a): $HoFe_2$ and $LuFe_2$ Fe K-edge XMCD signals recorded at T = 300 K and H = 20 kOe and the respective extracted $XMCD_{Ho}$ contribution. Panels (b)-(d): composed signal by using parallel $XMCD_{Fe}$ contribution (green solid line) and both parallel and antiparallel contributions (red solid line) to match the experimental dichroic signal of $Ho_{0.5}Lu_{0.5}Fe_2$ (black, •) measured at T_{Comp} = 300 K and H = 20 (b), 50 (c) and 100 kOe (d) (see text for details).

the agreement for all the magnetic fields is better for the case b) than for the case a). Therefore, to recover the XMCD signal at T = 288 K by composition of $XMCD_{Ho}$ and $XMCD_{Fe}$ components it is needed to consider both, parallel and antiparallel, contributions of $XMCD_{Fe}$. Moreover, the antiparallel contribution grows at expenses of the parallel one as the magnetic field increases. The $XMCD_{Ho}$ contribution also grows when the magnetic field increases [see inset in Fig. 4.20(d)]. **These results indicate that both Fe and R magnetic sublattices are decoupled at T_{Comp} and, when the compound is driven out from the compensation point the ferrimagnetic ordering is progressively recovered.**

4.5 Conclusions

- The analysis of the R L_2-edge and the T K-edge XMCD spectra in R-T intermetallic compounds has proved that the atomic selectivity is not lost when XMCD probes delocalized states. On the contrary, XMCD is a simultaneous fingerprint of the magnetic contributions to the conduction band coming from the different elements in the material. These *crossed* contributions stem from the hybridization of the conduction band states.

- It has been demonstrated that it is possible to perform element-specific magnetometry by taking advantage of the presence of these *crossed* contributions. We have proved that the temperature dependence of the XMCD_T and XMCD_R components of the XMCD dichroic signal reflect the temperature dependence of the transition metal and rare-earth magnetic sublattices, i.e., $\mathrm{M}_T(\mathrm{T})$ and $\mathrm{M}_R(\mathrm{T})$ can be obtained from the XMCD spectra.

- We have studied the behavior of the Fe K-edge XMCD through the magnetic compensation occurring in the $\mathrm{Ho}_{1-x}\mathrm{Lu}_x\mathrm{Fe}_2$ series. Our results prove that both Ho and Fe sublattices contribute to the XMCD of Fe in an additive way. Only at T_{Comp}, when the net Ho sublattice magnetization is canceled, the Ho contribution to the Fe K-edge XMCD disappears and the spectrum becomes similar to that of LuFe_2, i.e., a system in which no localized $4f$ moment is present.

- These results show that the rare-earth contribution to the K-edge XMCD of the transition-metal reflects the net magnetization of the rare-earth and can be considered of atomic-like nature, i.e., the rare-earth $5d$ states become spin-polarized by the intra-atomic interaction with the $4f$ localized moments and the spin-polarization of the $5d$ states is probed in the photoabsorption process due to the R-T hybridization. The fact that it arises from the localized $4f$ states explain why for a fixed rare-earth in a R-T series the shape of the observed contribution to the K-edge XMCD of the transition-metal is similar independently of the specific transition-metal.

- Moreover, even when in several cases the rare-earth contribution dominates the observed XMCD, this work proves that the Fe intra-atomic $3d$ polarization always influences the Fe(sp)-band.

- We have studied the behavior of the rare-earth and Fe magnetic sublattices of $\mathrm{Ho}_{0.5}\mathrm{Lu}_{0.5}\mathrm{Fe}_2$ and $\mathrm{Er}_{0.5}\mathrm{Y}_{0.5}\mathrm{Fe}_2$ at the compensation temperature by means of XMCD. Our results indicate that the R sublattice is completely magnetically disordered at T_{Comp} while the Fe sublattice remains

locally ordered. Moreover, our XMCD data show that close to the compensation point both the rare-earth and Fe sublattices are magnetically decoupled and their magnetic moments are parallel to the applied magnetic field. As the compounds are driven out from the compensation point, the rare-earth moments begin to be orientated in the direction of the applied magnetic field and the R-Fe ferrimagnetic coupling of both magnetic sublattices is progressively recovered.

Chapter 5

XAS and XMCD study of the magnetic polarization of the conduction band states of *non-magnetic* atoms

The magnetic polarization of *non-magnetic* states, or even of nominally *non-magnetic* atoms, plays an important role into determining the magnetic properties of many systems. However, the exact nature of the induced magnetic moments remains an open key problem for the understanding of the magnetic interactions in these systems. This is the case of the $5d$ states of the rare-earth in R-T intermetallics which mediate the R-T interaction via de R($5d$)-T($3d$) hybridization [7, 9, 10, 12].

XMCD measurements have revealed that the dichroic spectra at the T K- and R $L_{2,3}$-edges are a simultaneous fingerprint of the magnetism of both transition-metal and rare-earth, even when only an atomic element is tuned, due to the strong R($5d$)-Fe($3d, 4p$) hybridization [1, 91, 93–104]. So far, these contributions in the dichroic signals have been studied for atoms with $4f$ or $3d$ localized magnetic moments. However, little is known about the magnetic polarization of *non-magnetic* atoms in the presence of localized magnetic moments.

In this chapter, we have faced the problem of determining the mechanism that induces the magnetic polarization of the Lu($5d$) states in the presence of R($4f$) and Fe($3d$) localized magnetic moments. To this end, we have tailored two series, $Ho_{1-x}Lu_xFe_2$ and $Ho_{0.5}Lu_{0.5}(Fe_{1-y}Al_y)_2$, in which each of these competing effects is fixed while its counterpart is varied (see Table 5.1):

• **$Ho_{1-x}Lu_xFe_2$**: for a fixed Fe contribution, the magnetization of the rare-earth sublattice is progressively depleted by increasing the Lu content. Therefore, the polarization of the Lu($5d$) states due to the Fe($3d$) ones is maintained fixed, while that of the Ho($4f$) states decreases.

• **$Ho_{0.5}Lu_{0.5}(Fe_{1-y}Al_y)_2$**: The polarization of the Lu($5d$) states due to Ho is fixed, while that of Fe is modified by substituting Fe for the *non-magnetic* Al.

$Ho_{1-x}Lu_x(Fe_{1-y}Al_y)_2$

	(Ho-Lu) dilution →				
(Fe-Al) dilution ↓	$HoFe_2$	$Ho_{0.75}Lu_{0.25}Fe_2$	$Ho_{0.5}Lu_{0.5}Fe_2$	$Ho_{0.25}Lu_{0.75}Fe_2$	$LuFe_2$
	-	-	$Ho_{0.5}Lu_{0.5}(Fe_{0.75}Al_{0.25})_2$	-	-
	-	-	$Ho_{0.5}Lu_{0.5}(Fe_{0.5}Al_{0.5})_2$	-	-
	-	-	$Ho_{0.5}Lu_{0.5}(Fe_{0.25}Al_{0.75})_2$	-	-
	-	-	$Ho_{0.5}Lu_{0.5}Al_2$	-	-

Table 5.1: Members of the $Ho_{1-x}Lu_x(Fe_{1-y}Al_y)_2$ series regarding the dilution of the Fe and Ho magnetic sublattices: $Ho_{0.5}Lu_{0.5}(Fe_{1-y}Al_y)_2$ and $Ho_{1-x}Lu_xFe_2$ series.

We have shown in Chapter 3 that the dilution of the two magnetic species, R and Fe, through these series yields a very different modification of their magnetic properties. While the dilution of the magnetic rare-earth by *non-magnetic* Y or Lu acts as a simple magnetic dilution effect, a more complex magnetic behavior is observed when Fe is substituted by Al. This different behavior suggest that when Al substitutes Fe, the electronic structure of the system is significantly modified. Accordingly, it is expected that the R($4f$)-Fe($3d, 4p$) hybridization would be differently affected by the *non-magnetic* dilution at both R and Fe sites. Therefore, the use of atomic selective spectroscopic techniques as XAS and XMCD is appropriate to get a deeper insight on the origin of this observed behavior.

To this end, we have performed a systematic study, at different absorption edges (Fe K-, R L_1- and R L_3-edges), of the near-edge and XANES region of the XAS spectra. This study is mandatory to evaluate the effect of the Fe-Al substitution on the density of states (DOS) of the systems. Subsequently, we have performed an XMCD study at the Fe K-, Ho L_2- and Lu $L_{2,3}$-edges in order to get a deeper insight into the magnetic polarization of Lu($5d$) states through the $Ho_{1-x}Lu_x(Fe_{1-y}Al_y)_2$ series. Finally, we have used the acquire knowledge to study the magnetic polarization of the $4p$-states of Ga and Ge atoms in similar $R(Fe_{0.9}M_{0.1})_2$ systems (M = Ga, Ge).

5.1 XAS study of the $\mathbf{R_{1-x}R'_x(Fe_{1-y}Al_y)_2}$ series

The substitution of Fe by Al in the RT_2 compounds induces a drastic modification of the magnetic properties. These modifications have been tentatively ascribed to perturbations in the electronic structure caused by the substitution [8, 11, 119, 120]. However, a direct experimental confirmation is still missing.

To this end, we have performed a XAS study on the $R_{1-x}R'_x(Fe_{1-y}Al_y)_2$ (R = Ho, Er; R' = Lu, Y) compounds at the Fe K- and at the rare-earth $L_{1,3}$-edges.

The basic idea behind the following discussion comes from the well known relationship between the X-ray absorption coefficient, μ(E), and the angular-momentum-projected density of states, ρ(E), given by:

$$\mu(E) = f_{at}(E)\rho(E) \tag{5.1}$$

where f_{at}(E) is a smoothly varying function of the probed atom that does not depend of its local environment [121]. Therefore, the absorption of X-rays by excitation of lanthanide $2p$ electrons (L_3-edge) is a simple and sensitive probe of the local unoccupied lanthanide $5d$ states [122–124]. These spectra are characterized by exhibiting a pronounced peak at the absorption threshold, that corresponds to the atomic-like $2p \rightarrow 5d$ transitions, usually referred as the "white-line". Changes in the shape of the white lines with increasing atomic number are determined by the localization and hybridization of the d-unoccupied states and by the progressive filling of the d-band. At this point, it is instructive to compare X-ray absorption of the elements in the gaseous state with the absorption in the condensed metallic state. Fig. 5.1 shows this comparison of the spectra in vapor and in solid state for Ce.

The L_3-edge XAS spectrum in the gaseous state exhibits a pronounced peak followed by a rather structureless continuous absorption. Upon condensation into the metallic state the L_3-edge white line does not vanish as one might naively expect from the formation of a $5d$-band with free-conduction electrons. Instead, the atomic absorption line remains largely intact: it is merely broadened and acquires a somewhat distorted, asymmetrical shape, indicating that the $5d$ states maintain a significant atomic character upon condensation. However, the overlap of the $5d$ wave functions with neighboring atoms, i.e., the hybridization or the chemical binding, causes the variation of the atomic spectral shape. Therefore, the height of the L_3-edge white line can be directly related to the localization of the $5d$ states according to Eq. (5.1).

By contrast, the spectral shape of the L_1-edge XAS spectra of lanthanides in the gaseous state exhibits a step-like rise of the absorption at the threshold,

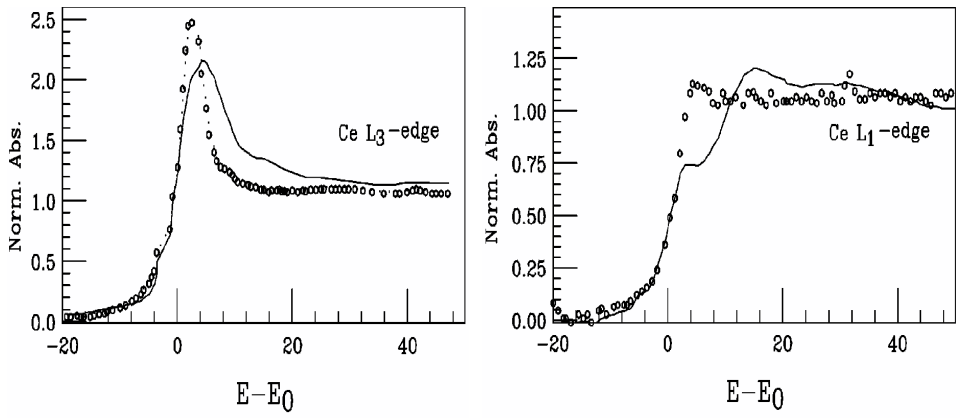

Figure 5.1: L_3-edge (left panel) and L_1-edge (right panel) X-ray absorption of Ce in the vapor state (black, ∘) at 2500 K and in the solid state (solid line) at room temperature (adapted from Ref. [126])

reflecting the local *p*-projected density of states in the band structure of the conduction electrons. However, in the solid state, the L_1-edge XAS spectra of lanthanides shows the occurrence of a shoulder-like feature at the threshold as a consequence of the overlapping of these *p*-states with the outer *s*- and *d*-symmetry orbitals, reflecting the high density of empty 5*d* states via *sp*-*d* hybridization. [125, 126]. Therefore, the modification of the width and the intensity of the double-step near-edge structure is a fingerprint of hybridization changes of the outermost orbitals between the absorbing atom and the nearest neighbors.

The sensitivity of the near-edge part of the absorption spectra to the details of the electronic structure provides a unique insight into the understanding of localization and hybridization phenomena as those occurring in the $R_{1-x}R'_x(Fe_{1-y}Al_y)_2$ series. Therefore we have performed a combined study of rare-earth at L_3- and L_1- absorption edges and of the Fe K-edge.

The normalized XANES spectra recorded at the Fe K-edge in the case of $Er_{1-x}Y_xFe_2$ and $Ho_{1-x}Y_xFe_2$ are shown in Fig. 5.2(a) and (b) respectively. In both cases the Fe K-edge near-edge region shows a step-like feature at the edge, characteristic of iron metal, reflecting the hybridization between the Fe $p-d$ conduction empty states at the Fermi level. As shown in the figure, no modification of this feature is observed as the magnetic rare-earth (Er or Ho) is substituted by the *non-magnetic* Y. This behavior is independent of the *non-magnetic* rare-earth (Y or Lu) substituting the magnetic rare-earth. Indeed, as shown in Fig. 5.2(c), a similar behavior is found in the case of the $Ho_{1-x}Lu_xFe_2$ substituted series. **These results suggest that the substitution at the rare-earth site does not induce any significative electronic change of**

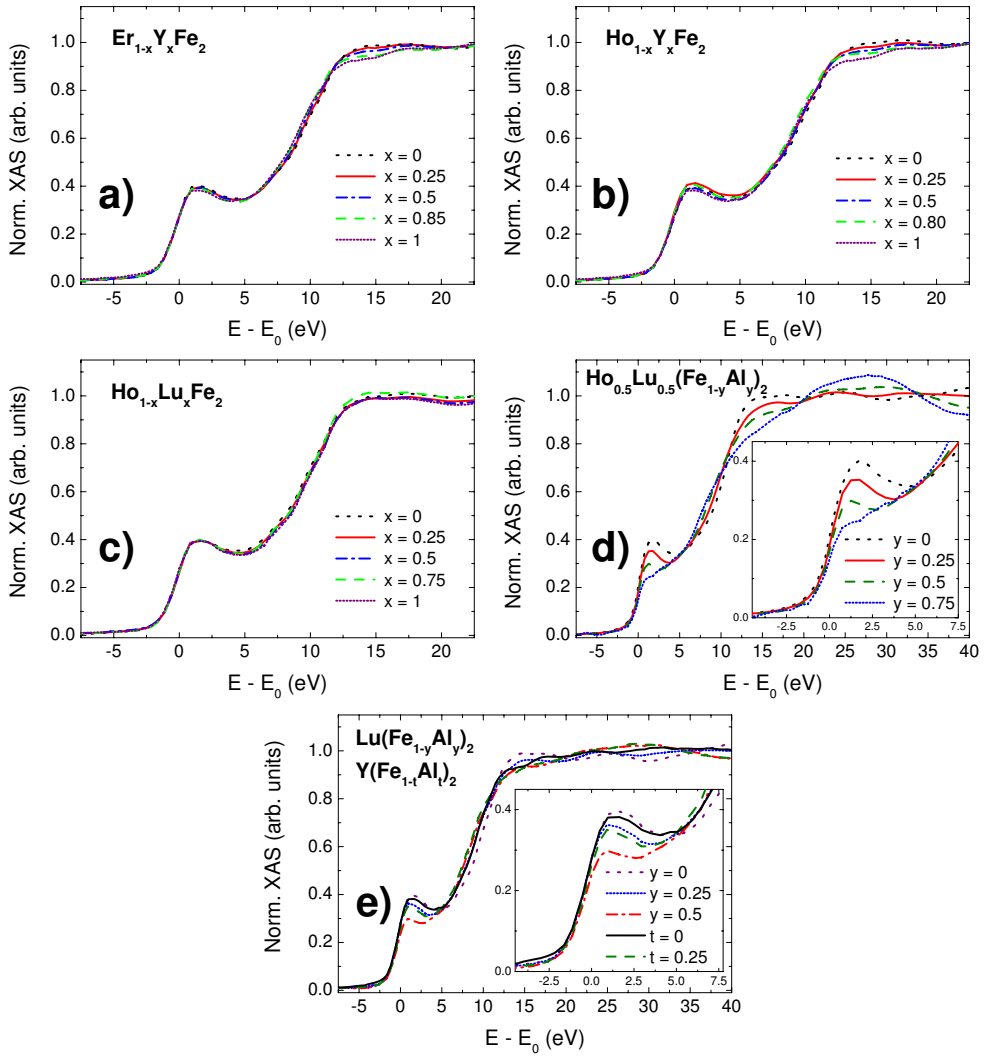

Figure 5.2: Comparison of XANES spectra at the Fe K-edge XANES recorded for: $Er_{1-x}Y_xFe_2$ (a), $Ho_{1-x}Y_xFe_2$ (b), $Ho_{1-x}Lu_xFe_2$ (c), $Ho_{1-x}Y_x(Fe_{1-y}Al_y)_2$ (d) and R'$(Fe_{1-y}Al_y)_2$ with R' = Lu, Y (e).

the system. However, this behavior strongly differs when the substitution proceeds at the Fe sites. As shown in Fig. 5.2(d) and (e), the intensity of the peak at the raising edge decreases as the Al content increases. The same trend is found in the case of *non-magnetic* rare-earth. **This result indicates that Al exerts a strong perturbation to the electronic state of the systems, i.e., the density of states is strongly modified as Al enters the RFe_2 frame.**

The results obtained at the Fe K-edge suggest that the effect of

the dilution of the atoms carrying the magnetism in the RFe_2 series is quite different whether Fe or the rare-earth are concerned. Indeed, no modification is observed when the rare-earth is diluted, whereas a strong electronic perturbation of the system takes place when Fe is substituted by Al. Moreover, the analysis of the Fe K-edge XANES spectra shows the weakening of the R-Fe hybridization when Al enters the lattice. As shown in the inset of Fig. 5.2(d) and (e), the intensity of the shoulder-like feature decreases as the Al content increases through the $Ho_{1-x}Y_x(Fe_{1-y}Al_y)_2$ and R'$(Fe_{1-y}Al_y)_2$ with R' = Lu, Y series respectively. This result clearly indicates that the Fe conduction states becomes more localized as the hybridization with those of neighboring atoms decreases upon Fe-Al dilution.

In order to confirm this hypothesis we have conducted a similar study at the L_3- and L_1-edges of the rare earth. As discussed above, the rare-earth L_3-edge absorption is characterized by a prominent white-line whose origin is due to the large density of empty states of d-symmetry R($5d$) above the Fermi level. Therefore, the comparison of the XANES spectra recorded at the Ho L_3-edge through the $Ho_{1-x}Lu_xFe_2$ series, shown in Fig. 5.3(a), provide a deeper insight on the modification of the hybridization due to the Fe-Al substitution. As shown in this figure, the changes of the white-line intensity are rather subtle when Lu substitutes Ho and, conversely, a similar result is observed at the Lu L_3-edge [Fig. 5.3(b)]. However, the intensity of the Lu L_3-edge white line significantly changes when Fe is substituted by Al in the same compounds, increasing when the Al content increases. **These results indicate that the R-Lu dilution has little effect concerning the localization of the $5d$-states and, consequently, the R-Fe hybridization is not significantly affected by the substitution. On the contrary, a progressive localization of the R($5d$) states takes place upon Al substitution, i.e., the dilution of Fe by Al implies a weakening of the R-Fe hybridization.**

An independent confirmation of these results can be obtained by studying the behavior of the L_1-edge absorption for the different magnetic dilutions (R-Lu and Fe-Al). As shown in Fig. 5.4, the dilution of the magnetic rare-earth by Lu does neither modify the absorption profile at the Er L_1- nor at the Lu L_1-edges. However, a reduction of the shoulder-like feature is observed when Fe is substituted by Al, indicating a more localized nature of the $p-d$ orbitals of the rare-earth, similar to the rare-earth vapors case. **These results support the hypothesis that a higher localization of the $5d$ band concomitant to the reduction of the R($5d$)-Fe($3d$) hybridization at the rare earth site takes place upon Al substitution.**

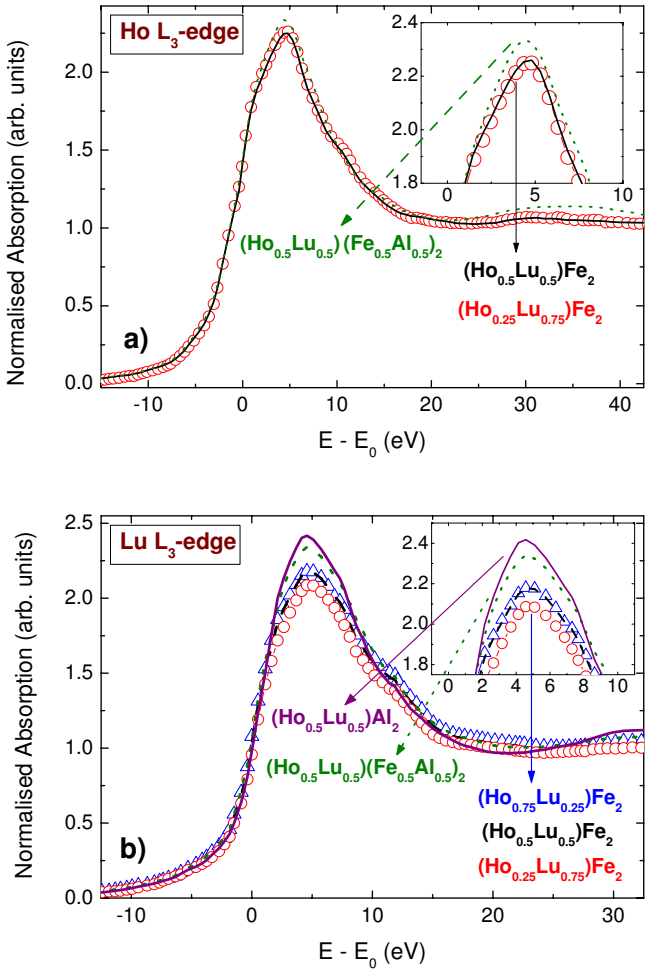

Figure 5.3: Comparison of XANES spectra recorded through the $(Ho_{1-x}Lu_x)(Fe_{1-y}Al_y)_2$ series at the Ho L_3-edge [panel (a)] and Lu L_3-edge [panel (b)]: $(Ho_{0.25}Lu_{0.75})Fe_2$ (red, ○), $(Ho_{0.5}Lu_{0.5})Fe_2$ (black dashed line), $(Ho_{0.75}Lu_{0.25})Fe_2$ (blue, △), $(Ho_{0.5}Lu_{0.5})(Fe_{0.5}Al_{0.5})_2$ (green dotted line) and $(Ho_{0.5}Lu_{0.5})Al_2$ (purple solid line).

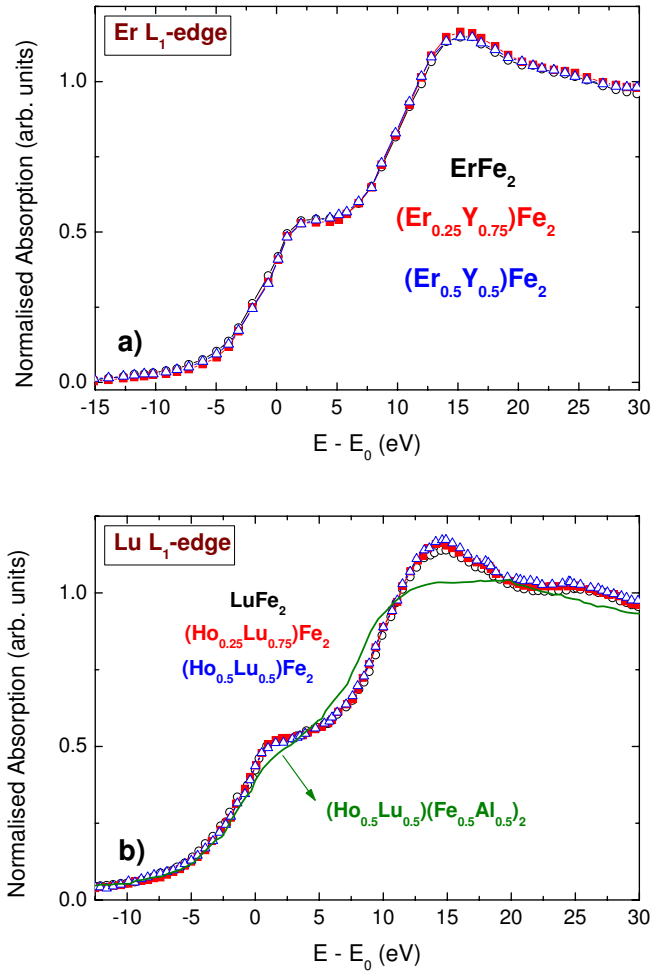

Figure 5.4: Comparison of XANES spectra recorded at the Er L_1-edge through the $(Er_{1-x}Y_x)Fe_2$ series [panel (a)] and at the Lu L_1-edge in the case of $(Ho_{1-x}Lu_x)(Fe_{1-y}Al_y)_2$ compounds [panel (b)]: on both panels x=1 (black, ○), x=0.5 (blue, △), x=0.25 (red, ■) and $(Ho_{0.5}Lu_{0.5})(Fe_{0.5}Al_{0.5})_2$ (green solid line) only in panel (b).

5.2 Magnetic polarization of the Lu atoms in $Ho_{1-x}Lu_x(Fe_{1-y}Al_y)_2$ series

As stated in the introduction, our main aim in this chapter is to determine the mechanism that induces the magnetic polarization of the Lu($5d$) states in the presence of the R($4f$) and Fe($3d$) localized magnetic moments. To this end, the study of the XMCD response of the Lu atoms at the $L_{2,3}$ absorption edges becomes a fundamental step.

The magnetization and XAS studies performed on the tailored $Ho_{1-x}Lu_x(Fe_{1-y}Al_y)_2$ series has demonstrated the different impact of the substitution of the magnetic atoms, Ho and Fe, by *non-magnetic* ones, Lu and Al respectively, on the magnetic properties of these systems. Therefore, first step in our XMCD study will be to determine if this behavior is also reflected in the XMCD recorded at the Fe K-edge and Ho L_2-edge through the series. The experience acquired through this Thesis on the different magnetic contributions to the XMCD signals at these absorption edges will allow us to determine how the R-Fe hybridization varies through the $Ho_{1-x}Lu_x(Fe_{1-y}Al_y)_2$ series depending on which magnetic atoms is substituted. Then, this knowledge will be applied to determine which magnetic atom, Ho or Fe, mainly determines the magnetic polarization of the Lu($5d$) states.

5.2.1 Fe K- and Ho L_2-edges

The Fe K-edge XMCD spectra recorded at T = 5 K and H = 50 kOe through the $Ho_{1-x}Lu_x(Fe_{1-y}Al_y)_2$ series are reported in Fig. 5.5.[1] The Fe K-edge XMCD spectra are characterized by a negative peak at the edge (peak A), two prominent positive peaks, B and D located, respectively, at $\sim$ 2 and $\sim$ 14 eV above the edge and a double negative peak, labeled as $C1$ at E-E_0 $\sim$ 4 eV and $C2$ at E-E_0 $\sim$ 10 eV. As discussed in the precedent chapter the Fe, $XMCD_{Fe}$, contribution is more intense close to the absorption threshold (peak A) while the contribution due to the rare-earth sublattice, $XMCD_R$, extends over a wider energy range and dominates the shape of the XMCD spectra (peaks $B, C1, C2$ and D).

In the case of the $Ho_{1-x}Lu_xFe_2$ compounds, i.e., when only Ho is substituted by Lu, both the shape and the energy position of the main spectral features remain unvaried. However, the amplitude of the spectral features associated to $XMCD_R$ ($B, C1, C2$ and D) decreases as the Lu content increases. By contrast, the intensity of peak A associate to $XMCD_{Fe}$, weakens

[1] All the XMCD spectra have been displayed with the same sign as for the compounds in which the Ho sublattice is the dominant one.

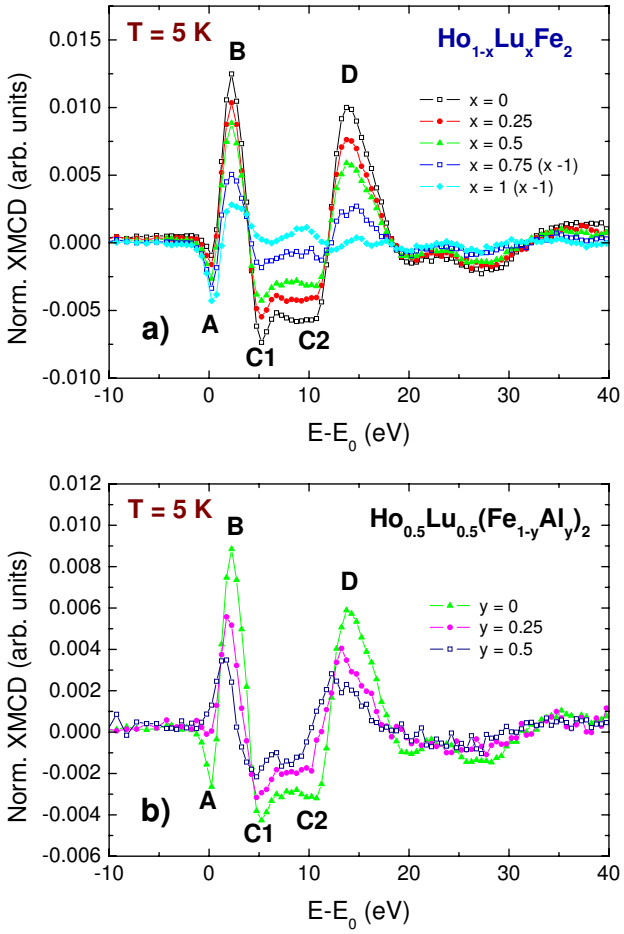

Figure 5.5: XMCD spectra at the Fe K-edge for $Ho_{1-x}Lu_xFe_2$ [panel (a)] and $Ho_{0.5}Lu_{0.5}(Fe_{1-y}Al_y)_2$ [panel (b)] series. All the XMCD spectra have been displayed with the same sign as for the case in which the Ho sublattice is the dominant one.

the $XMCD_{Ho}$ contribution to the total XMCD signal and the reduction of the amplitude of the peak B, overlapped with the $XMCD_{Fe}$ contribution reinforces the intensity of peak A. Moreover, the reduction of the $XMCD_R$ contribution scales with the Ho concentration which indicates that the substitution of Ho by Lu acts as a simple magnetic dilution effect.

By contrast, the substitution of Fe by Al affects both the shape and the amplitude of the XMCD spectra. As shown in Fig. 5.5(b) the increase of the Al content diminishes the intensity of the main absorption features ($A, B, C1, C2$ and D) and shifts them towards lower energy. We known from previous studies, see Chapter 4, that when Al atoms substitutes the Fe ones in $Ho_{0.5}Lu_{0.5}(Fe_{1-y}Al_y)_2$ the Ho magnetic moment remains close to their free-

ion value. Consequently, the observed reduction of the $XMCD_{Ho}$ contribution to the Fe K-edge XMCD directly reflects the progressive reduction of the R-Fe exchange induced by the Al substitution through the reduction of the Ho($5d$)-Fe($3d$) hybridization.

These results are confirmed by the study of the behavior of the Ho L_2-edge XMCD spectra through the substituted $Ho_{1-x}Lu_x(Fe_{1-y}Al_y)_2$ series. This is shown in Fig. 5.6, where the Ho L_2-edge XMCD spectra recorded at T = 5 K and H = 50 kOe through the series are compared. In the case of compounds in which the Fe content is fixed and only Ho is substituted by Lu, see Fig. 5.6(a), the dichroic signal is composed by a main negative peak A located at E-$E_0 \sim 1.5$ eV and a positive peak B at E-$E_0 \sim 7$ eV. As discussed previously, peak $A1$ is associated to the Fe contribution to the Ho L_2-edge XMCD spectrum, while peak B is mainly due to the rare-earth magnetization. As shown in Fig. 5.6(a), the intensity of peak $A1$ remains constant through the $Ho_{1-x}Lu_xFe_2$ series. By contrast, peak B undergoes a reduction of its intensity upon increasing the Lu content. These results indicate that the Ho-Fe hybridization is not affect by the Ho-Lu substitution and that only the magnetization of the rare-earth sublattice decreases as a consequence of the Ho-Lu dilution [110].

Similarly to the Fe K-edge cases, strong differences are found in the case of the $Ho_{0.5}Lu_{0.5}(Fe_{1-y}Al_y)_2$ series, i.e., when the rare-earth sublattice is kept constant and the atomic substitution only involves the $3d$ sublattice. As shown in Fig. 5.6(b), peak $A1$, associated to the Fe contribution, suffers a dramatic depletion upon dilution of Fe by Al, while the intensity of peak B does not vary appreciably. As expected, these results are just the opposite to those found for the $Ho_{1-x}Lu_xFe_2$ series.

The fact that the dilution of the Ho sublattice does not affect the $XMCD_{Fe}$ contribution through the $Ho_{1-x}Lu_xFe_2$ series can be easily assessed by comparing the Fe contributions to the Ho L_2-edge XMCD spectra. To this end we have extracted $XMCD_{Fe}$ by subtracting from the Ho L_2-edge XMCD spectra that of $Ho_{0.5}Lu_{0.5}Al_2$. The results, reported in Fig. 5.7(a), indicate that the $XMCD_{Fe}$ extracted from the $Ho_{1-x}Lu_xFe_2$ spectra does not change appreciably through the series. Indeed, the main peak matches for all the $Ho_{1-x}Lu_xFe_2$ compounds.

By contrast, the intensity of the $XMCD_{Fe}$ signal decreases abruptly through the $Ho_{0.5}Lu_{0.5}(Fe_{1-y}Al_y)_2$ series upon substitution of Fe by Al, as shown in Fig. 5.7(b). There is also a displacement of the main peak towards higher energy. This latter effect might be ascribed to the expansion of the lattice upon increasing the Al content. The amplitude reduction can not be accounted for the dilution of the Fe sublattice since it does not vary linearly with the Fe

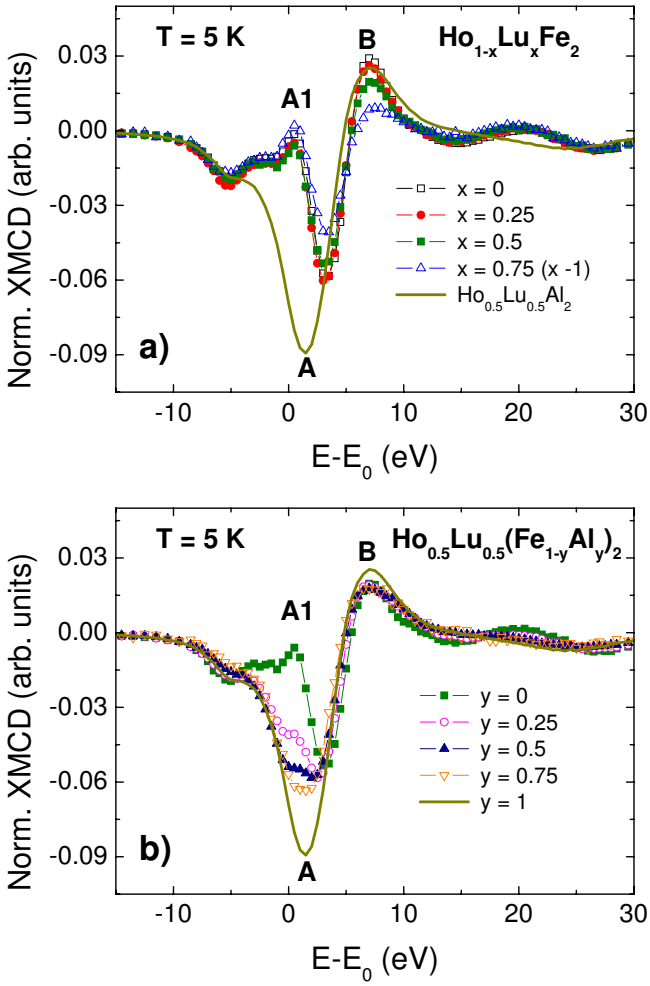

Figure 5.6: Ho L_2-edge XMCD signals measured at T = 5 K and under a magnetic field of H = 50 kOe for $Ho_{1-x}Lu_xFe_2$ [panel (a)] and $Ho_{0.5}Lu_{0.5}(Fe_{1-y}Al_y)_2$ [panel (b)] series of compounds. For sake of comparison it has been included the dichroic spectra of $Ho_{0.5}Lu_{0.5}Al_2$ in panel (a).

content, as shown in Fig. 5.8. The substitution of Fe by Al induces magnetic disorder in the 3*d* magnetic sublattice as well as the modification of the electronic structure (see the magnetization and XAS results). Consequently, the observed decrease of the $XMCD_{Fe}$ contribution can be ascribed to the reduction of the Ho(5*d*)-Fe(3*d*) hybridization associated with the modification of the magnetic properties of the 3*d* magnetic sublattice.

Therefore, these results are in agreement with those obtained from the XAS study. **The Ho-Lu substitution through the $Ho_{1-x}Lu_xFe_2$ series acts as a simple magnetic dilution and does not modify the**

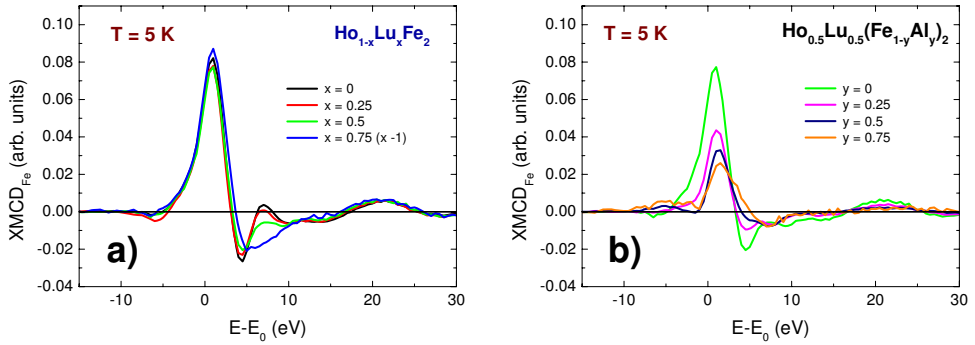

Figure 5.7: $XMCD_{Fe}$ contribution extracted from the Ho L_2-edge XMCD spectra of $Ho_{1-x}Lu_xFe_2$ [panel (a)] and $Ho_{0.5}Lu_{0.5}(Fe_{1-y}Al_y)_2$ [panel (b)]

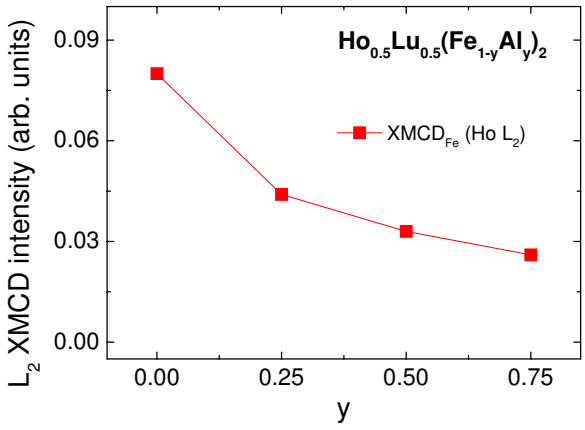

Figure 5.8: Amplitude variation of the $XMCD_{Fe}$ contribution upon increasing the Al content, y.

Ho($5d$)-Fe($3d$) hybridization. By contrast, the Fe-Al substitution through the $Ho_{0.5}Lu_{0.5}(Fe_{1-y}Al_y)_2$ series yields the depletion of the Ho($5d$)-Fe($3d$) hybridization.due to electronic impact of the substitution.

5.2.2 Lu $L_{2,3}$-edges

We have shown in the precedent subsections how the dilution of the Fe and Ho magnetic sublattices affects differently the XAS and XMCD spectra recorded at both Fe K- and Ho L_2-edges. Moreover, we have established a direct connection among the variation of the crossed contributions to the XMCD and the modification of the Ho-Fe hybridization through the series. Here, we will apply this acquired knowledge to the study of the magnetic polarization of the Lu($5d$) states. In particular, our aim is to determine which magnetic species,

Ho or Fe, is responsible for the appearance of a magnetic moment at the Lu sites [9, 12, 122, 127, 128]. To this end, we have performed a Lu $L_{2,3}$-edges XMCD study of the $Ho_{1-x}Lu_x(Fe_{1-y}Al_y)_2$ series.

Fig. 5.9 shows the Lu $L_{2,3}$-edges XMCD spectra of the $Ho_{1-x}Lu_xFe_2$ series recorded at T = 5 K and H = 50 kOe. The Lu L_3-edge dichroic signal, see Fig. 5.9(a), is composed by a main negative peak A located at E-E_0 $\sim$ 1 eV and a less intense positive peak B at $\sim$ 10 eV. The spectral feature A does not change through the series, whereas the intensity of peak B decreases upon increasing the Lu content up to almost vanishes for $LuFe_2$. In the case of the Lu L_2-edge XMCD spectra, see Fig. 5.9(b), the dichroic signal is composed by a main peak C located at E-E_0 $\sim$ 0 eV and two other less intense peaks, D and F, located at E-E_0 $\sim$ 4 eV and $\sim$ 7 eV, respectively. Peak C does not exhibit any variation upon dilution of the Ho sublattice whereas the intensity of both D and F peaks decreases upon increasing the Lu content. Consequently, these results suggest that peaks A and C are mainly due to the Fe contribution while peaks B, D and F originate from the Ho contribution.

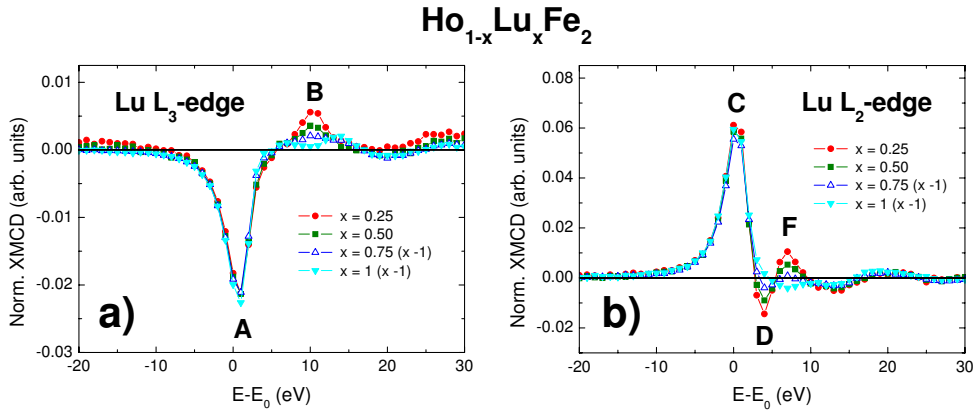

Figure 5.9: Lu $L_{2,3}$-edges XMCD signals measured at T = 5 K and under a magnetic field of H = 50 kOe for $Ho_{1-x}Lu_xFe_2$ series.

The spectral profile of the dichroic signals at the Lu L_3- and L_2-edges is dominated by the main peaks A and C, respectively. In both cases only minor changes are observed through the $Ho_{1-x}Lu_xFe_2$ series. In other words, the XMCD spectra at both Lu $L_{2,3}$-edges is mostly retained upon substitution of Ho by Lu. Since the Fe content is kept constant through the $Ho_{1-x}Lu_xFe_2$ series and only the Ho content is varied, we can conclude that the magnetic polarization at the Lu sites is mainly due to the Fe magnetic moments.

On the other hand, the intensity of the less intense peaks B (Lu L_3-edge) and, D and F (Lu L_2-edge) varies upon increasing the Lu content. The relative variation of their intensity, obtained by subtracting the $LuFe_2$ spectrum,

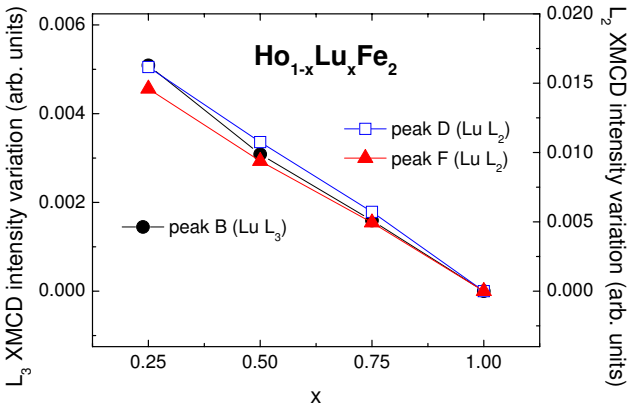

Figure 5.10: Relative variation of the peaks B (Lu L_3-edge) and, D and F (Lu L_2-edge) respect to the $LuFe_2$ values (see text for details).

shows a linear decrease (see Fig. 5.10). This decrease is linear with x, i.e., the intensity of these peaks is proportional to the Ho concentration. **Therefore, the effect of the magnetic polarization of the Lu($5d$) states due to the Ho atoms is clearly smaller than that due to the Fe ones.**

Similar comparisons performed for the $Ho_{0.5}Lu_{0.5}(Fe_{1-y}Al_y)_2$ series are shown in Fig. 5.11. The XMCD spectrum is composed by a mean negative peak A and a less intense peak B. The intensity of the main peak A decreases as the Al content increases. The intensity of peak B is clearly less affected by the substitution and only a slight narrowing together with a shift to lower energies is observed. Similar results are found in the Lu L_2-edge XMCD spectra (see panel (b) of Fig. 5.11). The main peak C decreases and the peaks above the absorption edge, D and F, are less affected.

The observed reduction of the intensity of the main peaks A and C at the Lu L_3- and L_2-edge, respectively, indicates that the Fe polarization of the Lu($5d$) states is dramatically affected by the Al substitution. As shown in Fig. 5.12, the amplitude of the main dichroic peak at both Lu $L_{2,3}$-edges follows the same dependence with the Fe content, a trend that coincides with that of the $XMCD_{Fe}$ contribution at the Ho L_2-edge. However, contrary to the case of the Ho-Lu substitution, this reduction does not scale with the Fe content. This result confirms our previous findings regarding the electronic impact of the Fe-Al substitution that cannot be regarded as a simple dilution effect in the $3d$ magnetic sublattice.

The conclusion that the main responsible of the magnetic polarization of the Lu($5d$) states is the $3d$ magnetic sublattice instead of the rare-earth one can be confirmed by studying the temperature dependence of the Lu $L_{2,3}$-edges XMCD signals. As discussed in the precedent Chapters the magnetization

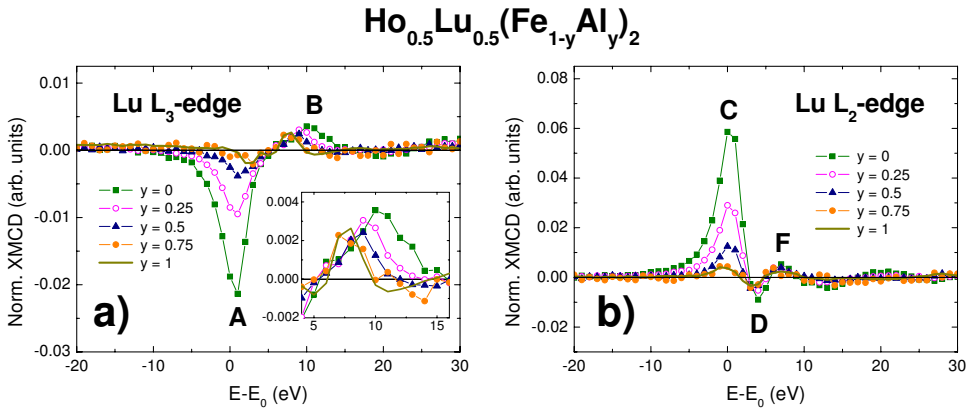

Figure 5.11: Lu $L_{2,3}$-edges XMCD signals measured at T = 5 K and under a magnetic field of H = 50 kOe for $Ho_{0.5}Lu_{0.5}(Fe_{1-y}Al_y)_2$ series. Inset in panel (a) shows an enlarge view of the peak B.

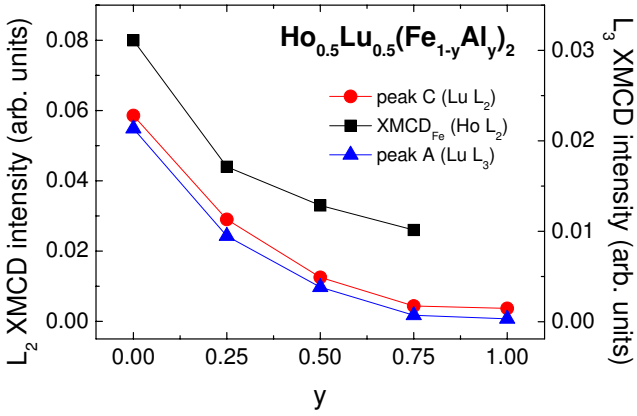

Figure 5.12: Variation with the Al content of the intensity of the peaks reflecting the Fe contribution at Lu $L_{2,3}$-edges and Ho L_2-edge recorded for the $Ho_{0.5}Lu_{0.5}(Fe_{1-y}Al_y)_2$ series.

of the Fe sublattice remains practically constant through the temperature range of our interest (from T = 5 K to ambient), while that of the rare-earth decreases very fast upon increasing temperature. Accordingly, if Fe is the main responsible into the polarization of the Lu($5d$) states, the intensity of the XMCD spectra should not vary appreciably between T = 5 K and room temperature. By contrast, if this polarization is mainly due to the Ho sublattice this intensity should be strongly depressed at high temperature.

Then, we have recorded the Lu $L_{2,3}$-edges XMCD spectra of $Ho_{1-x}Lu_xFe_2$ at T = 288 K. The results, displayed in Fig. 5.13, show that the amplitude of the XMCD spectra remain nearly unvaried and only a slight decrease is

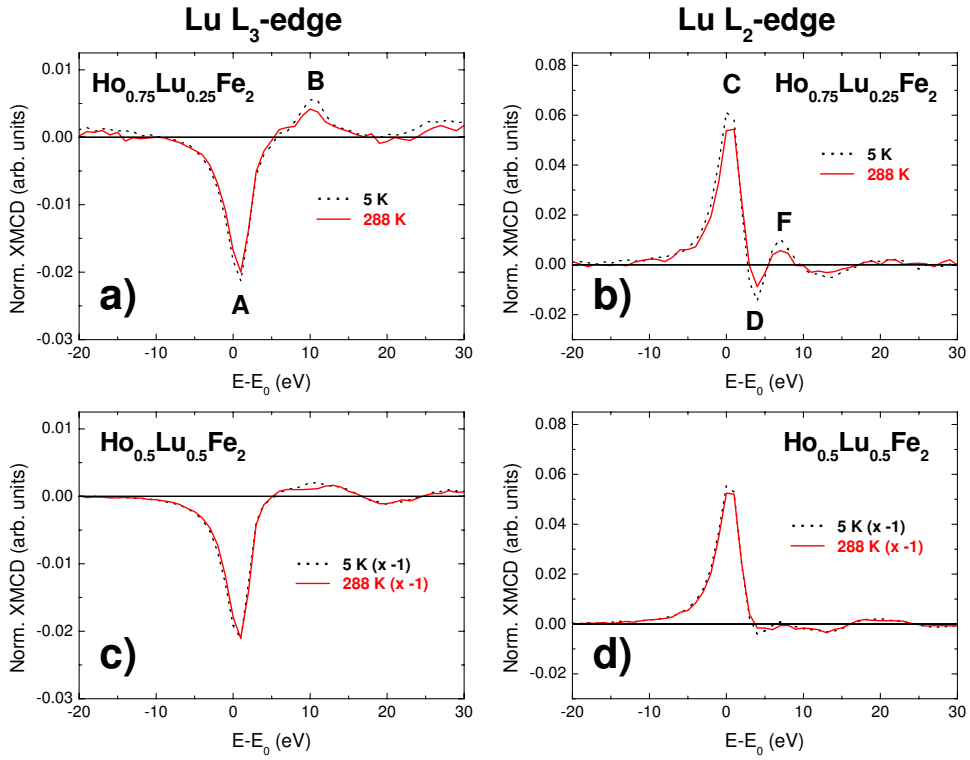

Figure 5.13: Temperature evolution of the XMCD signals at Lu L_3- (left panels) and L_2-edges (right panels) for $Ho_{0.75}Lu_{0.25}Fe_2$ and $Ho_{0.25}Lu_{0.75}Fe_2$.

observed when the temperature increases. A detailed analysis of the evolution of the dichroic features yields that upon warming, from T = 5 K to 288 K, the intensity of the main peaks exhibits a decrease of $\sim 7.5\%$ which is in agreement with the decreasing of the magnetization of the Fe sublattice. By contrast, the relative variation of the intensity of the less intense peaks, associated to the Ho sublattice (see above), is about $\sim 76\%$, in agreement with the variation of the Ho sublattice magnetization. Thus, these results confirm that the appearance of a magnetic polarization at the Lu sites in the $Ho_{1-x}Lu_x(Fe_{1-y}Al_y)_2$ series is mainly due to the Fe magnetic moments.

Finally, we have deserved attention to the particular case of the magnetic compensation point that $Ho_{0.5}Lu_{0.5}Fe_2$ exhibits at $T_{Comp} \sim 300$ K and H = 20 kOe. As shown in Fig. 5.14, the amplitude of the Lu $L_{2,3}$-edges XMCD spectra have been strongly reduced with respect to those spectra recorded at low temperature. This behavior is markedly different to that of $Ho_{0.75}Lu_{0.25}Fe_2$ and $Ho_{0.25}Lu_{0.75}Fe_2$,see Fig. 5.13, and it has to be accounted in terms of the compensation of the magnetization of both Ho and Fe sublattices. As discussed in the precedent Chapter, the Fe sublattice still presents some magnetic order

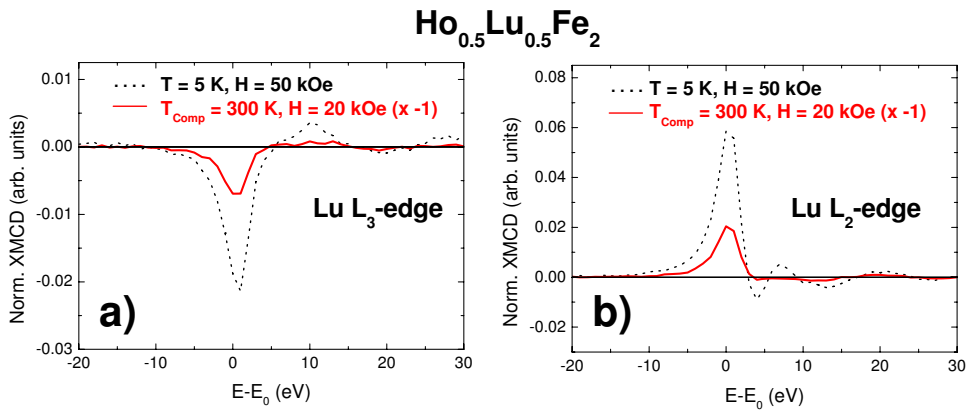

Figure 5.14: Temperature evolution of the XMCD signals at Lu L_3- [panel (a)] and L_2-edges [panel (b)] for $Ho_{0.5}Lu_{0.5}Fe_2$.

while it has completely disappear in the Ho one. According to our conclusions on the polarization of the Lu($5d$) states, it is expected that this local order polarizes the Lu($5d$) states although the magnitude of the effect should be dramatically reduced. This is exactly what is found in the Lu $L_{2,3}$-edges XMCD spectra at T_{Comp}. Indeed, the Lu $L_{2,3}$-edges XMCD signals shows only the Fe contribution while no hint of the Ho one is detected. This is further confirmed by the comparison of these spectra with those of $LuFe_2$, i.e., a compound in which no Ho contribution is present. As displayed in Fig. 5.15 both signals show a perfect match, after an appropriate scaling, which confirms that only the Fe contribution is present at T_{Comp}.

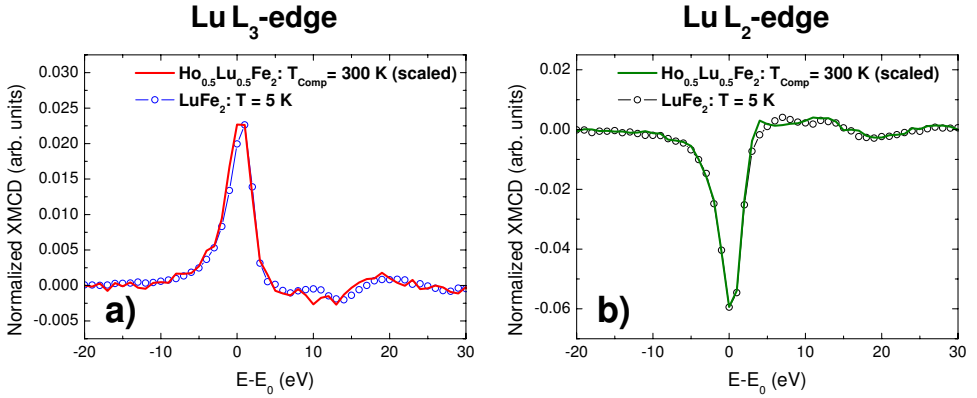

Figure 5.15: Comparison of Lu $L_{2,3}$-edges XMCD spectra of $Ho_{0.5}Lu_{0.5}Fe_2$ at the magnetic compensation point with the dichroic signals of $LuFe_2$ at low temperature.

5.3 Magnetic polarization of the *non-magnetic* atoms in $R(Fe_{1-x}M_x)_2$ series (M = Ga or Ge)

In the precedent section we have studied the magnetic polarization of *non-magnetic* Lu atoms in $Ho_{1-x}Lu_x(Fe_{1-y}Al_y)_2$ series. It has been proved that the Lu($5d$) states are mainly polarized by the Fe magnetic moments under the presence of competing magnetic polarizations of Fe and rare-earth atoms. In order to get a deeper insight into the magnetic polarization of *non-magnetic* atoms in the presence of competing magnetic polarizations, we propose to study the case of *non-magnetic* atoms with a completely filled d-band as Ga and Ge, in contrast to the previous study of Lu atoms in which the complete shell was the $4f$ one.

Hence, we have performed an XMCD study on $R(Fe_{1-x}M_x)_2$ compounds, where R is a magnetic or *non-magnetic* rare-earth (Ho or Gd and Y, respectively) and M is the *non-magnetic* element (Ga or Ge). Both Ga ($[Ar]3d^{10}4s^24p^1$) and Ge ($[Ar]3d^{10}4s^24p^2$) substitute Fe in the Laves RFe_2 compounds. This substitution leads to the modification of the RFe_2 crystal structure in such a way that the Laves phase structure is only preserved for low concentration of *non-magnetic* M atoms [62]. This result is expected because the crystal structure of both pure RGe_2 and RGa_2 differs from that of the RFe_2 compounds.[2] Therefore, we have kept constant the substitution percentage of M atoms equal to 10%, i.e., $R(Fe_{0.9}M_{0.1})_2$.

5.3.1 XMCD in $R(Fe_{0.9}Ga_{0.1})_2$ and $R(Fe_{0.9}Ge_{0.1})_2$ compounds

Ga K-edge

Fig. 5.16 shows both the XAS and XMCD spectra of the $Y(Fe_{0.9}Ga_{0.1})_2$ compound at the Ga K-edge recorded at T = 5 K and 288 K. The observed non-zero XMCD signal provides the experimental evidence that the Ga $4p$ states are magnetically polarized by the Fe atoms. The Ga K-edge XMCD spectra of $Y(Fe_{0.9}Ga_{0.1})_2$ are composed by a negative (peak A) and a positive (peak B) contributions at E-E_0 $\sim$ 2 eV and $\sim$ 9 eV, respectively. The peak A of the dichroic signal appears in the same energy range that the shoulder feature at the rising edge of the absorption spectra. Peak B is located at the energy of the white-line of the XAS spectra.

This spectral shape is retained when the temperature varies. Indeed, as

[2] RGa_2 crystallizes in the AlB_2-type hexagonal structure (space group P6/mmm) [59] whereas, on the other hand, the ideal composition RGe_2 is not realized in most cases and various polymorphic forms are off-stoichiometric compounds with different degrees of ordering of the Ge vacancy distribution [60, 61].

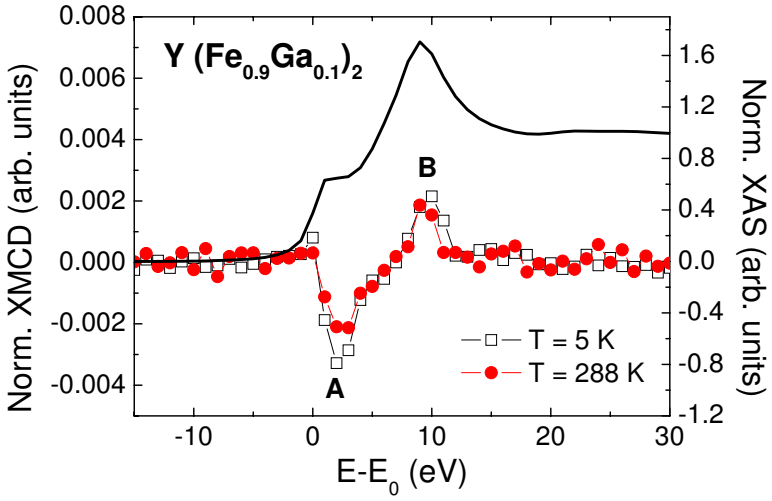

Figure 5.16: Comparison of the Ga K-edge XMCD spectra recorded at T = 5 K and 288 K in the case of $Y(Fe_{0.9}Ga_{0.1})_2$ compound. For the sake of completeness the XAS spectrum is also shown.

shown in Fig. 5.16, only the amplitude of the XMCD signal is concerned as temperature increases from T = 5 K to ambient. The relative variation of the integrated XMCD signal between both temperature is $\sim$ 40%, which agrees with the enhancement of the magnetization, $\sim$ 38%, in the same temperature range.

As shown in Fig. 5.17, the profile of the dichroic spectra of $Y(Fe_{0.9}Ga_{0.1})_2$ at the Ga K-edge is similar to those previously reported on other Ga compounds as $Ni_{51}Mn_{28}Ga_{21}$ (ferromagnetic Heusler alloys) [129] or Mn_3GaC (manganese carbide compounds) [130]. The XMCD signal is composed by two main peaks, negative (peak A) and positive (peak B). The energy position of the peak A is the same for the three compounds, $E\text{-}E_0 \sim 2$ eV, whereas the energy position of the peak B is different for each compound and it is aligned with the position of the white-line. Moreover, the amplitude of the XMCD signal is 0.5-0.7% of the absorption jump in all cases.

Consequently, these results show how the magnetic polarization of the Ga($4p$) states is, when the only source of localized magnetism in the compound is a transition metal. Now we would like to determine how this polarization changes when magnetic rare-earth atoms are also present in the compounds. To this end we have recorded the Ga K-edge XMCD signal in the case of $Ho(Fe_{0.9}Ga_{0.1})_2$ and $Gd(Fe_{0.9}Ga_{0.1})_2$.

As shown in Fig. 5.18 , both $Ho(Fe_{0.9}Ga_{0.1})_2$ and $Gd(Fe_{0.9}Ga_{0.1})_2$ XMCD

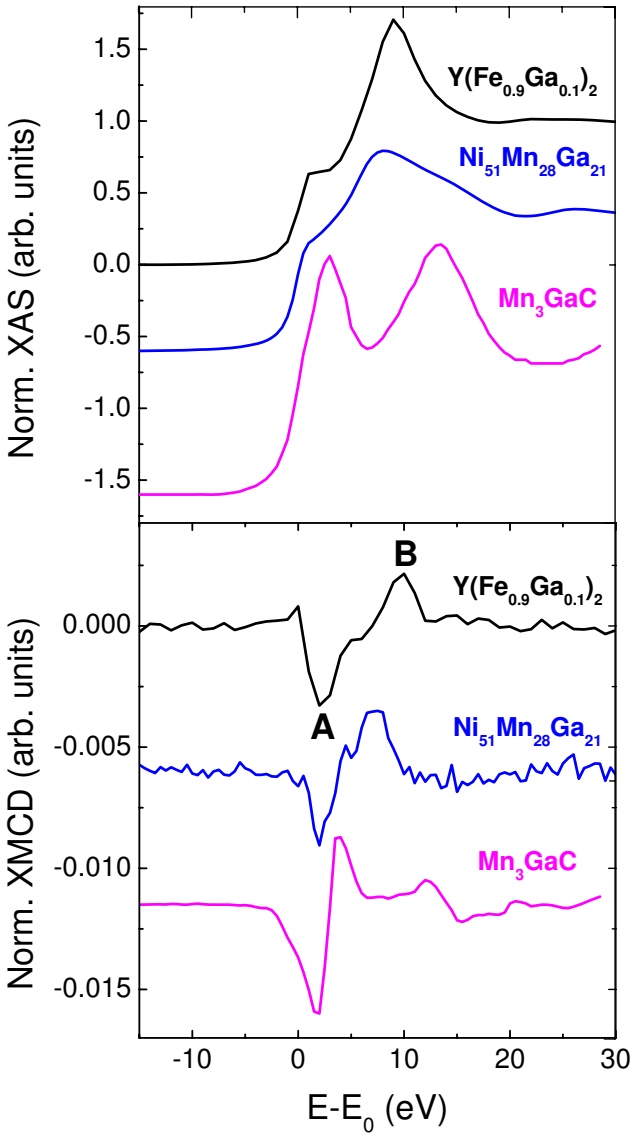

Figure 5.17: Comparison of the Ga K-edge XMCD and XAS spectra of $Y(Fe_{0.9}Ga_{0.1})_2$ with other Ga compounds as $Ni_{51}Mn_{28}Ga_{21}$ and Mn_3GaC (from Ref. [129] and [130], respectively).

signals are composed by three main contributions labeled C, D and F. This profile is clearly different from that of $Y(Fe_{0.9}Ga_{0.1})_2$, i.e., of the compound in which no $4f$ magnetic moment is present and, in addition, the amplitude is also enhanced.

In the case of $Y(Fe_{0.9}Ga_{0.1})_2$ the peak to peak amplitude of the XMCD

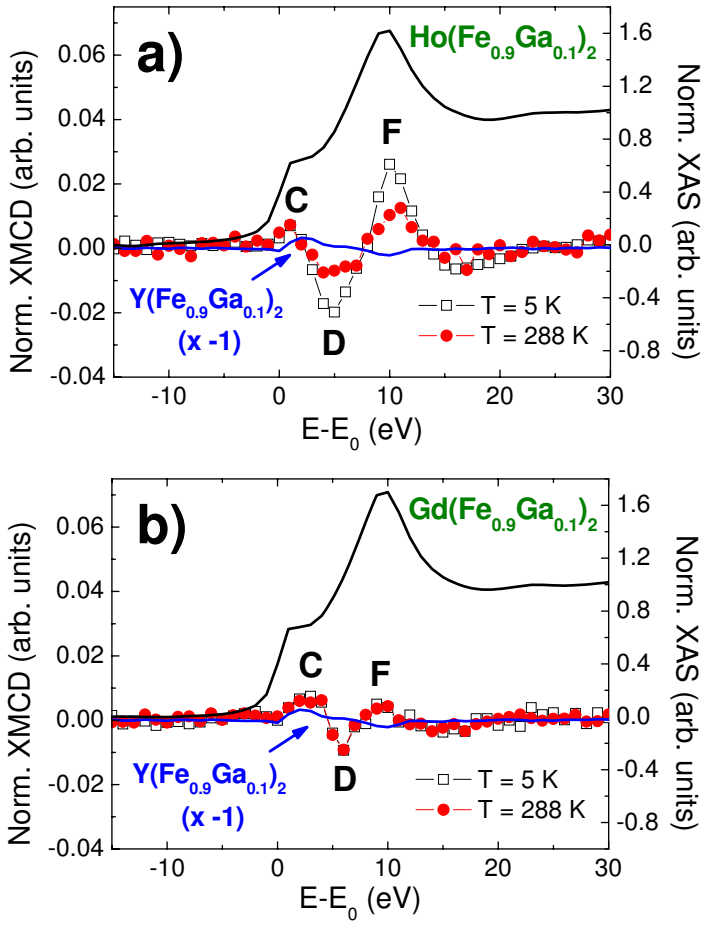

Figure 5.18: Comparison of XAS and XMCD spectra at Ga K-edge recorded at 5 and 288 K for $Ho(Fe_{0.9}Ga_{0.1})_2$ [panel (a)] and $Gd(Fe_{0.9}Ga_{0.1})_2$ [panel (b)] compounds. For the sake of comparison the dichroic spectrum of $Y(Fe_{0.9}Ga_{0.1})_2$ at 5 K is included.

spectrum recorded at T = 5 K is $\sim 0.5\%$ of the absorption jump. This amplitude is enhanced by an order of magnitude in the case of $Gd(Fe_{0.9}Ga_{0.1})_2$ and $Ho(Fe_{0.9}Ga_{0.1})_2$ being $\sim 1.7\%$ and $\sim 4.6\%$ of the absorption jump, respectively. This result indicates that the magnetic polarization of the Ga $4p$-states is enhanced by the presence of localized $4f$ magnetic moments. The substitution of 10% of Fe by Ga does not modify the magnetic properties of the compound beyond what is expected for a simple magnetic dilution effect. Consequently, we can assume that the magnetic properties of the Fe sublattice remains basically the same for $Y(Fe_{0.9}Ga_{0.1})_2$, $Gd(Fe_{0.9}Ga_{0.1})_2$ and $Ho(Fe_{0.9}Ga_{0.1})_2$. Under these assumptions, the observed variations of the XMCD signals should indicate that the polarization of the Ga $4p$-states due to the presence of $4f$ magnetic moment is greater than in the case of $3d$-moments.

The temperature dependence of the XMCD presents also interesting differences. In the case of $Ho(Fe_{0.9}Ga_{0.1})_2$ by integrating both D and F peaks we found that the Ga XMCD increases overall a $\sim$ 120% upon cooling from T = 288 K down to 5 K. This increment is of the same order of magnitude that the increase of the magnetization, $\sim$ 160%. Surprisingly, the amplitude of the XMCD spectra recorded on $Gd(Fe_{0.9}Ga_{0.1})_2$ does not change upon varying the temperature [see Fig. 5.18(b)]. However, the observed change of the macroscopic magnetization in this case only is $\sim$ 26%. These result suggest that the Ga K-edge XMCD stems from the competition of the contribution of both Fe and Ho (Gd) atoms. As the magnetic moments of both atomic species are ferrimagnetically coupled, the temperature dependence of those XMCD signals would depend on the particular temperature dependence of each magnetic moment and their coupling.

Fe K-edge

In precedent chapters we have demonstrated that in RFe_2 compounds the substitution of Fe by a *non-magnetic* atom such as Al modifies their electronic structure. This modification clearly influences both the XAS and XMCD recorded at the Fe K-edge. Aimed of verifying if similar effect is observed upon Ga substitution we have recorded also the XMCD signal at the Fe K-edge.

In the case of the $Y(Fe_{0.9}Ga_{0.1})_2$ compound, Fig. 5.19(a), the Fe K-edge XMCD signal presents the same shape and magnitude as its parent compound YFe_2. This result implies that, contrary to the Fe-Al substitution in the $Ho_{0.5}Lu_{0.5}(Fe_{1-y}Al_y)_2$ series, the 10% of Ga substitution does not provoke a disorder in the magnetic sublattice or a depletion of the Fe($3d$)-R($5d$) hybridization.

Notably, the peak to peak amplitude of the XMCD signal recorded at both Ga K- and Fe K-edges for $Y(Fe_{0.9}Ga_{0.1})_2$ compound is similar for both edges, $\sim$ 0.5% of the absorption jump (see Fig. 5.16 and Fig. 5.19(a) respectively). This is in contrast with the results reported on the Mn compounds, $Ni_{51}Mn_{28}Ga_{21}$ and Mn_3GaC, where the amplitude of the Ga K-edge XMCD is greater than at the Mn K-edge even when Mn, as Fe in our case, carries a localized magnetic moment [129, 130]. In particular, in the case of $Ni_{51}Mn_{28}Ga_{21}$ alloys the amplitude of the dichroic signal at the Ga K-edge is five times greater than at the Mn K-edge [129]. This different behavior can be tentatively ascribed to a larger $p-d$ hybridization at the Fe sites in the present $R(Fe_{0.9}Ga_{0.1})_2$ compounds, than that at the Mn sites in the Mn alloys.

Fig. 5.19 shows the comparison of the Fe K-edge XMCD of pure RFe_2 with that $R(Fe_{0.9}Ga_{0.1})_2$ compounds recorded at T = 5 K. As described in the precedent chapter the Fe K-edge XMCD signal of RFe_2 compounds is

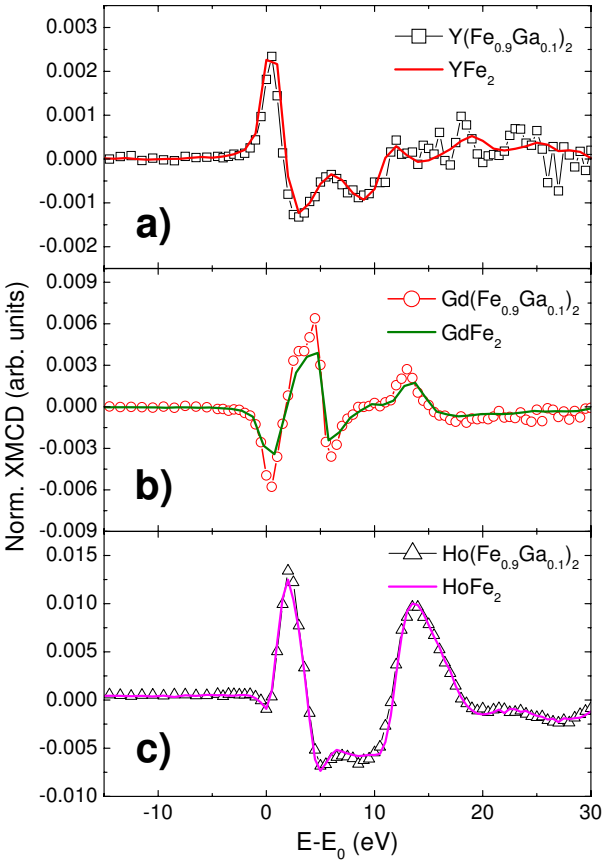

Figure 5.19: XMCD spectra at Fe K-edge recorded at 5 K for: (a) $Y(Fe_{0.9}Ga_{0.1})_2$ and YFe_2, (b) $Gd(Fe_{0.9}Ga_{0.1})_2$ and $GdFe_2$, and (c) $Ho(Fe_{0.9}Ga_{0.1})_2$ and $HoFe_2$ compounds.

composed by two contributions, $XMCD_{Fe}$ and $XMCD_R$, when the rare-earth is magnetic and only by $XMCD_{Fe}$ when the rare-earth is *non-magnetic*. It has been also shown that the substitution of Fe by Al in these RFe_2 compounds provokes a strong modification of both Fe and R contributions. However, in the present case, the substitution of 10% of Fe by Ga does not significantly modify the profile of the dichroic signals with respect to those of RFe_2 compounds. Moreover, the rare-earth contribution to the Fe K-edge XMCD spectra is of the same order for both RFe_2 and $R(Fe_{0.9}Ga_{0.1})_2$ compounds and, therefore, as in the case of RFe_2, the $XMCD_R$ contribution dominates the profile of the whole dichroic signal of $R(Fe_{0.9}Ga_{0.1})_2$ compounds.

Having demonstrated that the rare-earth influences both the Fe and Ga K-edges XMCD spectra, the next step in our study is to attempt the isolation of such rare-earth contribution. Our aim is to compare the rare-earth contri-

bution at both Fe and Ga K-edges for the same $R(Fe_{0.9}Ga_{0.1})_2$ compound in order to know if the magnetic polarization of the rare-earth is different for the $4p$ states of Fe and Ga. To this end we have applied the substraction procedure discussed in the previous chapter. In this way we have considered that the total XMCD signal recorded at the Fe and Ga K-edges can be expressed as the sum of two contributions, in the form: $XMCD(R(Fe_{0.9}Ga_{0.1})_2) = XMCD_R$ - $XMCD_{Fe}$. As done in the precedent chapter, at each Fe and Ga K-edges we have approximate the $XMCD_{Fe}$ contribution of $R(Fe_{0.9}Ga_{0.1})_2$ XMCD spectra as the total XMCD of $Y(Fe_{0.9}Ga_{0.1})_2$. Hence, the $XMCD_R$ contribution at each Fe and Ga K-edges can be extracted as:

$$XMCD_R = XMCD(R(Fe_{0.9}Ga_{0.1})_2) + XMCD(Y(Fe_{0.9}Ga_{0.1})_2).$$

Fig. 5.20 reports the rare-earth contributions obtained after applying this procedure. As shown in each panel of the figure both the spectral profile and the intensity of each $XMCD_R$ extracted signals are rather different at both Fe and Ga K-edges, and also for both Gd and Ho compounds at the same absorption edge. Indeed, the peak to peak amplitude of the Ho contribution at both Fe and Ga K-edges is respectively two and three times greater than the Gd one. In principle, this marked difference can be addressed to the different value of the Gd and Ho $4f$ moments. However, by considering their free-ion values, $\mu_{Ho} \sim 10\ \mu_B$ and $\mu_{Gd} \sim 7\ \mu_B$, the expected factor should be ~ 1.4, smaller than the experimentally observed, ~ 2, at both the Fe and Ga K-edges. These results indicate that in agreement with previous works, the rare-earth contribution is not directly correlated to the magnetization or to the value of the individual R magnetic moments, but it is related to the molecular field acting on the Fe and Ga sites [92].

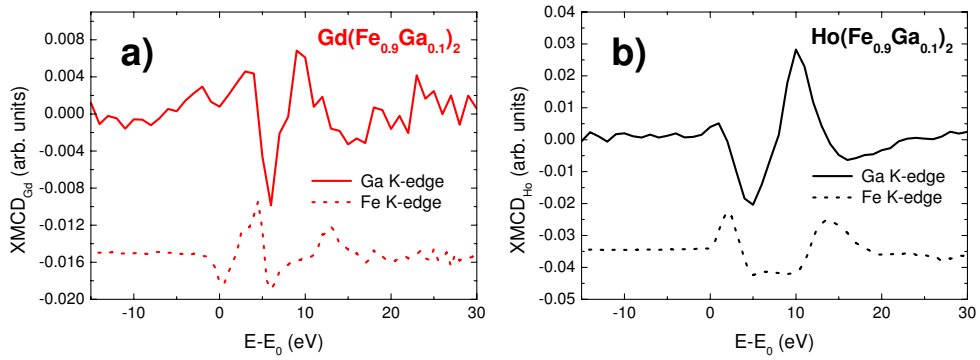

Figure 5.20: Comparison of the $XMCD_R$ extracted contributions at the Fe and Ga K-edges for Gd [panel (a)] and for Ho [panel (b)] compounds (see text for details).

Ge K-edge

In order to get a deeper insight into the magnetic polarization of *non-magnetic* atoms in presence of competing interactions we have synthesized a homologous compound to the $Ho(Fe_{0.9}Ga_{0.1})_2$ one but containing Ge instead of Ga, i. e., $Ho(Fe_{0.9}Ge_{0.1})_2$ compound.

Fig. 5.21 shows the XMCD spectra at the Ge K-edge of $Ho(Fe_{0.9}Ge_{0.1})_2$ at T = 5 K and H = 50 kOe. The presence of a non negligible dichroic signal reflects that there is a magnetic polarization of the 4*p*-states at the Ge site. The XMCD spectra is composed by a negative and a subsequent positive peaks, labeled *D* and *F* by analogy with the Ga K-edge XMCD of $Ho(Fe_{0.9}Ga_{0.1})_2$, which are centered at E-E_0 $\sim$ 3 eV and $\sim$ 8 eV respectively. Lower panel of Fig. 5.21 shows the comparison of the Ge K-edge XMCD spectra of $Ho(Fe_{0.9}Ge_{0.1})_2$ with that of $Ho(Fe_{0.9}Ga_{0.1})_2$ at Ga K-edge. The profile of

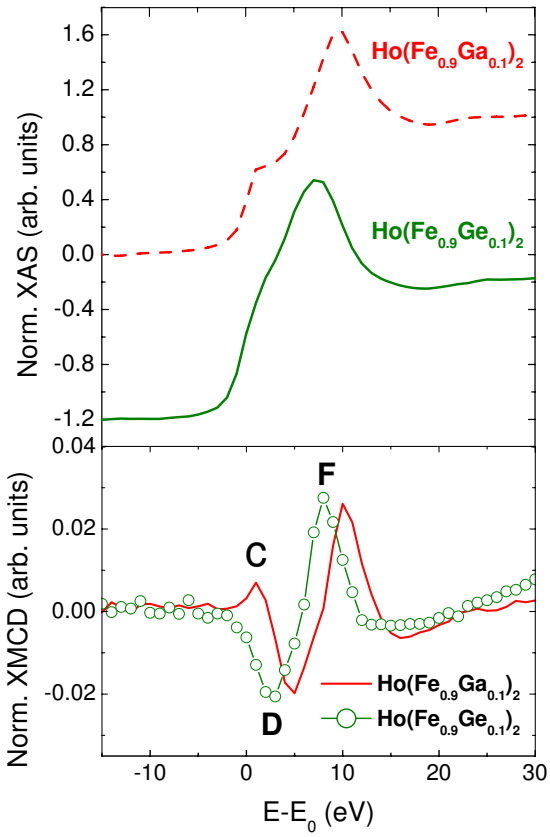

Figure 5.21: Comparison of the XAS and XMCD spectra recorded at the Ga and Ge K-edges for $Ho(Fe_{0.9}Ga_{0.1})_2$ and $Ho(Fe_{0.9}Ge_{0.1})_2$ compounds respectively at T = 5 K and H = 50 kOe.

both signals is similar and, moreover, both dichroic spectra possess similar peak to peak amplitude, $\sim 5\%$ of the absorption jump. Nevertheless, the Ge K-edge XMCD of the $Ho(Fe_{0.9}Ge_{0.1})_2$ compound is shifted ~ 2 eV towards lower energy and, moreover, the small positive peak C which appeared at E-E_0 ~ 1 eV at the Ga K-edge XMCD spectrum of $Ho(Fe_{0.9}Ga_{0.1})_2$ is not observed at the Ge K-edge XMCD of $Ho(Fe_{0.9}Ge_{0.1})_2$. These differences are in agreement with the observed modification of the XAS profile for both Ga and Ge compounds at their respective K-edges (see upper panel of Fig. 5.21).

While the Ga K-edge XAS of $Ho(Fe_{0.9}Ga_{0.1})_2$ shows a well-defined shoulder at the threshold, it is smoothed at the Ge K-edge of $Ho(Fe_{0.9}Ge_{0.1})_2$. This result indicates the different $p-d$ hybridization in both $Ho(Fe_{0.9}Ga_{0.1})_2$ and $Ho(Fe_{0.9}Ge_{0.1})_2$ compounds. On the other hand, the energy shift of the dichroic signal coincides with the energy shift of the white line of the XAS spectra between $Ho(Fe_{0.9}Ge_{0.1})_2$ and $Ho(Fe_{0.9}Ga_{0.1})_2$.

As in the case of $Ho(Fe_{0.9}Ga_{0.1})_2$ compound the Ge $4p$-states might be polarized by the both Fe atoms and magnetic rare-earth ones. Unfortunately, we have not a compound with a *non-magnetic* rare-earth to evaluate the magnetic polarization due solely to the Fe atoms. However, based on the similarity between the spectral shape and amplitude of the dichroic signals of $Ho(Fe_{0.9}Ga_{0.1})_2$ (Ga K-edge) and $Ho(Fe_{0.9}Ge_{0.1})_2$ (Ge K-edge) we can tentatively address, in analogy with the case of Ga compounds, that the Ho contribution to the Ge sites is also the dominant one, determining the profile of the whole dichroic signal.

In order to confirm our hypothesis, we need to know the effect that the substitution of the Fe atoms by Ge ones provokes on the magnetic interactions and, in particular, on the Fe($3d$)-Ho($5d$) hybridization. For this reason we have measured the Fe K-edge XMCD spectra of $Ho(Fe_{0.9}Ge_{0.1})_2$. Fig. 5.22 shows the comparison of the $Ho(Fe_{0.9}Ge_{0.1})_2$ Fe K-edge dichroic signal with those of $Ho(Fe_{0.9}Ga_{0.1})_2$ and $HoFe_2$ compounds. We found that the dichroic signal of $Ho(Fe_{0.9}Ge_{0.1})_2$ matches to that of the $Ho(Fe_{0.9}Ga_{0.1})_2$ and $HoFe_2$. Therefore, we can consider that the $XMCD_{Ho}$ is approximately the same in the three compounds and, as commented above, it dominates the whole dichroic spectra. This result suggest that the substitution of 10% of Fe atoms by Ge or Ga does not provoke drastic changes in the Fe($3d$)-Ho($5d$) hybridization. Therefore, the magnetic polarization scheme at the Fe sites is similar for both $Ho(Fe_{0.9}Ge_{0.1})_2$ and $Ho(Fe_{0.9}Ga_{0.1})_2$ compounds. Because of Fe atoms are replaced by Ga or Ge atoms, the previous assertion supports our idea that the magnetic polarization should be similar for both atoms. As a consequence, similarly to the $Ho(Fe_{0.9}Ga_{0.1})_2$ the Ge K-edge XMCD signal of $Ho(Fe_{0.9}Ge_{0.1})_2$ compound is mainly due to the Ho contribution to the total XMCD.

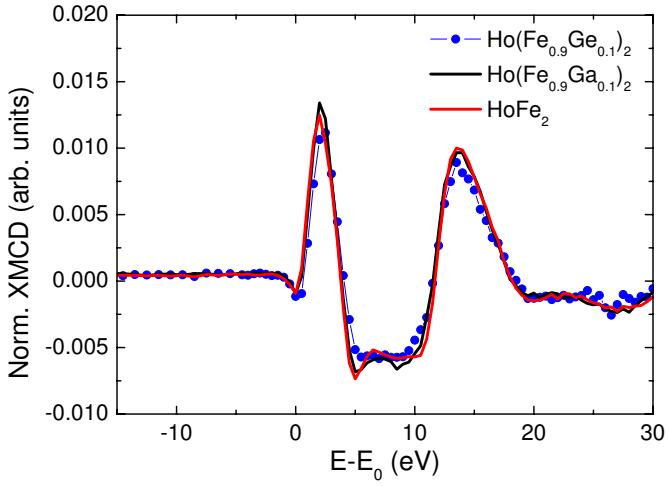

Figure 5.22: Comparison of the Fe K-edge XMCD spectra recorded at T = 5 K for $Ho(Fe_{0.9}Ge_{0.1})_2$, $Ho(Fe_{0.9}Ga_{0.1})_2$ and $HoFe_2$.

5.4 Conclusions

- The present XANES study provides a new insight into the electronic changes induced by the substitution of a magnetic atom by a *non-magnetic* one in the RFe_2 series. We have demonstrated that this effect is quite different as the substitution proceeds at the R or Fe sites. In this way, Fe-Al substitution induces changes at the near-edge region of the spectra, whereas no modification is observed when the magnetic rare-earth (Ho, Er) is substituted by a *non-magnetic* one (Lu, Y). These results point out the Fe substitution by Al leads to the decrease of the R($5d$)-Fe($3d$) hybridization.

- The Fe-Al substitution induces changes at the near-edge region of the spectra, whereas no modification is observed when the magnetic rare-earth (Ho, Er) is substituted by a *non-magnetic* one (Lu, Y). These results indicate that while the substitution of the rare-earth by Lu acts as a simple magnetic dilution effect, the Fe-Al substitution influences the electronic structure of the systems.

- These results have been confirmed from the analysis of the Fe K- and Ho L_2-edge XMCD spectra recorded in the $Ho_{1-x}Lu_x(Fe_{1-y}Al_y)_2$ series that also prove the depletion of the Ho(5d)-Fe($3d$) hybridization.driven by the Fe-Al substitution.

- The study of the Lu $L_{2,3}$-edges XMCD spectra through the $Ho_{1-x}Lu_x(Fe_{1-y}Al_y)_2$ series demonstrate that the appearance of a magnetic moment at the Lu sites is mainly due to the Fe magnetic moments.

- The XMCD study on $R(Fe_{1-x}M_x)_2$ compounds at the Ga and Ge K-edge have proved the existence of a magnetic signal at the *non-magnetic* atoms site. This magnetic polarization is due to the $p-d$ hybridization with the Fe neighbors atoms when the rare-earth is *non-magnetic*. When a magnetic rare-earth is present and additional contribution due to Fe($3d$)-R($5d$) hybridization enhances the magnetic polarization at the M sites.

Chapter 6

Element-Specific Magnetic Hysteresis measurements by using XMCD

As discussed previously, the atomic selectivity of the XMCD technique depends on the localized *vs.* delocalized nature of the final states probed in the photoabsorption process. When these states are localized the XMCD gives information about the magnetic properties of the tuned atomic shell. However, when the final states are delocalized the hybridization effects become important, and the XMCD spectra carries magnetic information not only about the selected atomic species (the photoabsorber) but also of its neighboring atoms.

The possibility of performing element-specific magnetic hysteresis measurements by using XMCD (ESMH) has received great attention in the last years. By tuning the absorption edges of the different atomic species in the material it would be possible to obtain the hysteresis cycle of each magnetic element separately. Accordingly, the role of each element into determining the magnetic properties of the material as the coercive field, magnetic anisotropy, etc, could be determined.

To our knowledge, no discussion has been deserved in the literature regarding the relationship between the absorption edge at which the ESMH cycles are recorded, and the magnetic properties of the atomic species selected. It is inherently assumed that the ESMH cycles obtained for the same atomic species in a given material should be the same no matter the absorption edge tuned. However, the results obtained through this Thesis and a critical re-examination of previous results [131, 132] suggest that this simple view of the ESMH is not correct.

As stressed in the precedents Chapters, the K-edge XMCD of the transition metal in R-T intermetallics carries magnetic information of both T and R atoms. A similar situation is found at the rare-earth L_2-edge in the same materials. However, this is not the case when the localized R($4f$) ($M_{4,5}$-edges) and the T($3d$) ($L_{2,3}$-edges) states are probed in the photoabsorption process. Then, it appears reasonable to expect that the ESMH response at both the K- and $L_{2,3}$-edges of the transition metal should be different, the same holding for the L_2- and $M_{4,5}$-edges of the rare-earth. This proposition is in agreement with previous results obtained at the L_3- [131] and at the K-edges [132] of Co in Fe/Cu/Co multilayers, for which the coercive fields obtained by ESMH differs one order of magnitude. Initially, the discrepancy was addressed to different deposition conditions of the samples, although the macroscopic magnetic behavior was similar in both cases [131, 132]. Our previous results points out that this disagreement might be due to the fact that the ESMH cycles depend not only on the atomic species selected in the XMCD measurements, but also on the particular absorption edge tuned.

To verify the aforesaid possibility we have performed a systematic and detailed experimental study of the ESMH technique capabilities in the case of different intermetallic systems at different absorption edges. To this aim we have selected the following samples: $ErFe_2$, $HoFe_2$, $LuFe_2$, Er_6Fe_{23}, $Er_{0.5}Y_{0.5}Fe_2$ $Ho_{0.5}Lu_{0.5}Fe_2$ and $Ho_{0.75}Lu_{0.25}Fe_2$. We have recorded the ESMH cycles at the Fe K-, R L_2- and Fe L_3-edges. The description of the experimental ESMH measurement methods as well as the procedures followed to normalize the ESMH cycles at the hard (BL39XU beamline) and at the soft (BL25SU beamline) X-ray regions have been already given in Chapter 2.

6.1 ESMH at the Fe K- and R L_2-edges.

We have started our systematic experimental study by measuring different ESMH cycles at the Fe K- and R L_2-edges of different intermetallic compounds. In both absorption edges the final states are delocalized and belong to the conduction band of the system.

The comparison of the XMCD signals recorded at both the Fe K- and at the Er L_2-edge of $ErFe_2$ are shown in Fig. 6.1. In both cases the XMCD spectra have been recorded at T = 5 K and 288 K. To perform the ESMH measurements the energy is fixed to the maximum of each peak of the XMCD spectra and the dichroic signal is recorded by varying the applied magnetic field. Table 6.1 reports on the energy points of the dichroic spectra tuned for measuring the ESMH cycles, as labeled in Fig. 6.1.

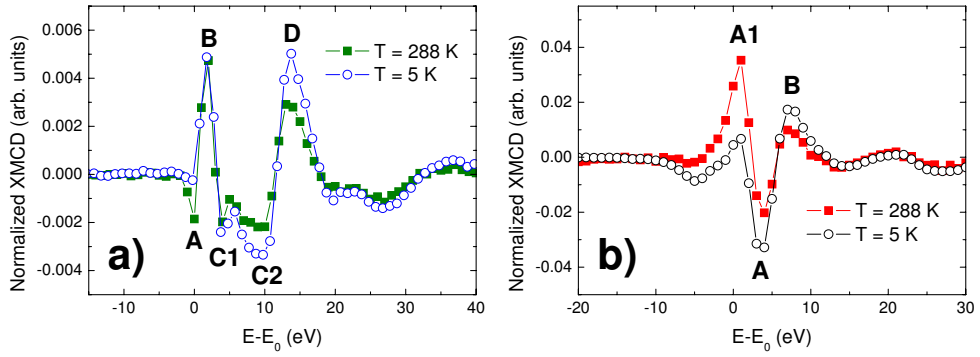

Figure 6.1: XMCD signals of the $ErFe_2$ compound recorded at H = 50 kOe: (a) at the Fe K-edge at T = 5 K (blue, ○) and 288 K (green, ■) and (b) at the Er L_2-edge at T = 5 K (black, ○) and 288 K (red, ■).

Fe K-edge		Er L_2-edge	
A	$\simeq$ 0 eV	A1	$\simeq$ 1 eV
B	$\simeq$ 2 eV	A	$\simeq$ 4 eV
C1	$\simeq$ 4 eV	B	$\simeq$ 7 eV
C2	$\simeq$ 9 eV		
D	$\simeq$ 13.5 eV		

Table 6.1: Energy position of the main dichroic peaks relative to the absorption threshold, $E\text{-}E_0$, as labeled in the Fig. 6.1.

The temperature dependence of the XMCD signals at both absorption edges displays all the hallmarks of the hybridization effects described in precedent Chapters. Accordingly, the Fe dichroic contribution at both Fe K- and R L_2-edges XMCD spectra is mainly limited to the absorption threshold (peaks *A* and *A*1), whereas the features at higher energies are mainly due to the R contribution.

The simplest interpretation of the R-Fe ESMH cycles is the following: (1) for a given element, R or Fe, the ESMH cycles are identical irrespective of the tuned absorption edge, and (2) they reflect the magnetic properties of the probed element. In this way, the ESMH cycles recoded at the Fe K- and L_3-edges would reflect the soft anisotropic character of the Fe sublattice, whereas the ESMH cycle recorded at the R L_2-edge will reflect the strong anisotropic character of the R sublattice.

According to this hypothesis, it is plausible that the ESMH loops recorded at different energy points of a single XMCD spectrum differs depending on which magnetic sublattice dominates the XMCD signal ($XMCD_{Fe}$ or $XMCD_R$)

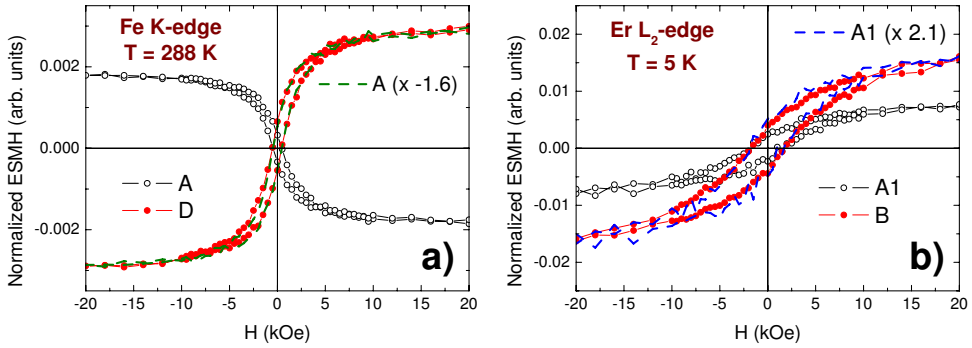

Figure 6.2: ESMH cycles of $ErFe_2$ recorded at different energy points of the XMCD signal: (a) A (black, ○) and D (red, ●) at the Fe K-edge and (b) $A1$ (black, ○) and B (red, ●) at the Er L_2-edge. For the sake of comparison some ESMH curves have been scaled (dotted lines in both panels).

at the selected energy.

We have assessed the above possibility by recording the ESMH cycles at the peaks A and D of the Fe K-edge, ESMH(A) and ESMH(D), and at the peaks $A1$ and B of the Er L_2-edge, ESMH($A1$) and ESMH(B) (see Fig. 6.1). They are compared in Fig. 6.2. Since the ESMH cycles reflect the intensity and the sign of the dichroic features, we have scaled and oriented the ESMH cycles with respect to that of the greatest amplitude, for the sake of comparison. After scaling, a perfect match of the ESMH cycles recorded at different points of the same absorption edge is obtained. That is, the ESMH cycles of $ErFe_2$ do not present any change of shape or coercive field when they are recorded at different points of the XMCD spectra. **This result points out that both the Fe and Er contributions to the total ESMH spectra exhibit the same magnetic field dependence at a given absorption edge, regardless the energy point probed.**

In order to extend the validity of the obtained results for $ErFe_2$ to other R-Fe intermetallic compounds we have performed the same comparison on $Ho_{0.5}Lu_{0.5}Fe_2$, $HoFe_2$, $Er_{0.5}Y_{0.5}Fe_2$ and Er_6Fe_{23} compounds. This is shown in Fig. 6.3 where the ESMH cycles[1] recorded at different energy points of the Fe K-edge XMCD spectrum of $Ho_{0.5}Lu_{0.5}Fe_2$ (a), $HoFe_2$ (b), $Er_{0.5}Y_{0.5}Fe_2$ (c) and Er_6Fe_{23} (d)[2] are compared. The cycles measured at different energy points exhibit, for each compound, similar shape and coercive field, confirming the results previously found in $ErFe_2$ at the Fe K-edge. Hence, these results

[1]For the sake of comparison, the ESMH cycles displayed have been scaled as in the case of $ErFe_2$.

[2]In the case of Er_6Fe_{23} compound a single peak C, E-E_0 $\simeq$ 6.5 eV, appears at the Fe K-edge XMCD signal instead of the characteristic features $C1$ and $C2$ present for RFe_2.

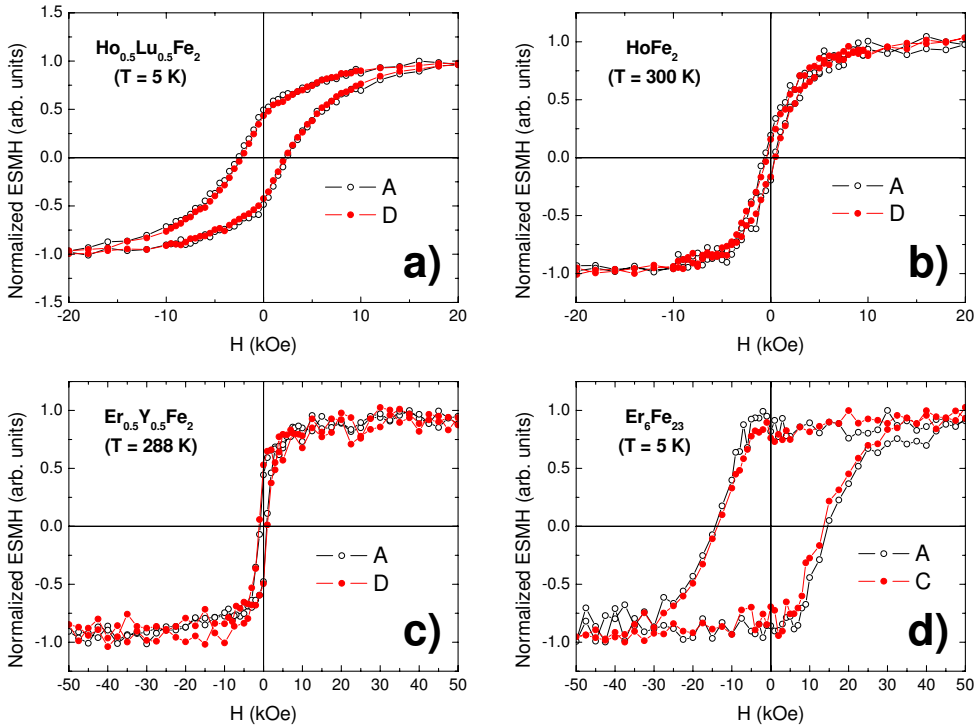

Figure 6.3: ESMH cycles recorded at the points A (black, ○) and C or D (red, ●) of the Fe K-edge XMCD spectrum of $Ho_{0.5}Lu_{0.5}Fe_2$ (a), $HoFe_2$ (b), $Er_{0.5}Y_{0.5}Fe_2$ (c) and Er_6Fe_{23} (d).

indicate that, in all the studied compounds, the coercive field of the ESMH cycle is always the same, irrespective of the chosen measuring energy point.

The anisotropy field, and thus the coercivity, varies with the temperature. Consequently, further confirmation to these results can be obtained by studying the ESMH cycles recorded at different temperatures. This is illustrated in Fig. 6.4 where the comparison of the Fe K-edge ESMH cycles of $ErFe_2$ recorded at T = 5 K and 288 K is shown. The ESMH cycle recorded at T = 288 K exhibits lower coercivity than at T = 5 K. Despite the Fe K-edge is tuned, this result indicates that the temperature evolution of the ESMH cycles reflects the enhancement of the magnetic anisotropy of the whole system upon cooling, which is mainly due to the temperature dependence of the rare-earth sublattice. These experimental findings point out that the magnetic field dependence of the magnetic moments of the Fe($4p$) states greatly differs from that expected for the localized $3d$ moments of Fe.

Similar behavior is found for the rare-earth $5d$ states probed at the rare-earth L_2-edge. As shown in Fig. 6.5, the ESMH cycles exhibit the same coercive field for each compound, regardless the energy point chosen. In some

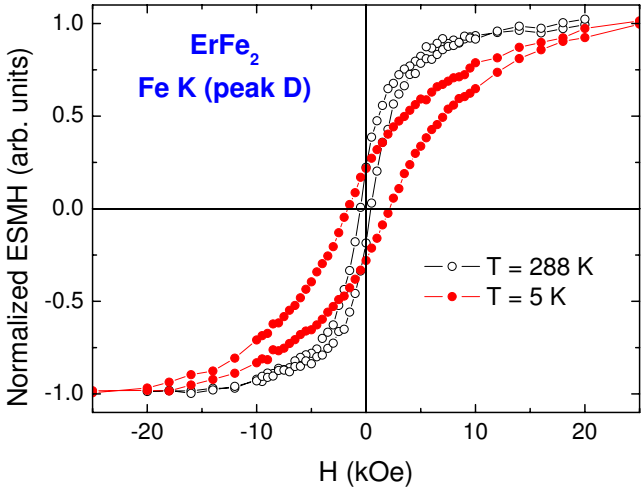

Figure 6.4: Comparison of ESMH cycles for the $ErFe_2$ compound recorded at the Fe K-edge at T = 5 K (red, •) and 288 K (black, ○).

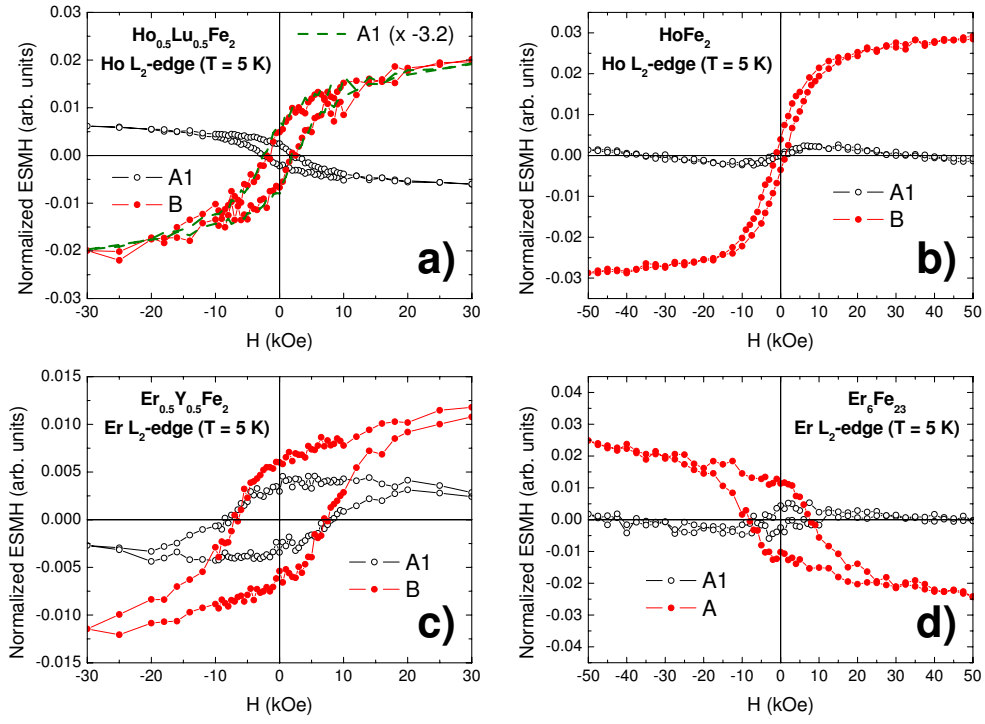

Figure 6.5: ESMH cycles recorded at the points $A1$ (black, ○) and A or B (red, •) of the Ho and Er L_2-edges XMCD spectrum of $Ho_{0.5}Lu_{0.5}Fe_2$ (a), $HoFe_2$ (b), $Er_{0.5}Y_{0.5}Fe_2$ (c) and Er_6Fe_{23} (d).

cases the shape, not the coercive field, of the ESMH cycles is different depending on the energy point measured. This is due to the unusual behavior of the ESMH cycles recorded at point $A1$, when XMCD is almost zero at this point. A detailed explanation of this unusual behavior is given in the Appendix A.

These results suggest that the magnetic field dependence of the conduction states, Fe($4p$) and R($5d$), in R-Fe intermetallics does not correspond to that of the localized magnetic moments, Fe($3d$) and R($4f$), respectively. On the contrary, **the obtained results point out that, due to the R-Fe hybridization, the conduction states do not reflect the magnetic properties of the localized Fe($3d$) and R($4f$) magnetic moments separately, but those magnetic properties resulting from the coupling of Fe and R.**

Further confirmation of these results can be obtained by comparing the ESMH cycles of R-Fe compounds showing a great variation of their coercive and anisotropy field properties. To this end we have performed a direct comparison of the ESMH cycles measured at both Fe K- and R L_2-edges at T = 5 K, see Fig. 6.6, for: $ErFe_2$, $HoFe_2$, $Er_{0.5}Y_{0.5}Fe_2$, $Ho_{0.5}Lu_{0.5}Fe_2$ and Er_6Fe_{23}. The coercive field values are reported on Table 6.2. In the case of the RFe_2 compounds the ESMH cycles recorded at both Fe K- and R L_2-edges can be superimposed. However, the ESMH cycles recorded at both edges show differences that increases as the hardness does. In particular, the greatest differences are found in the case of the Er_6Fe_{23} compounds for which the ESMH cycle recorded at the Fe K-edge is significantly *harder* than the Er L_2-edge one.

Samples	H_C (Oe)	
	Fe K-edge	R L_2-edge
$ErFe_2$	1900	1800
$Er_{0.5}Y_{0.5}Fe_2$	7800	6000
Er_6Fe_{23}	13200	8000
$HoFe_2$	1100	1300
$Ho_{0.5}Lu_{0.5}Fe_2$	2500	2300

Table 6.2: Coercive fields values, in Oe, of the Fe K- and R L_2-edges ESMH cycles displayed in Fig. 6.6.

This behavior might be understood in terms of the different degree of localization/delocalization of the $4p$ and $5d$ states. Despite they belong to the conduction band, the density of the $5d$ states is mostly localized at the rare-earth sites while the Fe $4p$ states are rather delocalized. As discussed in Chapter 5, this is the reason why the rare-earth $L_{2,3}$- absorption edges

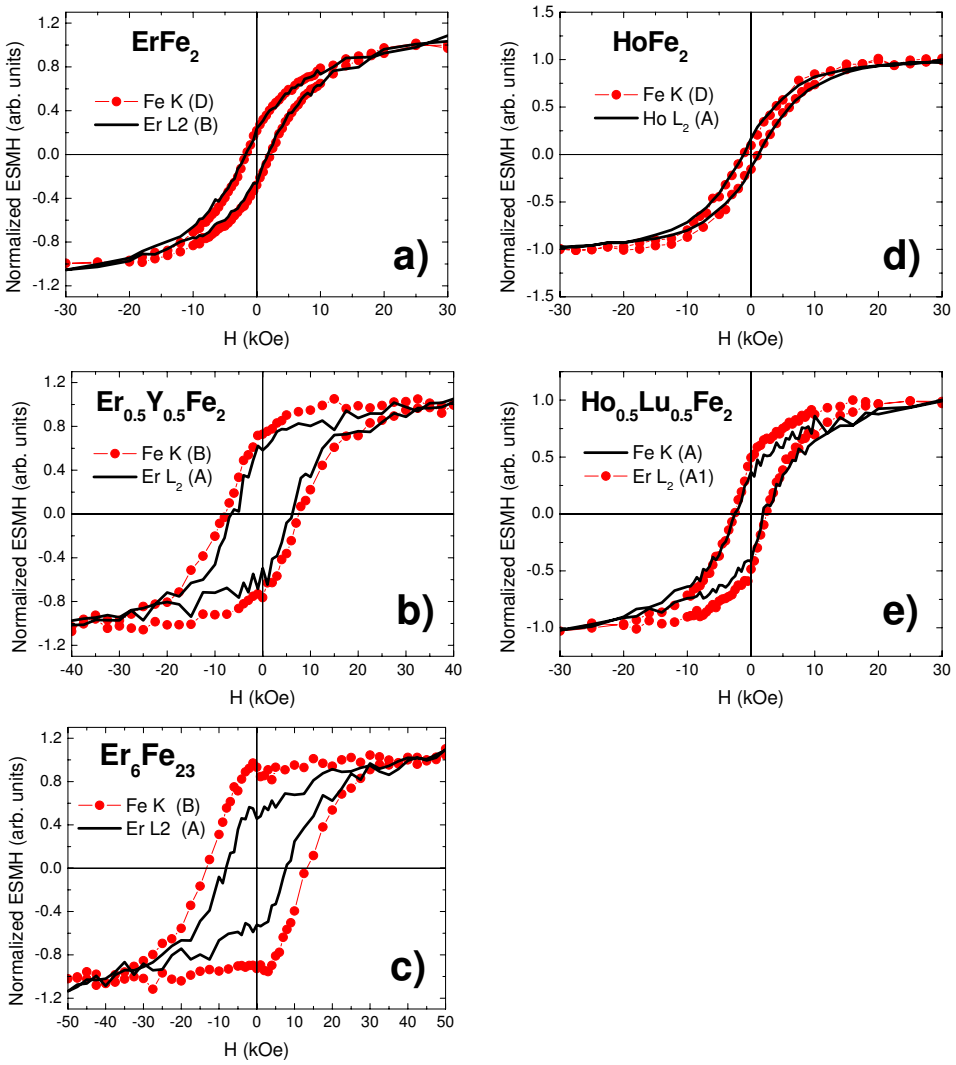

Figure 6.6: ESMH cycles recorded at the Fe K (red, •) and Er L_2 (black solid line) edges at T = 5 K on: (a) $ErFe_2$, (b) $Er_{0.5}Y_{0.5}Fe_2$, (c) Er_6Fe_{23}, (d) $HoFe_2$ and (e) $Ho_{0.5}Lu_{0.5}Fe_2$.

exhibit sharp white lines at the threshold that are absent in the case of the rare-earth L_1- and transition metal K-edge absorption. The different degree of localization is also reflected in the relative importance of the crossed contributions to the XMCD discussed in the precedent Chapter. In the case of the rare-earth L_2-edge, despite there is an iron contribution to the spectrum, the spectral shape is always dominated by the rare-earth sublattice due to the strong $4f - 5d$ intra-atomic interaction. By contrast, the contribution of the rare-earth to the Fe K-edge XMCD is sometimes as large as to determine the

spectral shape. These results suggest that, while the response of the R($5d$) states to the applied magnetic field resembles that expected for the $4f$ magnetic moments, the Fe($4p$) states acquires a hardness that is not associated to the localized Fe($3d$) states but to the R-Fe hybridization.

6.2 ESMH at the Fe L_3-edge

The conclusions derived in the precedent section suggest that the ESMH cycles recorded for the Fe conduction states (K-edge) should be similar to the macroscopic ones, in the sense that they are influenced by the hybridization between the R and Fe sublattices. In contrast, the ESMH recorded for the localized $3d$ states ($L_{2,3}$-edges) should reflect the atomic-like magnetic properties of Fe, provided that these states are less affected by the hybridization. In order to verify this hypothesis we have extended our ESMH study to the $L_{2,3}$-edge of Fe.

To this end we have measured both the XAS and the XMCD spectra at the Fe $L_{2,3}$-edges in the case of YFe_2, $HoFe_2$ and $Ho_{0.75}Lu_{0.25}Fe_2$ compounds. In all cases the ESMH cycle has been recorded at the energy of the maximum of the Fe L_3-edge dichroic signal, E $\sim$ 708 eV. The results of the measurements performed at T = 20 K and under a magnetic field of H = 20 kOe are shown in Fig. 6.7, and the coercive field values obtained are reported in Table 6.3. This comparison shows how the hardness of the compounds increases as the content of the magnetic rare-earth (Ho) does.

However, what is really important to note is the fact that the maximum coercive field obtained, 400 Oe for $HoFe_2$, is significantly smaller than that obtained by measuring the ESMH cycle at the Fe K-edge on the same compound (1100 Oe). This is also illustrated in Fig. 6.8, where the Fe K- and Fe L_3-edges ESMH cycles recorded at low temperature, T = 5 and 20 K, respectively, are directly compared. The difference in the obtained H_C cannot be ascribed to the different measuring temperatures [64].

These results confirm the hypothesis posed in the previous section. Accordingly, the ESMH cycles recorded for the Fe conduction and localized states shows different magnetic hardness behavior. Indeed, these results suggest that the magnetic rare-earth transfers, through the R-Fe hybridization, the magnetic hardness to the conduction band states whereas those more localized (Fe $3d$-states) remains nearly unvaried, i.e., $L_{2,3}$-edges should mainly reflect the atomic-like magnetic properties of Fe.

More importantly, the comparison of the ESMH cycles recorded for the Fe K- and Fe L_3-edges for $LuFe_2$ (T = 5 K) and YFe_2 (T = 20 K) respectively,

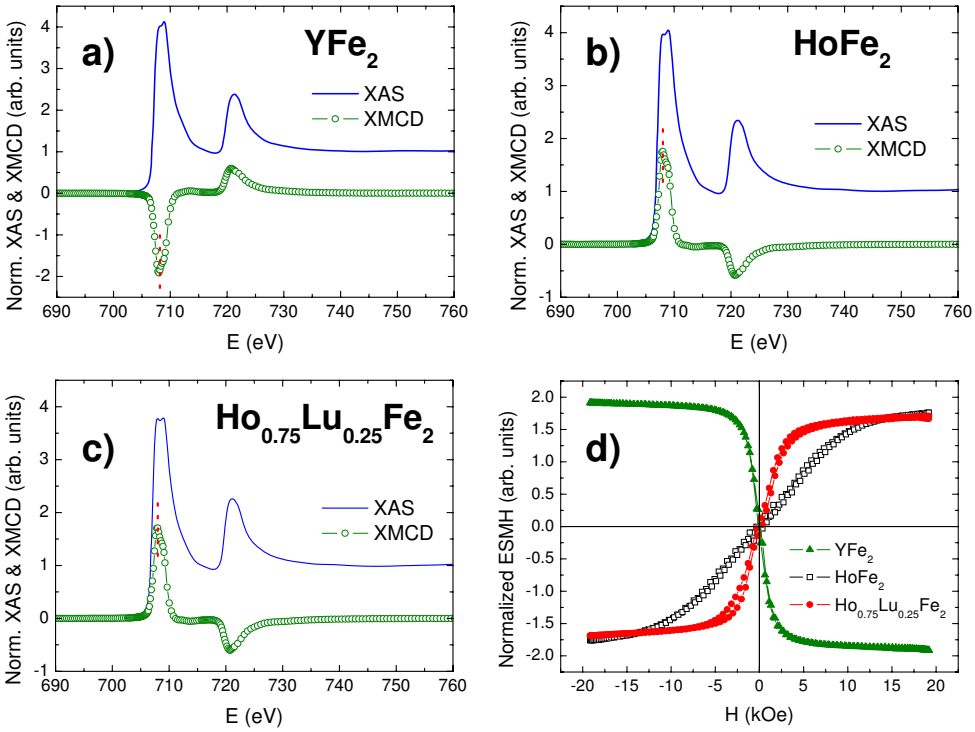

Figure 6.7: Fe $L_{2,3}$-edges XAS and XMCD spectra recorded at T = 20 K and H = 20 kOe for: YFe_2 (a), $HoFe_2$ (b) and $Ho_{0.75}Lu_{0.25}Fe_2$ (c). Panel (d): ESMH cycles measured at the maximum of the Fe L_3-edge dichroic signal for: YFe_2 (olive, ▲), $HoFe_2$ (black, □) and $Ho_{0.75}Lu_{0.25}Fe_2$ (red, ●).

Sample	H_C (Oe)	
	Fe L_3-edge (T = 20 K)	Fe K-edge (T = 5 K)
YFe_2	100	–
$LuFe_2$	–	250
$HoFe_2$	400	1100
$Ho_{0.75}Lu_{0.25}Fe_2$	250	–

Table 6.3: Comparison of the coercive field, H_C in Oe, of the ESMH cycles recorded at the Fe L_3- and Fe K-edge.

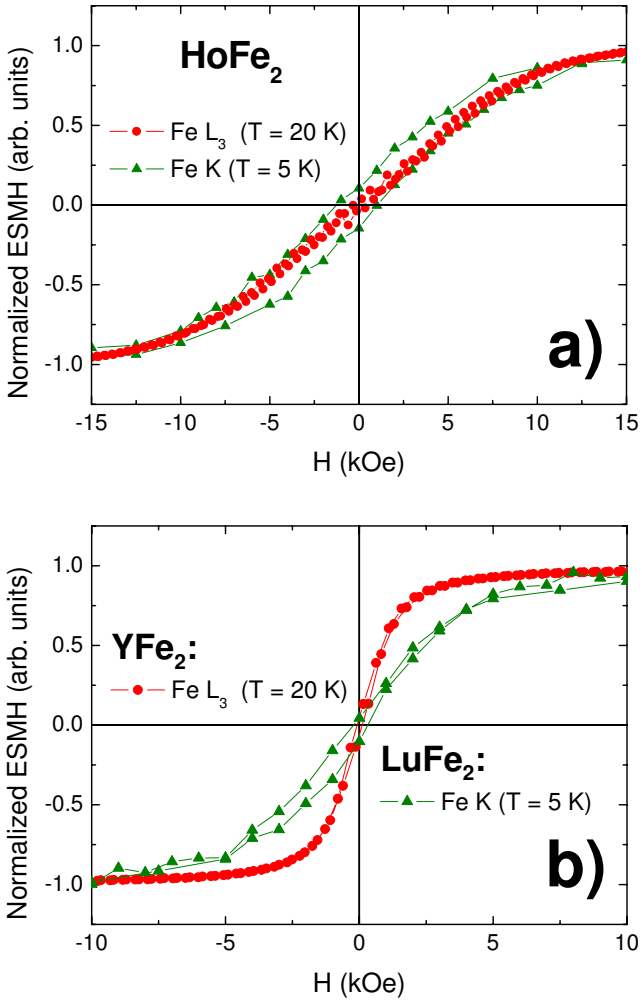

Figure 6.8: Comparison of the ESMH cycles recorded at Fe K- and Fe L_3-edges for (a) $HoFe_2$ and, (b) $LuFe_2$ and YFe_2 (see text for details).

i.e., for compounds in which the rare-earth is non-magnetic, yields coercive fields of the same order of magnitude, see Table 6.3, although, the magnitude of the H_C obtained from the Fe K-edge is more than twice the value obtained at the Fe L_3-edge. These results prove that for a same atomic species the magnetic hardness properties of its localized and delocalized states is different as the magnetocrystalline anisotropy associated with the $4p$ and $3d$ magnetic moments is. Consequently, our results suggest that the controversial issue of finding different ESMH properties for the same material depending which absorption edge is tuned [131, 132] is an intrinsic property of XMCD due to its shell-symmetry selectivity and it is not due to different sample conditions.

6.3 Comparison of the ESMH and macroscopic hysteresis cycles

At this point it is mandatory to investigate how the ESMH cycles compare with the macroscopic magnetization hysteresis loops obtained by using a SQUID magnetometer. Hereafter, the macroscopic hysteresis cycles will be simply labeled as "SQUID" cycles.[3]

Fig. 6.9 shows the comparison of the Fe K-edge ESMH with the SQUID cycles for $ErFe_2$ recorded at T = 5 K and 288 K. The coercive fields are reported on Table 6.4. The ESMH cycle recorded at T = 288 K exhibits lower magnetic hardness than at T = 5 K due to the influence of the magnetic rare-earth. Indeed, the similar temperature dependence found in the case of SQUID

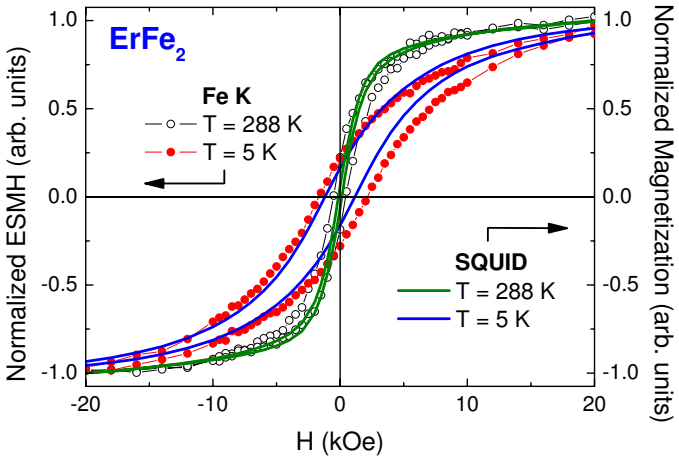

Figure 6.9: Comparison of ESMH cycles for the $ErFe_2$ compound recorded at the Fe K-edge at T = 5 K (red, •) and 288 K (black, ○). M(H) hysteresis curves measured by using a SQUID magnetometer at T = 5 K (blue solid line) and 288 K (green solid line) have been included (see text for details).

		H_C (Oe)	
	T (K)	ESMH	SQUID
$ErFe_2$	5	1900	1200
	288	500	150

Table 6.4: Coercive field, H_C, extracted from ESMH cycles and M(H) hysteresis loops displayed in Fig. 6.9.

[3]For the M(H) measurements we have used the same specimen of sample, powder spread onto adhesive tape (*film*), and the same geometry as for the XMCD measurements.

Samples	ESMH		SQUID	ESMH
	Fe K-edge (5 K)	R L_2-edge (5K)	FILM (5 K)	Fe L_3-edge (20 K)
$ErFe_2$	1900	1800	1200	–
$Er_{0.5}Y_{0.5}Fe_2$	7800	6000	5500	–
Er_6Fe_{23}	13200	8000	3400	–
$HoFe_2$	1100	1300	600	400
$Ho_{0.5}Lu_{0.5}Fe_2$	2500	2300	700	–
YFe_2	–	–	–	100
$LuFe_2$	250	–	25	–

Table 6.5: Coercive field values, in Oe, recorded at T = 5 K of the ESMH and SQUID cycles displayed in Fig. 6.6.

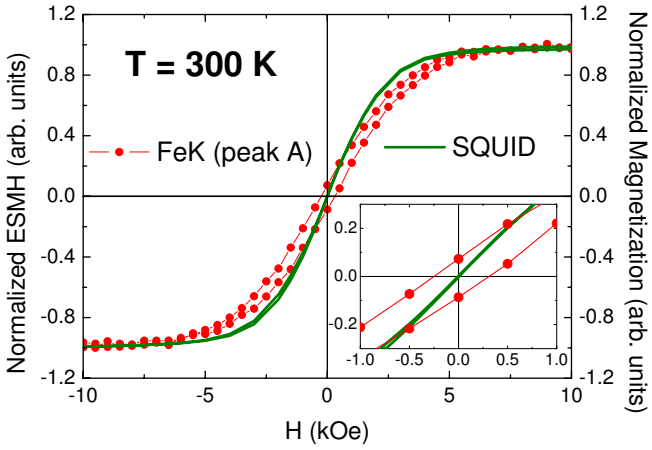

Figure 6.10: Comparison of the ESMH cycles and the M(H) hysteresis curves measured for $LuFe_2$ compound at T = 300 K. Inset show an enlarged view of the region close to zero magnetic field.

cycles is easily accounted for in terms of the enhancement of the anisotropy field associated to the rare-earth magnetic sublattice.

In all the investigated cases we have found that the ESMH cycles recorded at the Fe K-edge and those at the SQUID exhibit similar characteristics, being the obtained coercivity greater than for the ESMH cycles recorded at the L_3-edge (see Table 6.5). These results confirm the conclusions reached in the previous sections regarding the different magnetic hardness properties of both localized and delocalized states in the same atomic species.

We would like finally to note that despite H_C of both Fe K-edge and SQUID

ESMH cycles is similar, it is always greater in the case of the XMCD cycles.[4] In order to verify this result we have performed a similar comparison for $LuFe_2$, i.e., for a compound with no magnetic rare-earth. As shown in Fig. 6.10, in this case the coercive field obtained from the Fe K-edge XMCD measurements is also greater than the SQUID one.

Finally, Fig. 6.11 illustrates that the difference between the SQUID cycles and the ESMH increases as the magnetic hardness of the compound does. As shown in Fig. 6.11 this difference follows the same trend as that found in the comparison of the Fe K- and R L_2-edges ESMH discussed in the precedent section, see Fig. 6.6, as corresponding to the different magnetic hardness properties of the rare-earth $5d$ and Fe $4p$ states.

[4]Some authors have attributed the enhancement of the anisotropic character of the ESMH cycles to the effect of the demagnetizing field [133]. However, we have measured the magnetization by using the same specimen (film samples) as in the XMCD measurements and, moreover, by using the same experimental geometry in both cases. Hence, the differences observed between ESMH and SQUID cycles can not be due to demagnetizing effects.

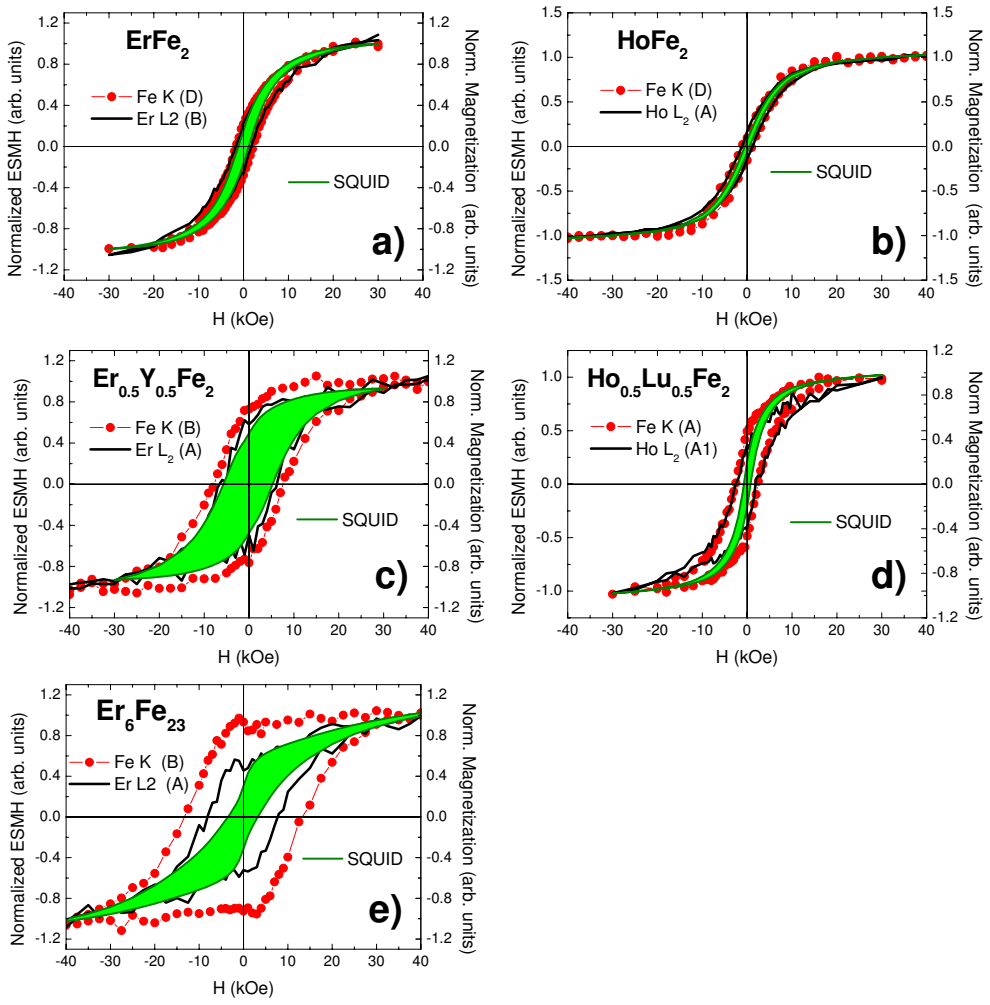

Figure 6.11: Comparison of the Fe K- and R L_2-edges ESMH and SQUID cycles recorded at T = 5 K for $ErFe_2$ (a), $HoFe_2$ (b), $Er_{0.5}Y_{0.5}Fe_2$ (c), $Ho_{0.5}Lu_{0.5}Fe_2$ (d) and Er_6Fe_{23} (f).

6.4 Conclusions

- We have demonstrated that the coercive fields of the ESMH cycles recorded at different energy points of the XMCD spectrum do not vary neither at the Fe K- nor the R L_2-edges in all the studied compounds.

- The temperature variation of the ESMH cycles recorded at the Fe K-edge reflects the enhancement of the magnetic anisotropy of the whole system upon cooling, which is mainly due to the temperature dependence of the rare-earth sublattice. These experimental findings point out that the magnetic field dependence of the magnetic moments of the Fe $4p$ states greatly differs from that expected for the localized $3d$ moments of Fe.

- The coercive field obtained by measuring the ESMH cycle at the Fe K-edge is always greater than the obtained H_C at the L_3-edge.

- These results suggest that the magnetic field dependence of the conduction states, Fe($4p$) and R($5d$), in R-Fe intermetallics does not correspond to that of the localized magnetic moments, Fe($3d$) and R($4f$) respectively. On the contrary, the obtained results point out that due to the R-Fe hybridization the conduction states acquire those magnetic properties resulting from the coupling of the Fe and R sublattices and not of the localized Fe($3d$) and R($4f$) magnetic moments separately.

- Consequently, our results suggest that the controversial issue of finding different ESMH properties for the same material depending which absorption edge is tuned is an intrinsic property of XMCD due to its shell-symmetry selectivity and it is not due to difference sample conditions.

Chapter 7

Design and development of an XMCD set-up at BL25-A–SpLine beamline.

We have shown in the precedent Chapters the capabilities of the XMCD technique as an outstanding tool to study magnetism. The exceptional possibilities presented by XMCD has attracted the interest of the scientific community working on magnetism. As a result the number of researchers who request XMCD measurements is growing as the capabilities of the technique does. However, the number XMCD dedicated beamlines available are limited. To overcome this difficulty we have proposed a different approach. We have explored the possibility of performing XMCD measurements on an adapted X-ray absorption spectroscopy (XAS) standard beamline.

7.1 Background

The existence of birefringence and polarized light has been known after Huygens when he discovered the double refraction property from a calcite crystal [134]. Subsequently, Faraday found that the plane of polarization is rotated when linearly polarized light is transmitted through glass with a magnetic field applied parallel to the propagation direction [135]. This phenomenon is called *Faraday effect* and constituted the first demonstration that magnetism and light are conected. Years after, Kerr observed the change of light polarization upon reflection from a magnetic material [136], that is known as magneto-optical *Kerr effect* (the so-called MOKE). These early experiments opened the door for future investigations of the magnetic properties of matter

by using electromagnetic radiation.

At this point, it is convenient to introduce the concept of dichroism:

> *Dichroism is the property of a sample to absorb or emit with different cross-section photon beams with different polarization. Linear dichroism is for two mutually perpendicular polarization of light, whereas circular dichroism concerns the difference of absorption between right and left polarized photons. This difference is due to the breaking of spherical symmetry of the absorbing atoms: it may be a structural anisotropy of the electronic density of the material and, in that case, the dichroism is natural, or it may be a magnetic anisotropy (for ferro- or ferrimagnetic compounds), and the dichroism is magnetic. From Ref. [137].*

Nowadays the Kerr effect forms the basis of the magnetooptical recording technology by utilizing powerful and small semiconductor lasers. Moreover, it is a powerful research tool for the study of modern magnetic materials, typically in the form of thin films. Scanning and imaging Kerr microscopy gives microscopic information with a resolution near the diffraction limit of light (about 200 nm). This diffraction limit is one of the Achilles' heals of visible light (and lasers) for the study of matter. The other one is the strong absorption of visible light by matter, making it difficult to look into or through many bulk materials. In principle, these limitations were overcome by Wilhelm Conrad Röntgen's discovery of X-rays in 1895 [138] but the use of X-ray for the study of magnetic materials had to wait for nearly another century.

In the visible range one typically uses linearly polarized light and measures the polarization rotation and ellipticity of the transmitted or reflected light. Optical methods rely on spin dependent transitions between valence band states at certain wave-vector (k) points in the Brillouin zone. In contrast, X-ray techniques utilize core to valence transitions. The resonant X-ray signal is element and even chemical state specific since core level binding energies depend on the atomic number and chemical state. Finally, as dimensions enter into the nanoscale, typically identified with dimensions below 100 nm, visible light becomes "blind" and one needs shorter wavelength, X-rays, to see the magnetic *nanoworld*. Despite the power of optical techniques for magnetic studies, we have already mentioned limitations set by the wavelength and energy of light. Today's most powerful applications of X-rays in magnetism utilize fully polarized and tuneable synchrotron radiation, where the X-ray energy is tuned to the absorption edge of a magnetic atom.[40]

As commented above, the use of X-rays for studies of the magnetic properties of matter is more than a simple extension of laser-based investigation because it offers unique capabilities. Indeed, the main general features of X-ray absorption spectroscopy (XAS) are:

(a) the absorption spectrum is element specific: the inner-shell absorption step occur at X-rays energies characteristics of the absorbing element, therefore the individual element absorption spectra can be obtained in samples containing a complex chemical mixture of different elements simply by changing the X-ray wavelength;

(b) by tuning the X-ray energy one can not only select specific elements in the sample but to select different absorption edges for the same atoms, i.e., select the final-state symmetry.

Therefore, since dichroic effects in XAS are associated with the fine structure near core-level absorption edges, one can, through X-rays, study the magnetic properties of a complex material element by element. Moreover, different edge of the same elements provide information on the magnetic contributions of different kinds of valence electrons through the dipole selection rules (see Chapter 1).

The interaction of photons with the absorbing atoms can be treated in the frame of the electric dipole approximation and, in some cases, in the quadrupole one. Because the dipole operator only acts on space variables, the spin moment of the atom is only indirectly involved in the transition of the photoelectron by the spin orbit interaction. For this reason, to observe XMCD it is necessary to satisfy three conditions: the **photons must be circularly polarized**, the material must possess a magnetic moment, and the spin-orbit interaction must be present.

7.1.1 Polarized X-rays

Before continuing the dissertation about polarized X-rays, it is mandatory to emphasized the importance of the sign convention for circularly polarized light. In Chapter 1, we commented that the sign convention used through this Thesis was the one employed in high energy physics which consider the "handedness" of E-vector circulation viewed from the source.[1] Here, we are going to explain in detail some basic concepts about light polarization.

Firstly, we choose the X-ray propagation direction k along $+z$, so that the electric field vector lies somewhere in the x, y plane of our coordinate system. We describe the electric and magnetic fields of an EM wave traveling in the direction of the wavevector $k = (\omega/c)k_0$ as

$$E(r,t) = \epsilon_p E_0 e^{i(k\cdot r - \omega t)} \tag{7.1}$$

[1] Contrary to the *optical* sign convention which consider the handedness view toward the source.

and

$$B(r,t) = \frac{1}{c}(k_0 \times \epsilon_p)E_0 e^{i(k\cdot r-\omega t)} \tag{7.2}$$

Here ϵ_p is a unit polarization vector, which is real for linear polarized waves and complex for circularly polarized waves as we will discussed below. In Fig. 7.1 are exemplified both the electric field vector E and the magnetic field vector B for a linearly polarized electromagnetic wave.

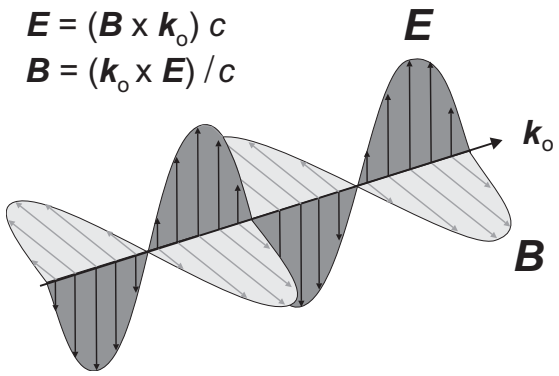

Figure 7.1: Amplitude and phase of a linearly polarized electromagnetic wave. The electric field vector, E, characterizes the polarization direction. Extracted from Ref. [40].

For circularly polarized light, E rotates in space and time and the end-points of E move on a circle, therefore the x and y components have equal magnitudes but are phase shifted relative to each other by $\pi/2$. The constant phase relationship of the two linear components therefore creates a coherent superposition as:

$$\epsilon_x \pm i\epsilon_y = \epsilon_x + e^{\pm\, i\phi/2}\epsilon_y \tag{7.3}$$

The two different linear combinations are commonly referred to as **left** and **right** circular polarization. The two complex circular states are also orthogonal and can be used as alternative basis states for the description of polarization. We define the rotation sense of the circularly polarized waves, described by Eq. (7.3), as depicted in Fig. 7.2. When the thumb points in the direction of $z \parallel k$ we determine the rotation sense of the E-vector in time according to the right or left hand rules, as shown in Fig. 7.2. When the right hand rule applies, we call the wave **right circular** (RCP). Similarly, we call a wave that follows the left hand rule **left circular** (LCP).

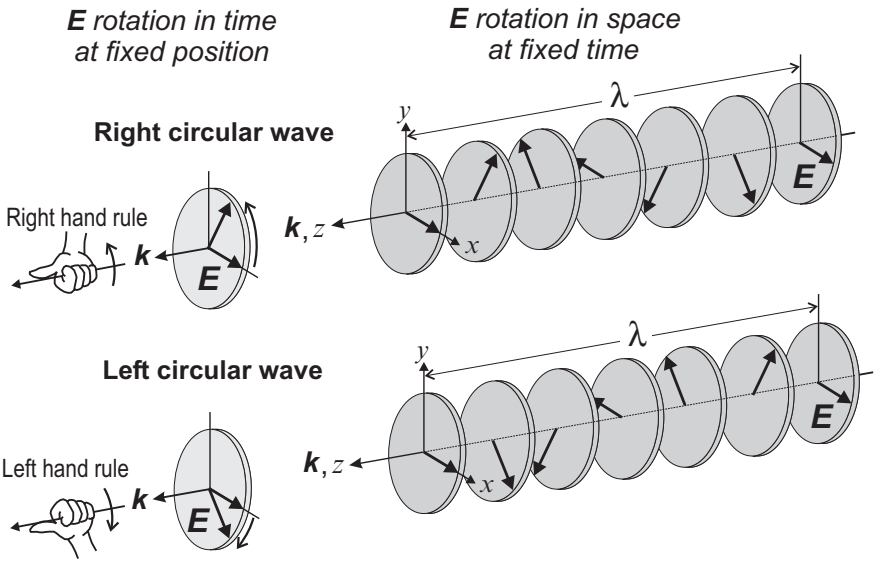

Figure 7.2: Definition of the rotation sense of the E-vector in space and time for right and left circularly polarized waves. See details in the text. Extracted from Ref. [40].

Mathematically, our definition corresponds to the following circular polarization basis states. A RCP wave is described by

$$E_{RCP}(z,t) = -\frac{1}{\sqrt{2}}(\epsilon_x + i\epsilon_y)E_0 e^{i(k\cdot z-\omega t)+i\phi_0} \tag{7.4}$$

and a LCP wave has the form

$$E_{LCP}(z,t) = \frac{1}{\sqrt{2}}(\epsilon_x - i\epsilon_y)E_0 e^{i(k\cdot z-\omega t)+i\phi_0} \tag{7.5}$$

where ϕ_0 defines the phase of the waves at $kz = \omega t = 0$ and it does not affect the relative phase shift of $\pm\pi/2$ between the two linear components.

On the other hand, the angular momentum of an electromagnetic wave is defined as the projection of the angular momentum vector L along the photon propagation direction k, taken to be the z-axis, i.e., the angular momentum expectation value $<L_z>$. To calculate $<L_z>$ it is necessary to describe the motion of the E vector in the x, y plane in terms of the well-known spherical harmonics $Y_{l,m}$ for $l = 1, m = \pm 1$ [40]. This leads to obtain $< L_z >= +\hbar$ for the wave $E_{RCP}(z,t)$ and $< L_z >= -\hbar$ for $E_{LCP}(z,t)$ one. Fig. 7.3 shows the relation between both the handedness of rotation of E-vector and the sense of the angular momentum L.

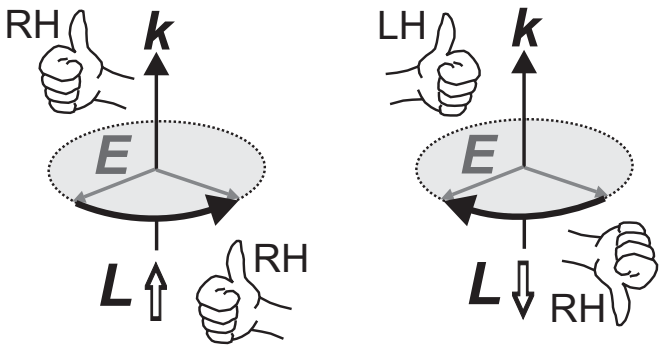

Figure 7.3: Illustration of relation of handedness of the circularly polarized light with the angular momentum L. See details in the text. Extracted from Ref. [40].

Once the concepts about circular polarization have been clarified we can consider the definition of XMCD signal which is given by:

$$\mu_c = \mu^- - \mu^+ \tag{7.6}$$

where μ^- and μ^+ are the X-ray absorption coefficients for antiparallel and parallel orientations of the incident photon helicity and the sample magnetization, i.e., applied magnetic field, respectively.

The definition given in Eq. (7.6) is general and embraces the two measurement methods displayed in Fig. 7.4:

Helicity reversal: the sense of the magnetic field remains fixed and the photon helicity is reversed.

Field reversal: the helicity remains fixed and the sense of the magnetic field is reversed.

In field-reversal method the hysteresis effects might affect the XMCD signal and, moreover, it might provoke sample vibration giving rise to noisy spectra. The helicity-reversal mode overcomes these limitations and is preferred to the conventional field-reversal mode.

Synchrotron Radiation

The need of a "very special source of polarized X-rays" has made that the research by using polarized X-rays has been emerged abruptly only in the last decades by the boom in the production of synchrotron radiation.

Synchrotron radiation is the electromagnetic field emitted by a relativistic

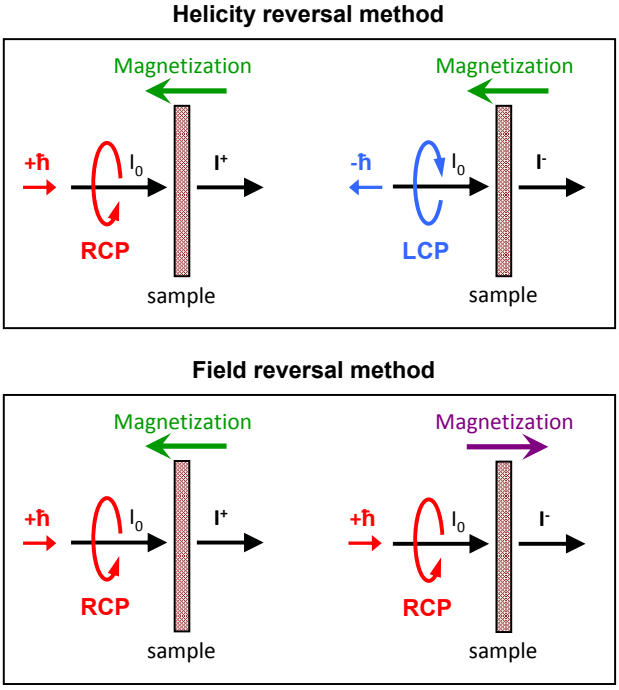

Figure 7.4: Sense of photon helicity and sample magnetization in the helicity reversal [panel (a)] and field reversal [panel (b)] XMCD measurement methods.

accelerated charged particle when it follows a curved trajectory.[2] The main outstanding properties of synchrotron radiation are: high brilliance, strong collimation (small vertical beam divergence), polarized radiation (linear on the orbital plane), broad range of energy (from the ultraviolet up to hard X-rays) and pulse emitted light (temporal width down to nanosecond).

As commented above, to perform XMCD measurement it is necessary to obtain polarized X-rays and we have just pointed out that the synchrotron radiation is polarized. The polarization of the emitted synchrotron radiation is governed by the conservation of angular momentum. This is illustrated for a bending magnet source in Fig. 7.5. The angular momentum of a circulating electron is defined according to the right hand rule. When the fingers of the right hand point in the direction of electron motion, the thumb defines the direction of angular momentum L. For the electron motion shown in Fig. 7.5, L therefore points in the down direction. In the radiation process, energy

[2]The frequency of the radiation is determined by the electron energy $E=\gamma m_0 c^2$, and the characteristic wavelength λ_C is given by: $\lambda_C=4\pi R/3\gamma^3$. For example, if we consider an electron storage ring of 2 GeV with the dipole magnets having a bending radius of 5.56 m and a field of 1.2 T, which results in a λ_C of 3.88 Å which is in the X-ray region of the electromagnetic spectrum [139].

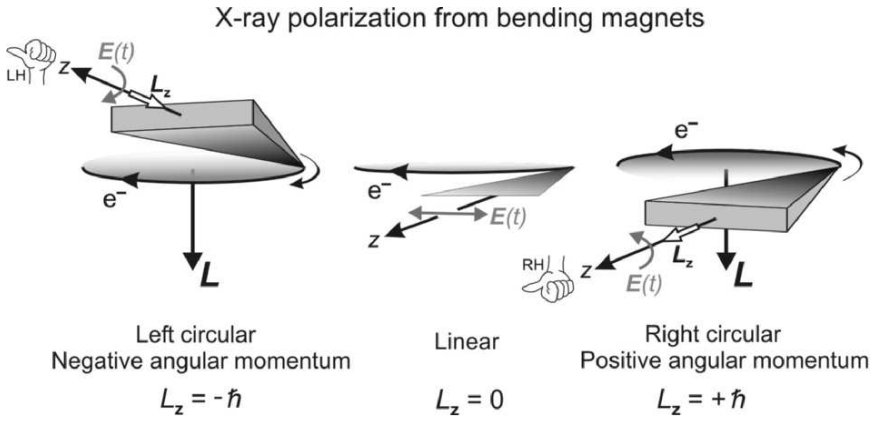

Figure 7.5: Origin of polarized synchrotron radiation from a bending magnet source. Extracted from Ref. [40].

and angular momentum from the circulating electron are transferred to the X-rays. If radiation in the plane of the electron orbit is selected by a suitable aperture[3], as illustrated in the middle of the figure, the X-ray propagation direction z is perpendicular to L and the angular momentum component L_z is zero. The emitted radiation is *linearly polarized*.

In contrast, radiation emitted at a finite angle above or below the orbit plane will have a finite angular momentum, since now L has a finite projection L_z along the X-ray propagation direction z. As illustrated in Fig. 7.5, above the orbit plane, the projection L_z is along $-z$ and the *circularly polarized* wave is called *left handed* and has an angular momentum L_z = -$\hbar$. As have been discussed above we define the "handedness" of the wave as the rotation sense of the E-vector in time relative to the X-ray propagation direction. This is illustrated for X-ray emission above and below the electron orbit plane on the left and right sides of Fig. 7.5, respectively.

Therefore, we have shown that the polarization state of synchrotron radiation produced by a bending magnet source. Additionally, the degree of circular polarization increase with angular aperture but unfortunately at expenses of flux [34, 140]

Therefore, synchrotron radiation emitted from bending magnets is highly polarized and the polarization depends on the angular aperture from the observer. Although bending magnets can provide any desired degree of polarization, this comes at a price. The flux falls dramatically as the aperture angle, φ, increases. This is exemplified in Fig. 7.6. The strongest XMCD is obtained

[3]Cone angle of order $1/\gamma^2$=1-$(v/c)^2$, where v is the speed of charged-particle bunches inside the storage ring and c is the speed of light.

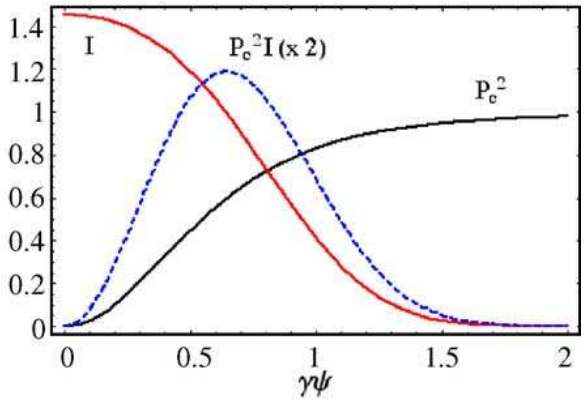

Figure 7.6: Degree of circular polarization P_C as a function of the vertical viewing angle, φ. Trade-off between flux and polarization, and the figure of merit $P_c^2 \times I$. Extracted from Ref. [140].

with pure circular polarization, but as $P_C \rightarrow 1$ then $I \rightarrow 0$. Therefore, there is a trade-off between flux and polarization. A figure of merit for most XMCD experiments is $P_C^2 I$, and the angle for optimal $P_C^2 I$ depends on the photon energy and the critical energy of the ring. Apart from limited P_C other drawbacks of bending magnets are modest brightness and the emission of LCP and RCP in different directions.

These disadvantages can be overcome by using radiation emitted from multipole insertion devices. These devices are periodic arrays of permanent magnets, so called wigglers and undulators, installed in the straight sections of the storage ring. They force the electrons to oscillate with a period of few centimeters over a length of several meters. Each wiggler emits synchrotron radiation in the same forward direction. Thus the intensities from each wiggler are superimposed. The more wiggles the electrons pass the higher the resulting light intensity. In undulators interference effects contribute to further enhance of the intensity.

Regular wigglers and undulator do not produce circularly polarized X-rays since contributions of right and left handed half periods, which positive and negative curvatures, do cancel. Several exotic designs have been proposed to bypass this limitation: helical undulator, asymmetric wiggler, crossed undulator, multipole wiggler, etc., designed with the aim of producing a fully polarized beam along the axis of the device. In other words, if the magnetic fields in a wiggler an undulator are confined to one transverse plane, the alternating poles cancel this elliptical polarization out of the plane and the radiation is linearly polarized everywhere. For insertion devices with helical magnetic fields the radiation is elliptical polarized. In Fig. 7.7 are displayed a

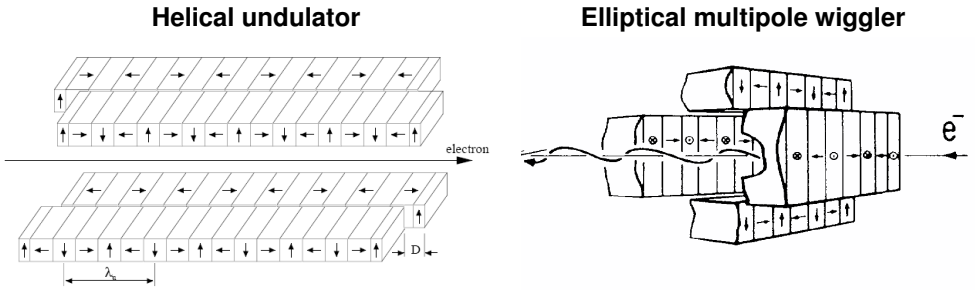

Figure 7.7: Exotic insertion devices to produce elliptically and circularly polarized X-rays.

helical undulator and an elliptical multipole wiggler [141].

However, quick reversal of the photon helicity by using the above cited exotic insertion devices is difficult because this procedure usually involves rearrangement of magnet arrays, also the available number of this insertion devices is limited. By contrast, the use of X-ray phase retarders (XPR) to convert incoming horizontal polarized X-rays to circular is in principle accessible to every hard X-ray beamline of each synchrotron radiation facilities [142] and this method has the advantage that helicity can be reversal very quick using the helicity modulation technique [37, 42, 143]. Moreover, X-ray phase plates can provide well-defined polarization without being affected by the finite emittance of the electron (positron) beams circulating in the storage ring [144].

Theory of the usage of perfect crystals as X-ray phase retarders.

The principle of the X-ray transmission phase plates is fully described by the dynamical theory of X-ray diffraction that allows for the full interference of the electromagnetic wave in the periodic crystal [145]. It is known that perfect crystals close to the Bragg condition are birefringent, i.e., a phase shift δ is introduced between π and σ polarization components of the incident beam (π is the component of the electric field that is parallel to the diffraction plane, and σ is orthogonal to the plane). In other words, the components of the electric field propagate through the crystal with different phase velocities which introduces the phase shift δ between them. If the diffraction planes are inclined by an angle φ with respect to the electric field of the incident linearly polarized X-ray beam, the circular polarization rate P_C depends on the phase shift δ through the following relation,

$$P_C = \sin(\delta) \cdot \sin(2\varphi) \tag{7.7}$$

To achieve full circular polarized X-rays both components π and σ must be coherently excited with equal electric field amplitude and the phase shift between both components must be $\pi/2$. The former condition can be fulfilled tilting 45º the diffraction plane with respect to the polarization plane of the incoming beam ($\varphi=\pi/4$). While $\delta=\pi/2$ is achieved adding a certain offset angle $\Delta\theta$ to move out of Bragg condition. The phase shift mainly depends on the phase plate thickness and on the offset angle [142] by,

$$\delta = -\frac{\pi}{2}[\frac{r_e^2 \Re(F_h F_{\overline{h}})}{\pi^2 V^2} \cdot \frac{\lambda^3 \sin(2\theta_B)}{\Delta\theta}]t \tag{7.8}$$

where r_e is the classical electron radius, F_h the crystal structure factor for the hkl reflection V the volume of the unit-cell, λ the wavelength, θ_B the Bragg angle and t the effective thickness of the phase retarder: $t=t_0/\cos(\theta_B)$ where t_0 the thickness of the crystal. Using the Bragg law $n\lambda=2d\cos(\theta_B)$ and doing some maths in Eq. (7.8), it can be easily obtained the following expression for the offset angle at circular polarization condition,

$$\Delta\theta_{\delta=\pi/2} = \frac{-r_e^2 \Re(F_h F_{\overline{h}}) t_0}{\pi^3 V^2 d}(\frac{hc}{E})^4 \tag{7.9}$$

Accordingly, chosen the phase plate and reflection, the offset angle variation depends on the energy like $\sim 1/\mathrm{E}^4$, i.e., $\Delta\theta$ decreases when the energy increases, but in practice this variation is negligible and for short energy scans the offset angle can be keep constant.

7.2 Design and development of the XMCD set-up

Here, we present the experimental XMCD set-up performed at BM25-A–SpLine beamline in the ESRF. SpLine is a non XMCD-dedicated beamline and the set-up was performed along the duration of an almost standard beamtime (10 days) with the handicap that is a bending magnet beamline with a large angular divergence. Linearly polarized X-rays were converted into circularly polarized ones by using a diamond X-ray phase retarder working as quarter wave plate. The performance of the XMCD set-up is illustrated by showing recorded XMCD spectra on intermetallic compounds studied in this Thesis.

7.2.1 BM25–A: a bending magnet beamline

The beamline BM25 (SpLine) at the ESRF, is a bending magnet beamline.[146] The beam is split into two branches, considering the variation of the critical energy across the horizontal fan and maximizing the separation between them. Fig. 7.8 shows the angular profile of the critical energy over the total angular acceptance on the beamline front end. Two different plateaus can be distinguished, each one with approximately 4 mrad horizontal opening angle, between -8 to -12 mrad the hard edge (Branch B) and between -1 to -5 mrad the soft edge (Branch A). The beam is splitted into two fans of an horizontal opening angle of 2 mrad each, with a central 5 mrad blocked. Each fan has been centered on a different plateau. The hatched zones in Fig. 7.8 correspond to the two regions selected for each branch. Branch A with a critical energy of 9.6 keV is centered on -3.5 mrad and Branch B with a critical energy of 20.6 keV is centered on -10.5 mrad. Branch A is dedicated to X-ray absorption spectroscopy (XAS) and high resolution X-ray powder diffraction.

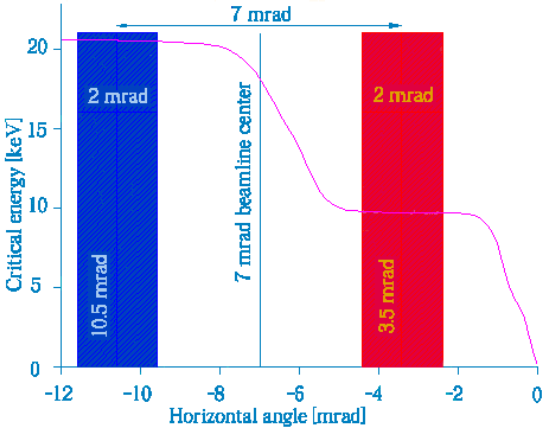

Figure 7.8: Angular profile of the critical energy of BM25 front end.

7.2.2 XMCD experimental set-up

The double-crystal monochromator used at Branch A is a pseudo channel-cut type with two fixed Si(111) crystals moved together by a simple goniometer circle in the (-n,+n) configuration. The first monochromator crystal is water cooled while the second is kept at room temperature. The second crystal can be finely tilted with respect to the first one in 3 perpendicular axes. The pitch angle (concentric to the Bragg angle of the crystal) can be regulated during an energy scan in order to keep the transmission of the monochromator optimized during the whole scan, and to reduce the higher order harmonic content of the

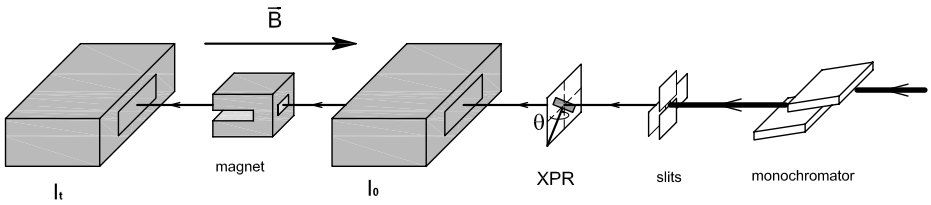

Figure 7.9: Schematic layout of the set-up for XMCD measurements.

beam if necessary. To guarantee a stable beam position and shape on the sample during the energy scan, pre-sample slits (1mm × 1mm as typical size) are placed in front of the sample, and the focusing is tuned to keep the beam just larger than the slits in their position. In this way, even if the beam is moving slightly during the scan, the beam position and shape on the sample are fixed. A schematic view of the beamline during XMCD measurements is given in Fig. 7.9.

For the XMCD measurements a synthetic 111-diamond plate (Sumitomo Corporation Ltd.) of thickness 0.5 mm (see left panel of Fig. 7.10). We have used the symmetric Laue geometry in which the (220) diffraction plane, perpendicular to the crystal surface, is chosen (see right panel of Fig. 7.10).

XPR was fixed by using beeswax onto a crystal holder plate which was mounted on a standard pin goniometer (see Fig. 7.11). The rotation axis was tilted 45° away from the polarization plane of the incident X-ray beam, i.e., orbit plane of the electrons inside the storage ring (see Fig. 7.12).

The transmissivity of the XPR for different energy ranges was tested in a previous experiment. The results shown that in the energy range from Fe K-edge to Gd L_2-edge (7-8 keV) the diamond slab transmitted the ∼30% of the incident beam, which is in good agreement with the theoretical simulations for this kind of diamond slab and geometry (see Fig. 7.13).

Two translational motors, perpendicular and parallel to the rotation axis (x and z axes, respectively), are used to center the diamond into the beam. A third motor is used to rotate the XPR in order to tune the Bragg condition, θ rotation (see Fig. 7.11). In order to obtain circularly polarized X-rays the Bragg peaks were measured for each energy point and then XPR was tuned out of diffraction condition by adding (subtracting) an offset angle $\Delta\theta$ to get LCP (RCP) light. A scintillation detector was used to detect the diamond (220) Bragg peaks as displayed in Fig. 7.12. The position of this detector was maintained fixed for each energy range since its solid acceptance angle is big enough to collect the diffracted beam for a whole energy scan.

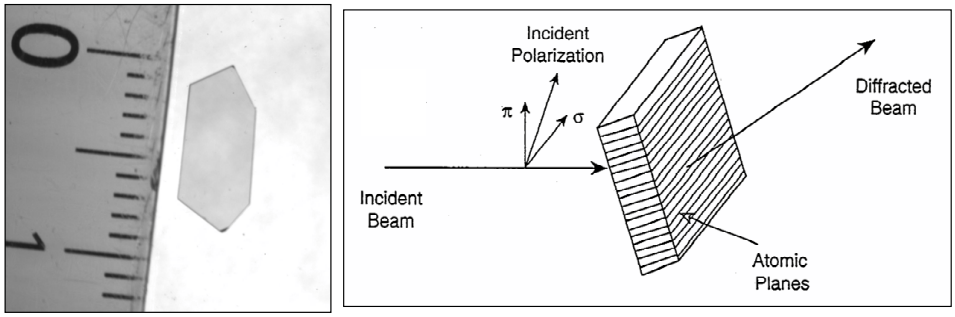

Figure 7.10: View of the 111-diamond slab of thickness 0.5 mm (left panel) and the schematic view of the symmetric Laue-220 diffraction geometry used (right panel).

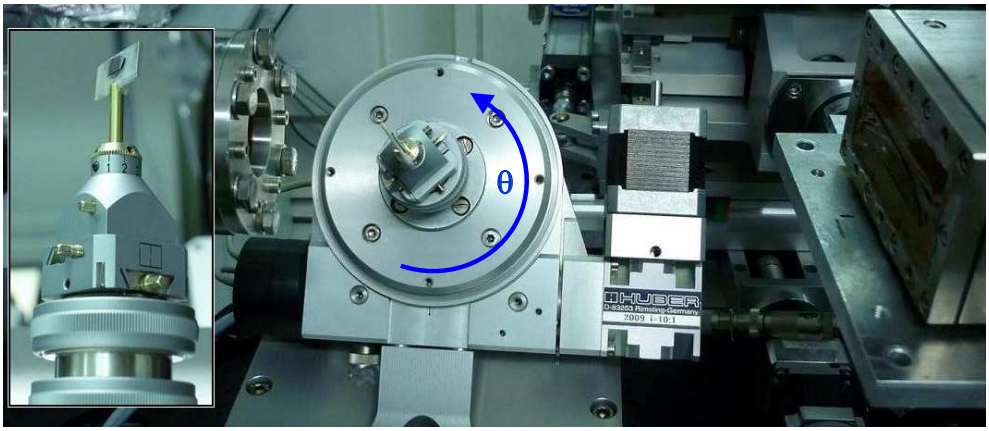

Figure 7.11: XPR holder and motor stage tilted 45° away from horizontal planes.

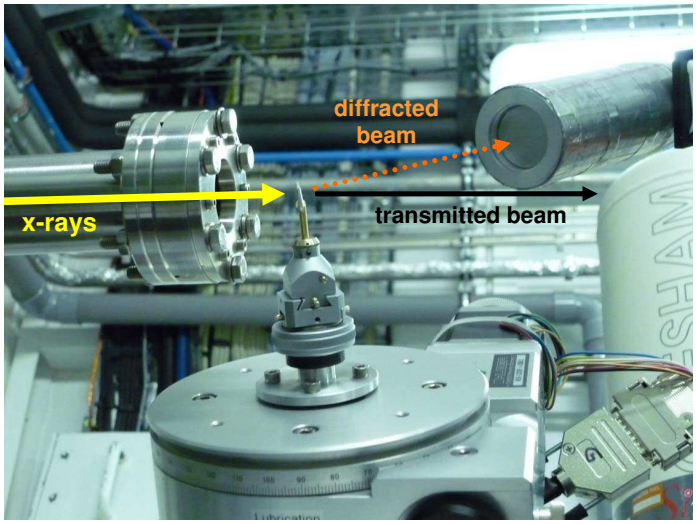

Figure 7.12: Schematic view of the diffracted and transmitted beams by the XPR.

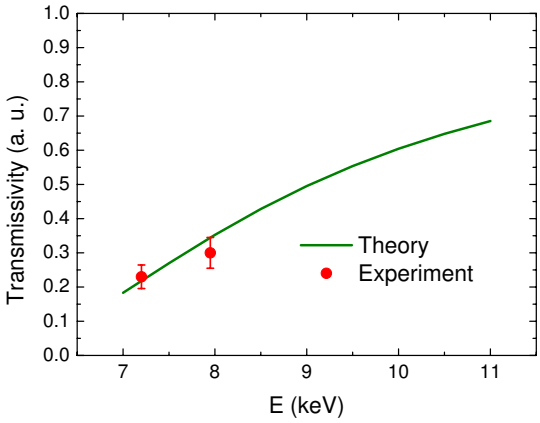

Figure 7.13: Calculated transmissivity of a 0.5 mm-thick diamond in Laue geometry and experimental data obtained at Fe K and Gd L_2 edge.

In-house design magnet for transmission mode measurements were made by using Nd-Fe-B permanent magnets (see Fig. 7.14). The magnetic field could be varied by changing the gap between pole pieces. For these experiments the minimum gap, 5 mm, was chosen to a get a magnetic field of H = 4.8 kOe at the sample position. The sample holder was designed to measure samples in transmission mode. In our case, the samples were fine powder spread onto adhesive Kapton tape and two of these tapes were put together to ensure good homogeneity. The final film was cut in the appropriate form to fit the hole of the sample holder and this piece was fixed using adhesive tape (see Fig. 7.14).

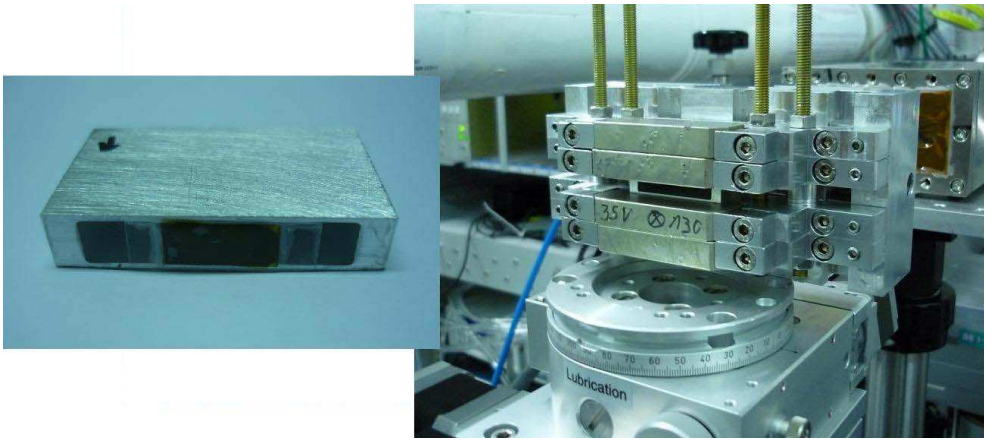

Figure 7.14: Sample holder for transmission measurements and permanent magnet used.

7.2.3 Simulations previous experiment

The offset needed to get circular polarization condition was chosen according to the theoretical curves for the circular polarization rate P_C=sinδ, where δ is substituted by Eq. (7.8). The theoretical P_C has been convoluted with a Gaussian function in order to account for the effective divergence of the incident beam, which causes a smearing of the polarization states through the spread of the δ phase shift. However, this effect is minimized by operating the phase plate at large offsets because δ is a slowly varying function of $\Delta\theta$ (see Fig. 7.15).

Unfortunately, we could not measure the experimental polarization curves as a function of the offset angle. This would serve us to fully characterize the polarization state of X-rays and to know the effective divergence of the beam at SpLine for this experimental set-up. However, the vertical divergence of the beamline has been estimated about 10 arcsec, while the horizontal divergence has been estimated between 20 and 80 arcsec, depending on the size of the pre-sample slits and the focalization point. The importance of this parameter into selecting a stable offset angle is illustrated in Fig. 7.16 where the energy dependence of both the circular polarization rate and the offset angle for different FWHM of the Gaussian used in the convolution (20, 50 and 80 arcsec) are shown. The simulated curves for effective divergences equal to 50 and 80 arcsec give rise similar P_C and $\Delta\theta$ values. Therefore, we can consider the curves obtained for a effective divergence of 80 arcsec as our reference of the worst case.

It is worth to note that the simulated data displayed in Fig. 7.16 consider the offset angle as the one which provides maximum/minimum value of P_C at both sides of Bragg angle position, i.e., $\Delta\theta = 0$ (see Fig. 7.15). However, to use this offset value is not recommendable because small variations could cause undesirable fluctuations in the polarization rate. Therefore, it is mandatory to work with higher offsets to avoid this region at expense of circular polarization rate. For this reason, we have considered an offset value higher than that of the maximum/minimum of the P_C curve obtained for an effective divergence of 80 arcsec.

7.2.4 XMCD Measurements

XMCD was measured at room temperature on reference $GdFe_2$ and $HoFe_2$ samples at the rare-earth L_2-edges. These samples were chosen since their XMCD signals are well characterized and their magnitude and shape allow us to verify that the observed signals are not affected by any spurious signal or derivative effect. Once the performance of the XMCD set-up was verified,

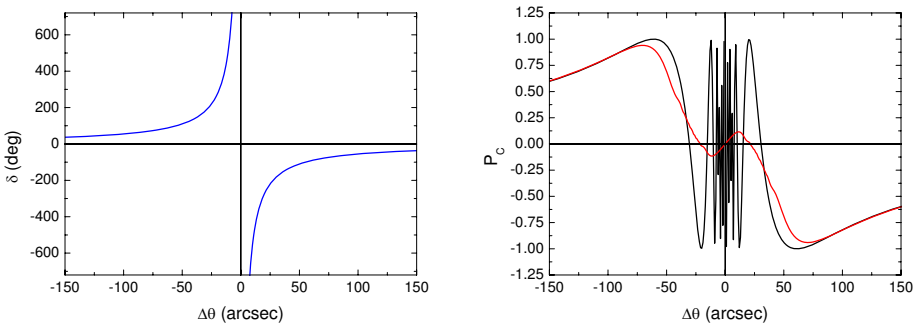

Figure 7.15: Phase shift (left panel) and circular polarization rate (right panel) curves as a function of the offset angle. The theoretical curve for P_C (black solid line) has been convoluted with a Gaussian (red solid line) to consider the effective divergence.

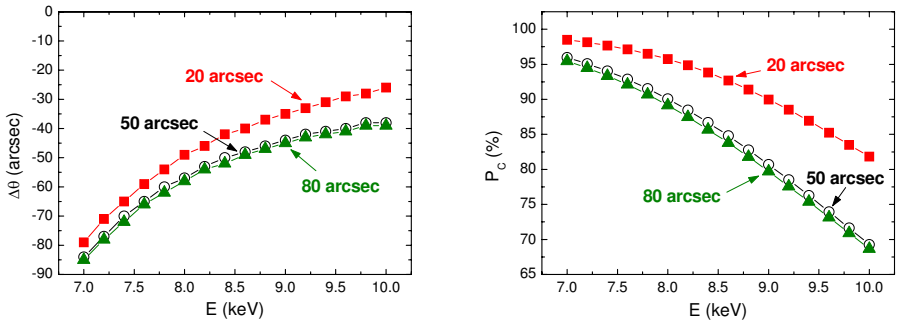

Figure 7.16: Variation of the offset angle (left panel) and circular polarization rate (right panel) with the energy. Theoretical data have been convoluted with Gaussian functions of 20, 50 and 80 arcsec FWHM to account the effective divergence.

the Ge K-edge XMCD was recorded on a $Gd(Fe_{0.9}Ge_{0.1})_2$ sample in which no magnetic role is *a priori* assigned to Ge atoms.

For the experiments, the XPR tuning was made as follows. At each absorption edge, several Bragg peaks were recorded through the energy range of interest by using a scintillation detector (see Fig. 7.12). The θ angle needed to move the XPR during the energy scan was obtained by fitting the diffraction peak positions *vs.* energy to $\arcsin(A/E)$ according to Bragg's law, where A is a constant. Nevertheless, we have verified that for a small energy window ($\sim$ 100 eV), as we use to record the XMCD spectra, the error introduced by a linear approximation is negligible. Moreover, we have considered a fixed offset for the whole energy scan. In the case of a 200 eV XMCD scan at the Ho L_2-edge the offset angle varies $\sim$ 2 arcsec. For these reasons the θ angle of the diamond phase plate has been varied linearly during the energy scan.

$GdFe_2$ GdL_2-edge

Previous studies have shown [91, 93, 94, 137] that $GdFe_2$ compound possess a big Gd L_2 XMCD signal which make it suitable as a good reference compound for checking the XMCD set-up.

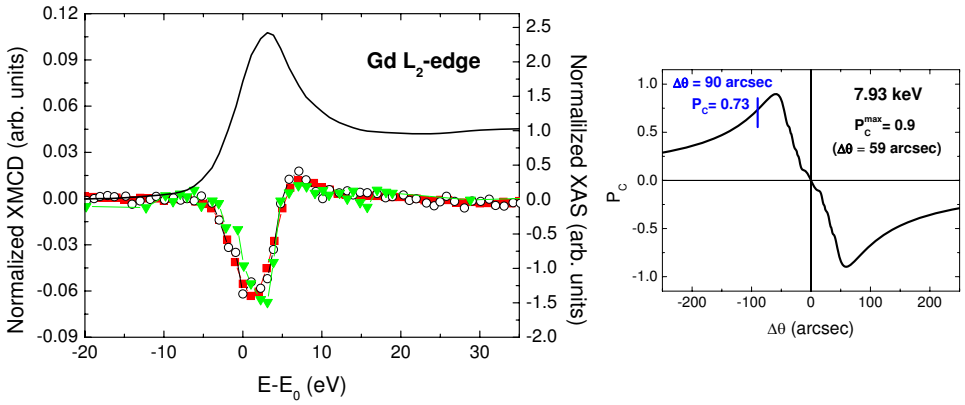

Figure 7.17: Left panel: normalized Gd L_2-edge XMCD spectra recorded on $GdFe_2$ by using field reversal (green, ▼), helicity reversal (black, ○) and helicity modulation (red, ■) configuration (see text for details). The normalized XANES spectrum is also shown (black solid line). Right panel: P_C curve at Gd L_2-edge energy. Offset used for the experiment is marked by a vertical line.

The Gd L_2-edge (7930 eV) XMCD spectra of $GdFe_2$ shown in Fig. 7.17 were recorded at room temperature and under a 4.8 kOe magnetic field. Both field reversal and helicity reversal techniques were used employing an angular offset equal to 90 arcsec. In all the cases we have adopted the same convention to display the spectra: the XMCD signal corresponds to the spin-dependent absorption coefficient obtained as the difference of the absorption coefficient $\mu_c = (\mu^- - \mu^+)$ for antiparallel, μ^-, and parallel, μ^+, orientations of the photon helicity and the magnetic field applied to the sample. The comparison of the results obtained by using both methods is reported in Fig. 7.17, where the XMCD signals have been normalized to the absorption jump and corrected by the estimated circular polarization rate (~ 0.8). Both measuring methods yield the same spectral shape characterized by a negative peak, ~ 5 eV wide, centered at ~ 1 eV above the edge, in agreement with previous results [91, 93, 94, 137]. For further verification of the reliability of these results, the same specimen was measured in transmission mode at the undulator beamline BL39XU at SPring-8. The helicity modulation technique was used with a 0.7 mm-thick diamond phase retarder. The good agreement between both

measurements, reported in Fig. 7.17, point out the high performance of the SpLine set-up.

$HoFe_2$ Ho L_2-edge

Similar results have been obtained in the case the Ho L_2-edge (8918 eV) XMCD of $HoFe_2$. The XMCD signal was recorded by using the helicity reversal method with an offset of 61 arcsec that corresponds to an estimated circular polarization rate higher than 0.7. As shown in Fig. 7.18, the XMCD signals recorded on the same specimen at both SpLine and BL39XU show a remarkable agreement: the Ho L_2-edge XMCD exhibits a positive peak at E-E_0 $\sim$ 1 eV above the edge, a negative peak at $\sim$4 eV and another positive peak centered at $\sim$7 eV above the edge.

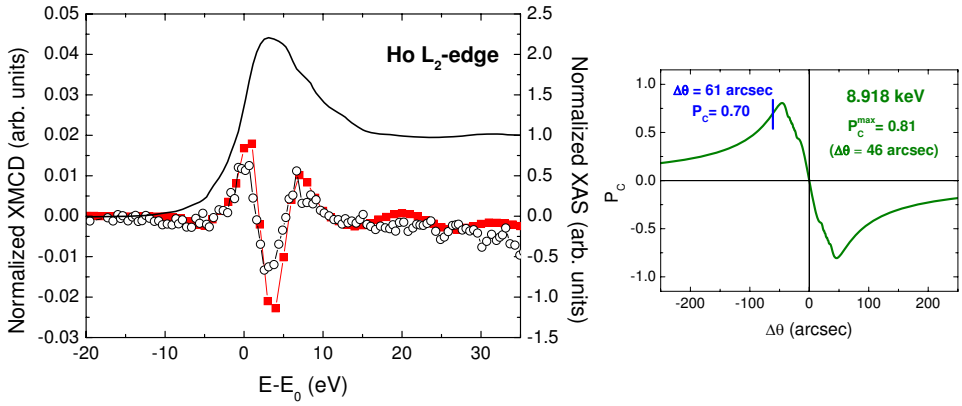

Figure 7.18: Left panel: comparison of normalized Ho L_2-edge XMCD signals recorded on $HoFe_2$ by using the helicity reversal (black, ○) and helicity modulation techniques (red, ■). The normalized XANES spectrum is also shown (black solid line). Right panel: P_C curve at Ho L_2-edge energy. Offset used for the experiment is marked by a vertical line.

The measurements at BL39XU were performed under the same experimental conditions as mentioned for the Gd L_2-edge case. It should be noted, however, that the amplitude of the spectrum recorded in our experimental set-up is slightly smaller than the recorded at BL39XU. This effect might be addressed to the loss of the correct XPR position during the measurement since no encoder was used for the θ-rotation. However, this hypothesis can be discarded because the diffraction peaks measured after the XMCD measurement are close to the expected values. Therefore, we tentatively assign this reduction to the different harmonic rejection method used (second crystal of DCM

detuning at SpLine and flat Rh-coated mirror after the XPR at BL39XU) since the high-order harmonics contamination can distort the XMCD measurement.

$Gd(Fe_{0.9}Ge_{0.1})_2$ Ge K-edge

Finally, in order to test the set-up at high energy, i.e., when the transmission through the diamond is higher hence the circular polarization is lower, we have recorded the XMCD at the Ge K-edge (11103 eV). To this end we have considered the case of $Gd(Fe_{0.9}Ge_{0.1})_2$ Laves phase compound in which magnetic Fe atoms have been substituted by non-magnetic Ge ones. In Chapter 5 we have shown the existence of non-zero XMCD signals at the K-edge of atoms like Ge or Ga. These results illustrate the importance of XMCD into determining the exact nature of the induced magnetic moments in traditionally non-magnetic atoms due to the interplay of the hybridization and of the modification of the electronic structure.

We have recorded the Ge K-edge XMCD by using an angular offset of 34 arcsec for which the theoretical estimate yields a circular polarization rate of ~ 0.6.[4] The results are reported in Fig. 7.19 where the XMCD signal measured in the set-up developed at SpLine is compared to that recorded at XMCD-dedicated station of BL39XU at SPring-8. At BL39XU the helicity modulation technique with a 1.4 mm-thick diamond XPR was used to record the XMCD signal in transmission mode. In both cases, the XMCD spectra show a spectral feature of positive sign centered at ~ 7 eV above the edge, whose amplitude is only about 0.1% of the absorption jump.[5] For the sake of comparison we also show, in Fig. 7.19, the XMCD signal of $Ho(Fe_{0.9}Ge_{0.1})_2$ at the Ge K-edge recorded at 5 K and under a magnetic field of 50 kOe. In this case, Ho Laves phase compound, the Ge magnetic polarization is bigger and the XMCD signal is clearer than in the Gd compound case. We have measured the Gd compound in stead the Ho one because the goal was to illustrate the performance of the XMCD set-up at SpLine at the detection limit observed at BL39XU.

[4]We are conscious that the circular polarization rate obtained with a 111-diamond of 0.5 mm-thick in Laue(220) symmetric geometry is not optimum at the Ge K-edge energies, being more convenient to use a thicker diamond phase plate to get a higher degree of circular polarization. However, it serves to our purpose of checking the circular polarization rate achieved at higher energy in our experimental set-up.

[5]The Ge K-edge signal recorded at SpLine shows a poorer signal to noise ratio than that recorded at BL39XU where a 1.4 mm-thick XPR, providing a higher circular polarization rate than the 0.5 mm-thick plate used at SpLine.

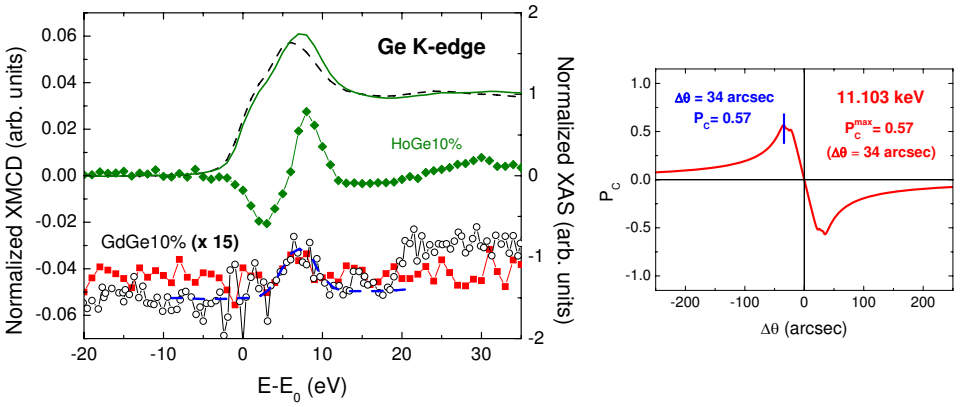

Figure 7.19: Left panel: comparison of normalized XMCD signals of $Gd(Fe_{0.9}Ge_{0.1})_2$ recorded at Ge K-edge by using helicity reversal (black, ○) and helicity modulation techniques (red, ■). The dotted (blue) line is a guide to the eye. The XMCD signal of $Ho(Fe_{0.9}Ge_{0.1})_2$ at 5 K and 50 kOe is also shown (olive, ⧫). For the sake of completion the normalized XANES spectra is also shown for $Gd(Fe_{0.9}Ge_{0.1})_2$(black dotted line) and $Ho(Fe_{0.9}Ge_{0.1})_2$ (green solid line). Right panel: P_C curve at Ge K-edge energy. Offset used for the experiment is marked by a vertical line.

7.3 Conclusions

- We have design and developed an XMCD experimental set-up at BM25-A–SpLine (ESRF) which is a non-dedicate XMCD beamline. The incoming linear polarized X-rays have been circularly polarized by using a 111-diamond slab of 0.5 mm of thickness as a quarter phase plate in the hard X-ray range. The diamond phase retarder has been mounted in Laue-220 symmetric configuration.

- The simulation of the polarization rate by taking into account the effective divergence of the beam has allowed us to perform a proper tuning of the offset angle out-of the Bragg condition necessary to achieve the maximum P_C but maintaining the operation stability.

- The reliability of the experimental set-up has been demonstrated by measuring the XMCD spectra of samples which possess a characteristic dichroic signal in order to verify that the measured XMCD spectra are not affected by any spurious derivative effect. The measurements have been performed by using both the *field-reversal* and *helicity-reversal* methods and the agreement of both methods corroborates the reliability of the XMCD set-up. Moreover, the dichroic signals obtained have been compared with those recorded in an undulator XMCD dedicated beamline (BL39XU at SPring-8). The well agreement point out the high performance of the XMCD set-up performed at SpLine.

- Finally, the set-up has been test at the limit condition measuring the XMCD spectra at higher energy for which the thickness of the XPR is not enough to give rise a well suited degree of circularly polarized X-ray. Therefore, we have measured a non negligible dichroic signal of the $Gd(Fe_{0.9}Ge_{0.1})_2$ Laves phase at Ge K-edge which is comparable to that obtained at BL39XU.

Appendix A

Behavior of the ESMH cycles at the energy point $A1$ at the R L_2-edge.

As commented in Chapter 6, the shape, not the coercive field, of the ESMH recorded at the R L_2-edge is different at the selected energy points in different in several cases. As shown in Fig. 6.5(b)-(d), the cycles recorded for $HoFe_2$, $Er_{0.5}Y_{0.5}Fe_2$ and Er_6Fe_{23} at the peak $A1$ exhibit opposite high field slope than those measured at peaks A and B. However, this is not a general behavior of the ESMH($A1$) cycles. Indeed the cycles recorded for both $ErFe_2$ and $Ho_{0.5}Lu_{0.5}Fe_2$ at $A1$ and B are equivalent [see Fig. 6.2 and Fig. 6.5(a)].

The different shape observed for the ESMH($A1$) cycles should stem from the difference between $ESMH_{Fe}$ and $ESMH_R$ cycles, since at the threshold energy, peak $A1$ of the R L_2-edge XMCD spectra, both Fe and R contributions overlaps and possess comparable amplitude. In order to verify this hypothesis we should unravel both $ESMH_{Fe}$ and $ESMH_R$ contributions. As an illustrative example we have considered the case of $HoFe_2$ at T = 5 K, because $HoFe_2$ exhibit the greatest differences between ESMH cycles (see Fig. A.1).

According to the additivity of Fe and Ho dichroic contributions, the ESMH cycle of the $HoFe_2$ can be decomposed as:

$$ESMH_{HoFe2} = ESMH_{Fe} + ESMH_{Ho} \tag{A.1}$$

thus, the Fe contribution can be obtained as:

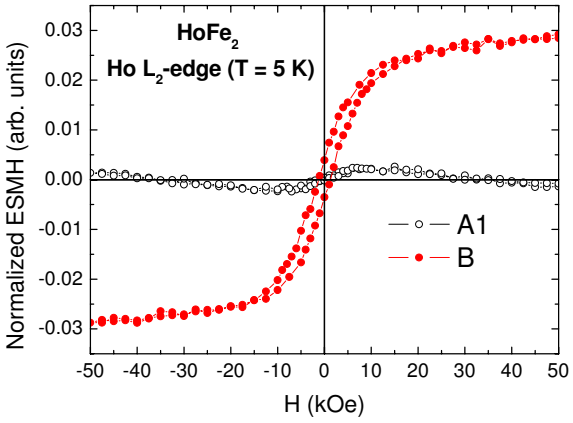

Figure A.1: ESMH cycles recorded at the points $A1$ (black, ○) and B (red, •) of the Ho L_2-edge XMCD spectrum of $HoFe_2$.

$$ESMH_{Fe} = ESMH_{HoFe2} - ESMH_{Ho} \tag{A.2}$$

At this point we have to considered the following assumptions:

i) each $ESMH_{Fe}$ and $ESMH_{Ho}$ contributions possess the same functional dependence with the magnetic field, regardless the energy point of the XMCD spectrum chosen;

ii) the amplitude of the $ESMH_{Ho}$ cycle of $HoFe_2$ at Ho L_2-edge should be approximately equal to that of the total ESMH of $HoAl_2$ which does not contain Fe.

As commented above, the Fe contribution at the R L_2-edge is limited to the energy threshold. Therefore, at the energy point B the Fe contribution to the XMCD spectra can be considered negligible. Thus, the ESMH cycle recorded at peak B can be approximated as the $ESMH_{Ho}$ contribution. Then, by using (i), the $ESMH_{Ho}$ cycles at both B and $A1$ energy points should exhibit the same shape, i.e. $ESMH_{Ho}(B) \propto ESMH_{Ho}(A1)$. Additionally, by using (ii), the amplitude of the $ESMH_{Ho}(A1)$ contribution should be equal to the intensity of the Ho L_2-edge XMCD spectra of $HoAl_2$ at the peak $A1$, and thus:

$$ESMH_{Ho}(A1) = XMCD_{HoAl2}(A1) \times \frac{ESMH_{Ho}(B)}{XMCD_{HoFe2}(B)} \tag{A.3}$$

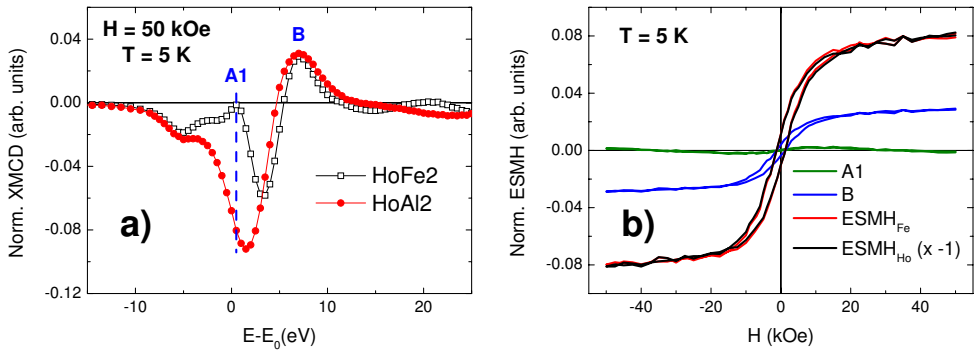

Figure A.2: Left panel: Ho L_2-edge XMCD signal of $HoFe_2$ and $HoAl_2$ measured at the H = 50 kOe and T = 5 K. Right panel: ESMH cycles of $HoFe_2$ recorded at the energy points $A1$ and B of the Ho L_2-edge and the extracted $ESMH_{Fe}$ and $ESMH_{Ho}$ contributions.

Therefore, by using Eqs. (A.2) and (A.3) we obtain the $ESMH_{Fe}$ contribution at the energy point $A1$ as:

$$ESMH_{Fe}(A1) = ESMH_{HoFe2}(A1) - ESMH_{Ho}(A1) \tag{A.4}$$

The results after applying this procedure are shown in Fig. A.2(b). We found that both $ESMH_{Fe}(A1)$ and $ESMH_{Ho}(A1)$ contributions possess the same coercive field, and similar shape and amplitude. This behavior can be understood when comparing the R L_2-edge XMCD spectra of the measured compounds (see Fig.A.3). [1] When the amplitudes of both $XMCD_{Fe}$ and $XMCD_R$ contributions are approximately equal, the intensity of the dichroic signal is close to zero and thus the ESMH($A1$) cycle reflects the tiny differences between both $ESMH_{Fe}$ and $ESMH_{Ho}$ cycles (30 times lower than their amplitudes). This is also the case of the Er L_2-edge ESMH($A1$) cycles of $Er_{0.5}Y_{0.5}Fe_2$ and Er_6Fe_{23} [see Fig. 6.5(c) and (d)]. In contrast, when the total XMCD($A1$) intensity is not so close to zero, $ErFe_2$ and $Ho_{0.5}Lu_{0.5}Fe_2$, the ESMH($A1$) cycles are equivalent to those measured at other energy points [see Fig. 6.2(b) and Fig. 6.5(d)].

In conclusion, the unusual shape of the ESMH($A1$) cycles found in several samples simply reflects the tiny shape differences between both $ESMH_{Fe}$ and $ESMH_{Ho}$ contributions.

[1] The pass through zero of the ESMH cycle recorded for $HoFe_2$ at $A1$ is due to the faster growing of Fe contribution with the field than the Ho one. This provokes that the intensity of the $A1$ decreases when the field increases up to be negative for H $\gtrsim$ 35 kOe.

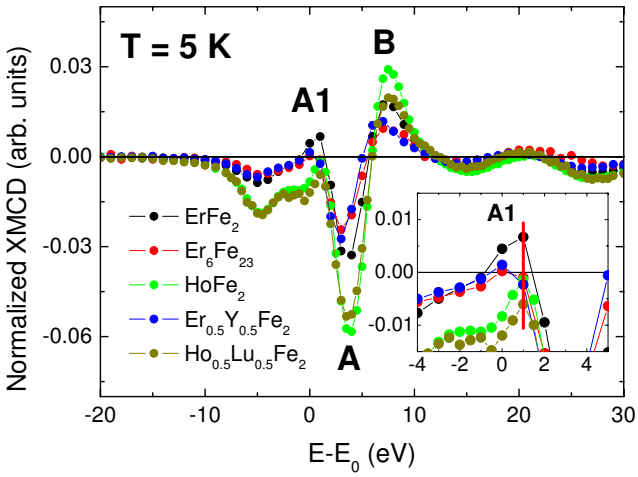

Figure A.3: Comparison of the R L_2-edge XMCD spectra at T = 5 K. The inset shows enlarged the peak *A*1.

Bibliography

[1] M. A. Laguna-Marco, *A new insight into the interpretation of the T K-edge and R $L_{2,3}$-edges XMCD spectra in R-T intermetallics.* (Prensas Universitarias de Zaragoza, Zaragoza, 2007).

[2] K. H. J. Buschow, *Handbook on Ferromagnetic Materials, vol. 4* (edited by E. P. Wohlfarth, North-Holland, Amsterdam, 1988).

[3] E. Burzo and H. R. Kirchmayr, *Handbook on the Physics and Chemistry of Rare Earths, vol.12* (edited by K. A. Gschneider Jr. and L. Eyring, North-Holland, Amsterdam, 1989).

[4] K. Yosida, *Theory of Magnetism* (Springer Series in Solid-State Sciences, Vol. 122, 1996).

[5] E. C. Stoner, Rev. Prog. Phys. **9**, 43 (1946).

[6] K. H. J. Buschow and F. R. de Boer, *Physics of Magnetism and Magnetic Materials* (Kluwer Academic Publishers, 2004).

[7] I. A. Campbell, J. of Phys. F: Met. Phys. **2**, L47 (1972).

[8] H. Yamada, J. Inoue and M. Shimizu, J. of Phys. F: Met. Phys. **15**, 169 (1986).

[9] H. Yamada and M. Shimizu, J. of Phys. F: Met. Phys. **16**, 1039 (1986).

[10] H. Yamada and M. Shimizu, J. of Phys. F: Met. Phys. **15**, L175 (1985).

[11] H. Yamada, J. Inoue, K. Terao, S. Kanda and M. Shimizu, J. of Phys. F: Met. Phys. **14**, 1943 (1984).

[12] M. S. S. Brooks, O. Eriksson and B. Johansson, J. Phys.: Condens. Matter **1**, 5861 (1989).

[13] M. S. S. Brooks, L. Nordstrom and B. Johansson, J. Phys.: Condens. Matter **3**, 2357 (1991).

[14] M. S. S. Brooks, L. Nordstrom and B. Johansson, J. Phys.: Condens. Matter **3**, 3393 (1991).

[15] K. H. J. Buschow, *Supermagnets, Hard Magnetic Materials. Chap. 4 and referenceds therein.* (edited by G. J. Long and F. Grandjean. Kluwer, Dordrecht, 1991).

[16] E. Belorizky, M. A. Fremy, J. P. Gavigan, D. Givord and H. S. Li, J. Appl. Phys. **61**, 8 (1987).

[17] J. Chaboy, T. A. Tyson, and A. Marcelli, *Relative Cross Sections for Bound-state Double-electron $LN_{4,5}$-edge Transitions of Rare-earths and Nonradioactive Elements of the Sixth Row.* (Prensas Universitarias, Zaragoza, 1995).

[18] M. Hof, *Handbook of Spectroscopy. Chap. 3 and references therein* (edited by G. Gauglitz and T. Vo-Dinh. WILEY-VCH Verlag GmbH, 2003).

[19] A. Bianconi, *X-ray Absorption: Principles, Applications, Techniques of EXAFS, SEXAFS and XANES. Chap. 11 and references therein* (edited by D.C. Koningsberger and R. Prins. John Wiley & Sons, New York, 1988).

[20] P. A. Lee, P. H. Citrin, P. Eisenberger, and B. M. Kincaid, Rev. Mod. Phys. **53**, 769 (1981).

[21] G. Schütz, M. Knülle, R. Wienke, W. Wilhelm, W. Wagner, P. Kienle and R. Frahm, Z. Phys. B **73**, 67 (1988).

[22] G. Schütz, R. Wienke, W. Wilhelm, W. Wagner, P. Kienle, R. Zeller and R. Frahm, Z. Phys. B **75**, 495 (1989).

[23] U. Fano, Phys. Rev. **178**, 131 (1969).

[24] J. Stöhr and Y. Wu, *Proceedings NATO Advanced Study Intitute: New Directions in Research with Third Generration Soft X-Ray Synchrotron Radiation Sources* (edited by A. S. Schlachter and F. J. Wuilleumier. Kluwer Academic Publishers, Netherlands, 1995).

[25] K. H. J. Buschow, Rev. Prog. Phys. **40**, 1179 (1977).

[26] K. H. J. Buschow, Rev. Prog. Phys. **42**, 1373 (1979).

[27] J. Rodriguez-Carvajal, Physica B **192**, 55 (1993).

[28] J. Rodriguez-Carvajal, Newsletter (IUCR) **26**, 12 (2001).

[29] J. Rodriguez-Carvajal, *Fullprof suite*, Website (2006), `http://www.ill.eu/sites/fullprof/`.

[30] R. A. Young, *The Rietveld Method* (Oxford University Press, 1995).

[31] B. H. Toby, Powder Diffr. **21**, 67 (2006).

[32] R. C. Black and F. C. Wellstood, *The SQUID Handbook. Vol II Applications of SQUIDs and SQUID systems. Chap. 12: Measurements of Magnetism and Magnetic Properties of Matter (and references therein).* (edited by J. Clarke and A. I. Braginsky. John Wiley & Sons, New York, 2006).

[33] Quantum Design, Website (2010), `http://www.qdusa.com/products/mpms`.

[34] P. J. Duke, *Synchrotron Radiation: Production and properties* (Oxford Science Publications, 2000).

[35] H. Maruyama, M. Suzuki, N. Kawamura, M. Ito, E. Arakawa, J. Kokubun, K. Hirano, K. Horie, S. Uemura, K. Hagiwara, M. Mizumaki, S. Goto, H. Kitamura, K. Namikawae and T. Ishikawa, Journal of Synchrotron Radiat. **6**, 1133 (1999).

[36] A. Rogalev, V. Gotte, J. Goulon, C. Gauthier, J. Chavanne and P. Elleaume, Journal of Synchrotron Radiat. **5**, 989 (1998).

[37] K. Hirano, T. Ishikawa, S. Koreeda, K. Fuchigami, K. Kanzai and S. Kikuta, Jpn. J. Appl. Phys. **31**, L1209 (1992).

[38] Y. Saitoh, H. Kimura, Y. Suzuki, T. Nakatani, T. Matsushita, T. Muro, T. Miyahara, M. Fujisawa, K. Soda, S. Ueda, H. Harada, M. Kotsugi, A. Sekiyama and S. Suga, Rev. Sci. Intrum. **71**, 3254 (2000).

[39] T. Hara, T. Tanaka, T. Tanabe, X.-M. Marechal, K. Kumagai and H. Kitamura, Journal of Synchrotron Radiat. **5**, 426 (1998).

[40] J. Stöhr and H.C. Siegmann, *Magnetism: From Fundamentals to Nanoscale Dynamics* (Springer Series in Solid-State Sciences, Vol. 152, Springer-Verlag, Berlin Heidelberg, 2006).

[41] H. Maruyama, Journal of Synchrotron Radiat. **8**, 125 (2001).

[42] M. Suzuki, N. Kawamura, M. Mizumaki, A. Urata and H. Maruyama, Jpn. J. Appl. Phys. **37**, L1488 (1998).

[43] D. Haskel, Y. Choi, D. R. Lee, J. C. Lang, G. Srajer, J. S. Jiang and S. D. Bader, J. Appl. Phys. **93**, 6507 (2003).

[44] M. Gruyters and D. Schmitz, Phys. Rev. Lett. **100**, 077205 (1998).

[45] H. Ohldag, A. Scholl, F. Nolting, E. Arenholz, S. Maat, A.T. Young, M. Carey, and J. Stöhr, Phys. Rev. Lett. **91**, 017203 (2003).

[46] H. Ohldag, H. Shi, E. Arenholz, J. Stöhr and D. Lederman, Phys. Rev. Lett. **96**, 027203 (2006).

[47] E. Goering, A. Fuss, W. Weber, J. Will and G. Schütz, J. Appl. Phys. **88**, 5920 (2000).

[48] E. Goering, S. Gold, A. Bayer and G. Schütz, Journal of Synchrotron Radiat. **8**, 434 (2001).

[49] J.B. Friauf, J. Am. Chem. Soc. **49**, 3107 (1927).

[50] J.B. Friauf, Phys. Rev. **29**, 34 (1927).

[51] F. Laves and H. Witte, Metallwirtschaft **14**, 645 (1935).

[52] F. Laves and H. Witte, Metallwirtschaft **15**, 840 (1935).

[53] G. E. R. Schulze, Z. Elektrochem. **45**, 849 (1939).

[54] F.C. Frank and J.S. Kasper, Acta Crystallogr. **11(3)**, 184 (1958).

[55] F.C. Frank and J.S. Kasper, Acta Crystallogr. **12(7)**, 483 (1959).

[56] H. Oesterreicher, Inorganic Chemistry **13**, 2807 (1974).

[57] F. Stein, M. Palm and G. Sauthoff, Intermetallics **12**, 713–720 (2004).

[58] F. Stein, M. Palm and G. Sauthoff, Intermetallics **13**, 1056–1074 (2005).

[59] A. Raman, Z. Metallkd. **58**, 179 (1967).

[60] G. Venturini, I. Ijjaali and B. Malaman, J. Alloys and Compounds **284**, 262–269 (1999).

[61] G. Venturini, I. Ijjaali and B. Malaman, J. Alloys and Compounds **285**, 194 (1999).

[62] Y.J. Tang, H.L. Luo and S.M. Pan, J. Magn. Magn. Mater. **152**, 70 (1996).

[63] C. M. Gilmore and F. E. Wang, Acta Crystallogr. **23**, 177 (1967).

[64] K. M. B. Alves, L. C. Sampaio, A. P. Guimãraes and S. F. Cunha, J. Alloys and Compounds **210**, 325 (1994).

[65] K. H. J. Buschow and R. P. van Stapele, J. Appl. Phys. **41**, 4066 (1970).

[66] A. P. Guimãraes and K. M. B. Alves, J. Magn. Magn. Mater. **104-107**, 1460 (1992).

[67] J. F. Herbst and J. J. Croat, J. Appl. Phys. **55**, 3023 (1984).

[68] J. Ostorero, J. Alloys and Compounds **317–318**, 450–454 (2001).

[69] X. H. Chen, K. Q. Wang, P. H. Hor, Y. Y. Xue, and C. W. Chu, Phys. Rev. B **72**, 054436 (2005).

[70] M. Reissner, W. Steiner, J. P. Kapplerl, Ph. Bauer and M. J. Besnus, J. of Phys. F: Met. Phys. **14**, 1249 (1984).

[71] C. Piquer, M. A. Laguna-Marco, R. Boada, F. Plazaola and J. Chaboy, IEEE Trans. Magn. **44**, 4206 (2008).

[72] M. J. Besnus, P. Bauer and J. M. Génin, J. of Phys. F: Met. Phys. **8**, 191 (1978).

[73] V. Sima, R. Grossinger, V. Sechovsky, Z. Smetana and H. Sassik, J. of Phys. F: Met. Phys. **14**, 981 (1984).

[74] J.M. Preston, J.R. Stewart, M. Reissner, W. Steiner, R.Cywinski, Appl. Phys. A **74**, S689–S691 (2002).

[75] R. Grössinger and W. Steiner, Phys. Stat. Sol. (a) **28**, K135–K138 (1975).

[76] H. Oesterreicher, J. Appl. Phys. **42**, 5137 (1971).

[77] A. del Moral, J. I. Arnaudas, C. de la Fuente, M. Ciria, E. Joven, and P. M. Gehring, J. Appl. Phys. **76**, 6180 (1994).

[78] A. del Moral, C. de la Fuente, and J. I. Arnaudas, Phys. Rev. B **54**, 12245 (1996).

[79] H. Oesterreicher, Phys. Stat. Sol. (a) **40**, K139 (1977).

[80] D. J. Germano and R. A. Butera, Phys. Rev. B **24**, 3912 (1981).

[81] M. J. Besnus, A. Herr and G. Fischer, J. of Phys. F: Met. Phys. **9**, 745 (1979).

[82] Wen-ding Zhong, Jian Lan and Zun-xiao Liu, J. Magn. Magn. Mater. **68**, 197 (1987).

[83] A. C. E. Burzo and H. R. Kirchmayr, *Landolt-Börnstein New series Vol. III 19d2: Compounds Between Rare Earth Elements and 3d, 4d or 5d Elements* (Springer-Verlag, Berlin, 1990).

[84] S. W. Lovesey and S. P. Collins, *X-ray Scattering and Absorption by Magnetic Materials.* (Oxford, Clarendon, London, 1996).

[85] J. Stöhr, J. Magn. Magn. Mater. **200**, 470 (1999).

[86] J. B. Kortright, D. D. Awschalom, J. Stöhr, S. D. Bader, Y. U. Idzerda, S. S. P. Parkin, Ivan K. Schuller and H.-C. Siegmann, J. Magn. Magn. Mater. **207**, 7 (1999).

[87] J. Chaboy, M. A. Laguna-Marco, N. Plugaru, R. Boada, C. Piquer, H. Maruyama and N. Kawamura, Journal of Synchrotron Radiat. **16**, 405 (2009).

[88] G. Schütz, W. Wagner, W. Wilhelm, P. Kienle, R. Zeller, R. Frahm and G. Materlik, Phys. Rev. Lett. **58**, 737 (1987).

[89] X. Wang, T. C. Leung, B. N. Harmon and P. Carra, Phys. Rev. B **47**, 9087 (1993).

[90] B. N. Harmon and A. J. Freeman, Phys. Rev. B **10**, 1979 (1974).

[91] M. A. Laguna-Marco, J. Chaboy and C. Piquer, Phys. Rev. B **77**, 125132 (2008).

[92] M. A. Laguna-Marco, C. Piquer and J. Chaboy, Phys. Rev. B **80**, 144419 (2009).

[93] M. A. Laguna-Marco, J. Chaboy and C. Piquer, J. Appl. Phys. **103**, 07E141 (2008).

[94] M. A. Laguna-Marco, J. Chaboy, C. Piquer, H. Maruyama, N. Ishimatsu, N. Kawamura, M. Takagaki and M. Suzuki, Phys. Rev. B **72**, 052412 (2005).

[95] C. Giorgetti, E. Dartyge, F. Baudelet and R.-M. Galéra, Phys. Rev. B **70**, 035105 (2004).

[96] M. A. Laguna-Marco, J. Chaboy and H. Maruyama, Phys. Rev. B **72**, 094408 (2005).

[97] J. Chaboy, M. A. Laguna-Marco, C. Piquer, H. Maruyama, and N. Kawamura, J. Phys.: Condens. Matter **19**, 436225 (2007).

[98] N. Ishimatsu, S. Miyamoto, H. Maruyama, J. Chaboy, M. A. Laguna-Marco and N. Kawamura, Phys. Rev. B **75**, 180402(R) (2007).

[99] J. Chaboy, H. Maruyama, L. M. García, J. Bartolomé, K. Kobayashi, N. Kawamura, A. Marcelli and L. Bozukov, Phys. Rev. B **54**, R15637 (1996).

[100] J. Chaboy, L. M. García, F. Bartolomé, H. Maruyama, A. Marcelli, and L. Bozukov, Phys. Rev. B **57**, 13386 (1998).

[101] J. Chaboy, M. A. Laguna-Marco, M. C. Sánchez, H. Maruyama, N. Kawamura and M. Suzuki, Phys. Rev. B **69**, 134421 (2004).

[102] J. Chaboy, C. Piquer, N. Plugaru, F. Bartolomé, M. A. Laguna-Marco and F. Plazaola, Phys. Rev. B **76**, 134408 (2007).

[103] J. P. Rueff, R. M. Galéra, C. Giorgetti, E. Dartyge, C. Brouder and M. Alouani, Phys. Rev. B **58**, 12271 (1998).

[104] J. Chaboy, M. A. Laguna-Marco, H. Maruyama, N. Ishimatsu, Y. Isohama and and N. Kawamura, Phys. Rev. B **75**, 144405 (2007).

[105] P. Carra, B. N. Harmon, B. T. Thole, M. Altarelli and G. A. Sawatzky, Phys. Rev. Lett. **66**, 2495 (1991).

[106] J. C. Lang, G. Srajer, C. Detlefs, A. I. Goldman, H. König, X. Wang, B. N. Harmon and R. W. McCallum, Phys. Rev. Lett. **74**, 4935 (1995).

[107] T. Jo and S. Imada, J. Phys. Soc. Jpn. **62**, 3721 (1993).

[108] H. Matsuyama, I. Harada and A. Kotani, J. Phys. Soc. Jpn. **66**, 337 (1997).

[109] M. van Veenendaal, J. B. Goedkoop and B. T. Thole, Phys. Rev. Lett. **78**, 1162 (1997).

[110] J.C. Parlebas, K. Asakura, A. Fujiwara, I. Harada and A. Kotani, Phys. Rep. **431**, 1 (2006).

[111] K. Fukui, H. Ogasawara, A. Kotani, I. Harada, H. Maruyama, N. Kawamura, K. Kobayashi, J. Chaboy, and A. Marcelli, Phys. Rev. B **64**, 104405 (2001).

[112] N. H. Duc and T. Goto, *Handbook on the Physics and Chemistry of Rare Earths Vol. 26* (Elsevier Science, Amsterdam, 1999).

[113] J. Herrero-Albillos and L. M. García and F. Bartolomé and A.T. Young and T. Funk, J. Magn. Magn. Mater. **316**, e442 (2007).

[114] J. Herrero-Albillos, D. Paudyal, F. Bartolomé, L. M.García, V. K. Pecharsky, K. A. Gschneider, Jr., A. T. Young, N. Jaouen and A. Rogalev, J. Appl. Phys. **103**, 07E146 (2008).

[115] E. Burzo, Rev. Prog. Phys. **61**, 1099 (1998).

[116] J. Chaboy, M. A. Laguna-Marco, C. Piquer, R. Boada, H. Maruyama and N. Kawamura, Journal of Synchrotron Radiat. **15**, 440 (2008).

[117] R. Boada and M. A. Laguna-Marco and J. Chaboy, Journal of Synchrotron Radiat. **16**, 38 (2009).

[118] R. Boada, C. Piquer, M. A. Laguna-Marco, and J. Chaboy, Phys. Rev. B **81**, 100404(R) (2010).

[119] M. Aoki and Y. Yamada, J. Magn. Magn. Mater. **78**, 377 (1989).

[120] M. Aoki and Y. Yamada, Physica B **177**, 259 (1979).

[121] J. E. Müller and J. W. Wilkins, Phys. Rev. B **29**, 4331 (1984).

[122] J. Chaboy, M. A. Laguna-Marco, C. Piquer, H. Maruyama, N. Kawamura, N. Ishimatsu, M. Suzuki, and M. Takagaki, Phys. Rev. B **75**, 064410 (2007).

[123] J. Chaboy and C. Piquer, Phys. Rev. B **66**, 104433 (2002).

[124] J.I. Espeso, J. C. Gomez-Sal and J. Chaboy, Phys. Rev. B **63**, 014416 (2000).

[125] G. Materlik, J.E. Müller and J.W. Wilkins, Phys. Rev. Lett. **50**, 267 (1983).

[126] G. Materlik, B. Sonntag and M. Tausch, Phys. Rev. Lett. **51**, 1300 (1983).

[127] F. Baudelet, C. Brouder, E. Dartyge, A. Fontaine, J. P. Kappler, and G. Krill, Europhys. Lett. **13**, 751 (1990).

[128] A.P. Murani, Physica B **345**, 89–92 (2004).

[129] J. Chaboy, P. Lázpita, J. M. Barandiarán, J. Gutiérrez, M. L. Fernández-Gubieda and N. Kawamura, J. Phys.: Condens. Matter **21**, 016002 (2009).

[130] N. Kawamura, H. Maruyama, M. Suzuki and T. Ishikawa, J. Phys. Soc. Jpn. **76**, 074716 (2007).

[131] C.T. Chen, Y. U. Idzerda, H. J. Lin, G. Meigs, A. Chaiken, G. A. Prinz and G. H. Ho, Phys. Rev. B **48**, 642 (1993).

[132] S. Pizzini, A. Fontaine, L. M. Garcia, J. F. Bobo, M. Piecuch, F. Baudelet, C. Malgrange, A. Alimoussa, E. Snoeck and M. J. Casanove, J. Magn. Magn. Mater. **166**, 38 (1997).

[133] I. Nakai, H. Tanaka, A. Kitabatake, J. Fukuoka, S. Yamada and N. Ohnishi, J. Magn. Magn. Mater. **310**, 1868 (2007).

[134] C. Huygens, *Traité de la lumière* (Leiden, 1690).

[135] M. Faraday, *Experimental Reserach, vol. 3* (London, 1855).

[136] J. Kerr, Phil. Mag. **3**, 321 (1877).

[137] E. Dartyge, F. Baudelet, C. Giorgetti and S. Odin, J. Alloys and Compounds **275-277**, 526 (1998).

[138] W.C. Röntgen, Physik. Med. Ges. **137**, 132 (1895).

[139] D. M. P. Holland, Physica Scripta **36**, 22 (1987).

[140] T. Funk, A. Deb, S. J. George, H. Wang and S. P. Cramer, Coord. Chem. Rev. **249**, 3 (2005).

[141] H. Kawata, T. Miyahara, S. Yamamoto, T. Shioya, H. Kitamura, S. Sato, S. Asaoka, N. Kanaya, A. Iida, A. Mikuni, M. Sato, T. Iwazumi, Y. Kitajima and M. Ando, Rev. Sci. Intrum. **60**, 1885 (1988).

[142] K. Hirano and H. Maruyama, Jpn. J. Appl. Phys. **36**, L1272 (1997).

[143] M. Suzuki, N. Kawamura and T. Ishikawa, Rev. Sci. Intrum. **74**, L1488 (2003).

[144] K. Hirano, K. Izumi, T. Ishikawa, S. Annaka and S. Kikuta, Jpn. J. Appl. Phys. **30**, L407 (1991).

[145] B.W. Batterman and H. Cole, Rev. Mod. Phys. **36**, 681 (1964).

[146] G. R. Castro, Journal of Synchrotron Radiat. **5**, 657 (1998).

ISBN 978-84-15274-01-8

Prensas Universitarias
Universidad Zaragoza